INGENIEURFAKULTÄT BAU GEO UMWELT

Accuracy of Current and Future Satellite Navigation Systems

Habilitation
von

Peter Steigenberger

TECHNISCHE UNIVERSITÄT MÜNCHEN

Technische Universität München

Institut für Astronomische und Physikalische Geodäsie

Genauigkeitspotential bestehender und zukünftiger Satellitennavigationssysteme

Peter Steigenberger

Von der Ingenieurfakultät Bau Geo Umwelt der Technischen Universität München zur Verleihung der Lehrbefähigung für das Fachgebiet

Geodätische Raumverfahren

genehmigte Habilitationsschrift.

Gutachter:
1. Univ.-Prof. Dr. phil. nat. U. Hugentobler
2. Univ.-Prof. Dr.-Ing. habil. Th. Wunderlich
3. Univ.-Prof. Dr.-Ing. Dr. h.c. Harald Schuh, Technische Universität Berlin

Die Habilitationsschrift wurde am 25. August 2014 bei der Technischen Universität München eingereicht. Der Antrag auf Erteilung der Lehrbefähigung wurde durch die Ingenieurfakultät Bau Geo Umwelt am 31. Mai 2016 angenommen.

Contents

1 Introduction **1**

I Global and Regional Navigation Satellite Systems **3**

2 GNSS Basics **4**
2.1 GNSS Design . . . 4
2.2 GNSS Signals . . . 5
2.3 Observation Equation . . . 6
2.4 Error Budget . . . 6

3 History and Current Status of Satellite Navigation Systems **10**
3.1 Global Positioning System . . . 10
3.2 GLONASS . . . 11
3.3 Galileo . . . 12
3.4 BeiDou/Compass . . . 14
3.5 Quasi Zenith Satellite System . . . 15
3.6 Indian Regional Navigation Satellite System . . . 15

4 Summary of the Papers **20**
4.1 Accuracy and Systematic Errors of GPS-derived Station Positions . . . 20
4.2 Orbit and Clock Determination of New GNSS . . . 21

II Papers **30**

5 GPS-Specific Local Effects at the Geodetic Observatory Wettzell **31**
5.1 Introduction . . . 31
5.2 GPS Processing . . . 32
5.3 Comparisons with Terrestrial Measurements . . . 33
5.4 Individual Antenna Calibrations . . . 34
5.5 Conclusions . . . 35

6 Precision and Accuracy of GPS-derived Station Displacements **37**
6.1 Introduction . . . 37
6.2 Space Geodetic Solutions . . . 38
6.3 Precision . . . 38
6.4 Accuracy . . . 44
6.5 Summary and Conclusions . . . 45

7 Vertical Deformations from Homogeneously Processed GRACE and Global GPS Long-Term Series **50**
7.1 Introduction . . . 50
7.2 Data Sets Used . . . 52
7.3 GPS and GRACE Deformation Signals, Results . . . 55
7.4 Further Discussion of the GPS/GRACE Height Residuals . . . 65
7.5 Summary and Outlook . . . 67

8 Precise Orbit Determination of GIOVE–B Based on the CONGO Network **72**
8.1 Introduction . . . 72
8.2 GNSS Processing . . . 74
8.3 Orbit Validation . . . 76
8.4 Summary . . . 80

9 Galileo Orbit Determination using Combined GNSS and SLR Observations 83
9.1 Introduction . . . 83
9.2 GNSS and SLR Processing . . . 84
9.3 Orbit Results . . . 86
9.4 Impact of Orbits on Satellite Clock Estimates . . . 89
9.5 Conclusions . . . 93

10 Signal, Orbit and Attitude Analysis of Japan's First QZSS Satellite Michibiki 97
10.1 Quasi-Zenith Satellite System Overview and Tracking Network . . . 97
10.2 Carrier-to-Noise Density Ratio . . . 98
10.3 Noise and Multipath Analysis . . . 99
10.4 Yaw-Attitude Profile . . . 101
10.5 Orbit Determination . . . 101
10.6 Conclusions . . . 103

11 Orbit and Clock Determination of QZS-1 Based on the CONGO Network 105
11.1 Introduction . . . 105
11.2 GNSS Processing . . . 107
11.3 Orbit Results . . . 108
11.4 Clock Results . . . 111
11.5 Conclusions . . . 114

12 Orbit and Clock Analysis of Compass GEO and IGSO Satellites 117
12.1 Introduction . . . 117
12.2 GNSS Processing . . . 120
12.3 Orbit Results . . . 123
12.4 Clock Results . . . 126
12.5 Compass-only PPP . . . 127
12.6 Conclusions . . . 128

III Appendices 132

A Abbreviations 133

B Multi-GNSS Receiver Tracking Capabilities 138

C Lists of Multi-GNSS stations 139
C.1 Cooperative Network for GNSS Observation . . . 139
C.2 IGS Multi-GNSS Experiment . . . 140
C.3 Additional Stations . . . 140

1 Introduction

Global Navigation Satellite Systems (GNSSs) have revolutionized geosciences and in particular geodesy in the past years. Determination of station coordinates and velocities is nowadays possible with unprecedented accuracy thanks to navigation satellites in Medium Earth Orbit (MEO). The well established and fully operational Global Positioning System (GPS) operated by American Department of Defense (DoD) and the Russian Globalnaya Navigatsionnaya Sputnikovaya Sistema (GLONASS) are in process of modernization to meet future requirements (Bonnor, 2012). Europe and China are building up their own GNSS, namely Galileo and BeiDou. These systems are expected to be operational until 2020. Whereas the systems mentioned so far are accessible worldwide and can be used independently from each other, the Japanese Quasi-Zenith Satellite System (QZSS; Inaba et al, 2009) is a regional augmentation system for GPS with satellites in Inclined Geosynchronous Orbit (IGSO) and Geostationary Earth Orbit (GEO). A four satellite constellation is planned to be operational until 2018 (Inside GNSS, 2012). The Indian Regional Navigation Satellite System (IRNSS) is also a regional system but independent from GPS. Altogether more than 120 GNSS satellites are expected to be in orbit until 2030 (Gao and Enge, 2012).

The scientific community started in the late eighties to use GPS for geodynamical studies. The establishment of the International GNSS Service (IGS) in 1994 (Beutler et al, 1994) was primarily motivated by the lack of precise orbit products. Already before the official start of the IGS as a service of the International Association of Geodesy (IAG) in 1994, several analysis centers provided orbits of the GPS satellites in the framework of the IGS Test Campaign and the IGS Pilot Service (Beutler, 1993). A combined orbit product generated by the IGS Analysis Center Coordinator (ACC) is provided since December 1993.

Public GNSS usage was basically limited to GPS until the end of the nineties. In 1998, the IGS initiated the International GLONASS Experiment (IGEX) to foster the usage of this GNSS (Slater et al, 1999). In 2001 the International GLONASS Service Pilot Project (IGLOS-PP) was started within the IGS with the goal to include GLONASS observation data as well as products in the operational IGS data and product flow (Dow et al, 2009). The pilot project was concluded when this goal was reached in December 2005. However, the number GLONASS tracking stations as well as analysis centers analyzing GLONASS data is still limited today.

In view of the emerging GNSSs, the IGS initiated a Multi-GNSS Experiment (MGEX). MGEX has basically the same components as the operational IGS: a global tracking network of GNSS stations, analysis centers generating orbit and clock products, and data centers providing the observation data as well as products to the users. Current precise MGEX products cover Galileo, BeiDou, and QZSS. However, it has to be emphasized that MGEX is still an experiment although the implementation of *all* GNSS into the operational IGS activities is the major goal for the future. Remaining major challenges of the new GNSS are the biases between different signals, frequencies and systems that have to be handled consistently in multi-GNSS analysis and a proper modeling of the solar radiation pressure.

An aspect that is not only important for the emerging GNSS but also for the legacy systems is the quality of GNSS-derived parameters. When talking about quality one has to distinguish between *precision* and *accuracy*. Precision describes the scatter of individual estimates that are expected to be identical around the mean value. It can be evaluated by, e.g., the Standard Deviation (STD). Utilization of formal errors derived from the parameter estimation process to assess the precision of GNSS-derived parameters is often problematic as the formal errors are usually too optimistic due to neglected correlations between observations of different epochs.

Accuracy describes the deviation of the estimates from the true value. It is more difficult to evaluate the accuracy than the precision due to the presence of systematic errors like multipath that might only affect the accuracy but not the precision and due to the difficulty to answer the question what the true value is. The accuracy can be evaluated by comparisons with results obtained from different observation techniques or geophysical models.

This thesis is divided into three parts. The first part shortly introduces the basic theory and the error sources of satellite navigation systems. The current status as well as the future plans for existing and evolving global and regional satellite navigation systems are presented. The stations and the general strategy used for orbit and clock determination in this thesis are discussed. The most important results of Sect. 5 – 12 are summarized in Sect. 4.

The second part deals with the precision and accuracy as well as accuracy-limiting factors of GNSSs available today. Coordinate time series of several co-located GPS receivers and precise terrestrial measurements allow for an assessment of technique-specific local effects at the Geodetic Observatory Wettzell. Homogeneously reprocessed long time series of station coordinates provide the basis for assessing the accuracy and precision of GPS-derived station coordinates and velocities. Vertical deformations derived from the GRACE satellite mission serve as validation tool for the GPS-derived station height and the impact of local (station-specific) effects on positioning is analyzed.

First applications of evolving satellite navigation systems, in particular the European Galileo, the Chinese Compass or BeiDou Navigation Satellite System (BDS), and the Japanese QZSS are topic of the third part. Different arc lengths and sets of parameterizations are tested for orbit and clock determination. The accuracy and precision of the derived orbit and clock products is evaluated by orbit fits, day boundary discontinuities, SLR residuals, and Allan deviations.

Bibliography

Beutler G (1993) The 1992 IGS Test Campaign, Epoch'92, and the IGS Pilot Service: An overview. In: Beutler G, Brockmann E (eds) Proceedings of the 1993 IGS Workshop, Druckerei der Univertität Bern, Berne, pp 3–9

Beutler G, Mueller I, Neilan R (1994) The International GPS Service for Geodynamics (IGS): Development and start of official service on 1 January 1994. Bulletin Geodesique 68(1):43–51

Bonnor N (2012) A brief history of Global Navigation Satellite Systems. The Journal of Navigation 65(1):1–14, DOI 10.1017/S0373463311000506

Dow JM, Neilan RE, Rizos C (2009) The International GNSS Service in a changing landscape of Global Navigation Satellite Systems. Journal of Geodesy 83(3-4):191–198, DOI 10.1007/s00190-008-0300-3

Gao GX, Enge P (2012) How many GNSS satellites are too many? IEEE Transactions on Aerospace and Electronic Systems 48(4):2865–2874

Inaba N, Matsumoto A, Hase H, Kogure S, Sawabe M, Terada K (2009) Design concept of Quasi Zenith Satellite System. Acta Astronautica 65(7-8):1068–1075, DOI 10.1016/j.actaastro.2009.03.068

Inside GNSS (2012) OHB and SSTL win second round of contracts for 8 Galileo FOC satellites. URL `http://www.insidegnss.com/node/2941`, accessed 12-04-2013

Slater JA, Willis P, Beutler G, Gurtner W, Lewandowski W, Noll C, Weber R, Neilan RE, Hein G (1999) The International GLONASS Experiment (IGEX-98): Organization, Preliminary Results and Future Plans. In: Proceedings of ION GPS-99, pp 2293–2302

Part I

Global and Regional Navigation Satellite Systems

2 GNSS Basics

2.1 GNSS Design

GNSSs utilize constellations of satellites in Medium Earth Orbit (MEO) transmitting navigation signals in the microwave band. Orbit characteristics of the American GPS, the Russian GLONASS, the European Galileo and the Chinese Compass or BeiDou system are given in Tab. 2.1. The orbit heights above the Earth surface vary between 19,000 and 23,000 km resulting in orbital periods between 11 and 14 hours. Distribution of the satellites in different positions within one inclined orbital plane and also in different orbital planes results in multi satellite visibility all around the world allowing for global positioning at any time.

Regional satellite navigation systems do not aim at global coverage but focus on a certain area with satellites in Inclined Geosynchronous Orbit (IGSO) or Geostationary Earth Orbit (GEO). GEO, IGSO, and MEO trajectories in the inertial frame are shown in the left part of Fig. 2.1 whereas the groundtracks in the Earth-fixed frame are shown in the right part. A pure regional system is the Indian Regional Navigation Satellite System (IRNSS; ISRO, 2014) whereas BeiDou is the only GNSS that also has a regional component of GEO and IGSO satellites.

In addition, regional Satellite Based Augmentation Systems (SBASs) enhance the capabilities of the global systems by providing ranging signals from additional satellites in IGSO or GEO and/or augmentation data transmitted by these satellites. Examples for SBASs are the American Wide Area Augmentation System (WAAS; FAA, 2008), the European Geostationary Navigation Overlay System (EGNOS; ESA, 2006), the Japanese Quasi-Zenith Satellite System (QZSS) and the Indian GPS-Aided Geo-Augmented Navigation (GAGAN; ISRO, 2014).

	GPS	GLONASS	Galileo	BeiDou
Semi major axis [km]	26,600	25,500	29,600	27,900
Time of revolution	$11^h\ 58^m$	$11^h\ 16^m$	$14^h\ 04^m$	$12^h\ 53^m$
Inclination	55°	65°	56°	55°
# orbital planes	6	3	3	3
# satellites	24 (3 spares)	24 (3 spares)	30 (3 spares)	27 MEOs, 5 GEOs, 3 IGSOs

Tab. 2.1: Orbit characteristics of GPS, GLONASS, Galileo, and BeiDou MEO satellites.

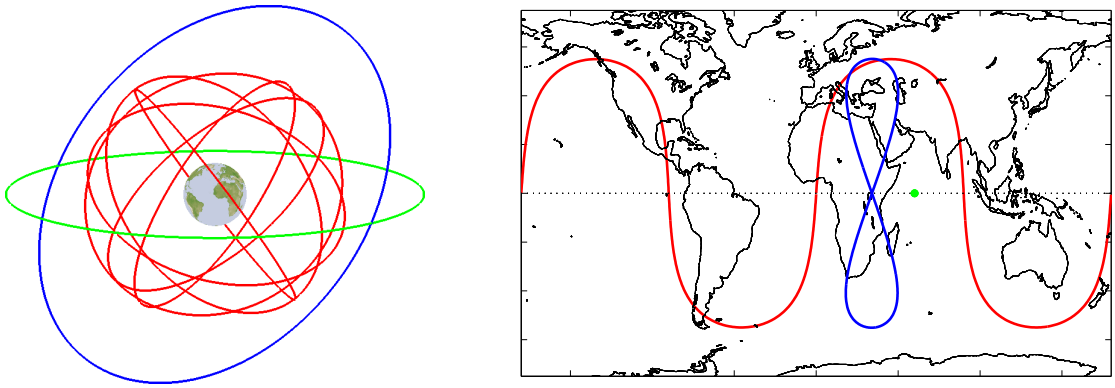

Fig. 2.1: Examples of Geostationary Earth Orbit (GEO, green), Inclined Geosynchronous Orbit (IGSO, blue) and Medium Earth Orbit (MEO, red, six orbital planes as for GPS are shown in the left plot, only one particular satellite in the right plot).

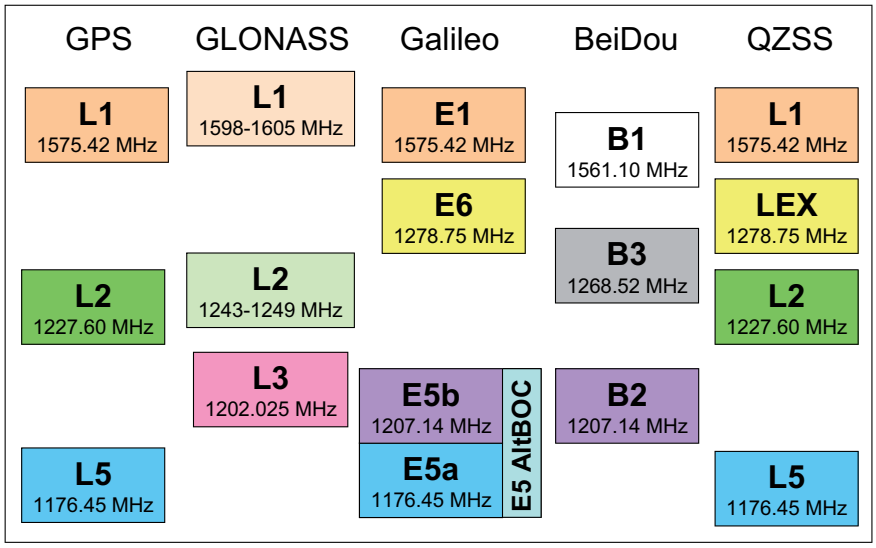

Fig. 2.2: GNSS signals transmitted by GPS, GLONASS, Galileo, Compass/BeiDou, and QZSS.

2.2 GNSS Signals

GNSS satellites transmit signals in the microwave L band covering frequencies between 1 and 2 GHz. Specifically the frequency ranges 1164 – 1300 MHz and 1559 – 1610 MHz are assigned to radio navigation satellites (ERC, 2011). An overview of the different frequencies used by GPS, GLONASS, Galileo, BeiDou, and QZSS is given in Fig. 2.2. The first GPS and GLONASS satellites were only capable of transmitting on two frequencies, namely L1 and L2. The latest generations of all GNSSs transmit signals on three frequencies, Galileo and QZSS even on four frequencies. In general, all satellites use the same frequencies and the individual satellites are distinguished by different code signals (Code Division Multiple Access). However, GLONASS satellites transmit the same code signals on different frequencies (Frequency Division Multiple Access). GPS started with the civil C/A code signal on the L1 frequency and the military (encrypted) P code on the L1 and L2 frequency. Latest generation GPS satellites and in particular the Galileo satellites transmit a variety of code signals on the different frequencies shown in Fig. 2.2. For a complete list see Gurtner and Estey (2009).

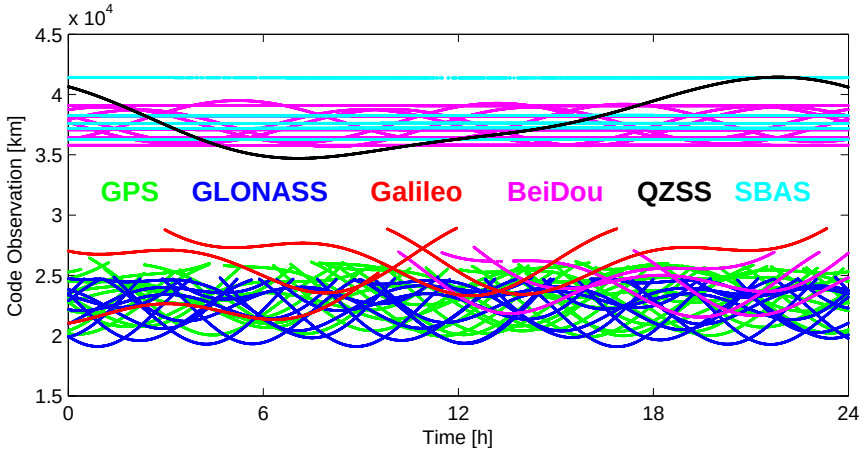

Fig. 2.3: Code observations of an up-to-date multi-GNSS receiver tracking GPS, GLONASS, QZSS, Galileo, BeiDou, and several SBAS satellites.

Figure 2.3 illustrates single-frequency observations of a multi-GNSS receiver. Dense bands can be seen for the fully deployed GPS and GLONASS constellations. Four BeiDou and Galileo MEOs were active at that time. The significantly different pseudoranges of the BeiDou and SBAS GEO satellites originate from unequal satellite clock offsets as well as unequal distances due to different longitudes of the satellites in the equatorial plane. The larger eccentricity of the QZSS orbit compared to the BeiDou IGSOs becomes also obvious in the code observations.

2.3 Observation Equation

The general principle of GNSS is measuring the travel time of microwave signals. As this travel time is measured with different clocks (in the receiver and at the satellite), these clocks have to be synchronized by estimating the receiver clock offset. In addition to the geometric distance between the satellite and receiver, atmospheric propagation delays caused by the ionosphere and the troposphere have to be considered. Smaller effects are related to biases of the code and phase observations, antenna-related effects, and relativistic effects. The code and phase observation equations read as

$$P_R^S = \rho_R^S + c \cdot \left(\Delta t_R - \Delta t^S + b_{R,C} + b^{S,C}\right) + \Delta\rho_{ion} + \delta\rho_{x,i} \tag{2.1}$$

and

$$L_R^S = \rho_R^S + c\left(\Delta t_R - \Delta t^S\right) - \Delta\rho_{ion} + \lambda \cdot \left[n_R^S + \delta n_R^S + \frac{c}{\lambda}\left(b_{R,P} + b^{S,P}\right)\right] + \delta\rho_{x,i} \tag{2.2}$$

with

ρ_R^S	geometric distance
c	vacuum speed of light
Δt_R	receiver clock correction
Δt^S	satellite clock correction
$\Delta\rho_{ion}$	ionospheric delay
n_R^S	integer ambiguity
δn_R^S	phase wind-up
$b_{R,C}, b^{S,C}$	receiver and satellite code biases
$b_{R,P}, b^{S,P}$	receiver and satellite phase biases.

For phase observations, ambiguities have to be estimated and the phase wind-up effect (Wu et al, 1993) has to be considered. $\Delta\rho_{x,i}$ summarizes several effects and models for an observable i whose order of magnitude and accuracy are discussed in Sect. 2.4.

$$\Delta\rho_{x,i} = \Delta\rho_{trp} + \Delta\rho_{mp,i} + \Delta\rho_{rel} + \Delta\rho_{pc,i} + \Delta\rho_{def} + \epsilon_{R,i}^S \tag{2.3}$$

$\Delta\rho_{trp}$	tropospheric delay
$\Delta\rho_{mp,i}$	influence of multipath
$\Delta\rho_{rel}$	relativistic effects
$\Delta\rho_{pc,i}$	phase center variations and offsets
$\Delta\rho_{def}$	deformation effects of the reference point
$\epsilon_{R,i}^S$	measurement error.

2.4 Error Budget

The error budget of GNSS observation modeling is composed of measurement errors, errors of the models used in the parameter estimation (e.g., models for deformations of the reference point), and errors of the estimated parameters (e.g., caused by mismodeling and correlations). Table 2.2 tries to summarize the error budget of the parameters and models involved in the GNSS analyses. Whereas orbit errors were the major error source in the early days of GPS, the largest error sources today are the tropospheric refraction and site-specific effects due to multipath.

In addition to the error sources listed in Tab. 2.2, GNSS-derived parameters are affected by systematic errors. Pronounced anomalous periods at 350 days and its integer harmonics are present in time series of GPS-derived station coordinates (Ray et al, 2008) as well as in the satellite orbits (Griffiths and Ray, 2013). The period of 350 days is related to the so-called draconitic year, i.e. the time after that the orientation of the orbital planes w.r.t. the Sun repeats. Due to deficiencies in the orbit modeling, these periods are propagated to other estimated

Model component	Max. Effect	Model/estim. error	References
Satellite orbits	–	few cm for GPS	IGS ACC[a]
Satellite clocks	up to 1 ms[b]	≈75 ps for GPS	IGS ACC[a]
Receiver clocks	up to 1 ms	≈75 ps	IGS ACC[a]
Polar motion	up to 0.5 as	30 μas	IGS ACC[a]
LOD	up to 3 ms	10 μs	IGS ACC[a]
Subdaily polar motion	±1 mas	0.2 mas[c]	Steigenberger et al (2006)
Subdaily LOD	±0.7 ms	0.1 ms[c]	Steigenberger et al (2006)
Troposphere (dry)	2.3 m[d]	2 – 6 mm	Bock and Doerflinger (2001); Heinkelmann et al (2009); Boehm (2014)
Troposphere (wet)	0 – 40 cm[d]	3 – 6 mm	Nilsson et al (2013) Teke et al (2011)
Ionosphere (1st order)	up to 30 m[e]	LC	Langley (1998)
Ionosphere (higher order)	0 – 2 cm	1 – 2 mm	Hoque and Jakowski (2007)
Plate motion	up to 1 dm/y	0.3 mm/y	Altamimi et al (2012)
Solid Earth tides	up to 40 cm	1 mm	Mathews et al (1997)
Ocean tidal loading	1 – 10 cm	1 – 2 mm	King et al (2010); Melachroinos et al (2008)
Ocean non-tidal loading	up to 15 mm	0.7 mm[f]	van Dam et al (2012)
Pole tides	up to 25 mm	n/a	Petit and Luzum (2010)
Atmospheric non-tidal loading	up to 20 mm	15% of total effect	Petrov and Boy (2003, 2004)
Atmospheric tidal loading	up to 1.5 mm	n/a	Petit and Luzum (2010)
Relativistic corrections	up to 7 m[g]	[h]	Ashby (2003)
Phase wind-up	few cm	[i]	Wu et al (1993)
Satellite antenna z-offsets	0.7 – 2.7 m	6 cm	Schmid et al (2007)
Satellite antenna PCVs	up to 12 mm	0.2 – 1.1 mm	Schmid et al (2007)
Receiver antenna PCOs	up to 16 cm	[j]	`igs08.atx`[k]
Receiver antenna PCVs	up to 3 cm	1 – 2 mm	`igs08.atx`;[k] Görres et al (2006)
Phase multipath	up to 6 cm	–	Rost (2011)
Monument noise	up to 3 mm	–	King and Williams (2009)
Phase measurement noise	1 – 2 mm	–	Kaplan and Hegarty (2006)

[a] `http://www.igs.org/products`
[b] maximum value based on the size of the clock correction field in the GPS navigation message (Global Positioning System Directorate, 2012)
[c] RMS differences of GPS-derived 2 h subdaily ERP estimates w.r.t. the IERS2003 model (Steigenberger et al, 2006)
[d] in zenith direction
[e] in zenith direction for GPS L1 frequency
[f] this value is the RMS of height differences obtained with two different ocean models (van Dam et al, 2012)
[g] eccentricity correction for satellite clocks (largest effect)
[h] depending on the order of magnitude of the neglected effects
[i] depending on satellite attitude errors
[j] usually assumed to be free of errors as defined conventionally, errors in the antenna calibration are therefore only present in the PCV values
[k] available at `ftp://ftp.igs.org/pub/station/general/igs08.atx`

Tab. 2.2: Error budget of GNSS phase observations.

parameters like station coordinates and Earth rotation parameters. Several authors found such periods also in parameters determined with Doppler Orbitography and Radiopositioning Integrated by Satellite (DORIS): station coordinates (Le Bail, 2006), Earth rotation parameters (Gambis, 2006), and geocenter coordinates (Gobinddass et al, 2009). Rodriguez-Solano et al (2014) showed that an improved modeling of the radiation pressure with a box-wing model can reduce the systematic errors at draconitic periods in GNSS-derived parameters. However, the further reduction of these systematic errors remains a challenging task for the future.

Bibliography

Altamimi Z, Métivier L, Collilieux X (2012) ITRF2008 plate motion model. Journal of Geophysical Research 117(B7):B07402, DOI 10.1029/2011JB008930

Ashby N (2003) Relativity in the Global Positioning System. Living Reviews 6(1), URL http://relativity.livingreviews.org/Articles/lrr-2003-1/

Bock O, Doerflinger E (2001) Atmospheric modeling in GPS data analysis for high accuracy positioning. Physics and Chemistry of the Earth 26(6-8):373–383

Boehm J (2014) personal communication

van Dam T, Collilieux X, Wuite J, Altamimi Z, Ray J (2012) Nontidal ocean loading: amplitudes and potential effects in GPS height time series. Journal of Geodesy 86(11):1043–1057, DOI 10.1007/s00190-012-0564-5

ERC (2011) The European table of frequency allocations and utilisations covering the frequency range 9 kHz to 3000 GHz. ERC Report, vol 25, Electronic Communications Committee (ECC) within the European Conference of Postal and Telecommunications Administrations (CEPT)

ESA (2006) EGNOS: The European Geostationary Navigation Overlay System: a Cornerstone of Galileo, vol ESA SP-1303. ESA Publications Division

FAA (2008) Global Positioning System Wide Area Augmentation System (WAAS) Performance Standard. Tech. rep., U.S. Department of Transportation

Gambis D (2006) DORIS and the determination of the Earth's polar motion. Journal of Geodesy 80(8-11):640–656, DOI 10.1007/s00190-006-0043-y

Global Positioning System Directorate (2012) Navstar GPS Space Segment/Navigation User Segment Interfaces IS-GPS200G. Tech. rep., URL http://www.gps.gov/technical/icwg/

Gobinddass M, Willis P, de Viron O, Sibthorpe A, Zelensky N, Ries J, Ferland R, Bar-Sever Y, Diament M (2009) Systematic biases in DORIS-derived geocenter time series related to solar radiation pressure mis-modeling. Journal of Geodesy 83(9):849–858, DOI 10.1007/s00190-009-0303-8

Görres B, Campbell J, Becker M, Siemes M (2006) Absolute calibration of GPS antennas: laboratory results and comparison with field and robot techniques. GPS Solutions 10(2):136–145, DOI 10.1007/s10291-005-0015-3

Griffiths J, Ray JR (2013) Sub-daily alias and draconitic errors in the IGS orbits. GPS Solutions 17(3):413–422, DOI 10.1007/s10291-012-0289-1

Gurtner W, Estey L (2009) RINEX, The Receiver Independent Exchange Format, Version 3.01. Tech. rep., URL ftp://ftp.igs.org/pub/data/format/rinex301.pdf

Heinkelmann R, Boehm J, Schuh H, Tesmer V (2009) The effect of meteorological input data on the VLBI reference frames. In: Drewes H (ed) Geodetic Reference Frames, International Association of Geodesy Symposia, vol 134, Springer, pp 245–251, DOI 10.1007/978-3-642-00860-3_38

Hoque MM, Jakowski N (2007) Higher order ionospheric effects in precise GNSS positioning. Journal of Geodesy 81(4):259–268, DOI 10.1007/s00190-006-0106-0

ISRO (2014) Indian Regional Navigation Satellite System (IRNSS). URL http://www.isro.gov.in/applications/satellite-navigation-programme, accessed 08-06-2016

Kaplan ED, Hegarty CJ (eds) (2006) Understanding GPS: Principles and Applications, 2nd edn. Artech House

King MA, Williams SDP (2009) Apparent stability of GPS monumentation from short-baseline time series. Journal of Geophysical Research 114:B10403, DOI 10.1029/2009JB006319

King MA, Altamimi Z, Boehm J, Bos M, Dach R, Elosegui P, Fund F, Hernandez-Pajares M, Lavallee D, Mendes Cerveira PJ, Penna N, Riva RE, Steigenberger P, van Dam T, Vittuari L, Williams S, Willis P (2010) Improved constraints on models of glacial isostatic adjustment: A review of the contribution of ground-based geodetic observations. Surveys in Geophysics 31(5):465–507, DOI 10.1007/s10712-010-9100-4

Langley RB (1998) GPS for Geodesy, Springer, chap Propagation of the GPS signals, pp 111–149

Le Bail K (2006) Estimating the noise in space-geodetic positioning: the case of DORIS. Journal of Geodesy 80(8-11):541–565, DOI 10.1007/s00190-006-0088-y

Mathews P, Dehant V, Gipson J (1997) Tidal station displacements. Journal of Geophysical Research 102(B9):20,469–20,477, DOI 10.1029/97JB01515

Melachroinos SA, Biancale R, Llubes M, Perosanz F, Lyard F, Vergnolle M, Bouin MN, Masson F, Nicolas J, Morel L, Durand S (2008) Ocean tide loading (OTL) displacements from global and local grids: comparisons to GPS estimates over the shelf of brittany, france. Journal of Geodesy 82(6):357–371, DOI 10.1007/s00190-007-0185-6

Nilsson T, Böhm J, Wijaya DD, Tresch A, Nafisi V, Schuh H (2013) Atmospheric Effects in Space Geodesy, Springer, chap Path Delays in the Neutral Atmosphere, pp 73–136. DOI 10.1007/978-3-642-36932-2_3

Petit G, Luzum B (2010) IERS Conventions (2010). IERS Technical Note 36, Verlag des Bundesamtes für Kartographie und Geodäsie, Frankfurt am Main

Petrov L, Boy JP (2003) Atmospheric pressure loading for routine data analysis. In: Proceedings of the workshop: The State of GPS Vertical Positioning Precision: Separation of Earth Processes by Space Geodesy, Cahiers du Centre Européen de Géodynamique et de Séismologie, vol 23, URL http://arxiv.org/abs/physics/0401117

Petrov L, Boy JP (2004) Study of the atmospheric pressure loading signal in very long baseline interferometry observations. Journal of Geophysical Research 109:B03405, DOI 10.1029/2003JB002500

Ray J, Altamimi Z, Collilieux X, van Dam T (2008) Anomalous harmonics in the spectra of GPS position estimates. GPS Solutions 12(1):55–64, DOI 10.1007/s10291-007-0067-7

Rodriguez-Solano CJ, Hugentobler U, Steigenberger P, Bloßfeld M, Fritsche M (2014) Reducing the draconitic errors in GNSS geodetic products. Journal of Geodesy 88(6):559–574, DOI 10.1007/s00190-014-0704-1

Rost C (2011) Phasenmehrwegereduzierung basierend auf Signalqualitätsmessungen geodätischer GNSS-Empfänger. DGK Reihe C, vol 665, Verlag der Bayerischen Akademie der Wissenschaften, Munich

Schmid R, Steigenberger P, Gendt G, Ge M, Rothacher M (2007) Generation of a consistent absolute phase center correction model for GPS receiver and satellite antennas. Journal of Geodesy 81(12):781–798, DOI 10.1007/s00190-007-0148-y

Steigenberger P, Rothacher M, Dietrich R, Fritsche M, Rülke A, Vey S (2006) Reprocessing of a global GPS network. Journal of Geophysical Research 111:B05402, DOI 10.1029/2005JB003747

Teke K, Böhm J, Nilsson T, Schuh H, Steigenberger P, Dach R, Heinkelmann R, Willis P, Haas R, García-Espada S, Hobiger T, Ichikawa R, Shimizu S (2011) Multi-technique comparison of troposphere zenith delays and gradients during CONT08. Journal of Geodesy 85(7):395–413, DOI 10.1007/s00190-010-0434-y

Wu J, Wu S, Hajj G, Bertiger W, Lichten S (1993) Effects of antenna orientation on GPS carrier phase. Manuscripta Geodaetica 18:91–98

3 History and Current Status of Satellite Navigation Systems

This chapter summarizes the most important milestones of the fully deployed and evolving GNSSs: the American Global Positioning System (GPS) and the Russian Globalnaya Navigatsionnaya Sputnikovaya Sistema (GLONASS) as well as the European Galileo and the Chinese BeiDou Navigation Satellite System (BDS). Furthermore, the status of the Indian Regional Navigation Satellite System (IRNSS) and the Japanese regional augmentation system for GPS, namely the Quasi-Zenith Satellite System (QZSS) are presented.

3.1 Global Positioning System

The Navigation System with Time and Ranging (NAVSTAR) GPS is operated by the DoD of the United States of America. It is the successor of the TRANSIT doppler satellite navigation system whose development started in 1959 and which was operational from January 1964 until December 1996 (Bonnor, 2012). The installation of the GPS satellite constellation started in 1978 with the launch of the first Block I satellite. Until 1985, altogether 10 Block I satellites were successfully launched with one launch failure in December 1981.

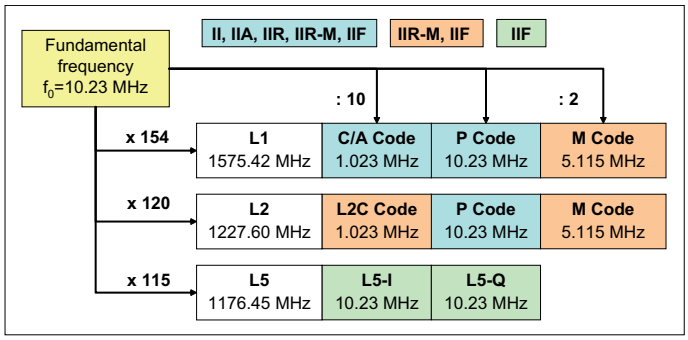

Fig. 3.1: Navigation signals transmitted by different generations of GPS satellites.

In 1989 and 1990 altogether 9 Block II satellites were launched followed by 19 Block IIA satellites between 1990 and 1997 (Dieter and Taylor, 1999). In December 1993 Initial Operational Capability (IOC) and in July 1995 Full Operational Capability (FOC) of the GPS were declared. 1997 marks the beginning of a new satellite generation, namely the Block IIR satellites (Kiser and Vaughan, 1998). Until 2009 21 Block IIR satellites have been launched, 8 of them belonging to the modernized IIR-M type (Hartman et al, 2000), capable of transmitting the civilian L2C signal (Rajan and Tracy, 2002) on the L2 frequency and the military M code on the L1 and L2 frequencies.

SVN49 was the first GNSS satellite simultaneously transmitting triple-frequency navigation signals. However, adding the L5 transmitter as additional payload to an already existing satellite caused systematic effects in the L1 and L2 signals (Springer and Dillssner, 2009; Hauschild et al, 2012a; Thoelert et al, 2012). This effect vanished with the Block IIF satellites (Braschak et al, 2010) but this satellite type suffers from line bias variations probably caused by temperature effects (Montenbruck et al, 2012). Figure 3.1 illustrates the navigation signals transmitted by different generations of GPS satellites. Milestones of the GPS are given in Tab. 3.1, for a more detailed history of the GPS see Bonnor (2012).

A contract for the next generation GPS Block III satellites (see Fig. 3.2) was awarded in 2008 and the first launch is planned for 2015 (Cooley, 2013). Block III satellites will also broadcast the new civilian L1C signal providing a better tracking and ranging performance (Marquis and Shaw, 2011).

22 Feb. 1978	Launch of the first Block I GPS satellite
14 Feb. 1989	Launch of the first Block II GPS satellite
26 Nov. 1990	Launch of the first Block IIA GPS satellite
04 Jul. 1991	Activation of SA
08 Dec. 1993	IOC with 21 satellites
17 Jul. 1995	FOC with 24 satellites
23 Jul. 1997	Launch of the first Block IIR-A GPS satellite
02 May 2000	Deactivation of SA
21 Dec. 2003	Launch of the first Block IIR-B GPS satellite
26 Sep. 2005	Launch of the first Block IIR-M GPS satellite
16 Dec. 2005	First transmission of a L2C signal
24 Mar. 2009	Launch of SVN49 carrying a L5 demonstration payload
10 Apr. 2009	Transmission of the first GPS L5 signal
28 May 2010	Launch of the first Block IIF GPS satellite
17 Jun. 2010	First L5 transmission of a Block IIF GPS satellite

Tab. 3.1: Milestones of the Global Positioning System (Bonnor, 2012; Marquis and Reigh, 2005; Montenbruck et al, 2010; USNO, 1996, 2013a,b).

Fig. 3.2: Artist view of a GPS Block III satellite (Image courtesy of Lockheed Martin).

3.2 GLONASS

The Russian counterpart of GPS, the Globalnaya Navigatsionnaya Sputnikovaya Sistema (GLONASS), was established during the cold war. Like for GPS the nominal satellite number is 24 but the satellites are employed in three orbital planes instead of six. The inclination is 10° larger than for GPS providing a better coverage in higher latitudes. According to Polischuk et al (2002) GLONASS was built up in three phases:

1983 – 1985 Phase 1: experimental tests and system concept refinement with a constellation of 4 – 6 satellites,

1986 – 1993 Phase 2: flight test completion and initial system operation with a constellation of 12 satellites,

1993 – 1995 Phase 3: deployment of the full nominal constellation.

After completing phase 2 the system was declared operational (May, 2012). The nominal number of 24 satellites was reached in 1995. Between 1996 and 1998 the GLONASS constellation was not maintained due to lack of funding (Polischuk et al, 2002). As a consequence, the number of operational satellites rapidly decreased to seven active satellites in 2001. In the following years the constellation again increased due to more frequent launches and reached the number of 24 satellites again in 2011.

16 Dec. 1976	Decree of the Soviet Union Communist Party Central Committee to create a Global Navigation Satellite System
12 Oct. 1982	Launch of the 1st GLONASS satellite
24 Sep. 1993	Initial operational capability with 12 satellites
Jan. 1996	Full constellation of 24 satellites reached for the first time
20 Aug. 2001	Long-term program of GLONASS system modernization approved by the Russian Federation Government
01 Dec. 2001	Launch of a prototype GLONASS-M satellite
10 Dec. 2003	Launch of the 1st operational GLONASS-M satellite
26 Feb. 2011	Launch of the 1st GLONASS-K satellite (IGS: 801)
08 Dec. 2011	Full constellation of 24 satellites reached again

Tab. 3.2: Milestones of the Globalnaya Navigatsionnaya Sputnikovaya Sistema (CANSPACE, 2012; Glotov et al, 2008; Habrich, 2000; Inside GNSS, 2011; Langley, 1997, 2011b; May, 2012).

None of the first generation GLONASS satellites is active anymore. Almost the whole constellation consists of GLONASS-M satellites. However, one satellite of the latest generation of GLONASS-K is already in orbit which is also able to transmit a Code Division Multiple Access (CDMA) signal (Ipatov and Shebshayevich, 2010) on a third frequency called L3. The maintenance of the GLONASS constellation had two major drawbacks in the recent time: two triple launches failed in December 2010 (Inside GNSS, 2013e) and July 2013 (Inside GNSS, 2013f) and the satellites were destroyed. The next generation GLONASS-K2 satellites (Urlichich et al, 2011) will transmit the traditional Frequency Division Multiple Access (FDMA) signals on L1 and L2 and new CDMA signals on L1, L2, and L3. The first launch is planned for 2015 (Russian Space Web, 2014) and the complete constellation should be updated by 2021.

3.3 Galileo

Galileo is a European GNSS initiated in the early 1990s by the European Space Agency (ESA) and the European Commission (EC). The project was significantly delayed by trying to finance it with a public private partnership (Hansen and Wouters, 2012). Finally the EC provided the full funding and ESA is responsible for the technical implementation. The technological development started with the Galileo System Test Bed (GSTB). The main goal of GSTB-V1 was the verification of the Galileo concepts and algorithms using the GPS constellation as space segment (Falcone et al, 2002). The establishment of the Galileo space segment started with two prototype satellites called Galileo in Orbit Validation Element (GIOVE) within the GSTB-V2. The primary goal of GIOVE-A (Benedicto et al, 2006) launched in 2005 was to secure the frequency allocation by the International Telecommunication Union (ITU). This goal was achieved on 12 January 2006 by the first transmission of a Galileo signal from space. GIOVE-B (Malik et al, 2009) was the first satellite carrying a Passive Hydrogen Maser (PHM) in addition to the well established Rubidium Atomic Frequency Standards (RAFSs). Well beyond their designated life time, GIOVE-A and -B were decommissioned in June and July 2012, respectively. In early 2013, after transition to a graveyard orbit, the GPS receiver onboard GIOVE-A was reactivated and tracked the first time GPS signals from an altitude higher than the GPS satellite orbits (Inside GNSS, 2013d).

In October 2011, the first two In-Orbit Validation (IOV) satellites (see Fig. 3.3) were launched from Kourou with a Soyuz launcher (GPS World, 2011). They are equipped with two hydrogen masers and two rubidium clocks and are denoted as PFM (Proto-Flight Model) and FM2 (Flight Model 2). Two further IOV satellites were launched in October 2012 (FM3 and FM4, GPS World, 2012). This mini constellation of four satellites in two different orbital planes serves for validation of the navigation payload and the infrastructure on ground. 14 satellites built by OHB were planned to be launched by end of 2014 to achieve Initial Operational Capability (called FOC Phase 1 by ESA) although this schedule seems not to be realistic anymore. However, according to Châtre (2013) early services for the Open Service (OS), the Search and Rescue (SAR), the Public Regulated Service (PRS), and the Commercial Service (CS) should be provided by 2014/2015. The main difference between the FOC and the IOV satellites is the slightly reduced transmit power of the FOC satellites (Inside GNSS, 2013c). The true FOC consists of 27 operational and 3 spare satellites and should be in place until 2018 (Châtre, 2013).

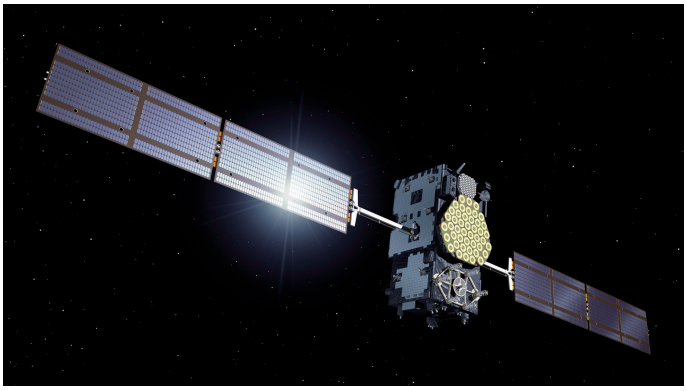

Fig. 3.3: Artist view of a Galileo IOV satellite (Image courtesy of ESA).

May 1996	Approval of the Galileo definition phase by the Ministerial Council of ESA
26 Mar. 2002	Funding of Galileo development phase approved by the European Council of Transport Ministers
2002	Start of GSTB-V1
July 2003	Start of GSTB-V2
22 Dec. 2004	GSTB-V1 completed
28 Dec. 2005	Launch of GIOVE-A
12 Jan. 2006	Start of GIOVE-A signal transmission
19 Jan. 2006	Contract for 4 Galileo IOV satellites signed
27 Apr. 2008	Launch of GIOVE-B
07 May 2008	Start of GIOVE-B signal transmission
07 Jan. 2010	Contract for 14 Galileo FOC satellites signed
25 Oct. 2010	Contract for system operations signed with Spaceopal
21 Oct. 2011	Launch of the first two IOV satellites PFM and FM2
10 Dec. 2011	E1 test transmission of IOV PFM
14 Dec. 2011	Start of IOV PFM E5 signal transmission
16 Jan. 2012	Start of IOV FM2 E1 transmission
18 Jan. 2012	Start of IOV FM2 E5 transmission
02 Feb. 2012	Contract for 8 further Galileo satellites signed
30 Jun. 2012	GIOVE-A decommissioned
23 Jul. 2012	GIOVE-B decommissioned
12 Oct. 2012	Launch of the IOV satellites FM3 and FM4
01 Dec. 2012	Start of IOV FM3 transmission
12 Dec. 2012	Start of IOV FM4 transmission
17 Jan. 2013	Start of IOV PFM and FM2 navigation message transmission
23 Jan. 2013	First SAR transponder put into service
12 Mar. 2013	First real-time Galileo-only positioning
09 Apr. 2013	In-orbit test review passed
03 May 2013	First GGTO transmission
01 July 2013	First positioning with PRS signals

Tab. 3.3: Milestones of the Galileo system (Châtre, 2013; EADS, 2013; ESA, 2005, 2006, 2010, 2013; Falcone et al, 2013; Gao et al, 2008; GPS World, 2011, 2012; Hofmann-Wellenhof et al, 2007; Inside GNSS, 2010, 2012b; Lindström and Gasparini, 2003; MGEX, 2013; Montenbruck et al, 2006; monitoring of CONGO tracking data). The ESA websites on GSTB-V1 and GIOVE are unfortunately no longer available.

3.4 BeiDou/Compass

In the 1980s China started with the development of a regional navigation system called BeiDou-1 consisting of nominally two GEO satellites and one backup satellite. A plan for BeiDou-1 was presented in 1983 and a first demonstration of positioning with two other GEO satellites was performed in 1989 (Bian et al, 2005). The operational BeiDou-1 satellites were launched in October and December 2000, respectively.

The following description of the BeiDou-1 system is extracted from Bian et al (2005): In contrast to other GNSSs, BeiDou-1 was based on two-way ranging. Navigation signals are transmitted via an S-band link from the control center to the GEO satellites, sent to the user's receiver and transmitted back in the L-band from the user via the GEO satellite to the control center. The distances from the satellites to the receiver are determined in the control center. As only two distances are known, a Digital Terrain Model (DTM) is necessary for 3D positioning (assuming that the receiver is on the Earth surface). Finally, the receiver position is transmitted to the user. According to Bian et al (2005) horizontal positioning accuracies between 20 and 100 m could be achieved.

The launch of the first MEO satellite in April 2007 was the first milestone of the BeiDou-2 system (also called Compass) aiming at global coverage. In contrast to the other GNSSs discussed so far, BeiDou comprises additional orbit types. BeiDou GEO and IGSO satellites are based on the same satellite bus and have a designated life time of 8 years (Dragon in Space, 2012). Based on a constellation of 4 MEO, 5 GEO, and 5 IGSO satellites, the regional availability for China was reached by end of 2012. Together with the official announcement of the completion of this regional service, the name BeiDou Navigation Satellite System (BDS) was issued at a press conference in December 2012 (Inside GNSS, 2013b). The regional service should be expanded to a global one by increasing the number of MEO satellites until 2020.

30 Oct. 2000	Launch of BeiDou-1A
20 Dec. 2000	Launch of BeiDou-1B
24 May 2003	Launch of BeiDou-1C
02 Feb. 2007	Launch of BeiDou-1D
13 Apr. 2007	Launch of 1st MEO satellite
14 Apr. 2009	Launch of 1st GEO satellite
16 Jan. 2010	Launch of 2nd GEO satellite
02 Jun. 2010	Launch of 3rd GEO satellite
31 Jul. 2010	Launch of the 1st IGSO satellite
31 Oct. 2010	Launch of 4th GEO satellite
17 Dec. 2010	Launch of the 2nd IGSO satellite
09 Apr. 2011	Launch of the 3rd IGSO satellite
26 Jul. 2011	Launch of the 4th IGSO satellite
01 Dec. 2011	Launch of the 5th IGSO satellite
27 Dec. 2011	Initial operational capability announced to China and surrounding area
	Release of the test version of the ICD
24 Feb. 2012	Launch of 5th GEO satellite
29 Apr. 2012	Launch of two MEO satellites (M3 and M4)
18 Sep. 2012	Launch of two MEO satellites (M5 and M6)
25 Oct. 2012	Launch of 6th GEO satellite
	BeiDou phase 1 completed
27 Dec. 2012	Release of Open Service Signal B1 ICD
27 Dec. 2013	Release of Open Service Signal ICD Version 2.0

Tab. 3.4: Milestones of the BeiDou system (Ding, 2011; GPS World, 2012; Inside GNSS, 2012a, 2013b, 2014; Meng et al, 2012). Please note that the launch dates given in Meng et al (2012) refer to local time at the launch site whereas the dates in this table refer to UTC.

Whereas several BeiDou-ready receivers are offered by a variety of manufacturers, only a few receiver types are actually capable of tracking the BeiDou signals. This limitation is attributed to the lack of availability of a complete ICD. A draft version of the ICD was released in December 2011 (China Satellite Navigation Office, 2011) and the Open Service Signal B1 ICD in December 2012 (Inside GNSS, 2013b). In December 2013 a second version of the ICD was published (Inside GNSS, 2014) also including the B2 signal description. Information on other services and signals is still missing. On the one hand, manufacturers like Trimble, Javad, and Septentrio used external information of the decoded signals, e.g. published in Gao et al (2009). On the other hand, there are also manufacturers not providing BeiDou capability before publication of the full ICD. According to Inside GNSS (2013a) the frequency of the B1 signal should be shifted from its current location at 1561.098 MHz to 1575.42 MHz, the same frequency as for GPS L1 and Galileo E1. This shift was originally planned for 2016 but will probably be delayed.

3.5 Quasi Zenith Satellite System

In contrast to the systems discussed so far, the Japanese Quasi-Zenith Satellite System (QZSS; Inaba et al, 2009) is a regional augmentation system for GPS. The major task of QZSS is improving the satellite visibility in difficult environments like urban canyons. Its initial design consists of three IGSO satellites. In 2011 the planned satellite number was increased to seven (Langley, 2011a). The first satellite QZS-1 (also called Michibiki) was launched in September 2010. In contrast to BeiDou IGSO satellites, the orbit has an eccentricity of 0.08 resulting in a groundtrack with the shape of an asymmetric figure of eight. This orbit design maximizes the visibility close to the zenith over Japan.

In addition to L1, L2, and L5 signals compatible with GPS, QZSS satellites transmit a Submeter-class Augmentation with Integrity Function (SAIF) signal in the L1 band and a L-Band Experimental (LEX) signal in the E6 band. The SAIF signal provides augmentation functionality with a positioning accuracy better than 1 m and additional integrity information (Sakai et al, 2009). QZS-1 is the first GNSS satellite transmitting its navigation signals via two different antennas. The L1 SAIF signal is transmitted from a dedicated antenna separated about 1.3 m from the main antenna. This allows for a determination of the satellite's attitude based on signals from both antennas as discussed in Hauschild et al (2012b).

In 2013 the Japanese government ordered three further QZSS satellites that should be launched until 2017 (Spaceflight Now, 2013). Two of them will be IGSO satellites whereas the third satellite will be placed in a geostationary orbit. These satellites will be operational in 2018.

11 Sep. 2010	Launch of QZS-1
27 Sep. 2010	Final orbit reached, begin of On-Orbit-Checkout (OOC) including transmission of non-standard codes
∼15 Dec. 2010	Transmission of standard codes
22 Jun. 2011	L1-C/A and L2C signals set healthy
14 Jul. 2011	L1C and L5 signals set healthy
29 Mar. 2013	Extension of QZSS by 3 further satellites announced

Tab. 3.5: Milestones of the Quasi-Zenith Satellite System (Kishimoto et al, 2012; Spaceflight Now, 2013).

3.6 Indian Regional Navigation Satellite System

In 2006 India decided to establish the Indian Regional Navigation Satellite System (IRNSS) consisting of 3 GEO and 4 IGSO satellites (Li et al, 2011). The satellites are equipped with three RAFSs (Mallette et al, 2010). The first satellite IRNSS-1A (see Fig. 3.4) was launched on 1 July 2013 (GPS World, 2013) into a geosynchronous orbit with 29° inclination. One special aspect of IRNSS is its selection of frequencies for the transmission of navigation signals. The first frequency is identical with GPS L5 but the second frequency is located in the S-band at 2492.028 MHz. Currently no commercial receivers are available covering both frequencies.

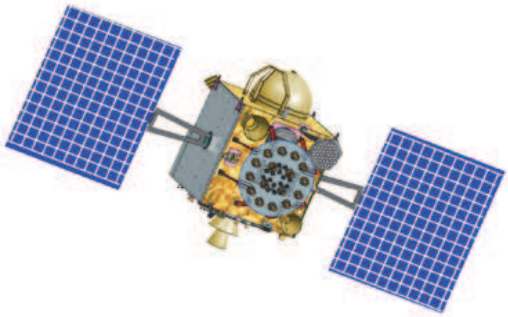

Fig. 3.4: Artist view of the first IRNSS satellite IRNSS-1A (Image courtesy of ISRO).

Bibliography

Benedicto J, Gatti G, Garutti A, Paffet J, Bradford A, Jackson C, Rooney E (2006) The triumph of GIOVE-A – the first Galileo satellite. ESA Bulletin 127:62–69

Bian S, Jin J, Fang Z (2005) The Beidou satellite positioning system and its positioning accuracy. Navigation 52(3):123–130

Bonnor N (2012) A brief history of Global Navigation Satellite Systems. The Journal of Navigation 65(1):1–14, DOI 10.1017/S0373463311000506

Braschak M, Jr HB, Carberry J, Grant T, Hatten G, Patocka R, Watts E (2010) GPS IIF satellite overview. In: Proceedings of ION GNSS 2010, pp 753–770

CANSPACE (2012) GLONASS constellation status. URL `http://www2.unb.ca/gge/Resources/GLONASSConstellationStatus.txt`

Châtre E (2013) Galileo programme status update. In: Proceedings of ION GNSS+ 2013, pp 555–579

China Satellite Navigation Office (2011) BeiDou Navigation Satellite System Signal In Space Interface Control Document (Test Version). Tech. rep., URL `http://www.beidou.gov.cn/attach/2011/12/27/201112273f3be6124f7d4c7bac428a36cc1d1363.pdf`

Cooley B (2013) GPS program update to ION GNSS+ 2013. In: Proceedings of ION GNSS+ 2013, pp 537–554

Dieter GL, Taylor J (1999) GPS Block II operations reach a ten year benchmark: Managing a mature constellation. In: Proceedings of ION GPS-99, pp 2261–2268

Ding X (2011) Development of BeiDou Navigation Satellite System. In: Proceedings of ION GNSS 2011, pp 882–912

Dragon in Space (2012) URL `http://web.archive.org/web/20121028161922/http://www.dragoninspace.com/navigation/beidou.aspx`, accessed 04-09-2012

EADS (2013) Astrium Galileo satellites: Last project milestone successfully completed. URL `http://www.astrium.eads.net/en/news2/-ky2.html`, accessed 02-05-2013

ESA (2005) Galileo System Test Bed Version 1 experimentation is now complete. URL `http://www.esa.int/Our_Activities/Navigation/Galileo_System_Test_Bed_Version_1_experimentation_is_now_complete`, accessed 28-02-2014

ESA (2006) Galileo In-Orbit Validation contract signed. URL `http://www.esa.int/About_Us/Industry/Galileo_in-orbit_validation_contract_signed`, accessed 03-07-2014

ESA (2010) Contract signing gives Galileo system its operators. URL `http://www.esa.int/Our_Activities/Navigation/Contract_signing_gives_Galileo_system_its_operators`, accessed 11-04-2013

ESA (2013) Galileo fixes Europe's position in history. URL `http://www.esa.int/Our_Activities/Navigation/Galileo_fixes_Europe_s_position_in_history`, accessed 11-04-2013

Falcone M, Amarillo-Fernandez F, Hahn J, Favin-Leveque H (2002) The GALILEO SYSTEM TEST BED for early prototyping and experimentation of Galileo algorithms. In: Proceedings of ION GPS 2002, pp 2148–2159

Falcone M, Binda S, Breeuwer E, Hahn J, Spinelli E, Gonzalez F, Risueno G, Giordano P, Swinden R, Galluzzo G, Hedquist A (2013) Galileo on its own: First position fix. InsideGNSS 8(2):50–53

Gao G, Akos D, Walter T, Enge P (2008) GIOVE-B on the Air. Inside GNSS 3(4):34–37

Gao GX, Chen A, Lo S, De Lorenzo D, Walter T, Enge P (2009) Compass-M1 broadcast codes in E2, E5b, and E6 frequency bands. IEEE Journal of Selected Topics in Signal Processing 3(4):599–612, DOI 10.1109/JSTSP.2009.2025635

Glotov V, Revnivykh S, Mitrikas V (2008) GLONASS status update. MCC activity in GLONASS program. In: Proceedings of the 15th International Workshop on Laser Ranging, pp 593–596

GPS World (2011) Galileo IOV satellites now in orbit. GPS World 22(11):14

GPS World (2012) Transmissions from Galileo satellite IOV-3 have begun. URL http://www.gpsworld.com/transmissions-from-galileo-satellite-iov-3-have-begun/, accessed 22-02-2014

GPS World (2012) Two Compass satellites launched. URL http://www.gpsworld.com/two-compass-satellites-launched/, accessed 22-02-2014

GPS World (2013) IRNSS success. GPS World 24(8):12

Habrich H (2000) Geodetic applications of the Global Navigation Satellite System (GLONASS) and of GLONASS/GPS combinations. Mitteilungen des Bundesamtes für Kartographie und Geodäsie, vol 15

Hansen R, Wouters J (2012) Towards an EU industrial policy for the space sector – lessons from Galileo. Space Policy 28(2):94–101, DOI 10.1016/j.spacepol.2012.02.009

Hartman T, Boyd LR, Koster D (2000) Modernizing the GPS Block IIR Spacecraft. In: Proceedings of ION GPS 2000, pp 2115–2121

Hauschild A, Montenbruck O, Thoelert S, Erker S, Meurer M, Ashjaee J (2012a) A multi-technique approach for characterizing the SVN49 signal anomaly, part 1: receiver tracking and IQ constellation. GPS Solutions 16(1):19–28, DOI 10.1007/s10291-011-0203-2

Hauschild A, Steigenberger P, Rodriguez-Solano C (2012b) QZS-1 yaw attitude estimation based on measurements from the CONGO network. Navigation, Journal of the Institute of Navigation 59(3):237–248, DOI 10.1002/navi.18

Hofmann-Wellenhof B, Lichtenegger H, Wasle E (2007) GNSS – Global Navigation Satellite Systems: GPS, GLONASS, Galileo & more, 1st edn. Springer, Wien

Inaba N, Matsumoto A, Hase H, Kogure S, Sawabe M, Terada K (2009) Design concept of Quasi Zenith Satellite System. Acta Astronautica 65(7-8):1068–1075, DOI 10.1016/j.actaastro.2009.03.068

Inside GNSS (2010) EC awards major Galileo contracts: GNSS satellites, launch services, support services. URL http://www.insidegnss.com/node/1811, accessed 03-07-2014

Inside GNSS (2011) First GLONASS-K launched; CDMA signals coming. Inside GNSS 6(2):17

Inside GNSS (2012a) 16th Beidou satellite launches. URL http://www.insidegnss.com/node/3246, accessed 14-04-2013

Inside GNSS (2012b) OHB and SSTL win second round of contracts for 8 Galileo FOC satellites. URL http://www.insidegnss.com/node/2941, accessed 12-04-2013

Inside GNSS (2013a) BeiDou to restart satellite launches next year, shift B1 signal frequency after 2016. URL http://www.insidegnss.com/node/3537, accessed 02-05-2013

Inside GNSS (2013b) China publishes official BeiDou civil signal ICD. Inside GNSS 8(1):12

Inside GNSS (2013c) Galileo program points to 2014 start of services. Inside GNSS 8(1):14–16

Inside GNSS (2013d) Galileo satellite achieves high Earth orbit positioning with GPS. URL http://www.insidegnss.com/node/3527, accessed 23-04-2013

Inside GNSS (2013e) GLONASS triple satellite launch suffers rare failure. URL http://www.insidegnss.com/node/2399, accessed 25-07-2013

Inside GNSS (2013f) Premature launch may have doomed GLONASS satellites. URL http://www.insidegnss.com/node/3617, accessed 25-07-2013

Inside GNSS (2014) New BeiDou ICD describes second civil signal; Officials describe progress, plans. URL http://www.insidegnss.com/node/3839, accessed 10-01-2014

Ipatov V, Shebshayevich B (2010) GLONASS CDMA: Some proposals on signal formats for future GNSS air interface. Inside GNSS 5(5):46–51

Kiser K, Vaughan SH (1998) GPS IIR joins the GPS constellation. In: Proceedings of ION GPS-98, pp 1915–1923

Kishimoto M, Myojin E, Kawate K, Miyoshi M, Kogure S, Noda H (2012) Technical verification status of Quasi-Zenith Satellite System. In: Proceedings of ION ITM 2012, pp 1223–1227

Langley R (1997) GLONASS: Review and update. GPS World 8(7):46–51

Langley R (2011a) Constellation updates from ION GNSS 2011. GPS World 22(11):16–17

Langley R (2011b) GLONASS fully operational. CANSPACE

Li B, Zhang S, Dempster AG, Rizos C (2011) Impact of RNSSs on Positioning in the Asia-Oceania Region. Journal of Global Positioning Systems 10(2):114–124, DOI 10.5081/jgps.10.2.114

Lindström G, Gasparini G (2003) The Galileo satellite system and its security implications. No. 44 in Occasional Papers, European Union, Institute for Security Studies

Malik M, Gatti G, Alpe V, Johansson M, Kieffer R, Robertson G (2009) GIOVE-B satellite & payload overview. In: Proceedings of the European Navigation Conference – Global Navigation Satellite Systems

Mallette L, White J, Rochat P (2010) Space Qualified Frequency Sources (Clocks) for Current and Future GNSS Applications. In: Proceedings of IEEE/ION PLANS 2010, pp 903–908, DOI 10.1109/PLANS.2010.5507225

Marquis W, Reigh D (2005) On-orbit performance of the improved GPS Block IIR antenna panel. In: Proceedings of ION GNSS 2005, pp 2418–2426

Marquis W, Shaw M (2011) Design of the GPS III Space Vehicle. In: Proceedings of ION GNSS 2011, pp 3067–3075

May M (2012) GLONASS in perspective. The Quaterly Newsletter of the Institute of Navigation 22(4):4–5

Meng W, Liu E, Han S, Yu Q (2012) Research and development on satellite positioning and navigation in China. IEICE Transactions on Communications E95-B(11):3385–3392

MGEX (2013) Home page of the IGS multi-GNSS experiment. URL http://mgex.igs.org, accessed 12-04-2013

Montenbruck O, Günther C, Graf S, Garcia-Fernandez M, Furthner J, Kuhlen H (2006) GIOVE-A initial signal analysis. Journal of Geodesy 10(2):146–153, DOI 10.1007/s10291-006-0027-7

Montenbruck O, Hauschild A, Erker S, Meurer M, Langley R, Steigenberger P (2010) GPS L5: The real stuff. GPS World 21(7):13–14

Montenbruck O, Hugentobler U, Dach R, Steigenberger P, Hauschild A (2012) Apparent clock variations of the Block IIF-1 (SVN62) GPS satellite. GPS Solutions 16(3):303–313, DOI 10.1007/s10291-011-0232-x

Polischuk G, Kozlov V, Ilitchov VV, Kozlov A, Bartenev VA, Kossenko V, Anphimov N, Revnivykh S, Pisarev S, Tyulyakov A, Shebshaevitch B, Basevitch A, Vorokhovsky Y (2002) The Global Navigation Satellite System Glonass: Development and usage in the 21st century. In: 34 th Annual Precise Time and Time Interval (PTTI) Meeting, pp 151–160

Rajan JA, Tracy JA (2002) GPS IIR-M: Modernizing the signal-in-space. In: Proceedings of ION GPS 2002, pp 1585–1594

Russian Space Web (2014) URL http://www.russianspaceweb.com/uragan.html, accessed 03-03-2014

Sakai T, Fukushima S, Ito K (2009) Development of QZSS L1-SAIF augmentation signal. In: ICCAS-SICE 2009, pp 4462–4467

Spaceflight Now (2013) URL http://www.spaceflightnow.com/news/n1304/04qzss/#.UV78d4JuGKy, accessed 11-04-2013

Springer T, Dillssner F (2009) SVN49 and Other GPS Anomalies. Inside GNSS 4(4):32–36

Thoelert S, Meurer M, Erker S, Montenbruck O, Hauschild A, Fenton P (2012) A multi-technique approach for characterizing the SVN49 signal anomaly, part 2: chip shape analysis. GPS Solutions 16(1):29–39, DOI 10.1007/s10291-011-0204-1

Urlichich Y, Subbotin V, Stupak G, Dvorkin V, Povalyaev A, Karutin S (2011) GLONASS Modernization. In: Proceedings of ION GNSS 2011, pp 3125–3128

USNO (1996) Block I satellite information. URL `ftp://tycho.usno.navy.mil/pub/gps/gpsb1.txt`, accessed 12-04-2013

USNO (2013a) Block II satellite information. URL `ftp://tycho.usno.navy.mil/pub/gps/gpsb2.txt`, accessed 12-04-2013

USNO (2013b) GPS constellation status. URL `ftp://tycho.usno.navy.mil/pub/gps/gpstd.txt`, accaccessed 12-04-2013

4 Summary of the Papers

The papers of this thesis can be split into two groups: the first group deals with the accuracy assessment and systematic errors of GPS-derived position estimates. The second group focusses on observations and parameter estimation of the emerging navigation systems Galileo, BeiDou, and QZSS, in particular the determination and quality assessment of precise orbit and clock products.

4.1 Accuracy and Systematic Errors of GPS-derived Station Positions

The errors sources degrading the accuracy of GPS-derived station coordinates were already discussed in Sect. 2.4. Today's most important error sources are the tropospheric refraction and the impact of multipath. Although antennas designed to suppress multipath (like choke ring antennas; Langley, 1998) are widely used, the impact of multipath is still a major problem nowadays. Section 5 discusses the impact of local effects (in particular multipath) on station coordinates estimated from a network with very short baselines at the Geodetic Observatory Wettzell. Station coordinate time series of seven GPS permanent stations were computed from L1 and L2 observations as well as the ionosphere-free linear combination. In addition, highly accurate terrestrial measurements (local ties) are available for most of the GNSS sites and can also be used for validation.

Single-frequency L1 and L2 solutions and solutions from the ionosphere-free linear combination of L1 and L2 differ by up to 5 cm for the height component although most differences are smaller than 2 cm. The largest height difference is caused by an uncalibrated radome emphasizing the importance of proper antenna calibrations. The height differences w.r.t. the terrestrial measurements reach 4 cm for the station with the uncalibrated radome but also the other stations show discrepancies up to 15 mm, in particular for the ionosphere-free solutions. The horizontal discrepancies are in general smaller with about 3 mm for the L1 and L2 solutions and up to 6 mm for the ionosphere-free solutions.

For some of the stations, individual antenna calibrations are available. The differences between the type-mean calibrations used within the IGS and the individual calibrations are on the level of $1-4$ mm. The station coordinate solutions obtained with these calibrations differ by up to 5 mm. For some stations the agreement with the terrestrial measurements improves, for other station it degrades. Therefore, no clear conclusion can be drawn on the benefits of individual antenna calibrations.

The differences discussed above clearly exceed the measurement accuracy of the terrestrial measurements (about $1-2$ mm) and GPS on very short baselines (also mm level). The discrepancies are most probably caused by GPS-specific systematic errors that have a different impact on different observables. Multipath is such a frequency-dependent error source that could be caused by reflecting material in the vicinity of the antennas. The minimization of such effects remains a challenge for the future.

In the past, the precision and accuracy of station positions and velocities estimated from long time series of GPS data suffered from the inhomogeneity of the input solutions. Improvements in models and processing strategies as well as changes in the reference frame result in inconsistencies and even discontinuities in long time series based on operational solutions of the IGS Analysis Centers (ACs). All International Terrestrial Reference System (ITRS) realizations prior to ITRF2008 are based on these operational solutions and suffer from these shortcomings. The only way to overcome these inconsistencies is a complete reprocessing starting with the observation files. First reprocessing efforts of global GPS data are documented in Nikolaidis (2002) and Steigenberger et al (2006). The first reprocessing campaign of the IGS started in February 2008 and was concluded in April 2010 (Gendt and Ferland, 2010) although only preliminary clock products were available at that time. The resulting combined IGS solution was used for ITRF2008, the first ITRS realization solely based on reprocessed input data.

However, no efforts were made to homogenize the modeling options of the different space geodetic techniques, namely GNSS, Satellite Laser Ranging (SLR), Very Long Baseline Interferometry (VLBI), and DORIS. To overcome this problem, common standards for modeling and parameterization were defined for the reprocessing of GPS, SLR, and VLBI data in the framework of the GGOS-D project (Rothacher et al, 2011). Together with the contribution of the Center for Orbit Determination in Europe (CODE) to the first IGS reprocessing (Steigenberger

et al, 2011), these solutions provide the basis for the assessment of the accuracy and precision of GPS-derived station positions and velocities discussed in Sect. 6.

The consistency of the GPS solutions is assessed by so-called GPS/GPS colocations, i.e. GPS receivers operated simultaneously at one particular station with their antennas usually separated only a few meters. The horizontal precision obtained from these comparisons is on the level of $0.5-2$ mm whereas the vertical precision is worse with values of $1.5-4$ mm. Velocities derived independently from multi-year solutions covering different time intervals agree on the $0.1-1$ mm/y level for the horizontal and on the $0.3-2$ mm/y level for the vertical component.

The accuracy of GPS-derived velocity estimates can be evaluated by comparisons with velocities determined from independent techniques. Comparisons with SLR- and VLBI-derived velocities from solutions of the GGOS-D project result in general in velocity accuracies of $1-2$ mm/y. Major remaining error sources are troposphere modeling, receiver and satellite antenna calibrations, and orbit modeling deficiencies.

Section 7 uses a completely different method for the validation of GPS-derived station heights, namely height deformations computed from measurements of the time variable gravity field observed by the Gravity Recovery And Climate Experiment (GRACE; Tapley et al, 2004). The GPS height time series originates also from the GGOS-D project but was extended and referred to a reference frame computed from the same data set. Only a selected set of 115 stations with long observing intervals was used. Stations degraded by local or technique-specific artifacts were detected with a cluster analysis and excluded. Deformation time series were computed from monthly GRACE solutions provided by University of Texas Center for Space Research (UTCSR) and Deutsches GeoForschungsZentrum (GFZ) using the load Love numbers of Han and Wahr (1995). A critical issue when comparing GPS- and GRACE-derived deformation time series is the consistency of the reference frame of both series. As the GRACE Satellite-to-Satellite Tracking (SST) is not sensitive to the degree-1 terms of the gravity field (geocenter), these terms are set to zero. However, the degree-1 signals at the GPS stations used for datum definition differ from zero. Therefore, three translations were computed from the GRACE deformations at the datum stations and added to the GPS time series.

The first comparison is based on annual harmonic signals estimated from the GPS and GRACE time series. The mean phase difference is 10° but the GPS amplitudes are on average larger by a factor of 1.7 compared to the GRACE amplitudes. The correlation coefficients between the two different time series are larger than 0.5 for 60% of the stations. In order to account for station-specific differences from the simple harmonic model, mean annual signals were computed by averaging all available monthly solutions for each station. The correlation of mean annual signals is even larger: 77% of the stations exhibit a correlation larger than 0.5.

Residual signals in the GPS – GRACE differences could be attributed to thermal expansion of the GPS monuments and the very upper crust of the Earth. A correlation of the height residuals with thermal deformations derived from global weather model data resulted only for 55% of the stations in a positive correlation coefficient. However, a precision of the monthly GPS – GRACE differences of about 1.6 mm could be demonstrated.

4.2 Orbit and Clock Determination of New GNSS

A prerequisite for data analysis of the new GNSS is the availability of tracking data from a global network. In addition to the GPS legacy frequency bands L1 and L2, receivers and antennas must be able to receive the new signals in the L5/E5 and E6 band. Galileo E6 is limited to the Galileo PRS and CS. As no ICD is available for these services and none of the receivers used is capable of tracking these signals, E6 is not considered in this thesis. As only few receivers are able to track the QZSS LEX signal and the BeiDou B3 signal, these signals are also not considered.

In order to track all signals of all visible GNSS satellites, $200-250$ receiver channels are necessary. The tracking capabilities as regards the different GNSSs as well as the channel number of the receivers used in this thesis are summarized in Tab. B.1. Whereas the frontend of most receivers is capable of tracking the majority of GNSS signals, several receivers suffer from limitations of the current firmware version. E.g., Leica receivers are currently not capable of tracking BeiDou and SBAS L5 although the frontend would be capable of processing these signals. Leica receivers are also not capable of tracking Galileo signals if the clock of the corresponding satellite is not synchronized w.r.t. GPS time. The Trimble NetR9 is currently the only true multi-GNSS receiver capable of tracking all GNSS signals except for Galileo E6 due to the reasons mentioned above.

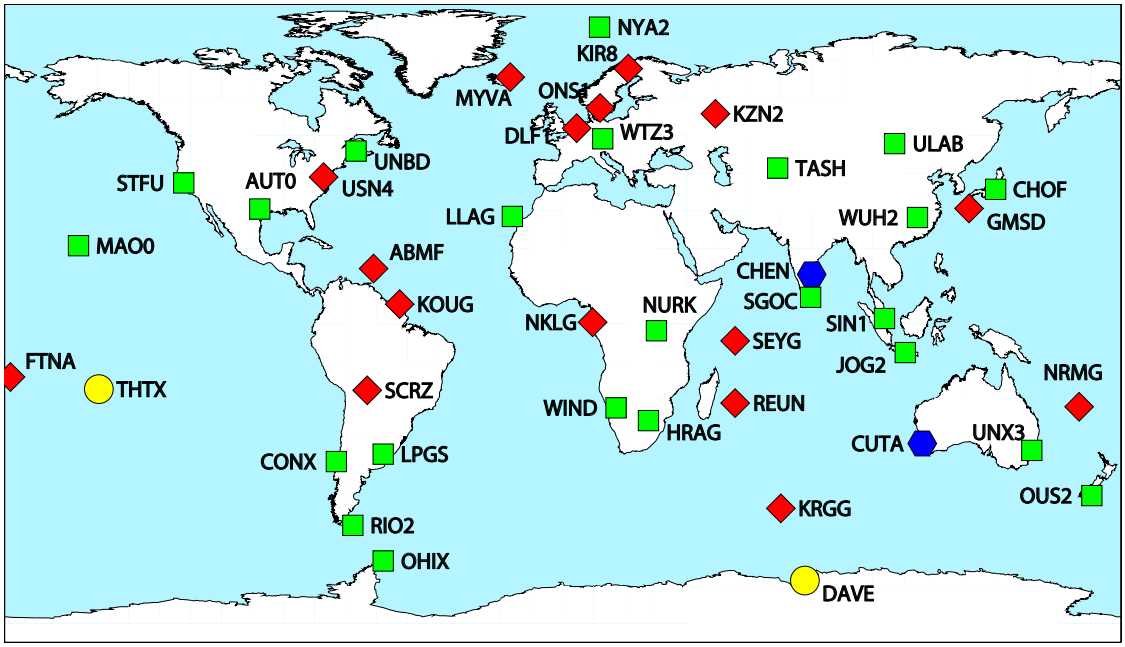

Fig. 4.1: Distribution of GNSS tracking stations used for orbit and clock determination of Galileo, BeiDou, and QZSS. MGEX stations are indicated by red diamonds, stations contributing to CONGO and MGEX by green squares, CONGO-only stations by yellow circles, and other stations by blue hexagons. Lists of the corresponding stations are given in Appendix C.

4.2.1 The Cooperative Network for GNSS Observation

In order to study the signals of new GNSSs, Deutsches Zentrum für Luft- und Raumfahrt (DLR) and Bundesamt für Kartographie und Geodäsie (BKG) started in late 2009 the installation of the Cooperative Network for GIOVE Observation (CONGO) network. In view of its capability to track also other new GNSS like QZSS it was later renamed to Cooperative Network for GNSS Observation. CONGO is a global multi-GNSS network transmitting its observations in real-time via the Ntrip protocol. Data is either streamed in proprietary formats of the receiver manufacturers or in BINary EXchange (BINEX; UNAVCO, 2011) format. In recent years, the network size grew and further institutions joined the network:

- Deutsches GeoForschungsZentrum (GFZ),
- Centre National d'Etudes Spaciales (CNES),
- Geoscience Australia (GA).

All stations are capable of tracking triple-frequency GPS (L1, L2, and L5) and dual-frequency Galileo (E1 and E5a) signals. Selected stations also track GLONASS, single- or dual-frequency SBAS, QZSS, BeiDou, and additional Galileo signals (E5b and E5 AltBOC). Most CONGO stations are equipped with Javad receivers as these were one of the first receivers with a Galileo-capable frontend *and* firmware. At the sites Singapore, Sydney, and Wettzell several receivers of different manufacturers are installed for comparison purposes. All CONGO stations are listed in Tab. C.1 and their geographical distribution is shown in Fig. 4.1.

4.2.2 The IGS Multi-GNSS Experiment

In recognition of the early support and analysis of the emerging GNSSs, the IGS published a call for participation for its Multi-GNSS Experiment in August 2011 (Hugentobler, 2011). Major purpose of the experiment is "to collect tracking data from the new satellites and foster engineering experimentation with the new signals". The initial period for MGEX was February 2012 to August 2012. At the 2012 IGS Workshop in Olsztyn (Poland) the experiment was extended until end of 2013. MGEX is carried out within the IGS GNSS Working Group. In view of its multi-GNSS activities, the working group was renamed to *Multi-GNSS Working Group* in December 2012 (Hugentobler, 2012).

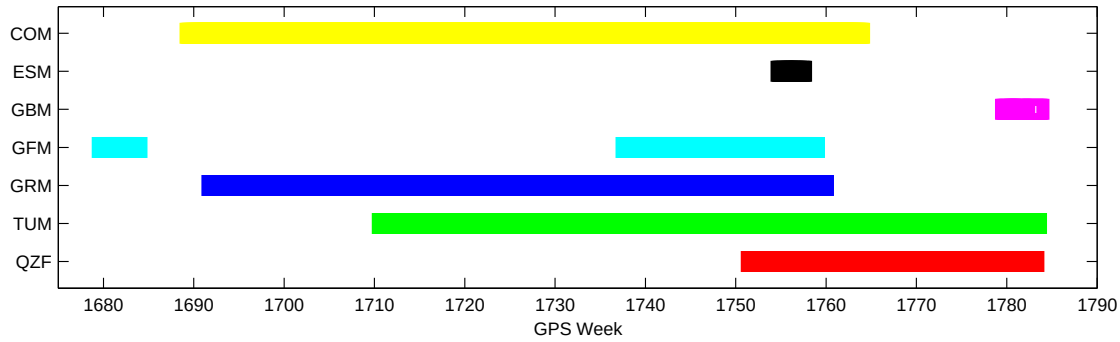

Fig. 4.2: MGEX product availability as of March 2014.

The MGEX network currently consists of about 90 tracking stations contributed by about 20 different institutions. In contrast to CONGO the station distribution is less homogeneous with many stations in Europe and the Pacific region. Three data centers are operated by the Crustal Dynamics Data Information System (CDDIS), Institut Géographique National (IGN), and Bundesamt für Kartographie und Geodäsie (BKG). Six ACs provide orbit and clock products:

- Centre National d'Etudes Spaciales (CNES), Collecte Localisation Satellites (CLS), Groupe de Recherche de Géodésie Spatial (GRGS), France: GRM,
- Center for Orbit Determination in Europe (CODE), Switzerland: COM,
- Deutsches GeoForschungsZentrum (GFZ), Germany: GBM and GFM,
- European Space Agency (ESA), Germany: ESM,
- Japan Aerospace Exploration Agency (JAXA), Japan: QZF,
- Technische Universität München (TUM), Germany: TUM.

GFZ provides separate products for Galileo (GFM) and BeiDou (GBM). All other products except for JAXA include Galileo, JAXA and TUM are the only ACs considering QZSS. The TUM product is based on the results discussed in Chapter 9 and 11. TUM is the only AC providing Galileo products with a latency of a few days only. The MGEX product availability as of March 2014 is shown in Fig. 4.2. For further details see the MGEX web site at `http://igs.org/mgex/`. The MGEX products as well as observation and navigation files in Receiver Independent Exchange (RINEX) format are available at the global data centers of the IGS, e.g., the CDDIS. For this thesis, only selected MGEX stations are used, in particular BeiDou-capable stations and stations in regions not covered by CONGO, see Tab. C.2 and Fig. 4.1. The additional stations listed in Tab. C.3 were provided by individual institutions or companies and were used for dedicated studies only.

4.2.3 Parameter Estimation Strategy

Observation data from the CONGO and MGEX networks are provided in RINEX 3 format. RINEX data recorded at TUM from real-time streams has 10 s sampling whereas the offline data has a 30 s sampling. As a consequence, all data are processed with 30 s sampling. GPS and Galileo/QZSS/BeiDou observations are processed in a two-step approach with a modified version of the Bernese GPS Software 5.0 (Dach et al, 2007). The software is capable of processing dual-frequency data of GPS, GLONASS, and one additional GNSS. The two frequencies of the additional GNSS have to be selected when importing the RINEX data into the Bernese-specific observation format. The following frequencies are used by default to form a ionosphere-free linear combination:

- Galileo: E1 and E5a,
- QZSS: L1 and L5, L1 and L2,
- BeiDou: B1 and B2.

Data are processed in a two-step approach, the first step is based on GPS data only and the second step on data of the other GNSS (Galileo, BeiDou, or QZSS). In a first preprocessing step, dual-frequency code and phase observations are used to detect outliers and cycle slips. If possible, the cycle slips are repaired, otherwise a new ambiguity is setup. The code observations are smoothed with the phase observations in this step, too.

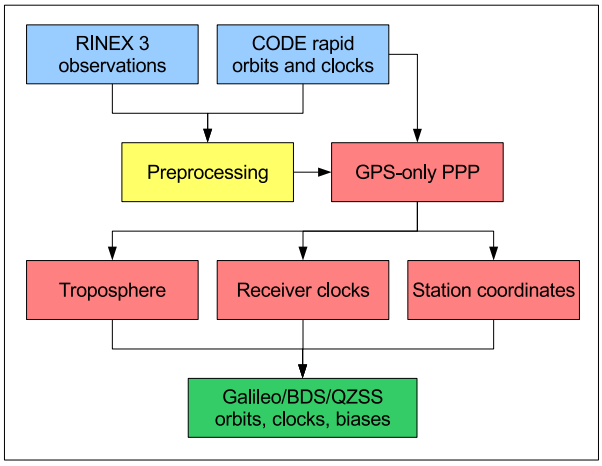

Fig. 4.3: Processing strategy for the estimation of Galileo, BeiDou, and QZSS orbit and clock determination.

Due to a near real-time processing GPS orbit and clock information as well as Earth Rotation Parameters (ERPs) are taken from the CODE rapid products. Depending on the satellite system, different a priori orbits are used:

- GIOVE/Galileo: SLR predictions in Consolidated Prediction Format (CPF) or own predictions from the previous day,
- QZSS: broadcast orbits from navigation files,
- BeiDou: Two-Line Elements (TLE).

One to two orbit iteration steps are necessary when using TLEs due to their limited accuracy.

Station coordinates, receiver clock corrections, troposphere zenith delays and gradients are estimated in a GPS-only Precise Point Positioning (PPP; Zumberge et al, 1997). First, the receiver clock is synchronized to GPS time based on the code observations. Outliers are detected in an iterative procedure with different screening levels. Finally, the above mentioned parameters and float ambiguities are estimated with a cutoff angle between 3 and 10° and elevation-dependent weighting with $w = \cos^2 z$ (z is the zenith distance).

The second step comprises the estimation of Galileo/BeiDou/QZSS orbit and satellite clock parameters. The station coordinates, receiver clock, and troposphere parameters estimated from GPS observations are kept fixed in this step, see Fig. 4.3. In order to account for systematic biases between the code observations of GPS and the second GNSS, Differential Code Biases (DCBs) are estimated for all stations but one. The estimated orbit parameters are the six Keplerian elements and one, three, five, or nine Radiation Pressure (RPR) parameters (depending on the GNSS and the satellite type, see below) of the model of Beutler et al (1994).

Normal Equations (NEQs) including the orbital elements and DCBs are saved for the generation of multi-day solutions. For these solutions, only one set of orbital elements (Keplerian elements and RPR parameters) are estimated in order to strengthen the stability of the orbits. In the context of this thesis arcs of three, five, and seven days are used. Due to their huge number, satellite clock parameters are not saved in the NEQs. In order to get satellite clock estimates consistent with the multi-day orbits, an additional clock solution is estimated on the one-day level. The multi-day orbits are kept fixed in this step and only satellite clock and DCB parameters are estimated.

Receiver antenna offsets and phase center variations determined in an anechoic chamber for GPS L1, L2, L5 and Galileo E1, E5a, E5b, E5, and E6 were provided by Becker et al (2010) for the most common antennas of the CONGO and MGEX networks. For BeiDou the L1/E1 calibrations are used for B1 and the E5b calibrations for B2. If no specific calibration values were available for the frequencies used, the GPS L1 and L2 calibrations from `igs08.atx`[1] (Rebischung et al, 2012) were used. `igs08.atx` was also the origin of the GPS satellite antenna offsets and phase center variations. Different sources for the Phase Center Offsets (PCOs) were used for the new GNSS:

[1] available at `ftp://ftp.igs.org/pub/station/general/igs08.atx`

- GIOVE: E1 and E5a offsets from Zandbergen and Navarro (2009),
- Galileo IOV: conventional offsets proposed by MGEX (Rizos et al, 2013),
- QZSS: identical values of Kogure (2011) for L1, L2, and L5,
- BeiDou: no PCO values publicly available, horizontal PCOs set to zero, z-component of the SLR offset (Weiguang, 2011) used as vertical PCO.

Although the transmission antenna of GIOVE-B shows pronounced variations of the antenna phase center (Horvath, 2010), no Phase Center Variations (PCVs) for the satellite antennas of GIOVE, Galileo IOV, QZSS, and BeiDou were applied due to lack of public availability.

Another important difference between the various GNSS satellites is their attitude behavior. The first attitude condition is that the transmitting antenna must always point to the center of the Earth. One possibility for the second condition is that the solar panels must be perpendicular to the direction to the Sun. This attitude mode is called nominal yaw steering and used for the GPS (Bar-Sever, 1996) and Galileo satellites.

QZSS satellites have an additional attitude mode for small elevations of the Sun above the orbital plane β. For $|\beta| < 20^\circ$ the satellite is operated on so-called orbit normal mode, i.e., the solar panels are perpendicular to the orbital plane (Inaba et al, 2009). For BeiDou, no attitude information was available at the time of writing. Therefore, the following attitude modes were assumed:

- BeiDou IGSOs: yaw steering,
- BeiDou GEOs: orbit normal mode.

4.2.4 Orbit results

The internal consistency of the estimated GNSS satellite orbits is assessed by

- Orbit fit RMS values: a multi-day arc is fitted through several orbits of consecutive days and the RMS of the individual arcs w.r.t. the new arc is computed,
- Day Boundary Discontinuities (DBDs): 3D position difference at midnight of two consecutive orbital arcs,
- Orbit comparisons: differences w.r.t. other orbits or orbit predictions.

The orbit accuracy is evaluated with SLR residuals as this optic measurement technique is independent from the microwave GNSS observations. However, due to the orbit height of the GNSS satellites SLR residuals mainly represent the radial accuracy of the orbits. A more detailed description of these quality indicators is given in Sect. 8.3.1 and 11.3.

Galileo Sections 8 and 9 discuss the orbit quality of the Galileo test satellite GIOVE–B and the first two Galileo IOV satellites. Due to outages and E6 transmissions of GIOVE–A only GIOVE–B is considered in Sect. 8. With a limited network of 8 stations a GIOVE–B orbit accuracy on the few decimeter level could be achieved. The phase residuals are on the $1-2$ cm level and the code residuals on the $1-2$ m level. Different arc lengths (three, five, seven, and nine days) and sets of RPR parameters (five vs. nine) have been tested to find the optimal orbit parameterization. The internal consistency as evaluated by 2-day orbit fits is on the $2-10$ cm level with smaller values for longer arc lengths due to their smoothing effect. The SLR residuals of GIOVE-B revealed a systematic bias of about $+5$ cm for the solutions with 5 RPR parameters and $+6-20$ cm for the solutions with 9 RPR parameters. The corresponding STDs are on the $1-2$ dm level.

An in general better orbit performance could be achieved for the Galileo IOV satellites in Sect. 9 due to the higher number of 24 stations and an improved tracking performance of these stations due to firmware updates. The phase residuals are on the same level as for GIOVE–B. The code residuals are smaller by a factor of $5-10$ compared to GIOVE–B as smoothed code was used instead of the raw code resulting in residuals at the few decimeter level. The resulting orbit consistency of multi-day arcs is on the 5 to 15 cm level evaluated by day boundary discontinuities and on the 2 to 4 cm level for 2-day orbit fits. On the one hand, the day boundary discontinuities are usually too pessimistic, as they only represent the position difference at a single epoch. On the other hand, 2-day orbit fits are usually too optimistic if multi-day arcs are used due to the smoothing effect of the latter caused by redundant data usage. As a consequence, the day boundary discontinuities are considered as upper bound and the 2-day orbit fits as lower bound for the orbit consistency. Galileo IOV-1 and IOV-2 show

both a consistent SLR bias of -5 cm for solutions with 5 RPR parameters with a STD also on the 5 cm level. The 9 RPR parameter solutions show partly smaller biases but also larger STDs. All Galileo IOV orbits suffer from systematic 1-CPR errors that are visible in the clock residuals of the highly stable PHMs and also in the time series of SLR residuals. The order of magnitude of these errors depends on the elevation of the Sun above the orbital plane indicating that they are related to radiation pressure mismodeling.

Combination of the microwave GNSS observations with optic SLR measurements helps to mitigate these systematic errors. However, due to the systematic bias in the SLR residuals, the internal consistency of the Galileo IOV is degraded by the combination. Changing the SLR reflector offset by 5 cm results in an improved orbit quality for solutions with 5 RPR parameters.

Another method to improve the orbit quality is the application of clock constraints w.r.t. a linear model. This is possible due to the high stability of the PHMs onboard the Galileo IOV satellites. Although the internal consistency is degraded by the clock constraints, the offset and STD of the SLR residuals improve.

QZSS The QZSS analysis discussed in Sect. 10 and 11 is based on five stations only as no more stations were available at that time. All stations are capable of tracking the QZSS L1, L1-SAIF, L2, and L5 signals whereas they do not track the LEX signal. The code multipath of these signals is on a similar level as for GPS for the L1 and L2 signals. QZSS L5 even shows a smaller multipath compared to GPS. No systematic effects can be seen in a triple-frequency geometry- and ionosphere-free linear combination of code and phase observations indicating that no significant line-bias variations are present.

Similar to the orbit determination of Galileo discussed in the previous paragraph, different arc lengths (three, five, seven days) and sets of RPR parameters (three vs. five vs. nine) have been tested. The day boundary discontinuities vary between 10 and 35 cm, the orbit fit RMS values between 2 and 8 cm. In contrast to Galileo no significant bias could be detected in the SLR residuals except for the 5- and 7-day solutions with 9 RPR parameters. However, the STD of the SLR residuals is with $3-6$ dm larger by a factor of about five.

QZS-1 was the first satellite of the new navigation systems transmitting valid navigation messages on a regular basis. The estimated orbits agree with the broadcast orbits on the level of $1-2$ m. As all tracking stations are capable of tracking triple-frequency QZSS observations the ionosphere-free linear combination used for the orbit determination can be formed from different observables: L1 and L2 as well as L1 and L5. Orbits estimated from L1/L2 and L1/L5 observations agree on the one decimeter level with a systematic 15 cm bias in the along-track component.

As already mentioned in Sect. 3.5 the transmission of navigation signals via two different antennas allows for a attitude determination of the satellite. QZS-1 operates in two attitude modes depending on the elevation of the Sun above the orbital plane β. For $|\beta| > 20^\circ$ yaw-steering is used, i.e. the transmission antenna points to the Earth and the solar panels perpendicular to the direction of the Sun. For $|\beta| < 20^\circ$ the satellite operates in the so-called orbit normal mode. The transmission antenna still points to the Earth but the solar panels are oriented perpendicular to the orbital plane. This attitude mode results in a small loss of electrical power but avoids rapid rotations of the satellite which are necessary in yaw-steering mode for small β-angles. Figure 10.6 shows the transition from yaw-steering to orbit normal mode as determined from L1 and L1-SAIF measurements of five stations. More detailed analysis of this attitude estimation in Hauschild et al (2012) revealed an accuracy better than 1°.

BeiDou No global BeiDou tracking network was available when starting the studies on BeiDou. Therefore, only IGSO and GEO satellites were considered. Whereas the modeling of the BeiDou IGSO satellites is similar to QZSS, orbit determination of the GEO satellites was a challenge. First tests with 3 RPR parameters resulted in orbit errors on the level of tens of meters even for multi-day arcs. A satisfactory orbit precision could be achieved by reducing the estimated orbit parameters to seven, i.e., the six Keplerian elements and one direct RPR parameter. Another important aspect for the GEO satellites are detection and handling of orbit maneuvers necessary to maintain the designated position of the geostationary satellites. Maneuvers were detected in a manual, iterative procedure. An automated maneuver detection remains a task for the future, Garcia Huerta (2013) already developed two methods for maneuver detection of dedicated SBAS satellites.

The internal consistency of the IGSO satellite orbits is on the one to two decimeter level. Unfortunately only a few SLR normal points were available for one of the GEO and one of the IGSO satellites. With offsets and standard deviations on the one to two decimeter level for both satellites, the results of the IGSOs are confirmed. The SLR validation of the GEO satellites even outperforms the internal consistency.

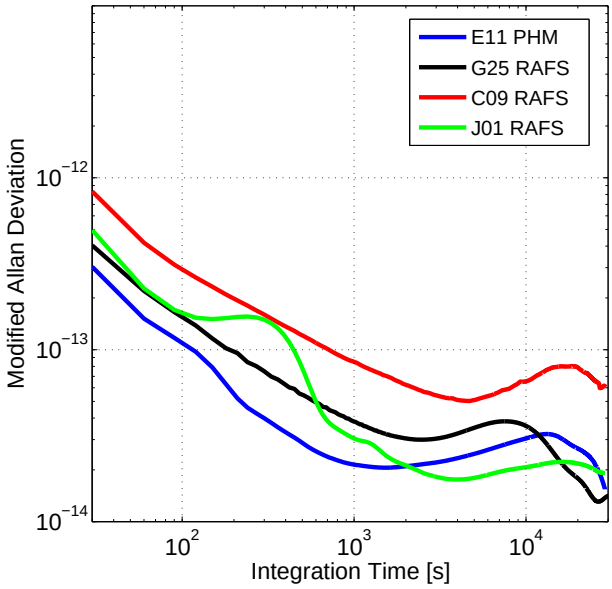

Fig. 4.4: Modified Allan Deviations of the satellite clocks of Galileo IOV-1 (E11), QZS-1 (J01), GPS SVN62 (G25), and BeiDou IGSO-4 (C09).

BeiDou was the first GNSS allowing for a positioning without observations from GPS or GLONASS. An accuracy of a few centimeters could be achieved compared to GPS-only results. First positioning results with two GIOVE and two IOV satellites are published by Langley et al (2012), results with four IOV satellites by Steigenberger et al (2013).

4.2.5 Clock results

Atomic clocks are the heart of each GNSS satellite as all navigation signals are deduced from their fundamental frequency. Basically two different types of clocks are used in recent GNSS satellites:

- Rubidium Atomic Frequency Standards (RAFSs),
- Passive Hydrogen Masers (PHMs).

The Allan Deviation is a common method to characterize the stability (NIST, 1990). In this thesis the Modified Allan Deviation (MADEV; Allan and Barnes, 1981) is used in addition. Selected MADEVs of the new GNSSs are summarized in Fig. 4.4. The latest generation RAFS used for the GPS Block IIF satellites (Dupuis et al, 2010) is included for comparison purposes. However, one has to be aware that GPS SVN62 suffers from line bias variations (Montenbruck et al, 2012a) visible as a bump in the MADEV at integration times of 3,000 – 20,000 s. A more detailed discussion of the clock performance of the new GNSSs is given in Montenbruck et al (2012b).

Galileo GIOVE-B was the first satellite with a PHM in space and also each Galileo IOV satellite is equipped with two PHMs (Ostillio et al, 2009). The PHM of Galileo IOV-1 (E11) shows the highest stability of the clocks in Fig. 4.4 for integration times up to 2,000 s. At longer integration times, orbital errors degrade the performance of the apparent clock. This degradation is visible as a 1-CPR signal in the clock residuals that is correlated with the SLR residuals. Including SLR observations in addition to the microwave observations in the GNSS orbit determination also improves the quality of the satellite clock parameters (GNSS+SLR orbits kept fixed), see Fig. 9.6 and 9.7.

BeiDou Only little is known about the RAFSs employed onboard the BeiDou satellites. According to Harvey (2013) and Jun et al (2012) Swiss as well as Chinese clocks are used. However, there is no public information about the currently active clock. The clock of the BeiDou IGSO-4 satellite (C09) shown as example in Fig. 4.4 has the worst stability of the clocks shown in that figure. The RAFSs onboard the IGSO and GEO satellites have in general a similar performance as well as the clocks of the MEO satellites (Chunhao et al, 2013).

QZSS The same type of RAFS as for the GPS Block IIF satellites is used for QZS-1. A clear bump at 400 s can be seen in the MADEV of QZS-1 in Fig. 4.4. It is caused by short-period variations of the QZS-1 clock with a peak-to-peak amplitude of 4 cm. These variations are visible in the satellite clock estimates of different observables, i.e., ionosphere linear combinations of L1/L2 as well as L1/L5. They could be confirmed with an independent method, namely the Three-way Carrier Phase (3WCP) approach. However, the triple-frequency linear combination of L1, L2, and L5 does not show any anomalies. Therefore it is reasonable to assume that this effect is caused by the satellite clock. Although the origin of this variation is not exactly known, the time keeping system is the most probable origin. At integration times shorter than 100 s, the GPS SVN62 clock and the QZS-1 clock have almost the same performance. At integration times longer than 700 s the QZS-1 clock shows even a better stability as the SVN62 clock suffers from line bias variations already mentioned above.

High-accuracy clocks can also be used as quality indicator for different orbits. In Sect. 11 the MADEVs of clock estimates computed with orbits of different parameterization and arc length supported the decision that an arc length of three days and the estimation of 5 RPR parameters provides the best orbit solution.

Bibliography

Allan D, Barnes J (1981) A modified "Allan variance" with increased oscillator characterization ability. In: Thirty Fifth Annual Frequency Control Symposium. 1981, pp 470–475, DOI 10.1109/FREQ.1981.200514

Bar-Sever YE (1996) A new model for GPS yaw attitude. Journal of Geodesy 70(1):714–723, DOI 10.1007/BF00867149

Becker M, Zeimetz P, Schönemann E (2010) Antenna chamber calibrations and antenna phase center variations for new and existing GNSS signals. In: IGS Workshop 2010, 28 June – 2 July 2010, Newcastle

Beutler G, Brockmann E, Gurtner W, Hugentobler U, Mervart L, Rothacher M, Verdun A (1994) Extended orbit modeling techniques at the CODE Processing Center of the International GPS Service (IGS): Theory and initial results. Manuscripta Geodaetica 19:367–386

Chunhao H, Zhiwu C, Yuting L, Li L, Shenghong X, Lingfeng Z, Xianglei W (2013) Time synchronization and performance of BeiDou satellite clocks in orbit. International Journal of Navigation and Observation DOI 10.1155/2013/371450

Dach R, Hugentobler U, Fridez P, Meindl M (eds) (2007) Bernese GPS Software Version 5.0. Astronomical Institute, University of Bern, Bern, Switzerland

Dupuis RT, Lynch TJ, Vaccaro JR, Watts ET (2010) Rubidium frequency standard for the GPS IIF program and modifications for the RAFSMOD program. In: Proceedings of ION GNSS 2010, Portland, pp 781–788

Garcia Huerta R (2013) SBAS orbit determination based on dual-frequency measurements. Master's thesis, Technische Universität München

Gendt G, Ferland R (2010) IGS Repro1 combined products – SINEX, orbit and (preliminary) clock products. IGSMAIL-6136

Han D, Wahr J (1995) The viscoelastic relaxation of a realistically stratified earth, and a further analysis of post-glacial rebound. Geophysical Journal International 120(2):287–311, DOI 10.1111/j.1365-246X.1995.tb01819.x

Harvey B (2013) China in Space: the Great Leap Forward. Springer, New York, Heidelberg, Dordrecht, London, DOI 10.1007/978-1-4614-5043-6

Hauschild A, Steigenberger P, Rodriguez-Solano C (2012) QZS-1 yaw attitude estimation based on measurements from the CONGO network. Navigation, Journal of the Institute of Navigation 59(3):237–248, DOI 10.1002/navi.18

Horvath A (2010) Analyse von GIOVE-A und -B Beobachtungen aus 2009 und 2010 des CONGO-Stationsnetzes. Master thesis, Technische Universität München

Hugentobler U (2011) IGS Multi-GNSS Global Experiment, Call for Participation. IGSMAIL-6459

Hugentobler U (2012) Short summary of the 41th IGS Governing Board Meeting. IGSMAIL-6706

Inaba N, Matsumoto A, Hase H, Kogure S, Sawabe M, Terada K (2009) Design concept of Quasi Zenith Satellite System. Acta Astronautica 65(7-8):1068–1075, DOI 10.1016/j.actaastro.2009.03.068

Jun X, Jingang W, Hong M (2012) Analysis of Beidou Navigation Satellites In-orbit State. In: Sun J, Liu J, Yang Y, Fan S (eds) China Satellite Navigation Conference (CSNC) 2012 Proceedings, Springer, Lecture Notes in Electrical Engineering, vol 161, pp 111–122, DOI 10.1007/978-3-642-29193-7_10

Kogure S (2011) personal communication

Langley R, Banville S, Steigenberger P (2012) First results: Precise positioning with Galileo prototype satellites. GPS World 23(9):45–49

Langley RB (1998) A primer on GPS antennas. GPS World 9(7):50–53

Montenbruck O, Hugentobler U, Dach R, Steigenberger P, Hauschild A (2012a) Apparent clock variations of the Block IIF-1 (SVN62) GPS satellite. GPS Solutions 16(3):303–313, DOI 10.1007/s10291-011-0232-x

Montenbruck O, Steigenberger P, Schönemann E, Hauschild A, Hugentober U, Dach R, Becker M (2012b) Flight characterization of new generation GNSS satellite clocks. Navigation, Journal of the Institute of Navigation 59(4):291–302

Nikolaidis R (2002) Observation of Geodetic and Seismic Deformation with the Global Positioning System. PhD thesis, University of California, San Diego

NIST (1990) Characterization of clocks and oscillators. No. 1337 in NIST Technical Note, National Institute of Standards and Technologie, Boulder

Ostillio A, Johansson M, Hannes D, Malik M, Waller ARP, Belloni M, Droz F, Mosset P (2009) Passive hydrogen maser (PHM): the heart of the Galileo navigation payload. In: Proceedings of the European Navigation Conference – Global Navigation Satellite Systems

Rebischung P, Griffiths J, Ray J, Schmid R, Collilieux X, Garayt B (2012) IGS08: the IGS realization of ITRF2008. GPS Solutions 16(4):483–494, DOI 10.1007/s10291-011-0248-2

Rizos C, Montenbruck O, Weber R, Weber G, Neilan R, Hugentobler U (2013) The IGS MGEX experiment as a milestone for a comprehensive multi-GNSS service. In: Proceedings of ION PNT 2013, pp 289–295

Rothacher M, Angermann D, Artz T, Bosch W, Drewes H, Gerstl M, Kelm R, König D, König R, Meisel B, Müller H, Nothnagel A, Panafidina N, Richter B, Rudenko S, Schwegmann W, Seitz M, Steigenberger P, Tesmer S, Tesmer V, Thaller D (2011) GGOS-D: homogeneous reprocessing and rigorous combination of space geodetic observations. Journal of Geodesy 85(10):679–705, DOI 10.1007/s00190-011-0475-x

Steigenberger P, Rothacher M, Dietrich R, Fritsche M, Rülke A, Vey S (2006) Reprocessing of a global GPS network. Journal of Geophysical Research 111:B05402, DOI 10.1029/2005JB003747

Steigenberger P, Hugentobler U, Lutz S, Dach R (2011) CODE Contribution to the IGS Reprocessing. Tech. rep., Institut für Astronomische und Physikalische Geodäsie, URL https://mediatum2.ub.tum.de/doc/1078108/1078108.pdf

Steigenberger P, Hugentobler U, Montenbruck O (2013) First demonstration of Galileo-only positioning. GPS World 24(2):14–15

Tapley BD, Bettadpur S, Watkins M, Reigber C (2004) The gravity recovery and climate experiment: Mission overview and early results. Geophysical Research Letters 31(9):L09607, DOI 10.1029/2004GL019920

UNAVCO (2011) BINEX: Binary Exchange Format. URL http://binex.unavco.org/binex.html, accessed 22-02-2014

Weiguang G (2011) ILRS SLR mission support request for Compass-I3. URL http://ilrs.gsfc.nasa.gov/docs/ilrsmsr_I31.pdf

Zandbergen R, Navarro D (2009) Specification of Galileo and GIOVE space segment properties relevant for satellite laser ranging. Tech. Rep. ESA-EUING-TN/10206, rev. 3.2, European Space Agency

Zumberge JF, Heflin MB, Jefferson DC, Watkins MM, Webb FH (1997) Precise point positioning for the efficient and robust analysis of GPS data from large networks. Journal of Geophysical Research 102(B3):5005–5017, DOI 10.1029/96JB03860

Part II

Papers

5 GPS-Specific Local Effects at the Geodetic Observatory Wettzell

Originally published as:

Steigenberger P., Hugentobler U., Schmid R., Hessels U., Klügel T., Seitz M. (2013): GPS-Specific Local Effects at the Geodetic Observatory Wettzell, in: Z. Altamimi and X. Collilieux, Reference Frames for Applications in Geosciences, International Association of Geodesy Symposia, Vol. 138, pp. 125-130, doi: 10.1007/978-3-642-32998-2_20

The final publication is available at Springer via http://dx.doi.org/10.1007/978-3-642-32998-2_20.

Abstract

Global Navigation Satellite Systems (GNSS) are important contributors to the realization of the International Terrestrial Reference System (ITRS). For the combination of different space geodetic techniques, terrestrial measurements between the corresponding reference points are necessary. Discrepancies between these so-called local ties on the one hand and the coordinate differences derived from space techniques on the other hand are a major limitation for the realization of the ITRS nowadays. In the past, these discrepancies have often been attributed to inaccurate terrestrial measurements. This paper shows that a major part of the differences can be explained by systematic GNSS-specific errors, if a global data analysis is simulated. One of the most important error sources for GNSS are interactions of the antenna with its immediate vicinity, primarily multipath.

At the Geodetic Observatory Wettzell (Germany), up to six GNSS permanent sites are operated in parallel at a distance of only a few meters. This antenna array is ideal to study the impact of local effects on the various GNSS observables and linear combinations. Comparisons of solutions obtained from different GNSS observables reveal cm-level discrepancies. Individual receiver antenna calibrations have an impact on the estimated station positions on the level of several millimeters. As other error sources dominate, their application does not lead to an improvement in all cases.

5.1 Introduction

At the Geodetic Observatory Wettzell, three of the space geodetic techniques used for the realization of the International Terrestrial Reference System (ITRS) are operated: Global Navigation Satellite System (GNSS) receivers, Satellite Laser Ranging (SLR), and Very Long Baseline Interferometry (VLBI). Doppler Orbitography and Radiopositioning Integrated by Satellite (DORIS) is the only technique not present at Wettzell due to signal interferences with VLBI. For the combination of the space geodetic techniques, terrestrial measurements (local ties) connecting the reference points of the different techniques are necessary. In the computation of the recent realization of the ITRS (ITRF2008), discrepancies between the local ties and the space geodetic techniques of up to 13.5 mm occurred (Seitz et al, 2013). This value is significantly larger than the precision that can be achieved with terrestrial as well as space geodetic observations. As several GNSS permanent sites are operated in parallel at Wettzell, a comparison of vectors obtained from different GNSS observables with the terrestrial measurements is possible. Differences between these solutions could indicate frequency-dependent systematic effects like near-field multipath (Dilßner et al, 2008). In this paper, all site-specific effects that could not clearly be identified are denoted as multipath, without knowing the exact mechanism how the signal is affected.

The first GPS permanent site at Wettzell was put into operation in 1991. The site WTZR installed in 1995 is still the one used by most of the Analysis Centers (ACs) of the International GNSS Service (IGS; Dow et al, 2009). Like most of the antennas at Wettzell, WTZR is mounted on the roof of a tower of the main building of the Geodetic Observatory, see Figure 5.1. However, one antenna (WTZS) is mounted on a steel mast with a height of about 7.5 m above the ground, about 67 m north-northwest of the tower. All GNSS permanent sites operated

Fig. 5.1: GNSS permanent sites on top of the tower of the main building of the Geodetic Observatory Wettzell. A webcam to monitor snow coverage of the antennas is mounted between WTZR and WTZJ.

at Wettzell are listed in Table 5.1. Most of the sites are part of the tracking network of the IGS. However, WTZL was part of the German GPS reference network DREF. This site was considered here, as individual antenna calibrations are available.

Rothacher et al (2004) already analyzed the local GPS network at Wettzell. They could achieve sub-mm repeatabilities of the coordinate time series and detected significant discontinuities due to antenna changes. Section 5.2 discusses the GPS processing of the antenna array at the Geodetic Observatory Wettzell. Three different combined solutions are computed from L1 and L2 observations as well as from the ionosphere-free linear combination L3. These solutions are compared with terrestrial measurements in Section 5.3. The impact of individual receiver antenna calibrations is studied in Section 5.4.

5.2 GPS Processing

In order to study the discrepancies between local ties and GNSS-derived coordinates, an analysis strategy similar to that of the IGS ACs was applied. All available RINEX observation files between November 1997 and August 2010 were processed in daily batches with the current development version 5.1 of the Bernese GPS Software (Dach et al, 2007). As only a few sites are equipped with GLONASS-capable receivers, only GPS observations were considered for this analysis. For the time period until the end of 2008 the reprocessed orbits and Earth rotation parameters of the Center for Orbit Determination in Europe (CODE; Dach et al, 2009) were used, for 2009 and 2010 the operational products instead. The IGS05 coordinates of WTZA were chosen to be fixed, as this is the only site without discontinuities. For all other sites, baselines w.r.t. WTZA were formed and daily station coordinates were estimated.

Troposphere zenith delays were estimated as piecewise linear functions with a parameter spacing of 2 h using the Global Mapping Function (GMF; Boehm et al, 2006). The hydrostatic a priori delays were computed with pressure from the Global Pressure and Temperature model (GPT; Boehm et al, 2007) using the equation of Saastamoinen (1973). One pair of troposphere gradients per day was estimated in north-south and east-west direction. As it is not possible to determine absolute values for the tropospheric delays with such a small network, the estimated zenith delays of WTZR from the CODE solution were introduced and fixed. Observations were weighted with a weight of $w = \sin^2 \epsilon$ depending on the elevation ϵ, and an elevation cut-off angle of 3° was applied.

Ambiguities were fixed separately for L1 and L2 with the so-called Sigma method (Dach et al, 2007). The average resolution rate was 94 %. After an outlier detection based on residual screening, three different solutions were computed: L1 and L2 single-frequency solutions and a dual-frequency solution based on the ionosphere-free linear combination L3. Normal Equations (NEQs) were saved to generate a combined solution. For these standard solutions, the official IGS antenna phase center model igs05.atx (Schmid et al, 2007) was used. A solution based on individual antenna calibrations is discussed in Section 5.4. The solution setup described above was chosen to be as similar as possible to the global solution approach in order to study the systematic effects visible in the International Terrestrial Reference Frame (ITRF) combination. Therefore, e.g., troposphere zenith delays were estimated for *all* sites but one although estimating one common troposphere zenith delay parameter would be

Site	Network	# ACs	Sol. no.	Antenna	Radome	Start	End
WTZR 14201M010	IGS	7	1	AOAD/M_T	NONE	02/1995	07/2002
			2	AOAD/M_T	NONE	07/2002	01/2009
			3	LEIAR25	LEIT	01/2009	06/2010
			4	LEIAR25.R3	LEIT*	06/2010	
WTZT 14201M011	IGS	–	1	TRM22020.00+GP	NONE	02/1997	12/1997
			2	TRM22020.00+GP	DOME	12/1997	11/1998
			3	TRM22020.00+GP	NONE	11/1998	01/2000
			4	TRM29659.00	NONE	01/2000	05/2005
WTZA 14201M013	IGS	3	Ref.	ASH700936C_M	SNOW	11/1997	
WTZZ 14201M014	IGS	4	1	ASH701073.1	SNOW	02/1999	06/2003
			2	TPSCR3_GGD	CONE	06/2003	
WTZJ 14201M012	IGS	2	1	TRM29659.00	NONE	07/2001	04/2002
			2	JPSREGANT_SD_E	NONE	04/2002	08/2005
			3	TRM29659.00	NONE*	08/2005	12/2009
			4	LEIAR25	LEIT*	12/2009	11/2010
WTZL 14201M022	DREF	–	1	LEIAX1202	NONE	03/2004	04/2007
			2	LEIAX1202GG	NONE	04/2007	12/2007
			3	LEIAT504GG	LEIS	12/2007	01/2008
			4	TPSCR.G3	TPSH*	01/2008	07/2008
			5	TPSCR3_GGD	CONE*	07/2008	09/2008
WTZS 14201M015	IGS	1	1	ASH701945G_M	SNOW	07/2005	02/2010
			2	LEIAR25.R3	NONE	02/2010	06/2010
			3	LEIAR25.R3	LEIT	06/2010	

Tab. 5.1: GNSS sites operated at the Geodetic Observatory Wettzell and their current usage by the IGS ACs for their final solutions. The sites are ordered by their start of operation. *Sol. no.* refers to solution numbers introduced due to discontinuities caused by antenna changes. For antenna/radome combinations marked with an asterisk, individual antenna calibrations are available.

sufficient for such a small network. Dilßner et al (2008) showed that the estimation of troposphere parameters can cause a significant increase of systematic biases due to near-field multipath.

All antenna changes listed in Table 5.1 resulted in significant discontinuities that are clearly visible in the station coordinate time series. Therefore, independent sets of station coordinates (denoted by separate solution numbers) were estimated for the time intervals given in Table 5.1. After pre-eliminating the troposphere parameters, three separately combined solutions were computed by accumulating the L1, L2, and L3 NEQs for the full time interval from 1997 – 2010. As the formal errors of these combined solutions are by far too optimistic, realistic errors for the position estimates were computed from time series residuals according to Steigenberger et al (2012). The errors for the height component range from 0.1 to 1.1, 1.4, and 1.9 mm for L1, L2, and L3, respectively, with a median value of 0.3 mm in all three cases. The comparisons with terrestrial measurements discussed in the next section are based on these combined solutions.

5.3 Comparisons with Terrestrial Measurements

The terrestrial measurements used here were performed in 2002 (Schlüter et al, 2005). They include all GNSS sites except for WTZS and are given in the file 14201_BKG_2002-266.SNX[1]. As WTZA was fixed for the GPS processing, the comparisons with the terrestrial measurements are also done w.r.t. WTZA. Height differences between GPS and terrestrial measurements in a local system centered at WTZA are given in Figure 5.2. The largest height difference of more than 40 mm occurs for the L3 solution of WTZT when the site was equipped with an uncalibrated radome (WTZT, sol. no. 2, see Table 5.1). Ray et al (2007) showed for the Fortaleza station that a major part of its GPS/VLBI local tie discrepancy could be explained by the effect of an uncalibrated

[1] available at http://itrf.ensg.ign.fr/ties/ITRF2005/ITRF2005-SNX-localties.tar.gz

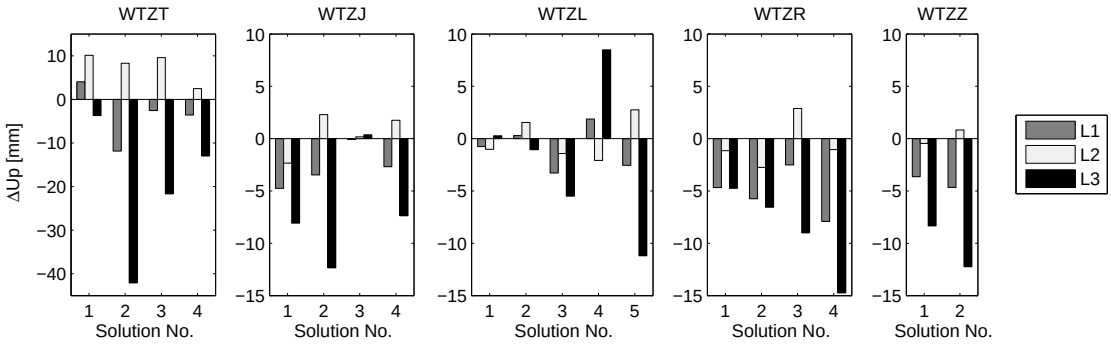

Fig. 5.2: Differences between L1, L2, or L3 GPS solutions and terrestrial measurements. Note the different scale for WTZT.

radome. The height discrepancy could be reduced by 15.8 mm when the radome was removed. But also for antennas without radomes or with calibrated radomes, height discrepancies of up to 10 mm for L1 and L2 and of up to 15 mm for L3 are present. The L3 differences are particularly large for solutions with large differences between L1 and L2 as the latter are amplified by forming the ionosphere-free linear combination L3 (e.g., WTZR, sol. no. 4).

The horizontal L3 discrepancies (not shown here) are generally smaller than 6 mm except for WTZL (sol. no. 1 and 2) where they almost reach 12 mm. With about 4 mm, the horizontal L1 and L2 discrepancies are also the largest for the same two solutions, all other discrepancies are below 3 mm.

The differences shown in Figure 5.2 exceed the sub-mm precision one can achieve with GPS on such short baselines by far. They also exceed the precision of the terrestrial measurements which is on the $1-2$ mm level (based on the comparison of several terrestrial measurement campaigns from different years; Mähler et al, 2010).

The L3 differences are generally larger than the differences resulting from the single-frequency solutions. This is of particular importance as global solutions that are used as input for ITRF computations are always based on this linear combination. As the GPS-internal differences between the L1, L2, and L3 solutions are sometimes even larger than the discrepancies w.r.t. the terrestrial measurements, one can assume that they are caused by frequency-dependent systematic effects of the GPS technique. Deficiencies in the antenna calibration are one possible error source. Therefore, the impact of a more sophisticated antenna model will be discussed in the next section.

5.4 Individual Antenna Calibrations

For five antennas (marked with an asterisk in Table 5.1), individual receiver antenna calibrations are available besides the type-mean values from igs05.atx. All these calibrations are robot calibrations performed by Geo++ (Menge et al, 1998). As an example, Figure 5.3 shows the L1 phase center differences between the type-mean and the individual calibration of the `LEIAR25.R3 LEIT` antenna of WTZR. The differences range from -2 to $+1.5$ mm. The L2 differences have a similar order of magnitude and shape. For the other antennas, the differences can reach ± 4 mm with sometimes significant differences between L1 and L2.

The coordinate differences w.r.t. the terrestrial measurements already discussed in the previous section are now given for solutions using type-mean or individual antenna calibrations in Figure 5.4. The solutions differ by up to 5 mm in the horizontal and the vertical component, except for WTZL (sol. no. 5) with a height difference of almost 13 mm. The phase center differences shown in Figure 5.3 affect the horizontal coordinates of WTZR only on the sub-mm level whereas the height changes by about 5 mm. The discrepancies w.r.t. the terrestrial measurements decrease by one third for the height component when using the individual antenna calibration.

The largest differences for the horizontal components are visible for WTZJ (sol. no. 3). On the one hand, the discrepancy w.r.t. the terrestrial measurements gets smaller by more than 4 mm for the North component. On the other hand, it increases by about the same order of magnitude for the East component. The discrepancy for the WTZJ (sol. no. 3) height component also increases. Most other sites show a similar behavior: sometimes the agreement is better with individual calibrations, sometimes with the type-mean calibrations. In summary, no clear conclusions can be drawn, as obviously other error sources dominate.

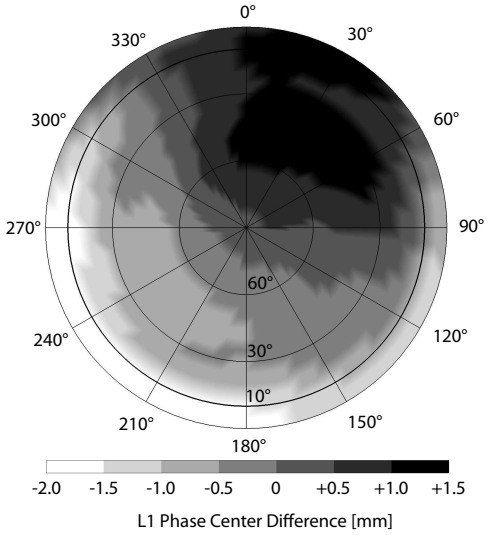

Fig. 5.3: L1 phase center differences between the type-mean values from igs05.atx and the individual calibration of the `LEIAR25.R3 LEIT` antenna at WTZR. The phase center variations are referred to one common phase center offset.

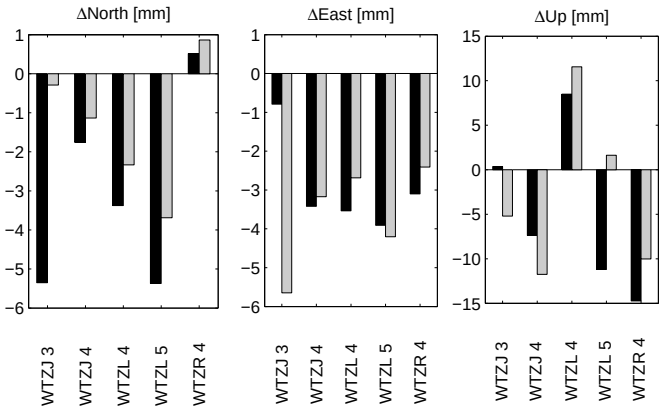

Fig. 5.4: Differences of L3 GPS solutions using type-mean (black) or individual (gray) receiver antenna calibrations w.r.t. the terrestrial measurements. Note the different scale of the height component. The solution numbers given after the site name refer to Table 5.1.

5.5 Conclusions

The differences between the GPS-derived coordinates and the terrestrial measurements clearly exceed the precision of each technique. As even results derived from different frequencies and in particular from the ionosphere-free linear combination differ from each other by up to a few cm, it is reasonable to assume that a major part of the discrepancies w.r.t. the terrestrial measurements is caused by GPS-specific systematic errors. Deficiencies in the antenna phase center model could be a source for such systematic errors. The largest difference between terrestrial and GPS-derived coordinates is indeed caused by such a deficiency, namely by an uncalibrated radome. This is a worst case scenario for a geodetic co-location site that should be avoided in any circumstance. But also the application of individual antenna calibrations couldn't solve all the problems. The estimated station positions changed significantly by several mm compared to the solutions using type-mean calibrations. However, as obviously other error sources dominate, the agreement with the terrestrial measurements did not clearly improve.

Another possible error source are near-field multipath effects that most likely cause the frequency-dependent biases in the coordinate estimates. Dilßner et al (2008) showed that reflecting objects in the vicinity of the antenna can bias the coordinate estimates by up to 15 mm and that the simultaneous estimation of troposphere parameters as necessary in global GNSS solutions can even enlarge those biases. According to Dilßner et al (2008), the antenna near-field of Dorne Margolin type chokering antennas has a radius of about 1.4 m. For the Wettzell antenna array, possible multipath sources within this distance could be the railing of the tower that is covered with a metal sheet or a webcam mounted on a metal pole (see Figure 5.1) to monitor the snow coverage of the antennas.

One possibility to account for the biases caused by near-field effects is the estimation of correction values from carrier phase residuals as it is, e.g., done for GNSS receiver antennas operated on LEO satellites (Montenbruck et al, 2009; Jäggi et al, 2009). The coordinates derived from terrestrial measurements could be fixed in order to determine residual maps from the analysis of the GPS observations. These corrections could be introduced for GPS solutions solving for empirically corrected coordinates. Another possibility would be a calibration system as proposed by Park et al (2004) using a directional antenna to directly determine the multipath. Irrespective of the approach to be used, further studies are required to cope with the multipath problems at Wettzell. In particular a better understanding of the interaction of different antenna models, troposphere estimation, and multipath effects is desirable. A solution could also be to find a location at the Geodetic Observatory that is less affected by multipath.

Acknowledgements

The authors would like to thank the IGS (Dow et al, 2009) for providing GPS observation data.

Bibliography

Boehm J, Niell A, Tregoning P, Schuh H (2006) Global Mapping Function (GMF): A new empirical mapping function based on numerical weather model data. Geophysical Research Letters 33(7):L07304, DOI 10.1029/2005GL025546

Boehm J, Heinkelmann R, Schuh H (2007) Short Note: A global model of pressure and temperature for geodetic applications. Journal of Geodesy 81(10):679–683, DOI 10.1007/s00190-007-0135-3

Dach R, Hugentobler U, Fridez P, Meindl M (eds) (2007) Bernese GPS Software Version 5.0. Astronomical Institute, University of Bern, Switzerland

Dach R, Brockmann E, Schaer S, Beutler G, Meindl M, Prange L, Bock H, Jäggi A, Ostini L (2009) GNSS processing at CODE: status report. Journal of Geodesy 83(3-4):353–365, DOI 10.1007/s00190-008-0281-2

Dilßner F, Seeber G, Wübbena G, Schmitz M (2008) Impact of near-field effects on the GNSS position solution. In: Proceedings of ION GNSS 2008, pp 612–624

Dow JM, Neilan RE, Rizos C (2009) The International GNSS Service in a changing landscape of Global Navigation Satellite Systems. Journal of Geodesy 83(3-4):191–198, DOI 10.1007/s00190-008-0300-3

Jäggi A, Dach R, Montenbruck O, Hugentobler U, Bock H, Beutler G (2009) Phase center modeling for LEO GPS receiver antennas and its impact on precise orbit determination. Journal of Geodesy 83(12):1145–1162, DOI 10.1007/s00190-009-0333-2

Mähler S, Schade C, Klügel T (2010) Local ties at the Geodetic Observatory Wettzell. Geophysical Research Abstracts 12, EGU2010-4815

Menge F, Seeber G, Völksen C, Wübbena G, Schmitz M (1998) Results of absolute field calibration of GPS antenna PCV. In: Proceedings of ION GPS-98, pp 31–38

Montenbruck O, Garcia-Fernandez M, Yoon Y, Schön S, Jäggi A (2009) Antenna phase center calibration for precise positioning of LEO satellites. GPS Solutions 13(1):23–34, DOI 10.1007/s10291-008-0094-z

Park KD, Elósegui P, Davis JL, Jarlemark POJ, Corey BE, Niell AE, Normandeau JE, Meertens CE, Andreatta VA (2004) Development of an antenna and multipath calibration system for Global Positioning System sites. Radio Science 39(5):RS5002, DOI 10.1029/2003RS002999

Ray J, Crump D, Chin M (2007) New global positioning system reference station in Brazil. GPS Solutions 11(1):1–10, DOI 10.1007/s10291-006-0032-x

Rothacher M, Lechner V, Schlüter W (2004) Local monitoring of a fundamental GPS site. IGS Workshop 2004, Bern

Saastamoinen J (1973) Contributions to the theory of atmospheric refraction. Bulletin Géodésique 107(1):13–34, DOI 10.1007/BF02522083

Schlüter W, Zernecke R, Becker S, Klügel T, Thaller D (2005) Local ties between the reference points at the Fundamentalstation Wettzell. In: Richter B, Dick WR, Schwegmann W (eds) Proceedings of the IERS Workshop on site co-location, no. 33 in IERS Technical Note, Verlag des Bundesamts für Kartographie und Geodäsie, pp 64–70

Schmid R, Steigenberger P, Gendt G, Ge M, Rothacher M (2007) Generation of a consistent absolute phase center correction model for GPS receiver and satellite antennas. Journal of Geodesy 81(12):781–798, DOI 10.1007/s00190-007-0148-y

Seitz M, Angermann D, Drewes H (2013) Accuracy assessment of the ITRS 2008 realization of DGFI, DGFI2008. In: Altamimi Z, Collilieux X (eds) Reference Frames for Applications in Geosciences, IAG Symposia, vol 138, Springer, pp 87–93, DOI 10.1007/978-3-642-32998-2_15

Steigenberger P, Seitz M, Böckmann S, Tesmer V, Hugentobler U (2012) Precision and accuracy of GPS-derived station displacements. Physics and Chemistry of the Earth 53-54:72–79, DOI 10.1016/j.pce.2010.07.035

6 Precision and Accuracy of GPS-derived Station Displacements

This is the authors version of a work that was accepted for publication in Physics and Chemistry of the Earth. Changes resulting from the publishing process, such as peer review, editing, corrections, structural formatting, and other quality control mechanisms may not be reflected in this document. Changes may have been made to this work since it was submitted for publication. A definitive version was subsequently published in:

Steigenberger P., Seitz M., Böckmann S., Tesmer V., Hugentobler U. (2012): Precision and accuracy of GPS-derived station displacements, Physics and Chemistry of the Earth, Vol. 53-54, pp. 72-79, doi: 10.1016/j.pce.2010.07.035

Abstract

Space geodetic techniques like Global Navigation Satellite Systems (GNSS), Satellite Laser Ranging (SLR) and Very Long Baseline Interferometry (VLBI) provide valuable input for, e.g., studies of Global Isostatic Adjustment (GIA). This paper discusses the current precision and accuracy of GPS-derived vertical and horizontal station displacements. The precision is evaluated by repeatabilities and solutions computed from different sub-intervals of the data available. However, due to systematic effects, the precision is often much better than the accuracy. The accuracy is evaluated by comparisons of the space geodetic techniques amongst each other and comparisons with geophysical models for atmospherical and hydrological loading. Besides the analysis of time series, co-located GNSS, SLR, and VLBI sites allow for a comparison of velocities estimated in Terrestrial Reference Frame (TRF) solutions of the different techniques.

6.1 Introduction

Deformation processes of the solid Earth can be monitored with the space geodetic techniques, e.g., Global Navigation Satellite Systems (GNSS), Satellite Laser Ranging (SLR) and Very Long Baseline Interferometry (VLBI). For most applications it is important to have an impression of the reliability of the estimated station coordinates and velocities. Precision and accuracy are two widely used terms to quantify the reliability. Accuracy describes the deviation of estimated parameters from the true value. Precision refers to the closeness of agreement (scatter) between individual parameters. Repeatability, on the other hand, quantifies the precision for a limited time interval, e.g. the standard deviation (STD, measure for the dispersion around a mean value) of daily solutions w.r.t. a weekly solution. If the parameters are computed in a least squares adjustment, formal errors can be derived from the covariance matrix. Due to unmodeled correlations of the observations and systematic errors, the formal errors resulting from the adjustment of GNSS observations are usually by far to optimistic. This is in particular true for the station positions and velocities estimated in a Terrestrial Reference Frame (TRF) solution.

Therefore, Williams et al (2004) used different noise models and a Maximum Likelihood (ML) approach to get more realistic error estimates. Several authors already assessed the accuracy by comparisons of space geodetic techniques amongst each other. Campbell (2003) compared the station heights of GPS and VLBI sites and found an agreement on the level of 1 mm/y. Kierulf et al (2009) studied the velocities from two GPS sites, three DORIS sites, and the VLBI telescope located at Ny-Ålesund. Although using outdated models for the GPS processing, they achieved velocity accuracies based on statistical methods of $0.2-0.9$ mm/y. Willis and Heflin (2004) found a consistency level between DORIS- and GPS-derived velocities of $2.4-3.3$ mm/y.

In contrast to the other space geodetic techniques, GNSS receivers are quite cheap and can thus be used as dense tracking networks. Therefore, primarily GNSS stations are used to study Global Isostatic Adjustment (GIA, e.g.,

Lidberg et al, 2007; Sella et al, 2007; Árnadóttir et al, 2009; Bradley et al, 2009) and also this paper focusses on the accuracy and precision of one particular GNSS, namely the Global Positioning System (GPS). However, the independent techniques SLR and VLBI are used for the validation of GPS-derived velocities.

Section 6.2 describes the GPS, SLR and VLBI solutions discussed in this paper. The precision of the GPS solutions is assessed in terms of repeatabilities and comparisons of co-located GPS sites for time series as well as TRF solutions in Sect. 6.3. Finally, Sect. 6.4 evaluates the accuracy by comparisons of the GPS solutions with SLR and VLBI as well as geophysical series.

6.2 Space Geodetic Solutions

Homogeneously reprocessed coordinate solutions are a prerequisite for a reliable assessment of the precision and accuracy. Therefore, the solution series discussed in this paper are all completely reprocessed starting with the observation data. The first GPS solution is the contribution of the CODE (Center for Orbit Determination in Europe; Dach et al, 2009) analysis center to the IGS (International GNSS Service; Dow et al, 2009) reprocessing (Steigenberger et al, 2008). This solution was computed with the Bernese GPS Software (Dach et al, 2007) and covers the time period January 1994 until December 2008 with a network of 244 sites. Different temporal resolutions (1-day, 3-day, weekly) are available but mainly the weekly solutions are discussed in this paper. Details on previous reprocessed GPS solutions generated with a similar processing scheme can be found in Steigenberger et al (2006) and Steigenberger et al (2009a).

The second GPS solution as well as the SLR and VLBI solutions (used for the validation of the GPS results of this paper) originate from the GGOS-D project (Rothacher et al, 2010). In this project, much effort was spent on the homogenization of the software packages used for the processing of space geodetic observations as regards modeling and parameterization. Therefore, a maximum level of consistency of the SLR and VLBI solutions used for the comparisons with GPS is guaranteed. The GPS solution was also computed with the Bernese GPS software and covers the time period January 1994 until December 2006. Only daily solutions are available. The SLR solution is a combination of two contributions from Deutsches Geodätisches Forschungsinstitut (DGFI) and Deutsches GeoForschungsZentrum (GFZ). Range measurement to Lageos-1 and -2 were processed for the time interval January 1993 until December 2006. The combined VLBI solution covers the time period January 1984 until December 2006. Two independent software packages were used to compute the contributions to the combination: OCCAM v6.1 (Titov et al, 2004) for the solution of DGFI and the Calc/Solve (Petrov, 2006) for the solution of Institut für Geodäsie und Geoinformation (IGG) of the University of Bonn. More details on the GPS, SLR and VLBI solutions as well as on the combination are given in Steigenberger et al (2010).

6.3 Precision

6.3.1 Time Series

The deviation of individual (e.g., daily) solutions from a combined (e.g., weekly) solution can be used to quantify the precision. These so-called repeatabilities of seven individual coordinate solutions compared to the corresponding weekly solutions are shown in Fig. 6.1 for the reprocessed CODE series (i.e., one dot per week and coordinate component). The repeatability values improve with time due to the densification of the network resulting in shorter baselines and thus enabling a more successful ambiguity resolution. A further aspect responsible for the larger repeatabilities in the early years is the quality of the measurements provided by the receivers, in particular the bad code quality of old ROGUE receivers (the dominating receiver type in the early years). As high-quality code observations are essential for the Melbourne-Wübbena ambiguity resolution, this solution strategy was skipped for baselines between sites with one or even both receivers belonging to the ROGUE group. With decreasing baseline lengths (due to an increasing number of sites) and the replacement of the ROGUE receivers, the repeatability decreases. The mean repeatabilities for the reprocessed solution are 1.7 mm, 2.3 mm and 4.4 mm for the north, east and up component with median values of 1.4 mm, 1.9 mm and 4.1 mm, respectively. The repeatability nowadays is on the level of about 1 mm for the horizontal and 3 mm for the vertical component.

Co-located GPS sites (i.e., two or more GPS antennas and receivers operated in parallel at one station) can also be used to assess the precision of GPS-derived station coordinate time series. However, the quality of the time series of one individual site or both sites might be affected by site-specific systematic effects. Table 6.1 lists STDs of co-located GPS sites of the CODE reprocessing. Only stations with more than 52 common weeks are

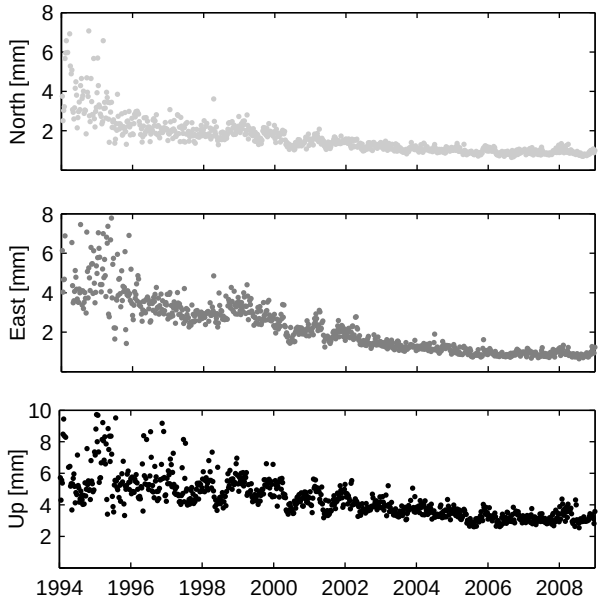

Fig. 6.1: Daily station coordinate repeatabilities w.r.t. weekly solutions derived from the CODE reprocessing. The mean repeatabilities are $\overline{N} = 1.7$ mm, $\overline{E} = 2.3$ mm, $\overline{U} = 4.4$ mm. Note the different scale of the height component.

Station	Site 1	Site 2	# weeks		North [mm]	East [mm]	Up [mm]
Hartebeesthoek	HRAO	HARK	127		1.82	4.18	4.42
Koganei	KGNI	KGN0	220		0.37	0.31	2.77
Lhasa	LHAS	LHAZ	372		0.71	0.66	4.05
Ny-Ålesund	NYAL	NYA1	558		2.31	1.58	2.22
Thule	THU1	THU3	66		1.87	1.72	7.16
Tromsø	TROM	TRO1	525	[a]	3.43	4.92	3.81
			295	[b]	3.44	4.36	3.05
			160	[c]	2.23	1.86	1.51
			70	[d]	1.17	1.42	4.17
Yarragadee	YARR	YAR2	263		0.68	0.44	2.46

[a] complete time series
[b] before TRO1 antenna change on 13 July 2004
[c] between TRO1 antenna changes on 13 July 2004 and 23 August 2007
[d] after TRO1 antenna change on 23 August 2007

Tab. 6.1: Standard deviations of the weekly coordinate difference time series of co-located GPS sites.

considered for the comparison. Several of the larger STD values can be explained by systematic effects. The huge STD of the up component of Thule is related to a degraded tracking performance of the THU1 site (observation rate of about 65% only) after an outage in the middle of 2001 resulting in quite noisy coordinate time series. As this problem persists until the end of the operation of THU1 (beginning of 2003) and THU3 tracking only started in September 2001, the whole comparisons of Thule are corrupted by this problem. As the time series of Tromsø is affected by two discontinuities due to antenna changes at the TRO1 site, also subintervals without discontinuities are given. After the antenna change in 2004, the STD values are significantly smaller except for the height component of the last interval. However, the STD values are in general below 2 mm for the horizontal and 4 mm for the vertical component. In addition, one has to keep in mind that the precision of a single station is smaller by a factor of $\sqrt{2}$ as the STD values of the differences of two stations are shown in Table 6.1.

6.3.2 Terrestrial Reference Frame

TRF solutions currently include the estimation of station positions for a reference epoch and linear station velocities. As a number of GPS stations are affected by discontinuities due to equipment changes, new station positions are estimated if a discontinuity has been detected. For the TRF studies described in this section, the GGOS-D data was used. The time spans of 13 years of data allow for stable TRF solution. The general strategy of estimating GPS-only TRFs follows Steigenberger et al (2009b). The geodetic datum was defined by No-Net-Rotation (NNR) conditions for coordinates and velocities of 84 stable IGS05 stations w.r.t. IGS05 (Ferland, 2006). The origin and the scale are realized from the GPS observations.

To test the stability of the TRF, 8 TRFs from limited time intervals were computed and compared with the TRF from the full time interval. Each limited TRF solution covers 6 years of data and the solutions are shifted by one year, i.e., 1994 – 1999, 1995 – 2000, and so on. 6 years are a sufficient amount of data to estimate reliable velocities as the impact of short periodic effects ist negligible for time series longer than 4.5 years (Blewitt and Lavallée, 2002). However, one has to be aware that not all stations are available for the full time period. The translation parameters (offsets and rates determined within a 14-parameter similarity transformation) of these limited TRF solutions w.r.t. the full TRF solution are shown in Fig. 6.2. Except for the first TRF solution, the translations are on the level of 1 – 2 mm whereas the translation rates are in general below 1 mm/y.

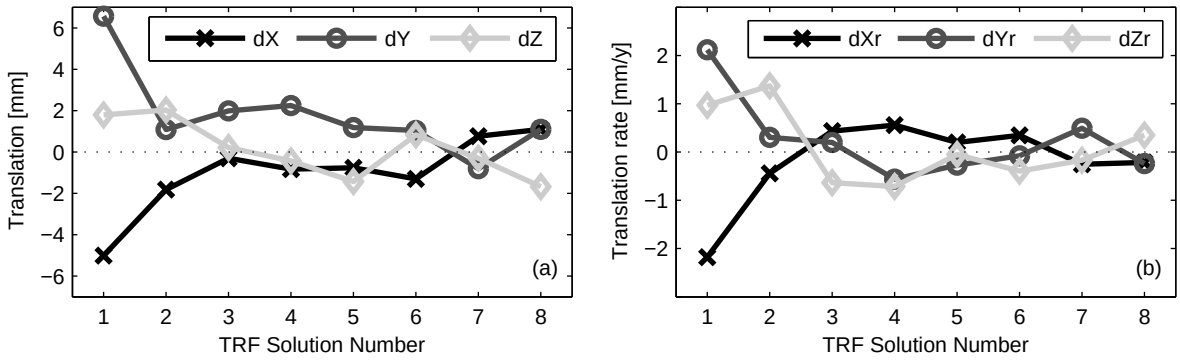

Fig. 6.2: Translations (a) and translation rates (b) of 8 TRF solutions from limited time intervals w.r.t. the full TRF solution.

The velocity estimates of the limited TRF solutions can be used to compute a velocity STD for each station. Figure 6.3 shows histograms of the velocity STDs derived from the 84 datum stations of the limited TRF solutions. The mean STDs are 1.2 mm/y for the horizontal components and 2.6 mm/y for the vertical component. After removing outliers larger than 10 mm/y (actually 9 stations), the mean standard deviation of the vertical velocities is 1.9 mm/y. However, these values are only valid for TRFs based on 6 years of data.

To assess the precision of velocity estimates based on longer time series, the convergence of the velocities can be used. Instead of computing TRF solutions from different time intervals, integer multiples of 2 weeks were added to the basic time interval from January 1994 until December 1999. Altogether 189 TRF solutions were computed. The time series of velocity estimates of the two selected stations Nicosia (NICO, Cyprus) and Wettzell (WTZR, Germany) are shown in Fig. 6.4. The difference Δv between the maximum and the minimum velocity is an indicator for the stability of the velocity estimates. For Nicosia Δv is 4.3 mm/y whereas it is only 1.0 mm/y for Wettzell. The major part of the larger value for Nicosia can be attributed to the shorter observation period: NICO started its operation in August 1997, WTZR in September 1995. Therefore, the velocity estimates until the epoch 2000 are based on 2.4 years of data for NICO but on 4.3 years for WTZR. If Δv for NICO is computed from the same minimum observation period as for WTZR, the value decreases to 1.5 mm.

This example clearly demonstrates the dependence of the stability on the length of the time series. Therefore, Δv in dependence of the minimum length of the time series can be used to assess the convergence of the vertical velocity estimates. Figure 6.5 shows the mean Δv values of up to 56 sites starting their operation before 2000. Due to a limited number of sites with long time series, their number decreases to 52 for 7 and 8 years, 44 for 9 years, and 36 for 10 years. One can see that a time series of at least 7 years is needed to get a stability better than 1 mm/y and a length of 10 years is necessary to fall below a value of 0.5 mm/y. The latter value is in good agreement for the best performing solutions studied by Teferle et al (2007) with an ML approach. Wöppelmann et al (2009) also achieved a similar precision level with their reprocessed GPS series of 180 stations: the mean

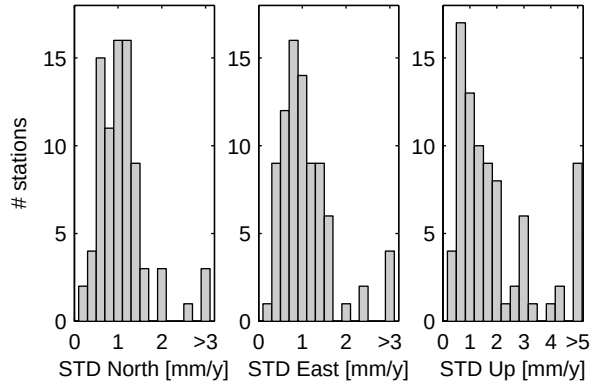

Fig. 6.3: Histograms of station velocity standard deviations from the 8 limited TRF solutions. The mean standard deviations are $\overline{\mathrm{STD}}_N$=1.2 mm/y, $\overline{\mathrm{STD}}_E$=1.2 mm/y, $\overline{\mathrm{STD}}_U$=2.6 mm/y. Only the 84 datum stations are considered.

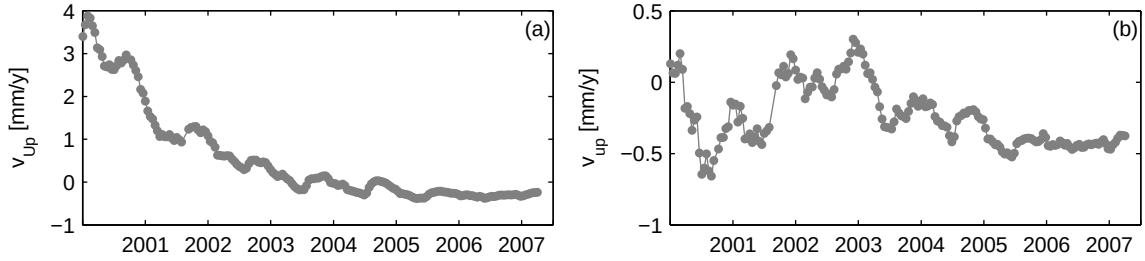

Fig. 6.4: Station height velocity time series for (a) Nicosia (NICO) and (b) Wettzell (WTZR). The velocities are based on TRF solutions from January 1994 until the epoch given on the x-axis.

vertical velocity uncertainty based on an ML analysis (power-law plus white noise) with CATS (Williams, 2008) is 0.58 mm/y with an average time series length of 8.1 years.

As for the station positions, co-located GPS sites can be used for the evaluation of the station velocity precision. Table 6.2 lists velocity estimates based on at least 2.5 years of observation time. The horizonal velocities in general agree within one millimeter per year. Several discrepancies can be explained by individual station problems, see footnotes of Tab. 6.2. For the vertical velocities, differences of more than 2 mm/y occur for almost half of the stations. The different sampling of periodic signals in the height component that are not considered by the linear model of the TRF solution might explain that effect to some extent. Ny-Ålesund, O'Higgins, Thule and Tromsø are located in postglacial rebound regions responsible for the large positive vertical velocities.

Ny-Ålesund and Tromsø are the only stations where both sites have observation periods longer than 8 years. Whereas the velocities of Ny-Ålesund agree well below 1 mm/y, the north velocities of Tromsø differ by 1 mm/y and the east velocities even by 2.1 mm/y. The reason for this behavior is unknown. The velocity differences of

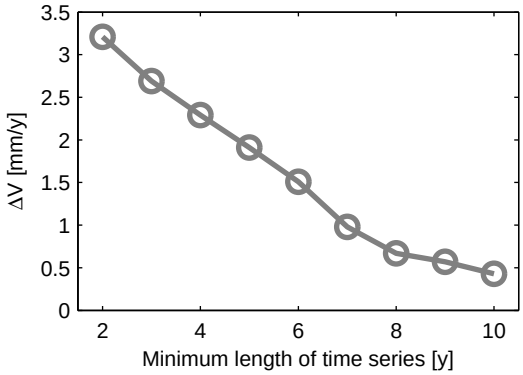

Fig. 6.5: Convergence of vertical velocity estimates based on up to 56 stations (see text).

Station	Site	# days	North	East	Up
			[mm/y]		
Easter Island	EISL	3161	−5.6	68.0	−1.0
	ISPA	1114	−5.2	66.8	1.4
Galapagos	GALA[a]	2042	11.9	51.1	−1.7
	GLPS	1458	10.2	50.3	−0.7
Miami	MIA1	941	3.7	−12.4	−4.0
	AOML	2251	2.9	−10.1	0.0
Noto	NOTO	1675	19.5	21.6	−1.6
	NOT1	2363	20.3	21.2	−0.6
Ny-Ålesund	NYAL	4427	14.3	10.2	8.5
	NYA1	3164	14.9	10.1	8.6
O'Higgins	OHIG	1709	10.8	14.1	4.2
	OHI2	1514	10.6	14.9	4.1
Taejon	TAEJ	1196	−12.5	28.8	−1.4
	DAEJ	2741	−12.1	26.9	0.9
Thule	THU1	2235	4.3	−22.3	3.1
	THU3	1998	4.9	−22.6	4.1
Tidbinbilla	TIDB	1380	58.6	18.5	−6.4
	TID2	3290	55.5	18.8	0.6
Toulouse	TOUL	1318	17.0	19.1	−0.8
	TLSE	2222	16.2	19.4	0.3
Tromsø	TROM	4025	15.5	14.8	2.6
	TRO1	3210	16.5	16.9	2.9
Wettzell	WETT[b]	991	18.6	24.4	−0.8
	WTZR	3989	16.0	20.3	−0.4
Yakutsk	YAKZ[c]	1262	−7.2	19.7	1.2
	YAKT[d]	1764	−12.8	19.3	0.8
Yarragadee	YARR	489	57.6	39.6	0.8
	YAR1	2224	57.7	39.6	−2.1
	YAR2	2425	58.1	39.5	2.0

[a] noisy data before receiver change in January 2000
[b] tracking problem, see Steigenberger (2009)
[c] annual signal of unknown origin in the north component
[d] snow-induced effects, see Steigenberger (2009)

Tab. 6.2: Velocity estimates of all co-located GPS sites with more than 2.5 years of data. Horizontal velocities differing by more than 1 mm/y and vertical velocities differing by more than 2 mm/y are given in gray.

Station	Markers GPS	Markers VLBI	Velocity Difference N [mm/y]	Velocity Difference E [mm/y]	Velocity Difference U [mm/y]	Obs. time span GPS [y]	Obs. time span VLBI [y]
Algonquin Park	ALGO	ALGOPARK	−0.67	−0.27	1.77	13.2	21.9
Hartebeesthoek	HRAO	HARTRAO	−1.80	−2.80	−0.56	10.3	19.8
Hobart	HOB2	HOBART26	−1.04	1.37	−1.04	7.7	17.0
Kokee Park	KOKB	KOKEE	0.67	1.67	−0.59	2.8	13.5
Ny-Ålesund	NYA1	NYALES20	−0.37	−1.49	0.38	9.0	12.2
Onsala	ONSA	ONSALA60	−0.73	−2.01	−1.38	8.1	22.9
Shanghai	SHAO	SESHAN25	0.31	−0.33	−0.62	11.6	18.0
Tsukuba	TSKB	TSUKUB32	1.63	0.26	1.79	13.2	7.5
Wettzell	WTZR	WETTZELL	−0.40	−1.98	−0.31	11.5	22.8
Station	GPS	SLR	N [mm/y]	E [mm/y]	U [mm/y]	GPS [y]	SLR [y]
Borowiec	BOR1	7811	−0.92	−1.37	0.15	7.8	12.8
Hartebeesthoek	HRAO	7501	1.23	−2.08	3.55	10.2	6.4
Herstmonceux	HERS	7840	−1.00	−1.26	0.16	5.6	14.0
Matera	MATE	7939	−0.62	0.36	−0.79	7.8	7.8
Monument Peak	MONP	7110	0.81	0.70	−0.43	13.0	14.0
Potsdam	POTS	7836	0.65	1.53	−0.04	12.4	11.4
Shanghai	SHAO	7837	−0.54	−2.15	3.29	11.6	12.2
Washington	GODE	7105	1.08	0.72	−0.53	13.2	14.0
Wettzell	WTZR	8834	−2.25	−0.57	−1.36	11.5	10.0
Yarragadee	YAR1	7090	1.07	0.27	−2.06	13.2	14.0

Tab. 6.3: Velocity differences of co-located GPS and VLBI/SLR sites.

the two GPS sites at Ny-Ålesund are in good agreement with the double difference results of Kierulf et al (2009) although the absolute values of the height differ by about 1 mm/y. At two stations, namely Tidbinbilla and Yarragadee (YAR1 and YAR2) two receivers are operated at the same antenna with an antenna splitter. Only one of the receivers for each station was considered during a certain time period, i.e. there is no overlap for these sites: after November 1997 TID2 was used instead of TIDB and in June 2001 YAR1 was replaced by YAR2. These sites were treated completely independently in the TRF solution, i.e. no constraints on the velocities were applied. Whereas for Yarragadee the horizontal velocities are in almost perfect agreement, the north velocity of Tidbinbilla differs by 3.1 mm/y. For both sites, the vertical velocities differ by more than 4 mm/y. However, one has to be aware that there is no temporal overlap for these stations. For Tidbinbilla, the TIDB height component shows a higher noise compared to TID2 whereas TID2 shows a pronounced annual signal. These effects can explain the largest differences in the vertical velocity of all co-locations to some extent.

For several of the stations without known problems, the horizontal velocities agree within a few tenth of a mm/y and the vertical velocities within 1 mm/y. These numbers provide a realistic measure for the precision of the estimated velocities (the mean formal errors of 0.15, 0.14 and 0.28 mm/y for the north, east and up velocities are by far too optimistic). On the other hand, in particular the vertical velocities can show discrepancies larger than 4 mm/y for stations with few or even no overlap in the time series. Irregularly sampled seasonal signals in the height component, data gaps or a true velocity change are possible explanations for that.

6.3.3 Precision of the Reference Frame Derived from Residual Time Series

It was mentioned above, that the formal errors of station positions and velocities estimated from the analysis of the GPS observations are unrealistic, because of non-considered correlations between consecutive GPS observations. More reliable precision values can be derived from the weekly or daily resolved station position time series: The RMS of the time series gives the daily repeatability of the position and allows for a quantification of the precision. First we compute RMS values of the position residual time series r separately for the x-, y- and the z-component of the station positions:

$$RMS_a = \sqrt{\frac{\sum_{i=1}^{n} r_{a,i}^2}{n}} \qquad \text{with } a = x, y, z \tag{6.1}$$

where n is the number of positions. We assume, that the RMS_x, RMS_y and RMS_z are the precision for each individual position of the time series. Now, the standard deviations for each component of the mean position of the time series can be computed with

$$\sigma_a^{pos} = \frac{RMS_a}{\sqrt{n}}. \tag{6.2}$$

The standard deviations σ^{vel} of the velocity components v_x, v_y, v_z can be computed from the RMS of the corresponding time series using

$$\sigma_a^{vel} = \frac{RMS_a}{\sqrt{\sum_{i=1}^{n}(t_i - t_{mean})^2}} \tag{6.3}$$

where t_i are the epochs of the position residuals in [years] and t_{mean} is the mean epoch of the time series. Equation 3 is the result of an error propagation for the time dependent part of a linear fit of a time series.

If we assume, that the time series is continuous and homogeneous the mean epoch is in the middle between first and last epoch. Mean GPS standard deviations derived from 10 year time series are 0.12 mm for positions and 0.06 mm/y for velocities. Formal errors estimated directly from the analysis of the GPS observations are smaller by a factor of about 0.6. For comparison: if we derive standard deviations of SLR and VLBI from the residual time series, there is no significant factor between these values and the standard deviations resulting from the position/velocity adjustment. This was expected as for both techniques the correlations between single observations are much smaller than for GPS. So, the results prove, that the chosen approach is suitable to empirically derive numerical values for the precision. Using this approach, we still make the following assumptions: (i) the daily positions are uncorrelated and show white noise. This is definitely not the case because the daily positions are mathematically correlated because the satellite constellation only varies marginally from day to day and there is an additional physical correlation due to non-considered seasonal variation of the station positions caused by loading effects. Williams (2003) presented a method that accounts for this so-called colored noise. However, the correlations of the daily positions are much smaller than for consecutive GPS observations themselves. Therefore, this method is not considered here. (ii) the RMS as a reliable measure for the precision of the daily solution is the same for all positions of the time series. This assumption is true if the 10 last years of GPS data are considered, however the RMS of the earlier years is quite larger. If we want to switch to weighted RMS values, weights have also to be considered computing the mean epoch (t_{mean}).

6.4 Accuracy

The accuracy of the estimates from space geodetic techniques is mostly limited by the deficiencies of models used in the observation analysis. GPS-derived station heights are especially sensitive to the used elevation cut off angle, the adopted functions for the mapping of the tropospheric zenith delay to the elevation of observation and the antenna phase center corrections (Rothacher, 2002). The station velocities are less sensitive to the models, however, they might be affected by unmodeled periodic variations of the station positions. The accuracy of station coordinates can only be quantified by comparisons with independent measurements or geophysical models. VLBI and SLR stations provide long time series of observations, so that the estimated STDs for station positions and velocities are below 1 mm and 1 mm/yr, respectively.

Therefore, these techniques are suitable for an assessment of the accuracy of GPS-derived station positions and velocities. For the purpose of consistency, the VLBI and SLR solutions generated within the GGOS-D project are used for the validation. In order to ensure the same geodetic datum for all technique solutions, the VLBI and SLR TRFs are aligned to ITRF2005. The origin and the orientation of the VLBI solution are realized by no-net-rotation and no-net-translation conditions w.r.t. ITRF2005. The orientation of the SLR network is also realized by a no-net-rotation condition w.r.t. ITRF2005. As the observations of the different space geodetic techniques do not refer to common reference points, the station positions cannot be compared directly without additional terrestrial measurements between the neighboring stations. But the comparison of station velocities for close sites provides information about the accuracy. Additionally, the seasonal signals mainly occurring in the station height component can be analyzed. That was already published for these solutions in Tesmer et al (2009). One of the intentions of this paper was, to compare the mean annual signals of GPS and VLBI stations. Thus, time series used in this study are strongly smoothed in order to reconstruct a clear annual signal. The agreement of

the series is on the level of 1 – 2 mm for good stations. Seasonal variations in the height components are mainly induced by atmospherical and hydrological mass load. Comparisons with geophysical loading models allow to study, to what extent station movement can be explained by the actual atmosphere and hydrology models.

6.4.1 Co-locations with VLBI and SLR

Co-locations of GPS sites with SLR or VLBI telescopes offer the possibility to compare the results of two or even three different techniques and an assessment of the accuracy. Many of the stations provide continuous observation time series of 10 years or more. Thus, they are well suited for comparisons. Table 6.3 lists differences between GPS- and SLR- or VLBI-derived velocities. The results show, that for many of the co-locations the differences in station velocities are smaller than 1.5 mm/y. The agreement is on the same level as for the GPS/GPS comparisons in Tab. 6.2. The horizontal GPS/VLBI velocity differences for Ny-Ålesund are slightly worse than the values reported by Kierulf et al (2009) whereas the vertical velocity difference is smaller than that of Kierulf et al (2009). In accordance with Kierulf et al (2009), the results of the two GPS sites agree better than the GPS and VLBI estimates. But for Wettzell the internal GPS comparison gives large discrepancies while the GPS site WTZR and VLBI agree within 2 mm/y. This is another indicator that the WETT site suffers from a tracking problem as already mentioned in the footnotes of Tab. 6.2. Slightly larger differences are derived from GPS/SLR comparisons. Although VLBI and SLR provide suitable information for an accuracy assessment, one has to be aware that especially the height component of the velocities might be affected by subsidence or deformation of the heavy VLBI and SLR telescopes.

6.4.2 Comparisons with Geophysical Series

Seasonal signals, mainly occurring in the time series of the station heights, are induced by atmospherical and hydrological loading (tidal ocean loading is well modeled and a priori reduced from the observations). Mass variations in the atmosphere and in the continental hydrology lead to an elastic compression and relaxation of the Earth's crust (Lambeck, 1988). Seitz and Krügel (2009) derived geophysical loading signals from atmospherical and hydrological mass variations using a Green's functions approach together with Love numbers and an alternative approach, that considers the regional differences of the crust. The model is based on atmospheric pressure data from NCEP (National Centers for Environmental Prediction; Kalnay et al, 1996) and hydrological data from the GLDAS model (Global Land Data Assimilation Systems; Rodell et al, 2004). In Fig. 6.6 weekly station height components of selected stations are compared with the model values.

For the station Wettzell the variations of the GPS-derived station heights and the model values agree quite well, see Fig. 6.6(a). However, the RMS of the difference is still 3.7 mm. The results for Ny-Ålesund (Fig. 6.6(b)) are in fact sobering. While the time series of the two GPS sites agree very well, the amplitude of the modeled seasonal signal is obviously too small to explain the variations of the GPS sites. However, station Ny-Ålesund is an exception: The bad agreement might arise from unmodeled effects of the permafrost soil. For Fairbanks the degree of agreement varies with time. During the first years the time series look quite different (Fig. 6.6(c)), between 2004 and 2007 the correlation becomes much better (Fig. 6.6(d)). The figures demonstrate that geophysical modeling of loading helps to understand the station behavior. However, there are still geophysical signals not comprised in the current modeling, e.g. the stretching characteristics of the permafrost soil. Additionally, the global models for atmospherical and hydrological loading might have deficiencies and are not sufficient to explain the station height variations to full extent. But, additionally to the model deficiencies, also inadequate modeling within the GPS observation analysis can contribute to a small extent to some of the differences.

6.5 Summary and Conclusions

This paper assessed the quality of GPS-derived station positions and velocities in terms of precision and accuracy. The internal consistency of weekly GPS solutions heavily depends on the density of the tracking network. Whereas the daily repeatabilities of weekly solutions in the middle of the nineties are 3 – 5 mm for the horizontal and 6 mm for the vertical component, corresponding values of 1 mm and 3 mm, respectively, can be achieved nowadays. The difference time series of co-located GPS sites show in general horizontal STDs of 0.5 – 2 mm and vertical STDs of 1.5 – 4 mm. Velocity estimates of GPS/GPS co-locations agree within 0.1 – 1 mm/y for the horizonal and 0.3 – 2 mm/y for the vertical component depending on the length and the overlap of the time series. For

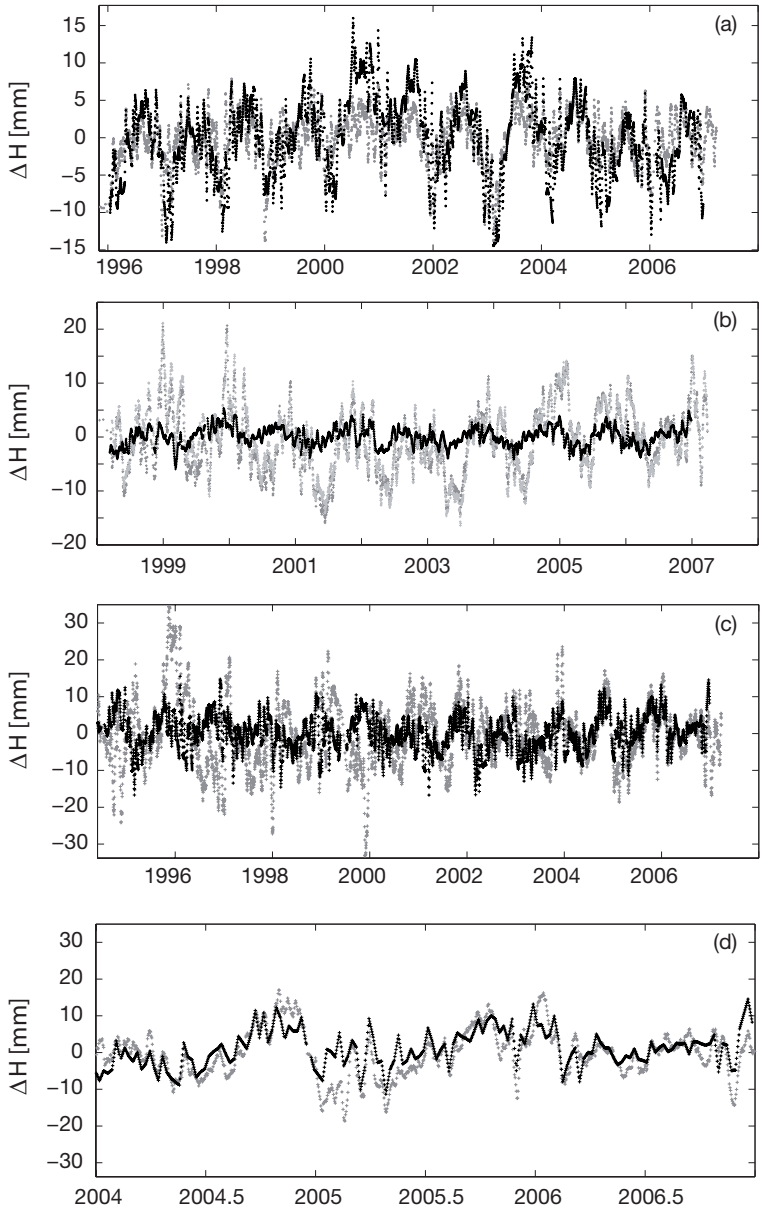

Fig. 6.6: GPS-derived station height time series (gray) and loading model (black) for (a) Wettzell (WTZR); (b) Ny-Ålesund (NYAL in dark gray, NYA1 in light gray); (c) Fairbanks (FAIR) and (d) a zoom of the Fairbanks time series.

the height component (which is in particular important for GIA modeling) observation time spans of at least 10 years are necessary to achieve a velocity stability better than 0.5 mm/y.

The accuracy of the GPS station velocities can be assessed by comparisons with independent estimates derived from VLBI and SLR observations. The velocities for good stations agree within 1 – 2 mm/yr. The agreement is on almost the same level as for the internal GPS comparisons. The validation of the GPS station height variations with a geophysical loading model does not provide satisfactory results. Unmodeled or not well known effects, as e.g. the seasonal behavior of permafrost soil, prevent a sufficient modeling of the height variations. However, the comparisons of GPS-derived station height variations and loading model values show that in some regions loading is responsible to a large extent for seasonal station height variations.

Currently, the accuracy and precision of GPS-derived station positions and velocities is limited by deficiencies in the modeling of the GPS observations (King et al, 2010). Major error sources include the troposphere modeling (a priori delays and mapping functions), the phase center model for receiver and satellite antennas, and the orbit modeling (in particular radiation pressure). More sophisticated modeling approaches like a priori troposphere slant delays from ray tracing (Hobiger et al, 2008) or the inclusion of albedo and power thrust in the orbit model (Rodriguez-Solano et al, 2012) might contribute to an improved precision and accuracy of GPS-derived station positions and velocities.

Acknowledgements

This is publication no. GEOTECH-1307 of the R&D-Programme GEOTECHNOLOGIEN funded by the German Ministry of Education and Research (BMBF) and German Research Foundation (DFG), Grants 03F0425A and 03F0425C. Part of this work was supported by COST Action ES0701 "Improved constraints on models of Glacial Isostatic Adjustment". The authors would like to thank the International GNSS Service (IGS; Dow et al, 2009), the International Laser Ranging Service (ILRS, Pearlman et al, 2002) and the International VLBI Service for Geodesy & Astrometry (IVS; Schlüter and Behrend, 2007) for providing GPS, SLR and VLBI observation data.

Bibliography

Árnadóttir T, Lund B, Jiang W, Geirsson H, Björnsson H, Einarsson P, Sigurdsson T (2009) Glacial rebound and plate spreading: results from the first countrywide GPS observations in Iceland. Geophysical Journal International 177(2):691–716, DOI 10.1111/j.1365-246X.2008.04059.x

Blewitt G, Lavallée D (2002) Effect of annual signals on geodetic velocity. Journal of Geophysical Research 107(B7), DOI 10.1029/2001JB000570

Bradley SL, Milne GA, Teferle FN, Bingley RM, Orliac EJ (2009) Glacial isostatic adjustment of the British Isles: new constraints from GPS measurements of crustal motion. Geophysical Journal International 178(1):14–22, DOI 10.1111/j.1365-246X.2008.04033.x

Campbell J (2003) European vertical site motions by VLBI and GPS: An update. In: Schwegmann W, Thorandt V (eds) Proceedings 16th Working Meeting on European VLBI for Geodesy and Astrometry, Bundesamt für Kartographie und Geodäsie, Leipzig/Frankfurt am Main, pp 267–277

Dach R, Hugentobler U, Fridez P, Meindl M (eds) (2007) Bernese GPS Software Version 5.0. Astronomical Institute, University of Bern, Bern, Switzerland

Dach R, Brockmann E, Schaer S, Beutler G, Meindl M, Prange L, Bock H, Jäggi A, Ostini L (2009) GNSS processing at CODE: status report. Journal of Geodesy 83(3-4):353–365, DOI 10.1007/s00190-008-0281-2

Dow J, Neilan R, Rizos C (2009) The International GNSS Service in a changing landscape of Global Navigation Satellite Systems. Journal of Geodesy 83(3-4):191–198, DOI 10.1007/s00190-008-0300-3

Ferland R (2006) IGS05 fine tuning. IGSMAIL-5455, `https://igscb.jpl.nasa.gov/pipermail/igsmail/2006/005526.html`

Hobiger T, Ichikawa R, Kondo T, Koyama Y (2008) Fast and accurate ray-tracing algorithms for real-time space geodetic applications using numerical weather models. Journal of Geophysical Research 113(D20):D20302, DOI 10.1029/2008JD010503

Kalnay E, Kanamitsu M, Kistler R, Collins W, Deaven D, Gandin L, Iredell M, Saha S, White G, Wollen J, Zhu Y, Chelliah M, Ebisuzaki W, Higgins W, Janowiak J, Mo KC, Ropelewski C, Wang J, Leetmaa A, Reynolds R, Jenne R, Joseph D (1996) The NMC/NCAR 40-year reanalysis project. Bulletin of the American Meteorological Society 77(3):437–471, DOI 10.1175/1520-0477(1996)077⟨0437:TNYRP⟩2.0.CO;2

Kierulf HP, Pettersen BR, MacMillan DS, Willis P (2009) The kinematics of Ny-Ålesund from space geodetic data. Journal of Geodynamics 48(1):37–46, DOI 10.1016/j.jog.2009.05.002

King M, Altamimi Z, Boehm J, Bos M, Dach R, Elosegui P, Fund F, Hernandez-Pajares M, Lavallee D, Cerveira PM, Penna N, Riva R, Steigenberger P, van Dam T, Vittuari L, Williams S, Willis P (2010) Improved constraints on models of glacial isostatic adjustment: A review of the contribution of ground-based geodetic observations. Surveys in Geophysics 31(5):465–507, DOI 10.1007/s10712-010-9100-4

Lambeck K (1988) Geophysical Geodesy. Clarendon Press, Oxford

Lidberg M, Johansson J, Scherneck H, Davis J (2007) An improved and extended GPS-derived 3D velocity field of the glacial isostatic adjustment (GIA) in Fennoscandia. Journal of Geodesy 81(3):213–230, DOI 10.1007/s00190-006-0102-4

Pearlman MR, Degnan JJ, Bosworth JM (2002) The International Laser Ranging Service. Advances in Space Research 30(2):125–143, DOI 10.1016/S0273-1177(02)00277-6

Petrov L (2006) Mark V VLBI Analysis Software Calc/Solve. URL `http://gemini.gsfc.nasa.gov/solve`

Rodell M, Houser PR, Jambor U, Gottschalck J, Mitchell K, Meng CJ, Arsenault K, Cosgrove B, Radakovich J, Bosilovich M, Entin JK, Walker JP, Lohmann D, Toll D (2004) The Global Land Data Assimilation System. Bulletin of the American Meteorological Society 85(3):381–394, DOI 10.1175/BAMS-85-3-381

Rodriguez-Solano C, Hugentobler U, Steigenberger P (2012) Impact of albedo radiation on GPS satellites. In: Kenyon S, Pacino MC, Marti U (eds) Geodesy for Planet Earth, Springer, International Association of Geodesy Symposia, vol 136, pp 113–119, DOI 10.1007/978-3-642-20338-1_14

Rothacher M (2002) Estimation of station heights with GPS. In: Drewes, Dodson, Fortes, Sanchez, Sandoval (eds) Vertical Reference Systems, Springer, International Association of Geodesy Symposia, vol 124, pp 81–90

Rothacher M, Drewes H, Nothnagel A, Richter B (2010) Integration of space geodetic techniques as the basis for a global geodetic-geophysical observing system (GGOS-D): An overview. In: Flechtner FM, Gruber T, Güntner A, Mandea M, Rothacher M, Schöne T, Wickert J (eds) System Earth via geodetic-geophysical Space Techniques, Springer, pp 529–537, DOI 10.1007/978-3-642-10228-8_43

Schlüter W, Behrend D (2007) The International VLBI Service for Geodesy and Astrometry (IVS): current capabilities and future prospects. Journal of Geodesy 81(6-8):379–384, DOI 10.1007/s00190-006-0131-z

Seitz F, Krügel M (2009) Modelling vertical site displacements due to surface loads in consideration of crustal inhomogenities. In: Drewes H (ed) Geodetic Reference Frames, Springer, International Association of Geodesy Symposia, vol 134, pp 23–29, DOI 10.1007/978-3-642-00860-3_4

Sella GF, Stein S, Dixon TH, Craymer M, James TS, Mazzotti S, Dokka RK (2007) Observation of glacial isostatic adjustment in "stable" North America with GPS. Geophysical Research Letters 34(2):L02306, DOI 10.1029/2006GL027081

Steigenberger P (2009) Reprocessing of a global GPS network. Deutsche Geodätische Kommission, Reihe C 640, URL `http://dgk.badw.de/fileadmin/docs/c-640.pdf`

Steigenberger P, Rothacher M, Dietrich R, Fritsche M, Rülke A, Vey S (2006) Reprocessing of a global GPS network. Journal of Geophysical Research 111(B5):B05402, DOI 10.1029/2005JB003747

Steigenberger P, Romero I, Fang P (2008) Reprocessing Issues, Standardization, New Models. In: The International GNSS Service (IGS): Perspectives and Visions for 2010 and Beyond, IGS Workshop 2006, European Space Operations Center, European Space Agency, Darmstadt

Steigenberger P, Rothacher M, Fritsche M, Rülke A, Dietrich R (2009a) Quality of Reprocessed GPS Satellite Orbits. Journal of Geodesy 83(3-4):241–248, DOI 10.1007/s00190-008-0228-7

Steigenberger P, Tesmer V, Schmid R, Rothacher M, Rülke A, Fritsche M, Dietrich R (2009b) Effects of different antenna phase center models on GPS-derived reference frame. In: Drewes H (ed) Geodetic Reference Frames, Springer, International Association of Geodesy Symposia, vol 134, pp 83–88, DOI 10.1007/978-3-642-00860-3_13

Steigenberger P, Artz T, Böckmann S, Kelm R, König R, Meisel B, Müller H, Nothnagel A, Rudenko S, Tesmer V, Thaller D (2010) GGOS-D consistent, high-accuracy technique-specific solutions. In: Flechtner FM, Gruber T, Güntner A, Mandea M, Rothacher M, Schöne T, Wickert J (eds) System Earth via geodetic-geophysical Space Techniques, Springer, pp 545–554, DOI 10.1007/978-3-642-10228-8

Teferle FN, Orliac E, Bingley RM (2007) An assessment of Bernese GPS software precise point positioning using IGS final products for global site velocities. GPS Solutions 11(3):205–213, DOI 10.1007/s10291-006-0051-7

Tesmer V, Steigenberger P, Rothacher M, Boehm J, Meisel B (2009) Annual deformation signals from homogeneously reprocessed VLBI and GPS height time series. Journal of Geodesy 83(10):973–988, DOI 10.1007/s00190-009-0316-3

Titov O, Tesmer V, Boehm J (2004) Occam v6.0 software for VLBI data analysis. In: Vandenberg N, Baver K (eds) International VLBI Service for Geodesy and Astrometry 2004 General Meeting Proceedings, NASA/CP-2004-212255, NASA, Greenbelt, pp 267–271

Williams SDP (2003) The effect of coloured noise on the uncertainties of rates estimated from geodetic time series. Journal of Geodesy 76(9-10):483–494, DOI 10.1007/s00190-002-0283-4

Williams SDP (2008) CATS: GPS coordinate time series analysis software. GPS Solutions 12(2):147–153, DOI 10.1007/s10291-007-0086-4

Williams SDP, Bock Y, Fang P, Jamason P, Nikolaidis RM, Prawirodirdjo L, Miller M, Johnson DJ (2004) Error analysis of continuous GPS position time series. Journal of Geophysical Research 109(B3):B03412, DOI 10.1029/2003JB002741

Willis P, Heflin MB (2004) External validation of the GRACE GGM01C gravity field using GPS and DORIS positioning results. Geophysical Research Letters 31(13):L13616, DOI 10.1029/2004GL020038

Wöppelmann G, Letetrel C, Santamaria A, Bouin M, Collilieux X, Altamimi Z, Williams SDP, Miguez BM (2009) Rates of sea-level change over the past century in a geocentric reference frame. Geophysical Research Letters 36(12):L12607, DOI 10.1029/2009GL038720

7 Vertical Deformations from Homogeneously Processed GRACE and Global GPS Long-Term Series

Originally published as:

Tesmer V., Steigenberger P., van Dam, T. (2012): Vertical deformations from homogeneously processed GRACE and global GPS long-term series, Journal of Geodesy, Vol. 85, No. 5, pp 291-310, doi: 10.1007/s00190-010-0437-8

The final publication is available at Springer via `http://dx.doi.org/10.1007/s00190-010-0437-8`.

Abstract

Temporal variations in the geographic distribution of surface mass cause surface displacements. Surface displacements derived from GRACE gravity field coefficient time series also should be observed in GPS coordinate time series, if both time series are sufficiently free of systematic errors. A successful validation can be an important contribution to climate change research, as the biggest contributors to mass variability in the system Earth include the movement of oceanic, atmospheric, and continental water and ice. In our analysis, we find that if the signals are larger than their precision, both geodetic sensor systems see common signals for almost all the 115 stations surveyed. Almost 80% of the stations have their signal WRMS decreased, when we subtract monthly GRACE surface displacements from those observed by GPS data. Almost all other stations are on ocean islands or small peninsulas, where the physically expected loading signals are very small. For a fair comparison, the data (79 months from September 2002 to April 2009) had to be treated appropriately: the GPS data were completely reprocessed with state-of-the-art models. We used an objective cluster analysis to identify and eliminate stations, where local effects or technical artifacts dominated the signals. In addition, it was necessary for both sets of results to be expressed in equivalent reference frames, meaning that net translations between the GPS and GRACE data sets had to be treated adequately. These data sets are then compared and statistically analyzed: we determine the stability (precision) of GRACE-derived, monthly vertical deformation data to be $\sim$1.2 mm, using the data from three GRACE processing centers. We statistically analyze the mean annual signals, computed from the GPS and GRACE series. There is a detailed discussion of the results for five overall representative stations, in order to help the reader to link the displayed criteria of similarity to real data. A series of tests were performed with the goal of explaining the remaining GPS$-$GRACE residuals.

7.1 Introduction

Temporal variations in the geographic distribution of surface mass (continental water, ice, ocean mass and atmospheric mass) cause a deformation of the Earth's surface. This displacement, primarily in the height component, can be observed directly using positioning techniques such as the Global Positioning System (GPS; Hofmann-Wellenhof et al, 2007), Very Long Baseline Interferometry (VLBI; Sovers et al, 1998), and Satellite Laser Ranging (SLR; Schillak, 2004). In addition, new geodetic sensors have been developed explicitly to determine the Earth's gravity field, like the satellite missions CHAMP (Reigber et al, 2002), GRACE (Tapley et al, 2004), and lately GOCE (Drinkwater et al, 2007). GOCE is proving to be particularly valuable for providing insight into the Earth's static gravity field. GRACE measurements are extremely insightful to understand the temporal variations in the redistribution of (surface) mass in the Earth system (see for example Chambers, 2005; Kuo et al, 2008; Morison et al, 2007; Rodell et al, 2009; Crowley et al, 2008; Velicogna and Wahr, 2006a,b; Chen et al, 2006a,b; Luthcke et al, 2008). These results, while somewhat limited in terms of temporal span, can make an important contribution to climate change research, as the biggest contributors to this variability include the movement of oceanic, atmospheric, and continental water and ice.

For example, Willis et al (2008) investigated the global mean sea level rise measured by tide gauges, as caused by global warming, amongst other factors. In order to track the constituents for the change of global mean sea level, they also used: data from profiling Argo floats for temperature and salinity, satellite altimetry (geometrical sea surface height), and the changes in the amount of freshwater (mass component), which were observed by GRACE. Despite excellent agreement in the seasonal and interannual terms, they found that the 4-year long-term trends do not agree, suggesting that systematic long-period errors remain in one or more of these observing systems. Other recent and detailed reviews of sea level rise are e.g. given by Cazenave and Llovel (2010) or Leuliette and Miller (2009). These publications suggest that the sea level long-term budget can be closed with today's data, within a certain error budget though.

The fact that GRACE and positioning techniques are highly sensitive to mass variability in completely different ways provides us with an opportunity to validate the GRACE data over the continents. However, a consequently satisfactory demonstration of the agreement between surface displacements computed from the GRACE gravity fields and positioning coordinates, e.g. those derived with a global network of GPS stations, has yet to be demonstrated. One of the major difficulties is that surface displacements computed from GRACE results are spatially smoothed, and GPS-derived site displacements are discrete point measurements. The latter are easily affected or even falsified by local effects, technical artifacts, or inadequate environmental models, see Ray et al (2008) or Penna et al (2007).

The first comparisons between GRACE-measured mass variations, converted to surface displacements, and GPS position measurements were successful for only the biggest signals. For example Davis et al (2004) found very good agreement between the surface height changes in the Amazon River Basin where $\sim$13 mm vertical annual displacement is observed. The agreement between GPS and GRACE in this instance is even better than that between GRACE and hydrology models in the region. King et al (2006) also found good correlation in regions with high mass variation signal, but were not successful in regions with moderate mass variations. van Dam et al (2007) compared the annual signal from GPS observations and deformations derived from GRACE-measured mass variations over Europe. The moderate agreement between the results was attributed to spurious periodic signals aliasing into the GPS annual. Tregoning et al (2009) found significant correlations between GRACE and a global set of GPS measured continental hydrology signals, approximately a quarter of the correlations had a value larger than 0.5. The improvement between the Tregoning et al (2009) study and that of van Dam et al (2007) was presumably due to the homogeneously reprocessed GPS time series computed with high quality modeling used by Tregoning et al (2009). Nevertheless, subtracting the GRACE-derived deformation from the GPS height time series still did not reduce the WRMS of their GPS residuals on about half of their stations. They concluded that local processes or site specific analysis errors dominated their GPS height estimates rather than the broad-scale hydrologic signals detected by GRACE.

The GPS series used by Horwath et al (2010) originated from a similar GPS reprocessing effort. Their GPS height time series are clearly correlated with the GRACE results for many sites all over the globe. The remaining discrepancies contain large-scale patterns in space and time (mostly seasonal), which far exceed the errors that would be expected in the GRACE-derived surface displacements. Horwath et al (2010) consider systematic errors in the GPS solutions as the most probable reason for the disagreement, in particular shortcomings in the orbit models, such as solar radiation pressure or Earth's albedo.

In this paper, we revisit the idea of comparing reprocessed GPS height coordinate time series with surface displacements computed from GRACE gravity field coefficients. Our results generally confirm many of the results of previous studies. However, we do observe a considerable improvement in the agreement between the GPS and GRACE displacement time series as compared to the results in Tregoning et al (2009), and to some extent those published in Horwath et al (2010). More importantly, however, our paper provides a thorough evaluation of the potential of the two totally independent geodetic observing systems.

Initially, we only use data from GPS stations that are proven not to have height signals dominated by local effects or technical artifacts by performing a cluster analysis (Tesmer et al, 2009). Additionally, we introduce the use of mean annual signals, which suppresses high frequency noise and all kinds of non-annually recurring signals, but without the unrealistic constraint that the signal has to be of pure harmonic nature (as many relevant geophysical processes are annually recurring but none is of harmonic nature). We provide a detailed discussion of the results for five overall representative stations. This shall help the reader to link a certain average value e.g. of GPS – GRACE similarity to the multitude of 115 stations used here, in order to get a better understanding if such GPS – GRACE residuals are rather noise than signal et cetera. There is also a summary of a series of tests with the goal of explaining the remaining GPS – GRACE residuals. Finally, we conclude that both GPS and GRACE are robust and reliable sensors of the Earth system, ready to take their part in modern Earth system science and climate research. As we demonstrate, this requires that their data are analyzed with adequate approaches and models of highest quality.

7.2 Data Sets Used

7.2.1 GPS Monthly Height Series

The GPS is nowadays widely used in the geosciences for the estimation of precise station coordinates (e.g. Hofmann-Wellenhof et al, 2007). The GPS height series used here were completely reprocessed in the context of the GGOS-D project (Global Geodetic-Geophysical Observing System - Deutschland, `http://www.ggos-d.de`; Rothacher et al, 2011), using the Bernese GPS Software 5.1 (Dach et al, 2007). Coordinate time series were computed with state-of-the-art models, including the Vienna Mapping Function 1 (VMF1; Boehm et al, 2006), a priori tropospheric zenith delays (ZDs) from the European Centre for Medium-Range Weather Forecasts (ECMWF; Simmons and Gibson, 2000), high-order ionospheric terms (Fritsche et al, 2005), as well as absolute antenna phase center corrections (Schmid et al, 2007). For more details on the GPS reprocessing see Steigenberger et al (2006) and Steigenberger et al (2010). As a final note, all critical models (e.g. for effects of the pole tide) are consistent with those used in the GRACE data processing.

Within GGOS-D, VLBI station height time series were also computed using the same fully homogenized state-of-the-art models, as those applied in the GPS data processing. These GPS and VLBI height time series were compared for 17 co-located sites by Tesmer et al (2009). It was found that if only those sites with acceptably dense data are considered, the two independent positioning techniques observe similar mean annual signals at nearly all co-located sites.

In addition, Tesmer et al (2009) determined a set of 131 globally distributed GPS stations where the height time series are not dominated by local effects or technical artifacts. This was achieved by performing a cluster analysis, that is, forming regional mean annual signals from signals of single GPS sites. If two sites in the same region (some thousand kilometers away) observed approximately the same mean annual height signal, it was concluded that they most likely predominantly reflect geophysical loading.

For the work presented in this paper, the GPS coordinate time series used in Tesmer et al (2009) were extended to include data beyond March 2007 and up to April 2009. However, only data from September 2002 onward were used in the comparison to be in accordance with our GRACE data. Additionally, 16 of the original 131 GPS stations were removed from the data set because they either had less than four years overlap with the GRACE data, or the new data after March 2007 contained extensive data gaps, was very noisy, or was identified as containing spurious signals, that were obviously not of geophysical origin. As a consequence, the 115 GPS stations used in this paper are not necessarily those where an extreme loading signal is known to exist, but are those that have been proven to contain regionally coherent signals as opposed to signals due to local effects or technical artifacts. For example, the station BRAZ in the Amazon River Basin is not one of the 115 stations used here, as there were no other GPS stations nearby to verify that the observed signal there is regionally consistent.

From each station's daily height coordinate time series, a trend was removed and monthly means were computed, in order to correspond to the data binning defined by the monthly GRACE data series. This monthly binning also provides an idea of the internal precision of these GPS values. Thus, in addition to the monthly means, formal errors (their precision) were estimated and found to be 1.0 mm on average. These formal errors depend on the RMS of the differences between the daily values and the monthly mean values (which consist of real station motion during the month superimposed with colored and white measurement noise), and on the number of values in the monthly bins.

7.2.2 GRACE Monthly Deformation Series

The GRACE gravity field solutions used here are from the University of Texas Center for Space Research (UTCSR; Bettadpur, 2007) and the Helmholtz-Zentrum Potsdam, Deutsches GeoForschungsZentrum (GFZ; Flechtner et al, 2010). This study also uses gravity field solutions of Jet Propulsion Laboratory (JPL; Watkins and Yuan, 2007). Throughout the paper, we use the monthly unconstrained (the solutions are computed without any regularization of the Stokes coefficients) CSR GRACE level 2 gravity products from Release 04, namely the 79 months of data from September 2002 to April 2009. Bettadpur (2007) describes the details of the processing standards, models, and parameters that have been used. Products from the other processing centers (GFZ and JPL) are only used in Sect. 7.2.2, to determine the stability (precision) of the GRACE deformation time series.

In order to compute a gravity field, using the original GRACE observed data (K-Band data, positions of both satellites, accelerometers, et cetera), the observation equations have to be solved in linearized form. Thus, several background models have to be removed from the original GRACE observation data in order to have sufficiently

precise values for the estimation process. Furthermore, the background models are used also for the reduction of short-term mass variations that cannot be well modeled by only monthly representations of the gravity field (the atmosphere/ocean dealiasing). The removed models for the gravitational potential include a static gravity field, a trend for the lower spherical harmonics, tides (direct tides, Earth, ocean and atmospheric tides), the effect of periodic changes of the centrifugal potential due to polar motion on the solid Earth (Solid Earth Pole Tide), and the atmospheric and non-tidal ocean mass variations. Estimated Stokes coefficients, then, primarily contain variations in the gravity field driven by the geographic redistribution of water mass (groundwater, soil moisture, snow and ice, as well as residual atmosphere and ocean mass). In order to be in accordance with the GPS measurements, which measure surface displacements due to the total environmental mass load, we have added the atmospheric and non-tidal ocean mass fields (also provided by UTCSR, using the original Atmosphere and Ocean De-aliasing Level-1B "AOD1B" data, see Flechtner, 2005) back to the Level-2 GRACE-estimated fields. The effect of the Earth tides, ocean tides, and pole tide were subtracted in both techniques, and are, in accordance with common practice, not restored.

We use the monthly GRACE-derived Stokes coefficients c_{nm}, s_{nm} for the gravity potential (of degree n and order m) in such a way, that they represent surface mass (Wahr et al, 1998), and use the degree n load Love numbers h'_n and k'_n of Han and Wahr (1995) to compute the vertical deformations $\Delta h(\lambda, \varphi)$ at the longitude λ and latitude φ for the points on the Earth surface (with reference radius R), where our 115 GPS stations are located:

$$\Delta h(\lambda,\varphi) = R \sum_{n=1}^{N} \frac{h'_n}{1+k'_n} \cdot \sum_{m=0}^{n} \overline{P}_{nm}(\sin\varphi)\,[c_{nm}\cos(m\lambda) + s_{nm}\sin(m\lambda)] \tag{7.1}$$

The functions $\overline{P}_{nm}(\sin\varphi)$ are normalized Legendre functions for degree n and order m. Please note that the coefficients of degree $n = 1$ are often not estimated and are thus often not explicitly mentioned.

The GRACE Stokes coefficients are dominated by larger uncertainties at high degrees (e.g. Wahr et al, 2004). To reduce the effects of those errors on our deformation estimates, we apply a Gaussian averaging kernel with a 400 km radius when scaling the Stokes coefficients to obtain surface mass with the weighting function W_n according to Wahr et al (1998). We chose a 400 km averaging radius as a compromise between trying to minimize the GRACE errors (by making the radius large) while trying to keep our smoothing and thus damping of signal amplitude to a minimum (by making the radius small). This means in effect, that for each point (locations of the GPS stations), our GRACE-derived deformations include only those components of mass redistribution that have scales larger than about 400 km around that point (see also van Dam et al, 2007).

GRACE monthly deformation signal precision In order to determine the stability (precision) of the surface displacements derived from the original GRACE data, deformation time series were computed using the Stokes coefficients from the three processing centers (CSR, which is the solution described before, JPL and GFZ), each using data from September 2002 to April 2009. The most important differences between the processing setups are first, that only unknowns up to degree 60 were estimated for the CSR solution of GRACE gravity coefficients, while JPL and GFZ go up to degree 120. Second, we replace the GRACE-derived C_{20} coefficients in the CSR solution with SLR estimates (as officially recommended by CSR, see Cheng and Tapley, 2004), while in the JPL and GFZ data sets we use the C_{20} as provided by the processing centers.

We expect that these and other minor inconsistencies in the data processing, for example where a conventional treatment is not defined ("analyst's noise"), should result in small differences in the computed surface displacements below their level of precision. Therefore, the agreement between the results derived from the different approaches provides an overall validation of the internal precision of GRACE-derived monthly deformation values. To begin, we computed GRACE-derived surface displacement time series for the locations of our set of 115 GPS stations. For this network, we then compared the translations between the three GRACE-derived data sets (CSR, GFZ, JPL) by computing translations in the X-, Y- and Z-directions for the differences between the three surface displacement time series. None of the CSR − JPL, CSR − GFZ and JPL − GFZ differences showed amplitudes of estimated annual harmonic signals in the translations larger than 0.4 mm. We conclude that the different GRACE deformation series do not have significant systematic differences with respect to the derived translational components.

The RMS of the original signals from the three series are 2.4 mm, 1.8 mm, and 2.1 mm for products from CSR, JPL, and GFZ respectively. For comparison, a pure annual sine wave (without any noise) having an amplitude of 3 mm, has a signal RMS of about 2.1 mm, if it is sampled with "monthly" values. The RMS of the differences

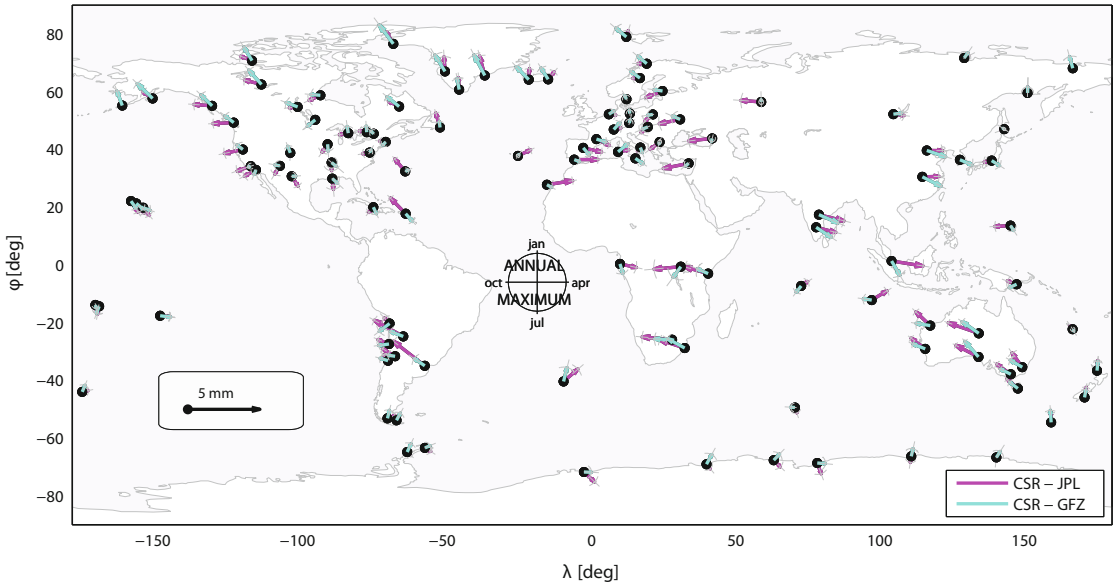

Fig. 7.1: Vectors representing the differences between the annual harmonic phasors from several GRACE-determined vertical surface displacement signals: CSR – JPL (magenta) and CSR – GFZ (cyan). The formal errors of the difference phasors (in phase and amplitude) are displayed in light grey at the arrowheads. In contrast to the customary approach, this figure does not display the phase of a sine wave, but the phasor points directly in the direction of the maximum ('up' = max in January, 'right' = max in April, 'down' = max in July, 'left' = max in October), meaning maximum vertical (up) site displacement.

between the different series is 1.7 mm for CSR − JPL and CSR − GFZ and 1.4 mm for JPL − GFZ. Thus, if we take the more pessimistic value 1.7 mm, we determine that the internal precision of our GRACE monthly deformation values can be estimated to be = 1.2 mm. Obviously, this approach does not account for (systematic) errors in the raw GRACE observation data used by all processing centers, that cannot be assessed by our method here. Thus, this value is derived in an attempt to quantify the precision, not the accuracy of the GRACE data. But, as there is no better source of information, we use the value of 1.2 mm as the formal error for the monthly GRACE surface displacements in the following discussion. The issue of the data precision is further discussed in Sect. 7.4 as a result of the comparisons with GPS height measurements.

Figure 7.1 illustrates the annual harmonic signals estimated from the CSR − JPL and CSR − GFZ height deformation residuals. The weighted mean amplitude of the 115 CSR − JPL difference phasors (magenta in Fig. 7.1) is 1.0 mm, the CSR − GFZ difference phasors (cyan) are even smaller (0.8 mm on average). The height time series from the different processing centers seem to also contain some small but regionally systematic differences that are evident in the surface displacement signals. However, these differences are quite small when compared to the amplitude of the full GRACE deformation signal (about 30%, see Fig. 7.3, which shows the CSR results in blue).

7.2.3 Degree-1 (translation-) Coefficients of the GPS and GRACE Data Sets

In order to compare GPS and GRACE deformation time series sensibly, it is necessary for both sets of results to be in equivalent reference frames. Satellite observations of the mass field are by definition given in the center of mass frame. But GRACE satellite-to-satellite tracking is insensitive to degree-1 mass effects. As a result, published GRACE gravity fields have the $n = 1$ (geocenter) terms set to zero.

For the GPS reference frame, Dong et al (2003) found that GPS network solutions, which have been transformed into the International Terrestrial Reference Frame (ITRF; Altamimi et al, 2007) are in fact in a frame defined by the Center of Figure of the Earth (see Blewitt (2003) and Dong et al (2003) for a thorough discussion of the GPS reference frame). Translation components (the degree-1 terms) of a global station network solution with respect to e.g. the ITRF can in practice be determined by computing $dX = \frac{1}{n}\sum dx_i$, $dY = \frac{1}{n}\sum dy_i$, $dZ = \frac{1}{n}\sum dz_i$ (where dx_i, dy_i, and dz_i are the individual station displacements of the ith = 1 . . . n station). These translation components dX, dY, and dZ can then be subtracted from the full station network in order to have the network in the Figure of the Earth frame.

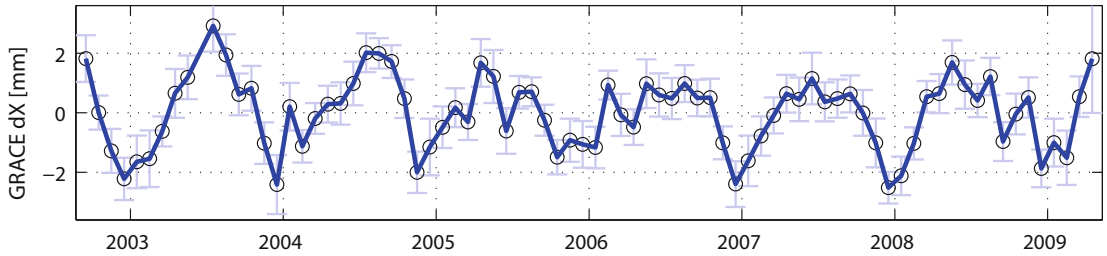

Fig. 7.2: Monthly dX-translations estimated from the GRACE-derived deformation signals of the 53 datum stations in the center of mass frame (with error bars); The X-translations are shown exemplarily for these 'apparent' degree-1 signals, because they have a much more distinct and larger signal than the Y- and Z-component.

In our GPS data set, the frame translations have been removed from the GPS monthly position time series as described before, based on our $i = 1 \ldots 53$ globally distributed datum stations (a subset of the IGS datum stations of the reference frame IGS05, Ferland 2006), by means of a least squares fit. With respect to this network of 53 stations, our original GPS height time series then do not have any translational components. But, as these 53 stations do not cover the Earth surface perfectly, we have to assume that their mathematical property to have zero-translations cannot fully fulfill the claim that the origin of the network is at the Center of Figure of the Earth.

In order to account for this deficiency, we derive the network effect from our GRACE data. For this, we assume that we can, on the whole, expect quite similar signals from GPS and GRACE, and that we have zero errors for the information on the center of the frame in the GRACE equation systems (due to aliasing et cetera).

For this, we determine the apparent degree-1 signals by computing $dX = \frac{1}{n}\sum dx_i$, $dY = \frac{1}{n}\sum dy_i$, $dZ = \frac{1}{n}\sum dz_i$ from the monthly GRACE-derived surface displacements at the locations of the $i = 1 \ldots 53$ reference (datum) stations as discussed above for GPS. Please note that the full GRACE-derived mass fields are translation free, but the discretization at the 53 locations (as we use here) is presumably not. The observed GRACE-derived translational network effect is largest in the X-component with maxima up to about 2 mm, dominated by an annual variation (Fig. 7.2). The signal WRMS of the translations are 1.1 mm in X, 0.7 mm in Y, and 0.6 mm in Z.

Finally, we add these GRACE-derived translations to the original GPS position time series (which have zero translational components with respect to the network of the 53 datum stations), and end up in equivalent reference frames for our GPS and GRACE data. As final note, we would like to point out, that adding the GRACE-derived translations to the GPS position time series makes the GPS results up to a certain extent dependent on the GRACE results. Removing all GRACE-derived translations from the GRACE data would also yield GRACE and GPS to be in appropriate frames, but this would not represent the original goal of this investigation as clearly, to find patterns for movement of mass in both time series.

7.3 GPS and GRACE Deformation Signals, Results

In the next sections, the monthly GPS height and GRACE height deformation data for the 115 stations introduced in Sect. 7.2 will be compared. Please note that the GPS data have the small translation components estimated from the monthly GRACE data added to them (see Sect. 7.2.3).

7.3.1 Similarity of Annual Harmonic Signals

Although many geophysical signals are annually recurring, an annual harmonic model will quite often be a bad approximation, and always has to be interpreted with care (see Sect. 7.3.2.4). On the other hand, comparing annual harmonic signals helps to get a quick (visual) overview of the general properties of annually recurring signals for a larger number of stations. Different from the customary approach used in many other publications, our such figures do not display the phase of a sine, but the phasors point directly in the direction of the maximum, which is much more direct (meaning maximum vertical site displacement: 'up' = max in January, 'right' = max in April, 'down' = max in July, 'left' = max in October). Figure 7.3 displays such phasors for our GPS and

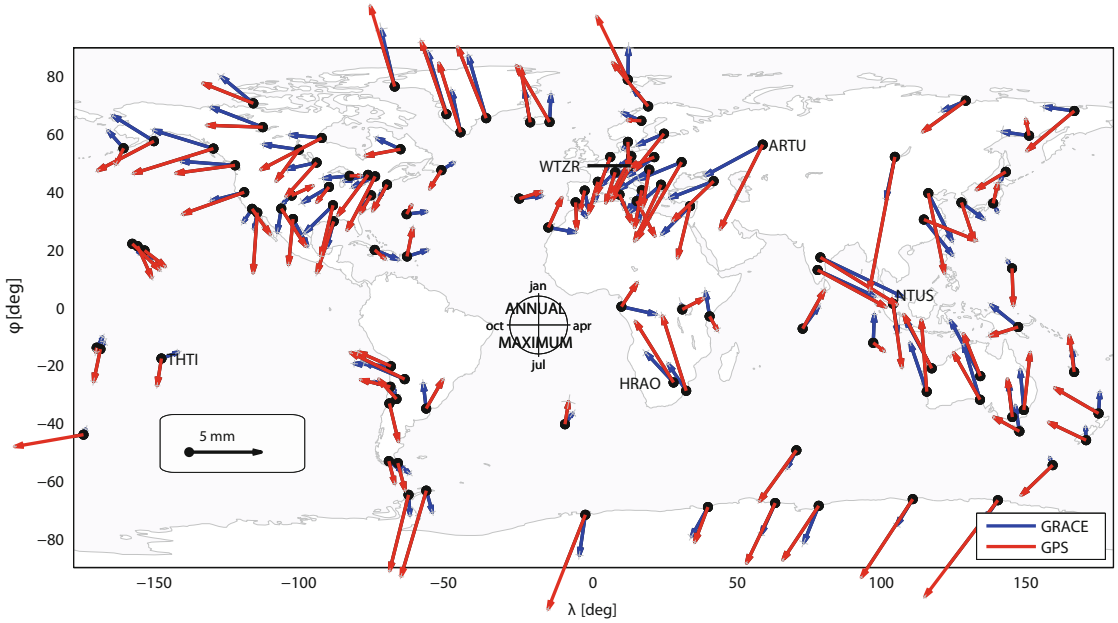

Fig. 7.3: Annual harmonic vertical deformation signals derived from GPS (red, with small translations from GRACE added, see Sect. 2.3) and GRACE (blue) measurements.

GRACE data sets. Generally, the two data sets have very similar fitted phasors. They tend to see the maxima in summer, which corresponds to a maximum continental water load in winter. In addition, GRACE and GPS both display similar patterns for many regions including the very high northern/southern latitudes, 'phase-twists' in North and South America, Australia as well as in Europe (e.g. the phases point to 'November' in the very north of Canada and continuously change to be earlier during the year, the more southerly the stations are, ending up to be in 'August' in the south of U.S.A.). The five stations marked in the figure are discussed in detail in Sect. 7.3.2.4.

Subtracting the phases of the GPS and GRACE annual harmonic phasors, the weighted mean of the phase differences for all 115 stations is 10°, indicating that there is almost no overall systematic phase difference between these data sets. The weighted mean amplitude is 3.7 mm (median 3.0 mm) for GPS, and 2.2 mm (median 1.8 mm) for GRACE. Thus, the GPS phasor amplitudes are larger than those of GRACE, on average by a factor of about 1.7. To some extent, this is to be expected as the Gaussian averaging used to smooth the GRACE data also has the effect of reducing the amplitude of the true signal. The difference vectors between the GPS and GRACE phasors (see Fig. 7.4) have a weighted mean amplitude of 2.3 mm (median 1.8 mm). This is significantly more than the 1.0 and 0.8 mm weighted mean amplitudes of the CSR − JPL and CSR − GFZ GRACE-internal difference vectors as displayed in Fig. 7.1. Taking the value 1.0 mm (from CSR − JPL) as precision of the GRACE annual harmonic signals (Sect. 7.2.2), it appears that GPS observes additional annual signals (for further discussions, see Sect. 7.3.2.4 and 7.4).

7.3.2 Similarity of Monthly Time Series and Mean Annual Signals

7.3.2.1 Monthly Time Series, Overview

Comparing the monthly time series, we first have to understand how much similarity we can expect in the ideal case that both techniques observe exactly the same signal, considering that both data sets contain a certain amount of 'white' measurement noise. As discussed in Sect. 7.2.2, we assume the monthly GRACE deformations to have a precision (overall formal error) of 1.2 mm. The monthly mean GPS values were estimated to have a precision (formal error) of about 1.0 mm on average. Thus, the precision of the monthly GPS − GRACE difference values cannot be less noisy than $\sqrt{(1.2\ \text{mm})^2 + (1.0\ \text{mm})^2} = 1.6$ mm (please note that this order of magnitude estimate neglects medium-term correlated, colored noise as e.g. caused by bedrock/monument thermal effects, mismodeled atmospheric delays, changing multipath effects or changes in satellite constellation and geometry; as discussed later in this section and in Sect. 7.4, this leads to an underestimation of the precision, see also Williams et al. 2004). The GPS overall (average) signal WRMS is 4.0 mm, and 2.4 mm for GRACE

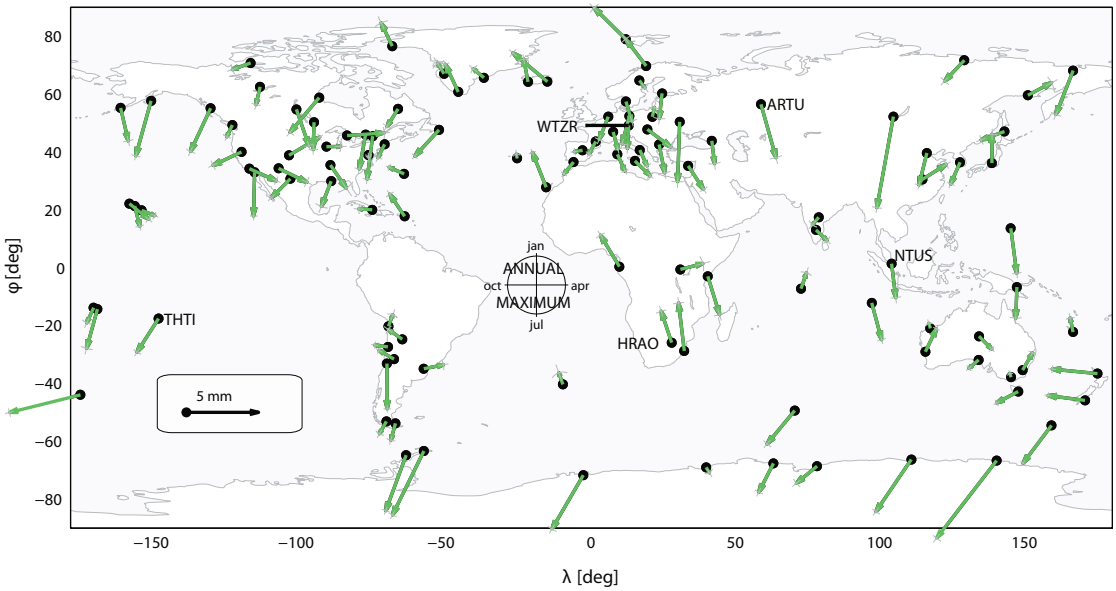

Fig. 7.4: GPS − GRACE difference vectors of annual harmonic phasors (GPS has small translations from GRACE added, see Sect. 7.2.3). The five stations marked in the figure are discussed in detail in Sect. 7.3.2.4

(see Tab. 7.1). For GRACE, it holds that RMS = WRMS, as we assume the same precision of 1.2 mm for each monthly data point.

If we compare our precision of the GPS – GRACE residuals of 1.6 mm, to the overall GRACE signal WRMS, 2.4 mm, we predict that for stations with quite small signals (such as those from stations on ocean islands), not much common signal can be recovered in the monthly time series. This means that correlation between GPS and GRACE signals for such stations should be very small. This result is illustrated by the (theoretical) example in Sect. 7.2.2, that is a 2.1 mm signal RMS corresponds to a pure annual sine with an amplitude of 3 mm, but under the assumption that there is zero noise contribution.

Unfortunately, the overall signal WRMS of the real GPS – GRACE residuals is 3.4 mm, which is much larger than 1.6 mm, as theoretically derived from the GPS and GRACE internal precisions. This, together with the results presented in Sect. 3.1 underlines the fact that the monthly GPS and maybe also the GRACE time series still contain residual signals, which are not reflected by their internal precisions (1.0 mm and 1.2 mm, respectively). Further discussion on this point is given in Sect. 7.4.

We expect the surface displacements to be relatively small for ocean islands and small peninsulas. This is due to the fact, that at periods greater than one day, the ocean responds to atmospheric pressure forcing as an inverted barometer. In addition, because the displacement of the surface scales almost linearly with the area over which a surface load is acting, islands of only limited geographic extent will not experience significant surface displacements due to variations in water storage. Only surface displacements due to non-tidal ocean mass variations should be seen in the loading time series for ocean islands, but this effect generally is the smallest of all the contributors, especially at annual periods (Nordman et al, 2009; Takiguchi et al, 2006; Zerbini et al, 2004).

Our first criterion for the measure of similarity between GPS and GRACE time series is the correlation between the two signals. However, this criterion generally suffers from two disadvantages: First, it is blind to the stochastic properties of the values. Second, it is only a measure for linear relationships, and not for similarity as such (e.g. two sine curves with identical phases are perfectly correlated with value 1, even if they have completely different amplitudes). Nevertheless, Fig. 7.5 displays correlation coefficients computed for the monthly GPS and GRACE time series (examples of such time series are given in Sect. 7.3.2.4). 60% of the stations have a correlation larger than 0.5, 34% have a correlation between 0 and 0.5. Only 6% of the stations have a negative correlation. The median correlation coefficient is 0.55 (mean is 0.48). The five stations with the biggest correlation coefficients between 0.89 and 0.76 are KULU, KELY, THU3 (all Greenland), HYDE (India), and NANO (Canada). The seven stations with slightly negative correlation coefficients are all stations on islands or small peninsulas in the Pacific, Atlantic, or Indian Ocean (CHAT, THTI, GUAM, STJO, BAY1, COCO), except for MALI in Africa.

The results presented in Fig. 7.3 support the fact that the stations with the worst correlation are almost all situated on ocean islands or small peninsulas with quite small signals. Additionally, Fig. 7.3 also illustrates that

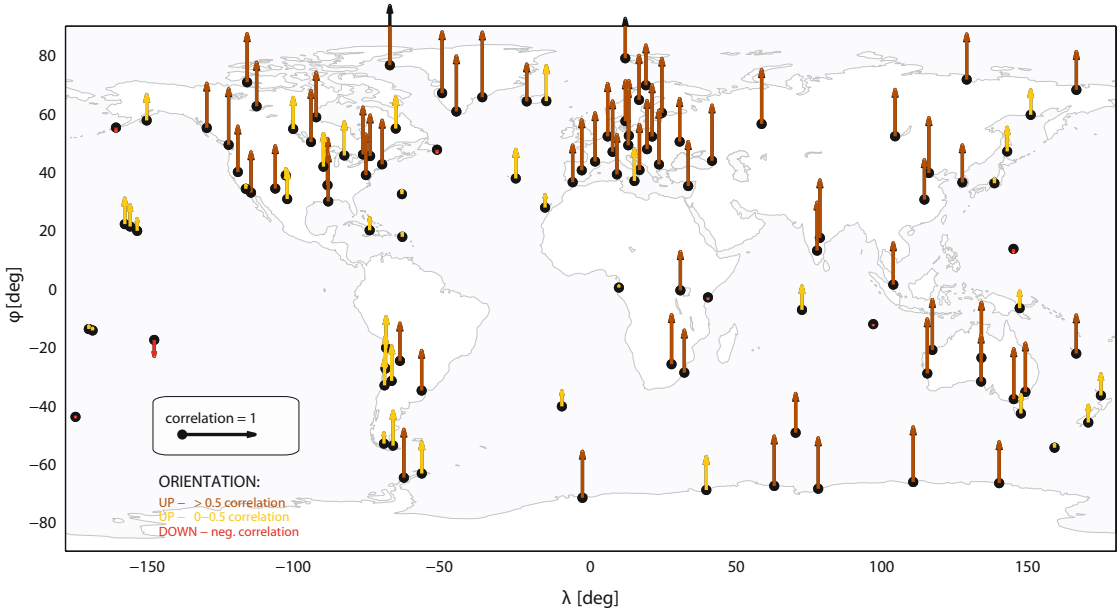

Fig. 7.5: Correlation coefficients computed for monthly time series of the 115 stations from the GPS (with small translations from GRACE added, see Sect. 2.3) and GRACE data sets. Brown depicts a correlation larger than 0.5 (60% of the stations), yellow between 0 and 0.5 (34% of the stations), and red negative correlation (6% of the stations).

almost all such stations have harmonic annual amplitudes smaller than 2 mm. This corroborates our assumption (confirmed by Fig. 7.5) that it should be very difficult to clearly detect common GPS and GRACE signals for ocean island stations, as the signal amplitude here is usually smaller than the precision of the GPS – GRACE residuals (1.6 mm).

The second criterion we use for determining the similarity between the monthly GPS and GRACE time series, namely the reduction of GPS signal WRMS by subtracting GRACE surface displacement series from GPS series, is demonstrated in Fig. 7.6. The reduction of GPS signal WRMS is computed in percent as

$$100 \cdot \left(\frac{\mathrm{WRMS}_{GPS} - \mathrm{WRMS}_{GPS-GRACE}}{\mathrm{WRMS}_{GPS}} \right)$$

where WRMS_{GPS} is the signal WRMS of the GPS data and $\mathrm{WRMS}_{GPS-GRACE}$ the signal WRMS of the GPS – GRACE residuals. In Fig. 7.6 we show the reduction of GPS signal WRMS in percent. 34% of the stations have a WRMS reduction larger than 20%, 43% have a WRMS reduction between 20% and 0%. For 23% of the stations the signal WRMS was increased. The median reduction is 14% (mean reduction is 12%). The five stations with the biggest reduction of GPS signal WRMS between 54 and 38% are KULU, KELY, THU3, QAQ1 (all Greenland) and WTZR (Europe). The six stations which have more than 15% signal WRMS added are all stations on islands or small peninsulas in the Pacific, Atlantic, Indian Ocean (BRMU, THTI, STJO, BAY1, COCO, SCUB).

Using the signal WRMS reduction, we arrive at the same conclusion as we drew from the correlation coefficients, that is, for the stations on ocean islands and small peninsulas, we cannot derive an improvement by subtracting GRACE from GPS, as the geophysical signals are smaller than the noise there. This is further emphasized by Fig. 7.7, where the red circles mark the 20 stations on ocean islands or small peninsulas in our data set.

7.3.2.2 Comparison to Previous Work

Tregoning et al (2009) were the first to use homogeneously reprocessed GPS time series computed with high quality modeling for comparison to GRACE. In contrast to our approach, Tregoning et al (2009) used 10-day data bins, compared with the monthly estimates here. Further, their GRACE and GPS data sets have atmospheric mass variations removed, whereas these effects remain in our data sets. Another important difference between this comparison and that of Tregoning et al (2009) is that we only used stations that are verified not to have height signals dominated by local effects or technical artifacts, which are not necessarily the ones with extreme

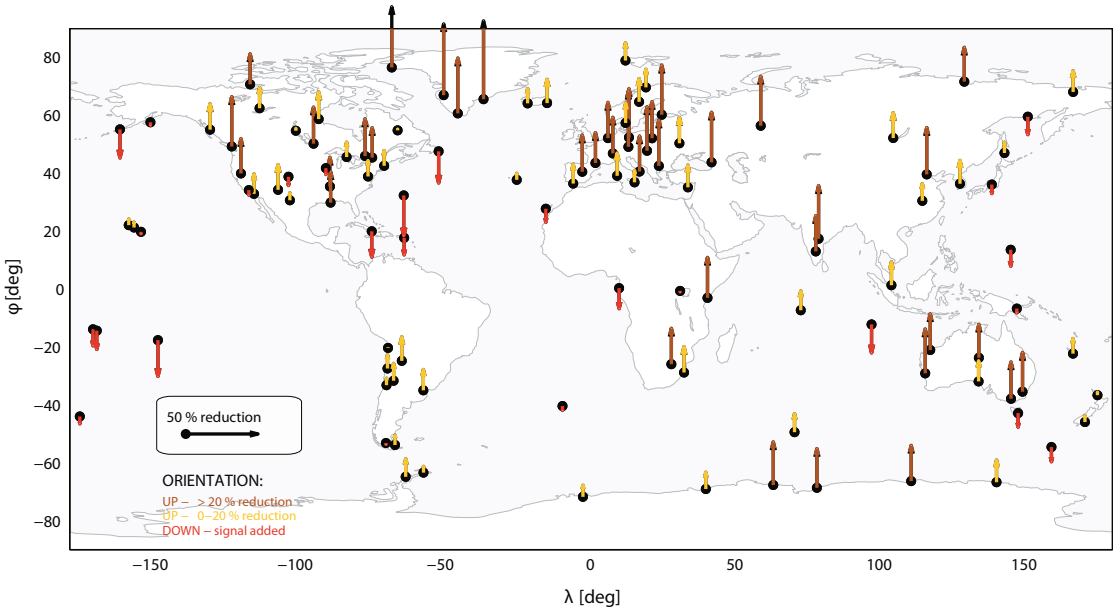

Fig. 7.6: Reduction of GPS signal WRMS [%] by subtracting GRACE deformation from GPS heights (with small translations from GRACE added, see Sect. 2.3), computed for the monthly time series of all 115 stations. Brown depicts a reduction larger than 20% (34% of the stations), yellow between 0 and 20% reduction (43% of the stations), and red if signal WRMS was added (23% of the stations).

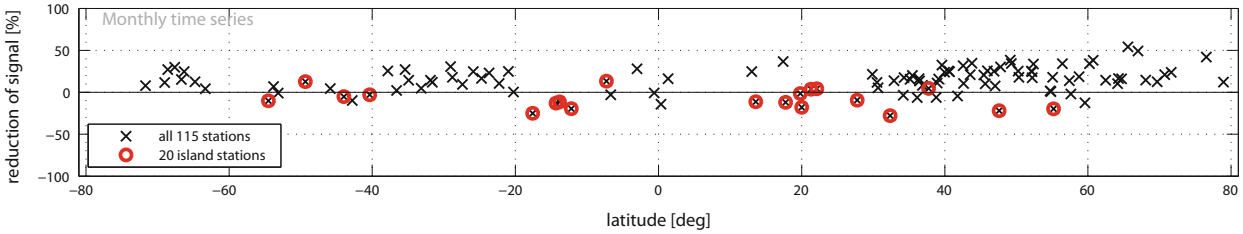

Fig. 7.7: Reduction of GPS signal WRMS [%] by subtracting GRACE deformation from GPS heights (with small translations from GRACE added, see Sect. 7.2.3), computed for the monthly time series of all 115 stations. The stations are sorted by latitude; the marked stations (red circles) are the 20 stations on ocean islands or small peninsulas (Pacific: KOKB, MKEA, HNLC, ASPA, FALE, THTI, CHAT, GUAM; Atlantic: PDEL, MAS1, BRMU, CRO1, SCUB, GOUG, STJO, BAY1; Southern: KERG, MAC1; Indian: COCO, DGAR). Only five of these 20 stations have GPS signal WRMS slightly reduced: KERG, DGAR, HNLC, KOKB, PDEL (4 to 13% reduction).

loading phenomena (Sect. 7.2.1 or Tesmer et al (2009)). Tregoning et al (2009) do not report on how they treated the degree-1 (translation) effects in the GRACE and GPS time series. As we have demonstrated in Sect. 7.2.3, this effect is significant in our data. Given these differences it is difficult to directly compare the results presented here with the results of Tregoning et al (2009).

Nevertheless, we find that Tregoning et al (2009) had only about a fourth of their stations (gleaned from their Figs. 1 and 3) to have correlations between GPS and GRACE height signals larger than 0.5. They give numerical examples for MATE, 0.6, and POTS, 0.4. Our analysis demonstrates that 60% of our 115 stations have a correlation larger than 0.5, with the examples MATE, 0.6, and POTS, 0.8. Further, Tregoning et al (2009) state that subtracting GRACE from GPS heights decreases GPS signal WRMS at almost 50% of the ∼80 sites used in their paper. Besides stations with extreme loading phenomena such as ones in the Amazon basin, they find most of the well fitting stations to be located in Europe (again gleaned from their Figs. 1 and 3), whereas almost half of the stations in their data set actually are in central Europe (36 out of 80). In comparison, we found that almost 80% of our 115 GPS sites have their WRMS decreased. Our central European stations are also amongst the best performing, however, only about a sixth of our stations (18 out of 115 stations) are located in central Europe.

With regards to the results of Horwath et al (2010), their GPS series were processed in an earlier reprocessing effort, from which our GGOS-D processing scheme was derived. The two GPS processing strategies differ in

that: First, our position time series are not derived with a TRF including time dependent low-degree spherical harmonics in addition to epoch station coordinates and velocities; Second, while Horwath et al (2010) used the Isobaric Mapping Function (IMF; Niell, 2001) and constant a priori ZDs, we used the more sophisticated VMF1 and a priori ZDs derived from ECMWF. Thus, all in all, the two series should not be extremely different in terms of their quality. Just as Tregoning et al (2009), Horwath et al (2010) do not specify their treatment of the translational reference frame effects.

Unfortunately, Horwath et al (2010) present only limited numerical results and a visual comparison is very difficult. The only numerical results to be extracted from that paper are "typical numbers" for correlation between the GPS and GRACE, and the percentage of GPS variance explained by GRACE. If we try to compare the two sets of results, we reach contradictory conclusions. On the one hand, our overall median GPS/GRACE correlation of all the 115 stations is 0.55 (see Tab. 7.1), which appears to be very good compared to the "typical numbers" of 0.2 and 0.8 of Horwath et al (2010). On the other hand, if we use our overall median WRMS values given in Tab. 7.1 ($\text{WRMS}_{GPS} = 3.8$ mm, $\text{WRMS}_{GPS-GRACE} = 3.3$ mm), and compute "percentage of GPS variance explained by GRACE" for these, we only find 25% as compared to the "typical numbers" 20% to 60% of Horwath et al (2010). Third, Horwath et al (2010) state that for small ocean island stations, they find small signals for GRACE (as physically expected) but big, unexplained GPS signals, which we find to be small for both, GPS and GRACE on ocean island stations.

7.3.2.3 Mean Annual Signals, Overview

The mean annual signals were computed by stacking all years of monthly GPS and GRACE time series into one "(weighted) mean year", for each station separately. These mean monthly values have formal errors derived with error propagation. A detailed description of the procedure is given in Tesmer et al (2009), or Freymueller (2009). Five examples for the GPS and GRACE data are given in Sect. 7.3.2.4.

The robustness of the mean annual signals depends on the amount of values that are available for computing the mean (which almost coincides with the number of years of the original series in our case), and the variability of the annual signal from year to year. As the mean annual signals are computed with error propagation, all these factors are well reflected by their formal errors. The formal errors are not homogeneous for all sites. They are slightly smaller for GPS (usually 0.4 to 0.5 mm) compared to GRACE (usually 0.6 to 0.7 mm).

In generating the mean annual signals, a good amount of noise is reduced compared to the monthly time series, just like fitting a harmonic function, but without the constraint that the behavior has to be harmonic. For example, the overall signal WRMS of the GPS – GRACE residuals of the monthly time series is 3.4 mm (Sect. 7.3.2.1), but only 1.7 mm for the mean annual signals. Besides real 'white' noise, forming the mean annual signal also suppresses all kinds of non-annually recurring signals as it assumes that the annual behavior is the same every year. Thus, we would expect that the GPS and GRACE mean annual signals are considerably more similar than the monthly time series themselves. As in Sect. 7.3.2.1, the similarity will be studied using correlation (Fig. 7.8), and reduction of GPS signal WRMS [%] by subtracting GRACE surface displacements (Figs. 7.9 and 7.10).

77% of the stations exhibit a correlation larger than 0.5 (versus 60% in the case of the monthly comparison), 11% a correlation between 0 and 0.5. 12% of the stations have negative correlation between the GPS and GRACE signals (versus 6% in the case of the monthly comparison). The median correlation coefficient is 0.77 (mean is 0.62). The six stations with the biggest correlation coefficients between 0.99 and 0.96 are KULU, KELY, THU3, QAQ1 (Greenland), KARR (Australia), and HYDE (India). Five of the six stations with very negative correlation coefficients between -0.2 and -0.7 are on small peninsulas or islands in the Pacific or Atlantic (STJO, ASPA, THTI, GUAM, FALE). The other is a station in the U.S.A. (CHB1).

70% of the GPS height time series have their signal WRMS reduced by more than 20% (versus 34% in the case of the monthly comparison), 11% have their signal WRMS reduced between 0 and 20%. 19% have signal WRMS increased (versus 23% in the case of the monthly comparison). The median reduction is 31% (mean reduction is 24%). The six stations with the biggest reduction of GPS signal WRMS between 67 and 82% are KULU, THU3, KELY (Greenland), MOBS, KARR (Australia), and HYDE (India). Seven of the ten stations, which have most signal WRMS added (all 27 to 160%), are stations on small peninsulas or islands in the Pacific, Atlantic or Indian Ocean (THTI, ASPA, FALE, SCUB, COCO, BAY1, STJO). The other three are CHB1 in North America, MAG0 in Russia, and MALI in Africa.

Thus, as in the case of the monthly time series, we reach the same conclusions using the mean annual signals. The stations where we do not observe any improvement when we subtract GRACE from GPS are, with some exceptions, those on ocean islands or small peninsulas (see Fig. 7.3 and the following Fig. 7.10). At these stations the signals are of the same magnitude or are smaller than the noise.

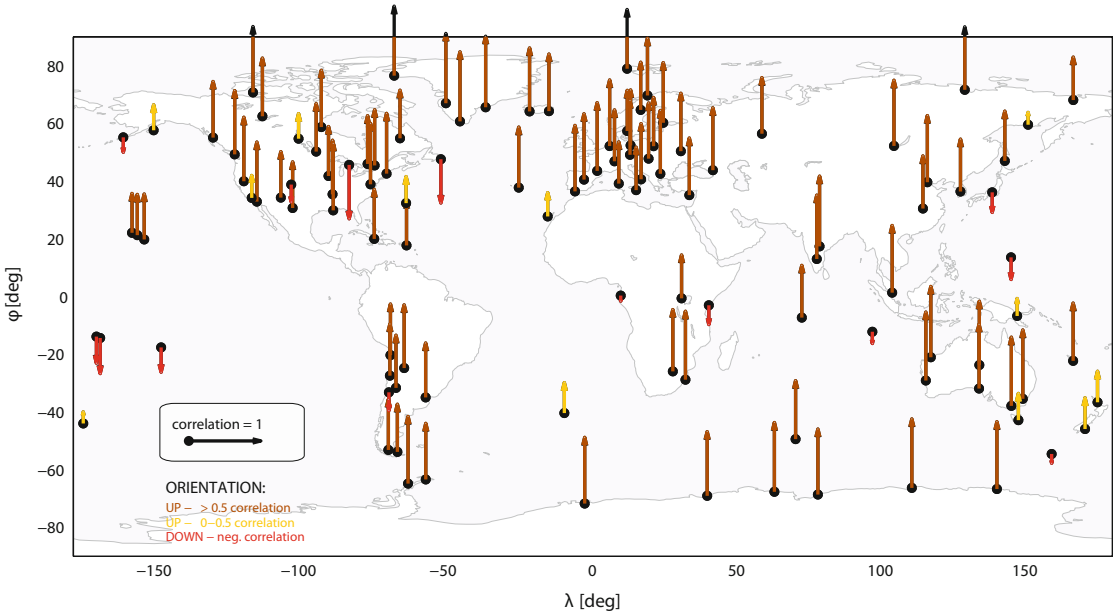

Fig. 7.8: Correlation coefficients computed for mean annual signals of the 115 stations from the GPS (with small translations from GRACE added, see Sect. 2.3) and GRACE data sets. Brown depicts a correlation larger than 0.5 (77% of the stations), yellow between 0 and 0.5 (11% of the stations), and red indicates negative correlation (12% of the stations).

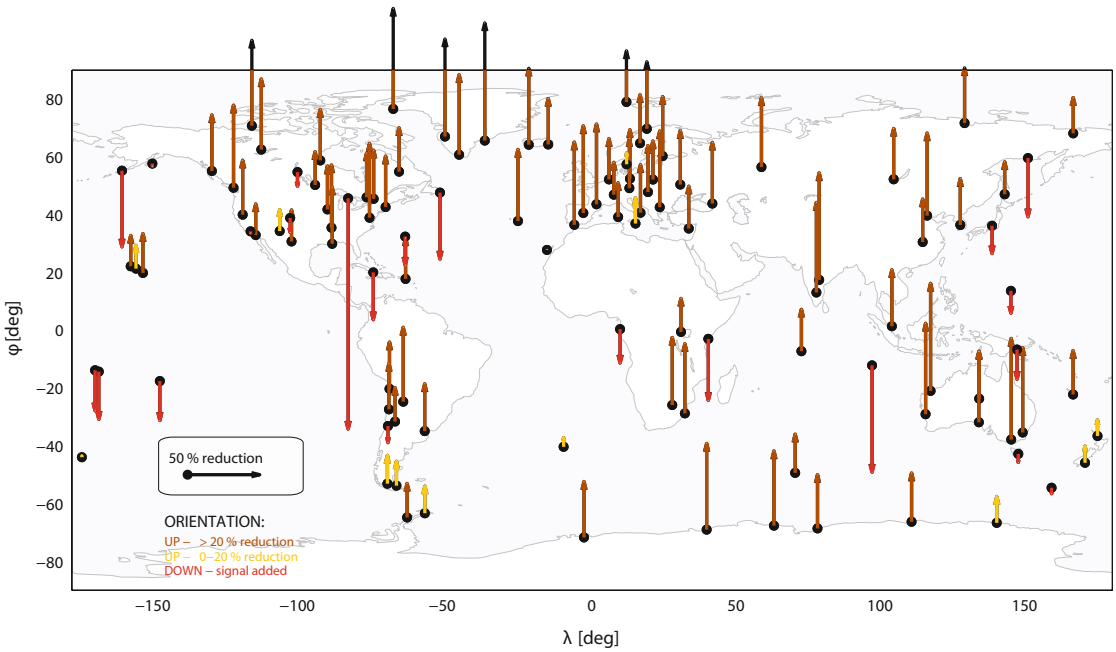

Fig. 7.9: Reduction of GPS signal WRMS [%] by subtracting GRACE deformation from GPS heights (with small translations from GRACE added, see Sect. 2.3), computed for the mean annual signals of all 115 stations. Brown depicts a reduction larger than 20% (70% of the stations), yellow between 0 and 20% reduction (11% of the stations), and red if signal WRMS was added (19% of the stations) .

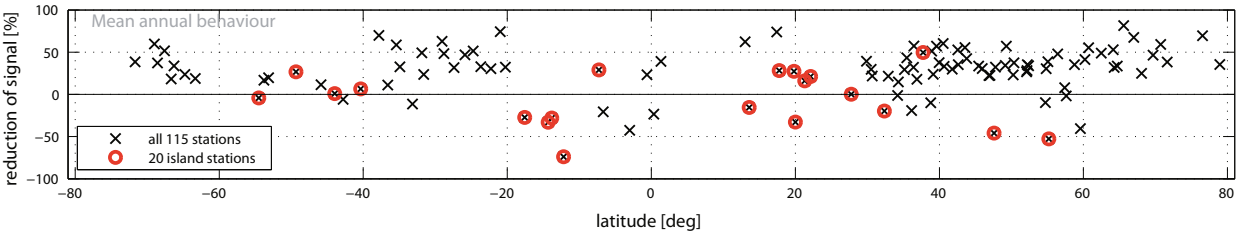

Fig. 7.10: Reduction of GPS signal WRMS [%] by subtracting GRACE surface displacements from GPS heights (with small translations from GRACE added, see Sect. 2.3), computed for the mean annual signals of all 115 stations. The stations are sorted by latitude; the marked stations (red circles) are the 20 stations on ocean islands or small peninsulas (given in the legend of Fig. 7.7). Eight of these 20 stations have GPS signal WRMS reduced: KERG, DGAR, CRO1, MKEA, HNLC, KOKB, PDEL.

As expected, the overall level of agreement between GPS heights and GRACE deformation signals is generally much better for the mean annual signals than for the monthly time series. The overall median GPS versus GRACE correlation coefficient for the monthly time series is 0.55 compared to 0.77 for the mean annual signals. In addition, the overall median GPS signal WRMS reduction for the monthly time series is 14% as compared to 31% for the mean annual signals.

But, the mean annual signal does not simply yield an improved level of similarity. As it expands the range of results for our chosen similarity criteria, it can sharpen the results of an analysis. First, for stations where there is common signal in the GPS and the GRACE data (generally non ocean island stations), the correlation and reduction of GPS signal WRMS can be much larger (maxima are 0.99 and 82%) compared to the monthly time series (maxima are 0.89 and 54%). Second, if the two data sets really disagree, e.g. if there is almost no signal in one time series but a signal in the other (which reveals a problem in any of the two techniques), the criteria degrade (e.g. minima are -0.75 and -160%) compared to the monthly time series (e.g. maxima are -0.23 and -28%).

7.3.2.4 Five Examples for the Monthly Time Series and Mean Annual Signals

This section discusses results for five stations: monthly GPS (with small translations from GRACE added, see Sect. 7.2.3) and GRACE time series and mean annual signals, as well as the GPS – GRACE residuals. These five stations are chosen such that they are globally distributed (the locations are indicated in Figs. 7.3 and 7.4). Some of the stations demonstrate an excellent agreement, others are average, while others match only poorly. Tab. 7.1 gives a summary of the similarity statistics for these five example stations and, as reference, the median of all the 115 single stations for the respective values.

A typical ocean island station is Papeete (THTI, Fig. 7.12). It is almost the worst of all 115 stations with respect to all our similarity criteria (see Tab. 7.1). There is no signal either in the GPS or in the GRACE time series, and it is obvious that the increase of signal WRMS of the GPS – GRACE residuals compared to the GPS series is simply because two series of distinct noise are superimposed. Nevertheless, even this result is a clear indication of the overall success of these GPS vs. GRACE comparisons, as the GPS – GRACE residuals seem to be dominated by noise, not unexplained signal. Besides, it is a very interesting example for how misleading the annual harmonic signals, presented in Fig. 7.4, can be: the phasor of the residual GPS – GRACE signal for Papeete has an amplitude of 2.8 mm, significantly larger than the weighted mean value of all 115 stations (2.3 mm), although the time series itself really only consists of noise and some random peaks.

Singapore (NTUS), a station in Asia represents "the average" of our set of stations well in the many respects: most of the criteria in Tab. 7.1 are average, the GPS series has got a data gap (receiver removed) and appears noisier than GRACE, the annual harmonic phasor of the GPS time series coincides well with the GRACE in phase but the NTUS GPS amplitude is much larger than that of GRACE (see Fig. 7.3), the amplitude of the fitted annual harmonic phasor of the GPS – GRACE residuals displayed in Fig. 7.4 has almost the same magnitude (2.4 mm) as the weighted mean value of all 115 stations (2.3 mm), et cetera.

Examining the African station Hartebeesthoek (HRAO, Fig. 7.14), we find that its monthly time series appear to fit quite nicely, except for the period between 2005.5 and 2006.5, with a remarkable 'jump-like' behavior in the GPS data around 2006.2. Although in that month, the antenna was changed, we do not assume this change to be the original cause for that remarkable pattern in the GPS series. Nevertheless, one should not suppose the

Station	Monthly time series				Mean annual signals			
	GPS signal WRMS	Corr.	Reduct. of GPS signal WRMS	GPS-GRACE signal WRMS	GPS signal WRMS	Corr.	Reduct. of GPS signal WRMS	GPS-GRACE signal WRMS
	3.8 mm	0.55	14%	3.3 mm	2.4 mm	0.77	31%	(1.7 mm)
WTZR	3.4 mm	0.76	38%	2.1 mm	1.6 mm	0.75	34%	1.1 mm
Europe		(r. 7)	(r. 4)			(r. 60)	(r. 45)	
THTI	2.7 mm	−0.23	−25%	3.4 mm	1.6 mm	−0.34	−27%	2.0 mm
Pac. Oc.		(r. 115)	(r. 114)			(r. 111)	(r. 106)	
NTUS	4.1 mm	0.57	16%	3.4 mm	3.0 mm	0.93	39%	1.8 mm
Asia		(r. 51)	(r. 48)			(r. 15)	(r. 34)	
HRAO	5.0 mm	0.68	25%	3.7 mm	3.4 mm	0.86	47%	1.8 mm
Africa		(r. 26)	(r. 28)			(r. 37)	(r. 28)	
ARTU	6.0 mm	0.74	34%	3.9 mm	4.4 mm	0.78	48%	2.3 mm
Russia		(r. 15)	(r. 10)			(r. 53)	(r. 27)	

Tab. 7.1: Summary of similarity statistics (GPS signal WRMS, GPS vs. GRACE correlation, reduction of GPS signal WRMS [%], signal WRMS for the GPS – GRACE residuals) for the monthly time series (on the left) and mean annual signals (on the right). The numbers in brackets in the header row represent the respective overall median values of all the 115 stations as reference. The numbers in the five rows below are the values for the five example stations discussed in details in Sect. 3.2.4. For these five rows, the numbers in brackets in the columns 'correlation' and 'reduction of GPS signal WRMS' depict these five stations' ranks on an overall 115 stations list for the two criteria.

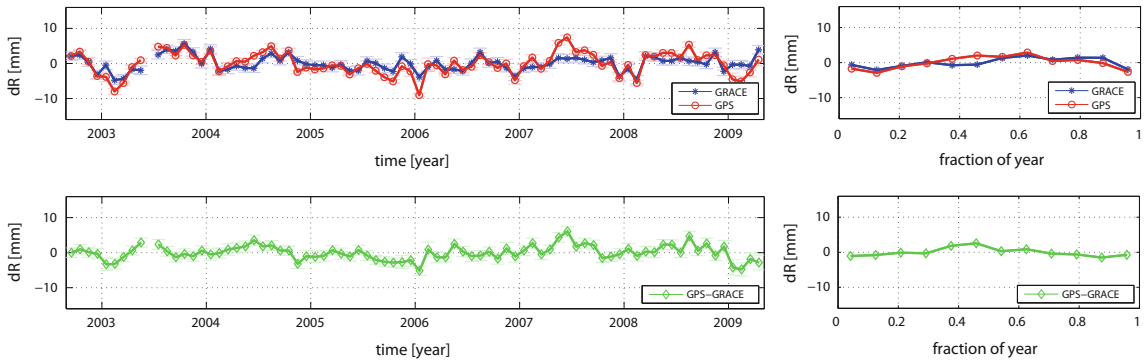

Fig. 7.11: Wettzell (WTZR, Germany): upper left are the monthly GPS and GRACE time series, upper right the GPS and GRACE mean annual signals, lower left the differences (residuals) between the GPS and GRACE monthly time series, lower right the differences (residuals) between the GPS and GRACE mean annual signals. Each data point has in light color error bars. Red is GPS (with small translations from GRACE added, see Sect. 7.2.3), blue is GRACE, green are the GPS - GRACE residuals.

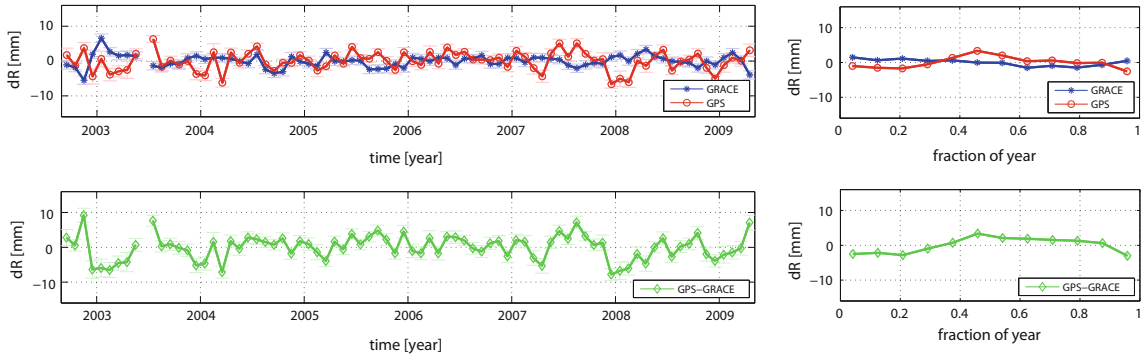

Fig. 7.12: Papeete (THTI, French Polynesia): monthly time series, mean annual signals, residuals between the monthly time series, and residuals between the mean annual signals.

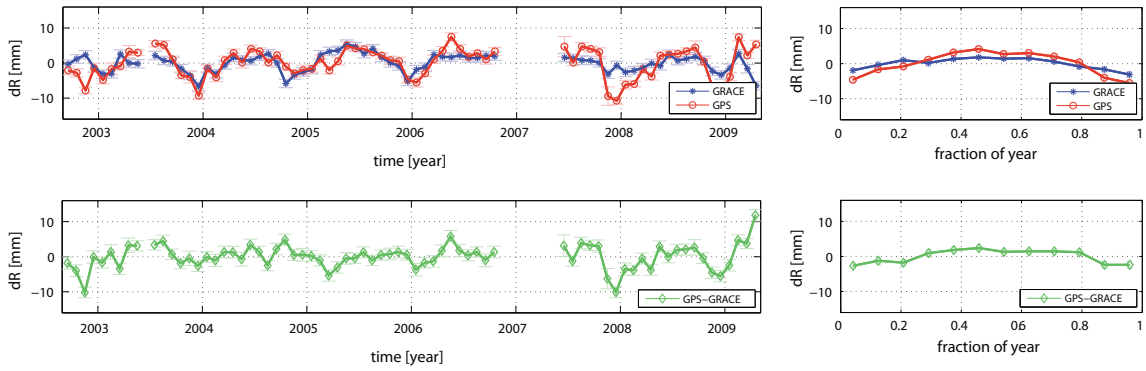

Fig. 7.13: Singapore (NTUS, Republic of Singapore): monthly time series, mean annual signals, residuals between the monthly time series, and residuals between the mean annual signals; only data points are displayed and used in the analysis, for which GPS and GRACE have simultaneous data.

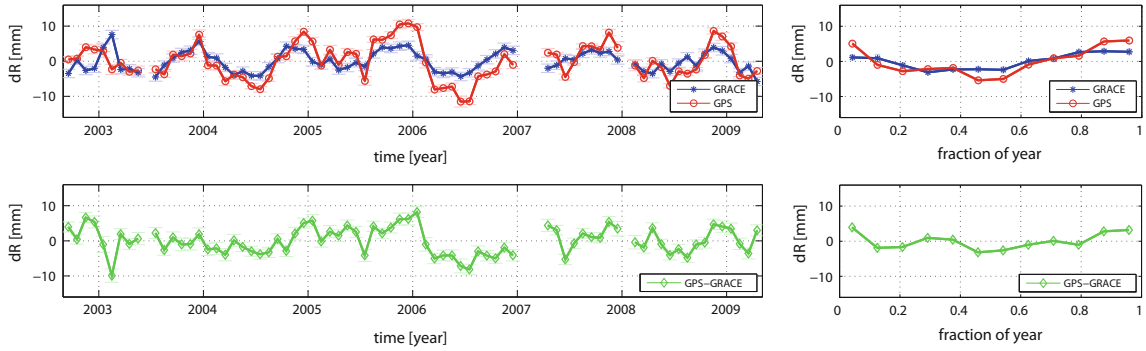

Fig. 7.14: Hartebeesthoek (HRAO, South Africa): monthly time series, mean annual signals, residuals between the monthly time series, and residuals between the mean annual signals.

pattern to be real physical station motion. Just as NTUS and THTI, the amplitude of the annual harmonic phasor, estimated from the HRAO GPS – GRACE residuals displayed in Fig. 7.4 has the same magnitude (2.3 mm) as the weighted mean value of all 115 stations (2.3 mm). Our explanation for this significant amplitude is very vague: The 'jump' around 2006.2 together with very small peaks in the beginning of two or three more years must be the driver for this fitted annual harmonic signal.

Arti, located in Russia (ARTU, Fig. 7.15), is subject to remarkably large surface displacements. The similarity between GPS and GRACE is quite good (see Tab. 7.1). Nevertheless, the GPS – GRACE residuals reveal a quite short but very pronounced dip in winter of almost every year. Even the mean annual signals of the residuals display that directly (not so distinct, as the minima of the dips vary between November and January over the years). This clear annually repeating pattern is also displayed by the significant amplitude of the fitted annual harmonic phasor (3.7 mm), which is clearly larger than the weighted mean value of all 115 stations (2.3 mm),

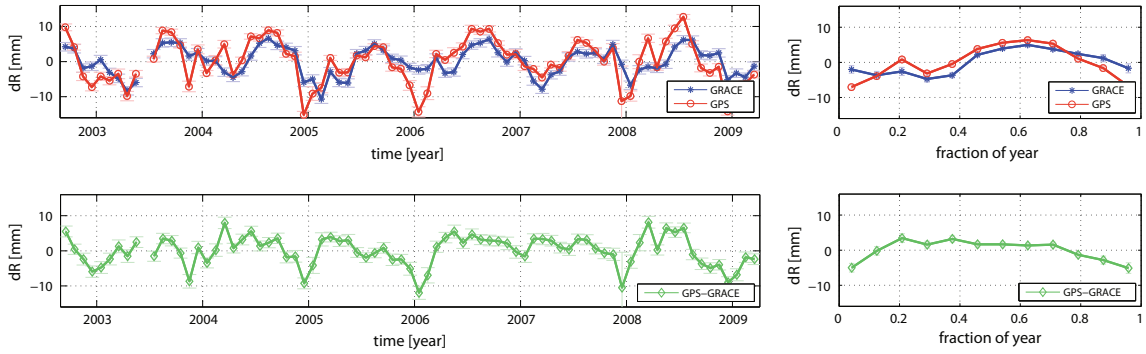

Fig. 7.15: Arti (ARTU, Russia): monthly time series, mean annual signals, residuals between the monthly time series, and residuals between the mean annual signals.

see Fig. 7.4. Most possible reasons for this signal are presence of snow during winter, and thermal expansion (as discussed in Sect. 7.4).

7.4 Further Discussion of the GPS/GRACE Height Residuals

We found that almost all stations without (at least partially) similar signals in the GPS and GRACE series are those with very small signals, such as ocean island stations or small peninsulas, whose time series are thus dominated by noise. But, there are stations where the GPS − GRACE height residuals appear to be signal rather than noise, presumably induced by GPS and not GRACE. This conclusion is supported by the fact that GPS generally has a larger mean annual harmonic amplitude (GPS: 3.7 mm, GRACE: 2.2 mm) and larger mean signal WRMS for the monthly time series (GPS: 4.0 mm, GRACE: 2.4 mm).

For four of the five stations (THTI, NTUS, HRAO, ARTU) discussed in Sect. 3.2.4, the annual harmonic signals fit to the monthly GPS – GRACE residuals appear to be quite large, namely with amplitudes between 2.3 and 3.7 mm (2.3 mm is the weighted mean amplitude of all 115 stations). Nevertheless, only one of these four stations (ARTU, Fig. 7.15) appears to have really clear annually repeating patterns in its residual GPS – GRACE time series. We can recognize that even single events such as strong peaks in either of the data sets can induce a significant estimated harmonic signal into the residuals, for example compare HRAO, Figs. 7.4 and 7.14. These should not be interpreted as annual geophysical signal, but rather noise or a strong single event due to a technical artifact.

In addition, Fig. 7.4 reveals some small regional systematic effects between the GPS − GRACE difference vectors, such as in the very high northern/southern latitudes, or much less clear in Europe and North America. The time series of the very northern/southern latitude stations indeed contain annually repeating fractions in the GPS data that cannot be explained by subtracting GRACE. This is a hint that not all relevant effects in either the GPS or the GRACE data sets are treated sufficiently in the respective equation systems.

7.4.1 Possible Error Sources in GPS

Previous papers comparing GPS and GRACE time series blame the GPS data for the disagreement. For example, Horwath et al (2010) find orbit mismodeling such as solar radiation pressure or Earth albedo to be the most likely sources for inducing large-scale residual patterns. Tregoning et al. (2009) suppose that local processes or site-specific analysis errors dominate their GPS height estimates as the main error sources. Unfortunately, none of the previous papers report of a proof of their quite general hypotheses. However, there are several effects that could evoke regionally systematic patterns in the GPS data, and are mainly of annually recurring nature. Kaniuth et al (2005) and Jaldehag et al (1996) found that height time series of some GPS stations do exhibit a big apparent signal during periods with presence of snow.

Errors in the subdaily EOP model can also propagate to the estimated station coordinates. The model currently recommended by the IERS conventions (McCarthy and Petit, 2004) and applied in our GPS processing, has deficiencies. It was demonstrated that applying different subdaily EOP models mainly results in a spectral peak at 13.6 days in station position estimates. However, this peak is not relevant for us as we use monthly values; the annual and semiannual fractions are much smaller. According to Penna et al (2007), errors (uncertainties) in the ocean models used to compute the Ocean Loading coefficients can locally cause amplitudes > 1 mm, with periods of 14 days, semiannual and annual (this topic is further discussed in the next subsection "Possible error sources in the GRACE-derived deformations"). Further, not considering the atmospheric tides S1 and S2 can also cause very small semiannual and annual signals (Penna et al, 2007), and investigations on the ideal model for the effect of the troposphere on GPS estimates are also still ongoing (e.g. Steigenberger et al, 2009).

In the following discussion, we briefly introduce two further options that could induce regional disagreement: First, thermal expansion of GPS monuments and the very upper part of the Earth's crust; Second, apparent height changes, mathematically induced by a negative correlation between estimated tropospheric ZD, and station heights in the original GPS equation systems. Effects due to thermal expansion (change of volume) can only be seen by the GPS measurements, not GRACE, which is only sensitive to mass variations. Several authors have discussed this effect (see Dong et al, 2002; Prawirodirdjo et al, 2006; Romagnoli et al, 2003; Yan et al, 2009).

However, none of these studies were particularly successful when comparing global data sets, only for single stations or regions. We tried to correlate our monthly GPS − GRACE residuals with temperature derived from the National Centers for Environmental Prediction globally gridded temperature data (Kalnay et al, 1996;

http://www.ncep.noaa.gov) for each of the 115 stations, using a simple regression approach. Dong et al (2002) discuss a time lag between the temperature variation and the expansion of the Earth's crust of about three months. We performed numerous tests using different combinations of delay and regression coefficients. A zero time lag and a factor of 0.01 cm/° gave the best overall fit:

$$\Delta h_{deformation}[\text{cm}] = \Delta t_{NCEP}[^\circ] \cdot 0.01[\text{cm}/^\circ] \tag{7.2}$$

Unfortunately, our thermal expansion signal $\Delta h_{deformation}$ is only slightly correlated with the monthly GPS – GRACE height residuals. For only about 55% of all 115 stations, there is positive correlation with maxima around 0.6 in Europe and North America. One example is the station ARTU (Section 7.3.2.4, Fig. 7.15), where daily mean temperatures range from -25° C during wintertime to more than 20° C during summer almost every year. Especially in the very high northern/southern latitudes, annual harmonic signals estimated for the GPS $-$ GRACE height residuals and height $\Delta h_{deformation}$ are almost antipodal in phase. Thus, we are forced to conclude that 1) either our very simple thermal expansion model is insufficient (it neglects regional and local site characteristics); or 2) that this effect in our GPS height time series is superimposed upon other phenomena of at least similar or an even larger order of magnitude.

The second effect under investigation is the influence of negative correlation between tropospheric ZD estimates and GPS station height estimates in the original GPS observation equations. The respective partial derivatives of the GPS carrier phase observations ϕ with respect to the station height h reads $\frac{\partial \phi}{\partial h} \approx \sin \epsilon$, and with respect to the ZD $\frac{\partial \phi}{\partial ZD} \approx \frac{1}{\sin \epsilon}$. Both are almost negatively linear dependent for observations with high elevation angles ϵ. We simulate an observation scenario, assuming one observation for each degree elevation angle between 5° and 90° elevation (namely 86 simulated observations). The station height and ZD estimated from these simulated observations are mathematically correlated with value -0.47 for stations in latitudes -55° to $+55^\circ$. The correlation is even stronger for stations with higher latitudes. For example, at the poles, receivers on the Earth surface cannot see GPS satellites above 45° elevation, which yields a correlation value -0.55. As a consequence, the physically independent phenomena ZD and height cannot fully be separated mathematically in the equation systems, and the height estimates can be slightly falsified if there are big ZD estimates. In our real GPS solutions, the a priori tropospheric hydrostatic delay is computed from ECMWF data, and the remaining wet delay, which has to be estimated, is comparably small. The wet delay is usually varying with an amplitude of a few cm (e.g. in Antarctica) to several decimeters (e.g. in East Asia), depending mainly on the regionally predominant variation of air moisture.

However, computing correlation coefficients between the time series of monthly mean tropospheric ZD estimates and the GPS – GRACE height residuals, we find that only about half of the stations have negative values, with strongest negative correlation (up to -0.8) to be in the very high northern/southern latitudes. In Europe and North America, predominantly small positive correlations are found. For nine stations in the northern mid latitudes, the ZD and the height estimates even have positive correlations larger than 0.5. Again, we have to conclude that either our method is inadequate, or that this effect in our GPS height time series is superimposed by other phenomena of at least a similar order of magnitude.

7.4.2 Possible Error Sources in the GRACE-derived Deformations

The strongest open question concerning GRACE-derived deformations might be the simplifying assumption that the Earth's crust reacts homogeneously to a change of mass loading, which could induce systematic regional effects. Another possible contributor (of mainly annual nature) is the C_{20} series used. The GRACE vs. GPS comparisons could be a good criterion to compare different C_{20} series concerning their geophysical plausibility.

A further, related effect is that the monthly GRACE solutions must be spatially filtered, in order to allow a meaningful interpretation of derived deformations. This is as the monthly GRACE solutions are estimated with high spherical harmonic degree while the accuracy of the GRACE monthly solutions decrease with increasing spherical harmonic degree (that is with increasing resolution). It is common practice to use an isotropic Gaussian averaging kernel with a 400 km radius. However, there are other decorrelation filters, such that proposed by Kusche (2007), which aim to take the striping of the GRACE observations into account. The choice of the filtering approach can significantly affect the derived surface displacements with respect to their noisiness, as well as regional systematic patterns. Other GRACE error sources might include systematic errors or unconsidered uncertainties in the atmospheric and oceanic water mass background fields, and aliasing effects (that is the aliasing of any mismodeled submonthly gravity signals into the GRACE monthly solutions).

High-frequency errors in ocean tide models alias to low frequencies in the GRACE gravity field solutions. The aliasing at 161 days is evident mostly at high-latitudes (Chen et al, 2009) but other regional effects can also be identified. Thus, any interpretation of our GRACE derived coordinate time-series at these periods and in these regions might be in error. Two such regions predicted to be strongly affected are the Timor Sea off the northwest coast of Australia and the Weddell Sea near Antarctica. We performed a spectral analysis of the GPS and GRACE heights for four stations in these regions: KARR at the Timor Sea, and PALM, OHI2 (and pretty distant VESL) near the Weddell Sea. For KARR, the annual signals match perfectly, without any signals at shorter periods than annual in both series. For the stations near the Weddell Sea, we find that first, the annual signals have larger amplitudes for GPS by a factor of two on average. Second, the power in the GPS data at periods from semiannual to ∼161 days is higher (1 to 3 mm amplitude) than what we observe in our GRACE displacements, where there is almost no signal in that frequency domain (less than 1 mm amplitude). One solution to the aliasing problem of the ocean tide models would be to filter the data in these regions for the 161-day signal. However, as the results and conclusions presented in this paper do not rely on our interpretation of comparisons between GPS and GRACE at this particular frequency, we choose not to do so. Please note that none of the enumerated error contributors have been considered in our evaluation of the precision of the GRACE-derived monthly deformations in Sect. 7.2.2.

7.4.3 Use of GRACE-derived Deformations for Reference Frame Purposes

In order to determine a Terrestrial Reference Frame, all known signals are removed from the observations of the space geodetic techniques that are not linear station motion. As for that purpose, only models and data series with clearly specified and sufficiently small precision (and especially accuracy) can be used, we do not propose to use GRACE-derived site displacements outright. But the order of magnitude estimate we deduced for the precision of the monthly GRACE-derived displacement values in Sect. 7.2.2 (about 1.2 mm) appears to be confirmed from the results of this paper. We assume most of the noise and unexplained signal in our monthly GPS – GRACE residuals to be due to the GPS height time series, not GRACE. Thus, this idea could be reconsidered after further progress in that field.

As the GPS and GRACE mean annual signals are much more similar than the monthly time series, the mean annual signals explain, on average, the largest part of the signal. Obviously, this neglects interannual variations, and that annual signals driven by climate patterns will not be exactly the same each year. Nevertheless, if one day GRACE-derived deformations are used for the a priori model of station motion for Reference Frame purposes, we propose to rediscuss the use of the mean annual GRACE signals to extrapolate such corrections, e.g. to process near-realtime positioning solutions.

7.5 Summary and Outlook

Generally, the results presented in this paper yield a considerable improvement over the analyses presented by previous works (van Dam et al, 2007; King et al, 2006; Tregoning et al, 2009; Horwath et al, 2010). The improvement is due to a number of factors. First, the GPS data is completely reprocessed with state-of-the-art models, such as the VMF1, a priori ZDs from a numerical weather model, high-order ionospheric terms, et cetera (some of the previous works also use reprocessed GPS data). Second, as GPS measures motion of discrete points, they can easily be corrupted by local effects or technical artifacts. We tried to sort out such stations by means of an objective cluster analysis (Tesmer et al, 2009). Third, GRACE data has to be used, which is processed with all critical models to be in accordance with those used in the GPS processing. Finally, both data sets have to be in equivalent reference frames, meaning that the translation signal components have to be treated adequately in the GPS and the GRACE data.

The paper gives a thorough evaluation of the potential of two totally independent geodetic observation systems to observe the loading signal: We find that, in general, the two data sets have very similar annual harmonic phasors. There are no significant, global systematic phase differences between these data sets and the median amplitude of all 115 stations is 3.0 mm for GPS, and 1.8 mm for GRACE. The median amplitude of the GPS – GRACE difference vectors is 1.8 mm, which means as a raw overview, that a lot of annual signal is removed from GPS by subtracting GRACE.

Comparing the monthly GPS and GRACE vertical deformation time series, we find that for 60% of the stations, the correlation is larger than 0.5 (the median for all stations is 0.55), and almost 80% of the stations have their GPS signal WRMS reduced by subtracting the signal from GRACE (median reduction for all stations is 14%).

Almost all stations where the GRACE and GPS deformations do not fit are stations on ocean islands or small peninsulas, where the geophysical signal is small. This nicely suits our assumption that the precision of the monthly GPS –GRACE differences is about 1.6 mm.

Section 7.3.2.4 discusses plots of GPS and GRACE time series for five representative stations, in order to examine whether the remaining GPS – GRACE residuals mainly contain unexplained signal or mainly noise. For example, there are several stations, where annual harmonic phasors fit to the GPS − GRACE residuals have a significant amplitude. But, most of the corresponding time series turn out to not really exhibit annually repeating patterns. Even single events such as strong peaks in either of the data sets can induce an estimated harmonic amplitude, which should not be interpreted as geophysical signal. Nevertheless, there are few stations, where the GPS – GRACE residuals do reveal an annually recurring signal: The time series of the very northern/southern latitude stations (and much less clear in Europe and North America) indeed contain annually (and partially semiannually) repeating fractions in the GPS data that cannot be explained by subtracting GRACE. A considerable fraction of this effect in the very southern latitudes should be due to high-frequency errors in ocean tide models which can alias to low frequencies in both, the GRACE gravity field solutions, and the GPS position time series (via ocean loading).

Two hypotheses were tested with the goal of explaining the further, remaining signals in the GPS data, which were only marginally successful. We neither found systematically significant annual signals due to the thermal expansion of GPS monuments and the very upper part of the Earth surface. Nor did we find systematically apparent annual height signals, mathematically induced by a negative correlation between estimated tropospheric ZD and station height in the original GPS equation systems. While the GPS data appears to be the most likely source of noise and apparent signal, there are also some fields of ongoing research in the GRACE context, that must be considered in the future, such as the approach to convert mass to deformation, the C_{20} series, as well as the background models used. Presumably, the origin of the remaining differences could be better identified if the apparent translational components between the GPS and the GRACE time series were better understood. Moreover, this work should be repeated with position time series from the ITRF2008 effort (not only GPS, but also VLBI, SLR), and, not only the height, but also the horizontal position components should be investigated.

Nevertheless, despite some remaining discrepancies, we can say that GPS and GRACE see the same signals for almost all 115 stations, the caveat being that the signals themselves must be larger than the precision of the observing systems. Thus, both, GPS and GRACE can be considered to be more than just isolated, traditional, geodetic measurement techniques. They are proven to be robust and reliable sensors of the Earth system, ready to take their part in modern Earth system science and climate research if and only if these data are treated appropriately. The most important goal for the near future would be to look for secular height/mass changes in the GPS and GRACE data, which will require a thorough treatment of all the real or apparent jumps, dips, et cetera in the GPS position time series, as well as a very thorough selection of the reference frames. If successful, this could e.g. significantly support the efforts, as carried out by Willis et al (2008). They tried to set up budgets of measurements from different sensor systems (such as GRACE), in order to understand details of the global mean sea level rise caused amongst others by global warming.

Acknowledgements

This study made extensive use of GPS observations provided by the International GNSS Service (IGS; Dow et al, 2009). Thanks to all IGS components. We would also like to thank the GRACE teams at the Center for Space Research, University of Texas, at the Deutsches GeoForschungsZentrum, Potsdam, and at the Jet Propulsion Laboratory, Pasadena, for making their gravity fields available. We are grateful to J. Ray, T. Artz, S. Böckmann and R. Heinkelmann for discussions, and the reviewers of the paper for helping to significantly improve the paper.

Bibliography

Altamimi Z, Collilieux X, Legrand J, Garayt B, Boucher C (2007) ITRF2005: A new release of the International Terrestrial Reference Frame based on time series of station positions and Earth Orientation Parameters. Journal of Geophysical Research 112(B9):B09401, DOI $10.1029/2007JB004949$

Bettadpur S (2007) Gravity Recovery and Climate Experiment, UTCSR Level-2 Processing Standards Document for Level-2 Product Release 004. Tech. rep., CSR Publ. GR-03-03

Blewitt G (2003) Self-consistency in reference frames, geocenter definition, and surface loading of the solid Earth. Journal of Geophysical Research 118(B2), DOI $10.1029/2002JB002082$

Boehm J, Werl B, Schuh H (2006) Troposphere mapping functions for GPS and very long baseline interferometry from European Centre for Medium-Range Weather Forecasts operational analysis data. Journal of Geophysical Research 111(B2):B02406, DOI 10.1029/2005JB003629

Cazenave A, Llovel W (2010) Contemporary Sea Level Rise. Annual Review of Marine Science 2:145–173, DOI 10.1146/annurev-marine-120308-081105

Chambers DP (2005) Observing seasonal steric sea level variations with GRACE and satellite altimetry. Journal of Geophysical Research 111(C3):C03010, DOI 10.1029/2005JC002914

Chen J, Wilson C, Blankenship D, Tapley B (2006a) Antarctic mass rates from GRACE. Geophysical Research Letters 33(11):L11502, DOI 10.1029/2006GL026369

Chen J, Wilson C, Tapley B (2006b) Satellite gravity measurements confirm accelerated melting of Greenland ice sheet. Science 313(5795):1958–1960, DOI 10.1126/science.1129007

Chen J, Wilson C, Seo KW (2009) S2 tide aliasing in GRACE time-variable gravity solutions. Journal of Geodesy 83(7):679–687, DOI 10.1007/s00190-008-0282-1

Cheng M, Tapley BD (2004) Variations in the Earth's oblateness during the past 28 years. Journal of Geophysical Research 109(B9):B09402, DOI 10.1029/2004JB003028

Crowley JW, Mitrovica JX, Bailey RC, Tamisiea ME, Davis JL (2008) Annual variations in water storage and precipitation in the Amazon Basin. Journal of Geodesy 82(1):9–13, DOI 10.1007/s00190-007-0153-1

Dach R, Hugentobler U, Fridez P, Meindl M (eds) (2007) Bernese GPS Software Version 5.0. Astronomical Institute, University of Bern, Bern, Switzerland

van Dam T, Wahr J, Lavallée D (2007) A comparison of annual vertical crustal displacements from GPS and Gravity Recovery and Climate Experiment (GRACE) over Europe. Journal of Geophysical Research 112(B3):B03404, DOI 10.1029/2006JB004335

Davis JL, Elosegui P, Mitrovica JX, Tamisiea ME (2004) Climate-driven deformation of the solid Earth from GRACE and GPS. Geophsical Research Letters 31(24):L24605, DOI 10.1029/2004GL021435

Dong D, Fang P, Bock Y, Cheng M, Miyazaki S (2002) Anatomy of apparent seasonal variations from GPS-derived site position time series. Journal of Geophysical Research 107(B4), DOI 10.1029/2001JB000573

Dong D, Yunck T, Heflin M (2003) Origin of the International Terrestrial Reference Frame. Journal of Geophysical Research 108(B4), DOI 10.1029/2002JB002035

Dow JM, Neilan RE, Rizos C (2009) The International GNSS Service in a changing landscape of Global Navigation Satellite Systems. Journal of Geodesy 83(3-4):191–198, DOI 10.1007/s00190-008-0300-3

Drinkwater MR, Haagmans R, Muzi D, Popescu A, Floberghagen R, Kern M, Fehringer M (2007) The GOCE gravity mission: ESA's first core earth explorer. In: Proceedings of the 3rd International GOCE User Workshop, vol ESA SP-627, pp 1–8

Flechtner F (2005) GRACE AOD1B product description document (Rev. 2.1). Tech. Rep. GRACE 327-750 (GR-GFZ-AOD-0001), GFZ German Research Centre for Geosciences

Flechtner F, Dahle C, Neumayer KH, König R, Foerste C (2010) The release 04 CHAMP and GRACE EIGEN gravity field models. In: Flechtner F, Mandea M, Gruber T, Rothacher M, Wickert J, Güntner A, Schöne T (eds) System Earth via Geodetic-Geophysical Space Techniques, Advanced Technologies in Earth Sciences, Springer, pp 41–58, DOI 10.1007/978-3-642-10228-8_4

Fritsche M, Dietrich R, Knöfel C, Rülke A, Vey S, Rothacher M, Steigenberger P (2005) Impact of higher-order ionospheric terms on GPS estimates. Geophysical Research Letters 32(23):L23311, DOI 10.1029/2005GL024342

Han D, Wahr J (1995) The viscoelastic relaxation of a realistically stratified earth, and a further analysis of post-glacial rebound. Geophysical Journal International 120(2):287–311, DOI 10.1111/j.1365-246X.1995.tb01819.x

Hofmann-Wellenhof B, Lichtenegger H, Wasle E (2007) GNSS - Global Navigation Satellite Systems: GPS, GLONASS, Galileo & more, 1st edn. Springer, Wien

Horwath M, Rülke A, Fritsche M, Dietrich R (2010) Mass variation signals in GRACE products and in crustal deformations from GPS: A comparison. In: Flechtner FM, Gruber T, Güntner A, Mandea M, Rothacher M, Schöne T, Wickert J (eds) System Earth via Geodetic-Geophysical Space Techniques, Advanced Technologies in Earth Sciences, Springer, pp 399–406, DOI 10.1007/978-3-642-10228-8_34

Jaldehag RTK, Johansson JM, Rönnäng BO, Elósegui P, Davis JL, Shapiro II, Niell AE (1996) Geodesy using the Swedish permanent GPS network: Effects of signal scattering on estimates of relative site positions. Journal of Geophysical Research 101(8):1601–1604, DOI 10.1029/96JB01183

Kalnay E, Kanamitsu M, Kistler R, Collins W, Deaven D, Gandin L, Iredell M, Saha S, White G, Wollen J, Zhu Y, Chelliah M, Ebisuzaki W, Higgins W, Janowiak J, Mo KC, Ropelewski C, Wang J, Leetmaa A, Reynolds R, Jenne R, Joseph D (1996) The NMC/NCAR 40-year reanalysis project. Bulletin of the American Meteorological Society 77(3):437–471, DOI 10.1175/1520-0477(1996)077⟨0437:TNYRP⟩2.0.CO;2

Kaniuth K, Stuber K, Vetter S (2005) Sensitivität von GPS-Höhenbestimmungen gegen Akkumulation von Schnee auf der Antenne. AVN 112(8-9):290–295

King M, Moore P, Clarke P, Lavallée D (2006) Choice of optimal averaging radii for temporal GRACE gravity solutions, a comparison with GPS and satellite altimetry. Geophysical Journal International 166(1):1–11, DOI 10.1111/j.1365-246X.2006.03017.x

Kuo CY, Shum C, Guo J, Yi Y, Braun A, Fukumori I, Matsumoto K, Sato T, Shibuya K (2008) Southern ocean mass variation studies using GRACE and satellite altimetry. Earth Planets Space 60:477–485

Kusche J (2007) Approximate decorrelation and non-isotropic smoothing of time-variable GRACE-type gravity field models. Journal of Geodesy 81(11):733–749, DOI 10.1007/s00190-007-0143-3

Leuliette EW, Miller L (2009) Closing the sea level rise budget with altimetry, Argo, and GRACE. Geophysical Research Letters 36(4):L04608, DOI 10.1029/2008GL036010

Luthcke SB, Arendt AA, Rowlands DD, McCarthy JJ, Larsen CF (2008) Recent glacier mass changes in the Gulf of Alaska region from GRACE mascon solutions. Journal of Glaciology 54(188):767–777, DOI 10.3189/002214308787779933

Morison J, Wahr J, Kwok R, Peralta-Ferriz C (2007) Recent trends in Arctic Ocean mass distribution revealed by GRACE. Geophysical Research Letters 34(7):L07602, DOI 10.1029/2006GL029016

Niell A (2001) Preliminary evaluation of atmospheric mapping functions based on numerical weather models. Physics and Chemistry of the Earth 26(6-8):475–480, DOI 10.1016/S1464-1895(01)00087-4

Nordman M, Mäkinen J, Virtanen H, Johansson JM, Bilker-Koivula M, Virtanen J (2009) Crustal loading in vertical GPS time series in Fennoscandia. Journal of Geodynamics 48(3-5):144–150, DOI 10.1016/j.jog.2009.09.003

Penna N, King MA, Stewart MP (2007) GPS height time series: Short-period origins of spurious long-period signals. Journal of Geophysical Research 112(B2):B02402, DOI 10.1029/2005JB004047

Prawirodirdjo L, Ben-Zion Y, Bock Y (2006) Observation and modeling of thermoelastic strain in Southern California Integrated GPS Network daily position time series. Journal of Geophysical Research 111(B2):B02408, DOI 10.1029/2005JB003716

Ray J, Altamimi Z, Collilieux X, van Dam T (2008) Anomalous harmonics in the spectra of GPS position estimates. GPS Solutions 12(1):55–64, DOI 10.1007/s10291-007-0067-7

Reigber C, Lühr H, Schwintzer P (2002) CHAMP mission status. Advances in Space Research 30(2):129–134, DOI 10.1016/S0273-1177(02)00276-4

Rodell M, Velicogna I, Famiglietti JS (2009) Satellite-based estimates of groundwater depletion in India. Nature 460:999–1002, DOI 10.1038/nature08238

Romagnoli C, Zerbini S, Lago L, Richter B, Simon D, Domenichini F, Elmi C, Ghirotti M (2003) Influence of soil consolidation and thermal expansion effects on height and gravity variations. Journal of Geodynamics 35(4-5):521–539, DOI 10.1016/S0264-3707(03)00012-7

Rothacher M, Angermann D, Artz T, Bosch W, Drewes H, Gerstl M, Kelm R, König D, König R, Meisel B, Müller H, Nothnagel A, Panafidina N, Richter B, Rudenko S, Schwegmann W, Seitz M, Steigenberger P, Tesmer S, Tesmer V, Thaller D (2011) GGOS-D: homogeneous reprocessing and rigorous combination of space geodetic observations. Journal of Geodesy 85(10):679–705, DOI 10.1007/s00190-011-0475-x

Schillak S (2004) Analysis of the process of the determination of station coordinates by the satellite laser ranging based on results of the Borowiec SLR station in 1993.5 - 2000.5, Part 1: Performance of the Satellite Laser Ranging. Artificial Satellites 39(3):217–263

Schmid R, Steigenberger P, Gendt G, Ge M, Rothacher M (2007) Generation of a consistent absolute phase center correction model for GPS receiver and satellite antennas. Journal of Geodesy 81(12):781–798, DOI 10.1007/s00190-007-0148-y

Simmons A, Gibson J (2000) The ERA-40 project plan. ERA-40 Project Report Series 1, ECMWF

Sovers OJ, Fanselow JL, Jacobs CS (1998) Astrometry and geodesy with radio interferometry: experiments, models, results. Reviews of Modern Physics 70(4):1393–1454, DOI 10.1103/RevModPhys.70.1393

Steigenberger P, Rothacher M, Dietrich R, Fritsche M, Rülke A, Vey S (2006) Reprocessing of a global GPS network. Journal of Geophysical Research 111(B5):B05402, DOI 10.1029/2005JB003747

Steigenberger P, Boehm J, Tesmer V (2009) Comparison of GMF/GPT with VMF1/ECMWF and implications for atmospheric loading. Journal of Geodesy 83(10):943–951, DOI 10.1007/s00190-009-0311-8

Steigenberger P, Artz T, Böckmann S, Kelm R, König R, Meisel B, Müller H, Nothnagel A, Rudenko S, Tesmer V, Thaller D (2010) GGOS-D consistent, high-accuracy technique-specific solutions. In: Flechtner F, Mandea M, Gruber T, Rothacher M, Wickert J, Güntner A, Schöne T (eds) System Earth via Geodetic-Geophysical Space Techniques, Advanced Technologies in Earth Sciences, Springer, pp 545–554, DOI 10.1007/978-3-642-10228-8

Takiguchi H, Otsubo T, Y F (2006) Mass-redistribution-induced crustal deformation of global satellite laser ranging stations due to non-tidal ocean and land water circulation. Earth Planets and Space 58(12):E13–E16

Tapley BD, Bettadpur S, Watkins M, Reigber C (2004) The gravity recovery and climate experiment: Mission overview and early results. Geophysical Research Letters 31(9):L09607, DOI 10.1029/2004GL019920

Tesmer V, Steigenberger P, Rothacher M, Boehm J, Meisel B (2009) Annual deformation signals from homogeneously reprocessed VLBI and GPS height time series. Journal of Geodesy 83(10):973–988, DOI 10.1007/s00190-009-0316-3

Tregoning P, Watson C, Ramillien G, McQueen H, Zhang J (2009) Detecting hydrologic deformation using GRACE and GPS. Geophysical Research Letters 36(15):L15401, DOI 10.1029/2009GL038718

Velicogna I, Wahr J (2006a) Acceleration of Greenland ice mass loss in spring 2004. Nature 443:329–331, DOI 10.1038/nature05168

Velicogna I, Wahr J (2006b) Measurements of time-variable gravity show mass loss in Antarctica. Science 311:1754–1756

Wahr J, Molenaar M, Bryan F (1998) Time variability of the Earth's gravity field: Hydrological and oceanic effects and their possible detection using GRACE. Journal of Geophysical Research 103(B12):30,205–30,229

Wahr J, Swenson S, Zlotnicki V, Velicogna I (2004) Time-variable gravity from GRACE: First results. Geophysical Research Letters 31(11):L11501, DOI 10.1029/2004GL019779

Watkins M, Yuan D (2007) GRACE JPL Level-2 Processing Standards Document For Level-2 Product Release 04. Tech. Rep. GRACE 327-744 (v 4.0), Jet Propulsion Laboratory

Willis JK, Chambers DP, Nerem RS (2008) Assessing the globally averaged sea level budget on seasonal to interannual timescales. Journal of Geophysical Research 113(C6):C06015, DOI 10.1029/2007JC004517

Yan H, Chen W, Zhu Y, Zhang W, Zhong M (2009) Contributions of thermal expansion of monuments and nearby bedrock to observed GPS height changes. Geophsical Research Letters 36(13):L13301, DOI 10.1029/2009GL038152

Zerbini S, Matonti F, Raicich F, Richter B, van Dam T (2004) Observing and assessing nontidal ocean loading using ocean, continuous GPS and gravity data in the Adriatic area. Geophysical Research Letters 31(23):L23609, DOI 10.1029/2004GL021185

8 Precise Orbit Determination of GIOVE–B Based on the CONGO Network

Originally published as:

Steigenberger P., Hugentobler U., Montenbruck O., Hauschild A. (2011): Precise orbit determination of GIOVE–B based on the CONGO network, Journal of Geodesy, Vol. 85, No. 6 , pp. 357-365, doi: 10.1007/s00190- 011-0443-5

The final publication is available at Springer via `http://dx.doi.org/10.1007/s00190-011-0443-5`.

Abstract

GIOVE–B is one of two test satellites for the future European Global Navigation Satellite System Galileo. The Cooperative Network for GIOVE Observation (CONGO) is a global tracking network of GIOVE–capable receivers established by Deutsches Zentrum für Luft- und Raumfahrt (DLR) and Bundesamt für Kartographie und Geodäsie (BKG). This network provides the basis for the precise orbit determination of the GIOVE–B satellite for the time period 29 June till 27 October 2009 with a modified version of the Bernese GPS Software. Different arc lengths and sets of orbit parameters were tested. These tests showed that the full set of nine radiation pressure parameters resulted in a better performance than the reduced set of five parameters. An internal precision of about one to two decimeters could be demonstrated for the central day of 5-day solutions. The orbit predictions have a precision of about one meter for a prediction period of 24 h. External validations with Satellite Laser Ranging (SLR) show residuals on the level of 12 cm. The accuracy of the final orbits is expected to be on the few decimeter level.

8.1 Introduction

The European Global Navigation Satellite System Galileo is being developed by the European Space Agency (ESA). Two test satellites (GIOVE–A and GIOVE–B, see Fig. 8.1) were launched as part of the Galileo in Orbit Validation Element (GIOVE; Benedicto et al, 2006; Malik et al, 2009). To gain experience with the signals transmitted by these satellites (see Tab. 8.1) and to estimate satellite orbit and clock parameters, a global network of GIOVE–capable receivers was established. This Cooperative Network for GIOVE Observation (CONGO) is operated by Deutsches Zentrum für Luft- und Raumfahrt (DLR, Oberpfaffenhofen, Germany) and Bundesamt für Kartographie und Geodäsie (BKG, Frankfurt am Main, Germany) in cooperation with local station hosts at the University of New Brunswick (UNB, Canada), the University of New South Wales (UNSW, Sydney, Australia), the Hartebeesthoek Radio Astronomy Observatory (HartRAO, South Africa), the Nanyang Technological University (NTU, Singapore), the Japanese Space Exploration Agency (JAXA, Chofu, Japan), and the Institute for Astronomy, University of Hawaii. The data archiving and the orbit determination are performed at Technische Universität München (TUM, Germany). For further details and initial results of the orbit determination, see Montenbruck et al (2009).

Altogether nine receivers are operated at eight stations, see Fig. 8.2 and Tab. 8.2. Three sites are equipped with Septentrio GeNeRx receivers (Simsky et al, 2007), the other sites with Javad TRE_G2T or TRE_G3T receivers (GPS World, 2008). All stations provide dual-frequency observations of the GIOVE satellites in the E1 and E5a bands in addition to tracking of legacy L1 and L2 GPS signals. Individual stations furthermore support modernized GPS L2C and L5 signals, SBAS and GLONASS tracking or GIOVE E5b, E5 AltBOC (a wide band signal covering the combined E5a and E5b frequency band), and E6 tracking. The GIOVE satellites are only capable of transmitting two frequencies at the same time. The choice which frequency pair is transmitted (E1 and E5a/E5b or E1 and E6) is changed from time to time by ESA.

As only three E6–capable receivers are available in the CONGO network, transmission periods with E1/E6 are not considered. The Javad TRE_G3T receiver is also capable of tracking GLONASS but this GNSS is not considered in this paper. Three different antenna types are used within the CONGO network: Leica surveying antennas

Fig. 8.1: Artist view of the GIOVE–B satellite (Image: ESA – P. Carril).

Band	Frequency [MHz]	Comment
E1	1575.420	same as GPS L1
E5a	1176.450	same as GPS L5
E5b	1207.140	
E6	1278.750	

Tab. 8.1: Frequencies of the four Galileo bands.

(LEIAX1203+GNSS), a Leica choke ring antenna (LEIAR25.R3), and the Trimble Zephyr Geodetic 2 antenna. The deployment of the CONGO network started in 2007 and reached the number of 8 stations on 29 July 2009. More details on the characteristics of the CONGO tracking stations are given in Montenbruck et al (2011). Due to frequent outages of the GIOVE–A satellite (mainly due to an orbit raising maneuver) during the time period considered, this paper is limited to GIOVE–B.

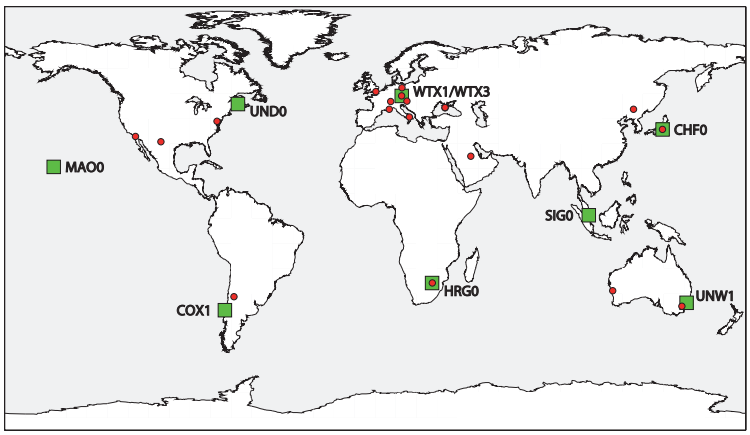

Fig. 8.2: GNSS stations of the CONGO network (squares) and SLR stations tracking the GIOVE satellites (circles).

All publications on GIOVE orbit determination up to now are based on ESA's GESS (Galileo Experimental Sensor Station; Giraud et al, 2009) network: Schönemann et al (2007) and García et al (2009) achieved an orbit accuracy of about 20 cm for GIOVE–A whereas Kirchner et al (2009) report the same value for both GIOVE satellites. Falcone et al (2006) achieved this accuracy level only by including Satellite Laser Ranging (SLR) observations in addition to the microwave observations. Urschl et al (2008) determined the GIOVE–A orbit solely based on SLR observations with an accuracy of about one meter.

This paper discusses the GIOVE orbit processing based on the CONGO network as implemented at TUM and evaluates the quality of different orbit products. It provides the first independent analysis of GIOVE precise orbit determination using a newly established network of GNSS monitoring stations with different types of receivers

Abb.	Location	Country	Receiver	Antenna	Radome
CHF0	Chofu	Japan	JAVAD TRE_G2T DELTA	TRM57971.00	NONE
COX1	Concepcion	Chile	SEPT GENERX	LEIAX1203+GNSS	NONE
HRG0	Hartebeesthoek	South Africa	JAVAD TRE_G2T DELTA	LEIAX1203+GNSS	NONE
MAO0	Maui	Hawaii, USA	JAVAD TRE_G3T DELTA	LEIAX1203+GNSS	NONE
SIG0	Singapore	Republic of Singapore	JAVAD TRE_G2T DELTA	LEIAX1203+GNSS	NONE
UND0	New Brunswick	Canada	JAVAD TRE_G2T DELTA	TRM55971.00	NONE
UNW1	Sydney	Australia	SEPT GENERX	LEIAX1203+GNSS	NONE
WTX1	Wettzell	Germany	SEPT GENERX	LEIAX1203+GNSS	NONE[a]
WTX3	Wettzell	Germany	JAVAD TRE_G2T DELTA	LEIAX1203+GNSS	NONE[a]

[a] WTX1 and WTX3 are operated at the same antenna with an antenna splitter. This antenna was replaced by a modified LEIAR25 without radome (LEIAR25.R3 NONE) on 7 August 2009.

Tab. 8.2: GNSS tracking stations of the CONGO network.

and antennas. The experience gained in this study may contribute to the build-up of dedicated Galileo processing capabilities within the International GNSS Service (IGS; Dow et al, 2009). Section 8.2 describes the options and strategies for processing the observations of the CONGO network. The quality of the orbits as well as orbit predictions computed with different strategies is assessed by comparisons, orbit fits, and SLR residuals in Sect. 8.3.

8.2 GNSS Processing

All CONGO stations transmit their data in real–time via the Ntrip protocol (Weber et al, 2005). The real–time streams are recorded, monitored, converted to RINEX 3.00 (Gurtner and Estey, 2007) data, and archived at TUM. The RINEX data of the CONGO network are processed with a modified version of the Bernese GPS Software (Dach et al, 2007; Svehla et al, 2008). This version allows to process a predefined selection of two frequencies, e.g. E1 and E5a. The preprocessing (detection of outliers and cycle–slips) is based on smoothed code observations, but the raw (unsmoothed but preprocessed) code observations are used for the further processing. After synchronizing the receiver clocks with the GPS observations, a GPS–only precise point positioning (PPP) solution is computed where the CODE (Center for Orbit Determination in Europe, one of the IGS analysis centers) final or rapid satellite orbits and clocks (Bock et al, 2009) are fixed. Daily station coordinates, epoch–wise receiver clock parameters, troposphere zenith delay parameters with 2 h parameter spacing and troposphere gradients with 24 h parameter spacing are estimated from the ionosphere–free linear combination (LC) of L1 and L2 phase and code observations. A cutoff angle of 10° and elevation–dependent weighting with $w = \cos^2(90^\circ - \epsilon)$ are applied. Outliers are detected and rejected in an iterative procedure. Typical values for the repeatabilities of the station coordinates are 2 – 5 mm for the horizontal components and 5 – 10 mm for the vertical component.

The station positions, troposphere zenith delays and gradients as well as the receiver clock parameters obtained in this GPS–only solution are introduced as known parameters in the GIOVE orbit and clock determination step. The ionosphere–free linear combination of E1 and E5a is processed with a sampling rate of 30 s. Only the orbital parameters of the GIOVE satellites, their satellite clocks, float ambiguities, and one combined inter–system/inter–frequency bias for each receiver but one are estimated. These biases originate from receiver–specific code biases for GPS and GIOVE signals and signals on different frequencies (L1/L2 for GPS and E1/E5a for GIOVE). The orbital parameters consist of the six Keplerian elements and up to nine Radiation Pressure (RPR) parameters of the model of Beutler et al (1994): three constant terms and six periodic terms. These RPR parameters are given in a Sun–oriented coordinate system with one axis pointing from the satellite to the Sun (D), the second axis parallel to the satellite's solar panel axis (Y), and the third axis (X) completing a right–handed system. No a priori RPR model is used. The estimated constant term in D–direction is typically $-1.5 \cdot 10^{-7}$ ms^{-2} whereas the other terms are about two orders of magnitude smaller. The a priori orbit information originates from predictions for SLR tracking of the GIOVE satellites provided through the International Laser Ranging Service (ILRS; Pearlman et al, 2002).

The satellite antenna offsets w.r.t. the center of mass for the ionosphere–free linear combination of E1 and E5a computed from the offsets of the basic frequencies given in Zandbergen and Navarro (2009) are listed in Tab. 8.3.

Type	X [mm]	Y [mm]	Z [mm]
MW GIOVE–A	−4.0	1.0	819.2
MW GIOVE–B	−3.2	3.4	1352.4
SLR GIOVE–A	828.0	655.0	688.0
SLR GIOVE–B	804.3	−294.1	1330.1

Tab. 8.3: GIOVE Microwave (MW) transmitter and SLR retroreflector offsets w.r.t. the center of mass. The MW offsets refer to the ionosphere–free linear combination of E1 and E5a.

In contrast to Zandbergen and Navarro (2009), the coordinate system definition of Tab. 8.3 is consistent with that of the Block IIA GPS satellites (X–axis positive to hemisphere containing the Sun, Y–axis along solar panel, Z–axis towards nadir). As no E1 and E5a calibrations for the receiver antennas were available, the GPS L1 and L2 offsets from igs05.atx (Schmid et al, 2007) were used for E1 and E5a, respectively. Becker et al (2010) showed that the L2 and E5a values obtained from anechoic chamber calibrations agree within 1 − 2 mm. Satellite and receiver antenna phase center variations were neglected for the GIOVE observations as they are unknown for all frequencies of the transmitting antennas and the GIOVE-specific frequencies of the receiving antennas. Solid Earth tides and pole tides were modeled according to the IERS Conventions 2003 (McCarthy and Petit, 2004), ocean loading corrections were provided by Scherneck (1991)[1] computed from FES2004 (Lyard et al, 2006).

Two different product lines are generated in the operational CONGO processing running once per day: a rapid solution including an orbit prediction and a final solution to get the best quality orbits but with a higher latency, see Fig. 8.3. The rapid solution is computed as soon as the CODE rapid orbit and clock products for the GPS–only PPP solution are available. It consists of a basic 1–day solution to generate Normal Equations (NEQs) including all parameters mentioned above. For comparison purposes two different solutions are computed: a combined code + phase solution and a phase–only solution. Significant differences between both solutions are an indicator of changes in the inter–frequency/inter–system biases, e.g., due to firmware updates or hardware changes.

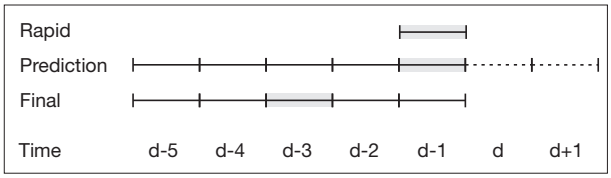

Fig. 8.3: CONGO rapid and final processing. For the current day *d* the rapid solution covers the previous day *d–1*. Five consecutive NEQs from *d–5* till *d–1* are combined to get an orbit prediction for the current and the next day. The final solution is computed with a delay of 3 days as the middle day of a 5–day arc is used.

The rapid 5–day solution as well as the final solutions are computed from the 1–day NEQs. The orbital elements and RPR parameters are stacked resulting in one set of parameters for the multi-day arc (Beutler et al, 1996). Based on the NEQs of the 5 previous days, an orbit prediction for the current and the next day are generated. For the final orbits, the middle day of a 5–day arc is used. This orbit is kept fixed to compute the final clock solution for the corresponding day. For the 1–day rapid orbits, only five RPR parameters are estimated (three direct parameters and two periodic parameters in X–direction). Based on the results of Sect. 8.3, the full set of nine RPR parameters is used for the 5–day solutions (orbit prediction as well as final solution).

The data discussed in this paper covers the time period 29 June 2009 (180/2009) until 27 October 2009 (300/2009). The station–specific RMS values of code and phase residuals of the rapid 1–day solution are plotted in Fig. 8.4 and their mean values are listed in Tab. 8.4. Whereas the order of magnitude of the phase residuals is quite similar for both receiver groups, the code residuals of the GeNeRx receivers are smaller by about 44% compared to the Javad receivers. This effect is related to narrower tracking loops of the GeNeRx receivers. Activating the receiver-internal smoothing option of the Javad receivers reduced the code residuals of this receiver type by about two-thirds. Therefore, this option is now used for recording the observation data of the Javad receivers in the CONGO network.

[1] `http://holt.oso.chalmers.se/loading/index.html`

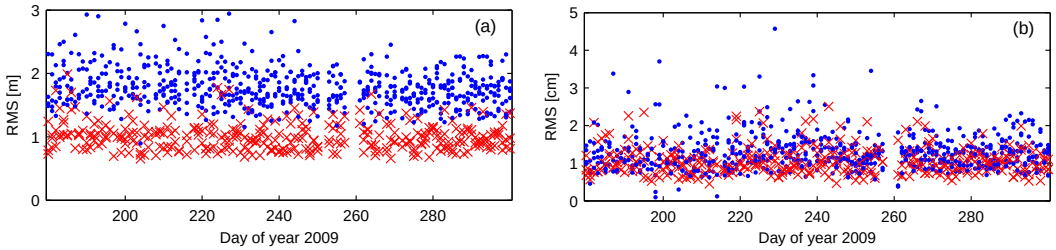

Fig. 8.4: Daily RMS values of the (a) code and (b) phase residuals of the 1–day rapid orbit solutions. Sites equipped with GeNeRx receivers are indicated by *red crosses*, sites with Javad receivers by *blue dots*. The gap at the days 258 – 260 is related to a GIOVE–B transmission outage.

Site	Receiver	Code [m]	Phase [cm]
COX1	GeNeRx	0.93	1.04
UNW1		1.01	1.08
WTX1		1.07	1.10
CHF0	Javad	1.97	1.69
HRG0		1.81	1.33
MAO0		1.73	1.98
SIG0		1.92	1.19
UND0		1.68	1.42
WTX3		1.63	1.22

Tab. 8.4: Mean RMS of the residuals of the 1–day CONGO rapid solution. The sites are grouped by receiver type.

8.3 Orbit Validation

8.3.1 Orbit Validation Methods

8.3.1.1 Internal Consistency

The easiest way to evaluate the internal consistency of satellite orbits is the direct comparison of positions from different orbit solutions of the same type, e.g., the last day of a 3–day arc with the middle day of a 3–day arc centered at the next day. The residuals are usually given in a satellite–centered orbit system in along–track, radial, and out of plane (cross–track) direction. The direct comparison can of course also be used for orbit predictions and allows for an assessment of the prediction accuracy. All direct orbit comparisons discussed in this paper were performed with a tabular spacing of 15 minutes.

The consistency of consecutive orbit solutions can be evaluated by the 3D RMS of multi–day orbit fits w.r.t. the original orbits. E.g., for a 2-day orbit fit, a new orbital arc with a validity of 48 h is determined from two orbits with 24 h validity from consecutive days, see Fig. 8.5. The two orbits with 24 h validity are completely independent if one uses 1-day arcs but also the middle day of multi–day orbital arc can be used. In the latter case, one has to be aware that the RMS gets smaller with increasing arc length since the orbits are based on overlapping data resulting in a smoothing effect of longer arcs. The RMS of the differences (in our case at 15 minute intervals) between all original 24 h orbits w.r.t. the multi-day arc can then be used as quality indicator for the internal consistency of the orbits.

8.3.1.2 Satellite Laser Ranging

Satellite Laser Ranging observations allow for an independent validation of GNSS orbits determined from microwave observations. The GIOVE satellites are observed on a regular basis by the SLR tracking stations of the

International Laser Ranging Service (ILRS). Although they have a quite low tracking priority among all satellites tracked by the ILRS[2], altogether 1614 Normal Points (NPs) are available for GIOVE–B in the time period 180–300/2009. Most NPs are obtained during nighttime due to the large distance of the GIOVE satellites resulting in difficult tracking conditions. However, the station distribution of the NPs is quite inhomogeneous: more than one third of the NPs are provided by the Zimmerwald station (Switzerland), 9 stations provide more than 50 NPs and only 5 stations more than 100 NPs. The Simeiz station (Ukraine) was excluded due to residuals in the range of several tens of meters. For the SLR validation of the GIOVE orbits based on microwave observations, the coordinates of the altogether 18 SLR stations shown in Fig. 8.2 were fixed to SLRF2005 (Luceri and Bianco, 2007). Two of these SLR stations are co-located with CONGO GNSS stations, namely Wettzell and Hartebeesthoek. Meteorological observations at the stations were used to model the tropospheric delay according to Marini (1972). The other models are completely identical to the microwave analysis to guarantee full consistency.

Besides the analysis of SLR residuals, a direct comparison of orbits determined from SLR and microwave observations can also be performed. SLR-based orbit solutions for such a comparison were computed by DLR using the SLRORB software (Kraft, 2009). In view of the sparseness of the GIOVE–B SLR observations (on average 10–15 NPs per day) 7–day solutions were computed employing a 9 parameter RPR model. The central day of each sliding 7–day arc was then used for comparison with the GNSS-based orbits. Position differences were evaluated at 15 minute intervals and the 3D RMS position error was computed on a daily basis for the performance comparison. No SLR orbits are available during the eclipse phase, where a proper fit of the SLR measurements over one week arcs could not be achieved with the employed dynamic force model.

8.3.2 Orbit Validation Results

To find the optimal orbit parameterization for GIOVE–B, orbits of different arc length (3, 5, 7, and 9 days) and with a different number of RPR parameters were computed. Two different parameterizations for the radiation pressure were used:

- 5 RPR parameters: three linear terms and two periodic terms in X–direction
- 9 RPR parameters: three linear terms and the full set of six periodic terms.

To evaluate the impact of the different number of RPR parameters, the last observed day and the first predicted day of final solutions with different arc lengths are compared with the middle day of the corresponding solutions. The mean RMS values in radial, along–track, and cross–track direction are shown in Fig. 8.6. The largest RMS values occur for the along–track direction: an almost linear increase of the RMS with increasing arc length for the solutions with 5 RPR parameters is obvious. For the solutions with 9 RPR parameters, almost no dependency on the arc length is visible. The radial RMS values are the smallest for both solution types but the 9 RPR parameter solutions show a decrease with increasing arc length whereas the 5 RPR parameter solutions show an increase.

The STDs and offsets of SLR residuals for orbits with different arc lengths and number of RPR parameters are given in Tab. 8.5. The microwave-based orbits are kept fixed and residuals are computed from the SLR observations as external validation of mainly the radial component. Outliers in the SLR residuals larger than 50 cm have been excluded. For 9 RPR parameters, a quite large offset of 20 cm as well as a STD of 21 cm

[2] http://ilrs.gsfc.nasa.gov/missions/mission_operations/priorities/index.html

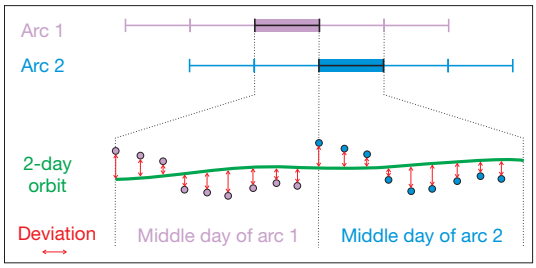

Fig. 8.5: 2-day orbit fit through middle days of 5-day arcs. The orbit positions of the middle days of arc 1 and arc 2 are used as input for the fit of a 2-day arc. The arrows represent the deviation of the original positions of arc 1 and arc 2 w.r.t. the newly adjusted 2-day orbit. The 3D RMS deviations are used as a measure for the internal consistency of the orbits.

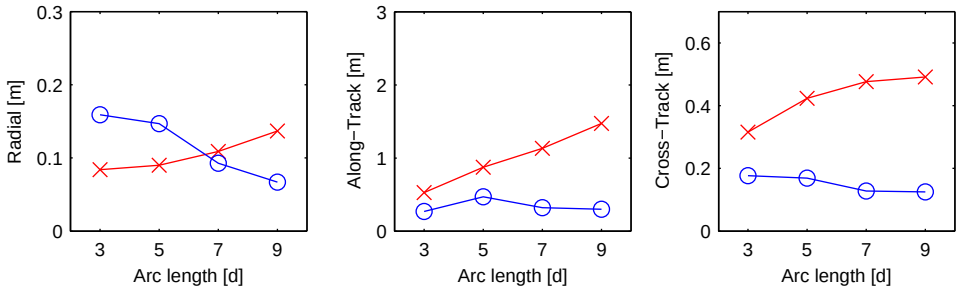

(a) Comparison of the middle day with the last day.

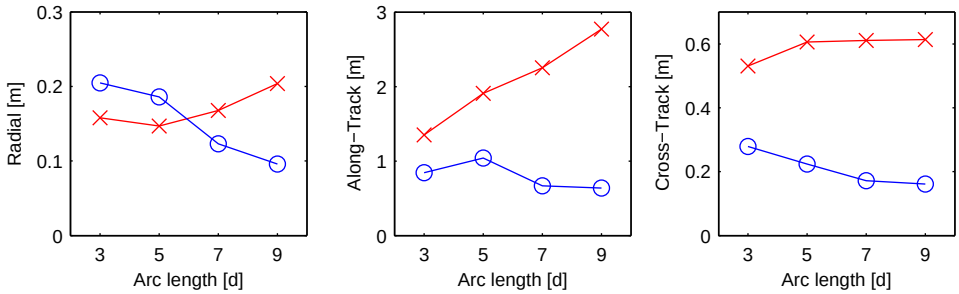

(b) Comparison of the middle day with the first predicted day.

Fig. 8.6: Mean RMS values for orbit comparisons of solutions with different arc length as well as 5 RPR parameters (*red crosses*) and 9 RPR parameters (*blue circles*).

Arc length [days]	# RPR	SLR residuals Mean [cm]	SLR residuals STD [cm]	Orbit fit 3D RMS [cm]
3	5	4.61	13.29	9.48
	9	20.13	20.87	7.74
5	5	4.84	11.89	7.37
	9	11.85	14.44	4.77
7	5	4.41	10.32	5.43
	9	8.28	11.58	2.78
9	5	5.10	11.08	4.64
	9	6.39	11.05	1.75

Tab. 8.5: SLR residuals and 3D RMS of 2–day orbit fits for different arc lengths and number of RPR parameters.

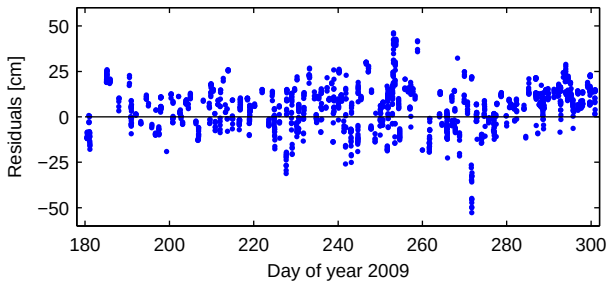

Fig. 8.7: SLR residual time series of the CONGO orbits (central day of a 5-day orbit arc with 5 RPR parameters).

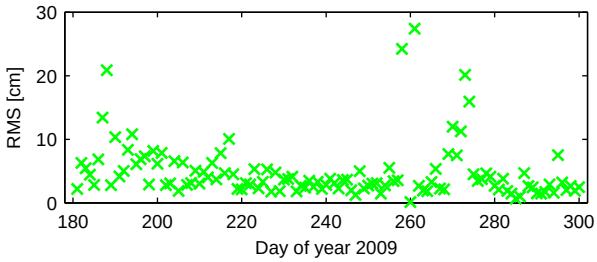

Fig. 8.8: 2–day orbit fit time series of the CONGO final orbits (central day of a 5-day orbit arc with 9 RPR parameters).

are visible for the 3–day arcs. Offset and STD decrease with increasing arc length. This result is in agreement with the RMS of the radial component of the orbit comparisons discussed above. For the solution with 5 RPR parameters, no significant dependence of offset and STD on the arc length are present. As an example, the time series of SLR residuals for the 5–day orbits with 5 RPR parameters is shown in Fig. 8.7. No significant elevation dependence of the SLR residuals is present (not shown here).

As internal validation, 3D RMS values are given in the last column of Tab. 8.5. These RMS values were obtained from 2–day orbit fits through middle days of consecutive multi-day arcs as shown in Fig. 8.5. It is clear that the RMS of the orbit fits decreases with increasing arc length due to the smoothing effect of the longer arcs. Therefore, the orbit fits can only be used for a comparison of the different number of RPR parameters. For all arc lengths, the solutions with 9 RPR parameters show smaller orbit fit RMS values due to the better fitting related to the higher number of parameters. Based on the results discussed above, a 9–day arc with 9 RPR parameters provides the best performance for orbit determination and prediction. However, due to practical reasons (initialization after outages), 5–day arcs are used for the operational CONGO processing.

The time series of the 2-day orbit fit RMS values is shown in Fig. 8.8 for the final CONGO orbits. The improvement after day 218 is probably related to the commissioning of the station in Singapore that significantly improved the global coverage of the CONGO network. The increased values around day 260 are related to the GIOVE transmission outage already mentioned above.

The daily 3D RMS position differences between orbits computed from SLR and microwave observations are plotted in Fig. 8.9. The comparison is confined to days 180 – 257 since no proper SLR–based orbits could be

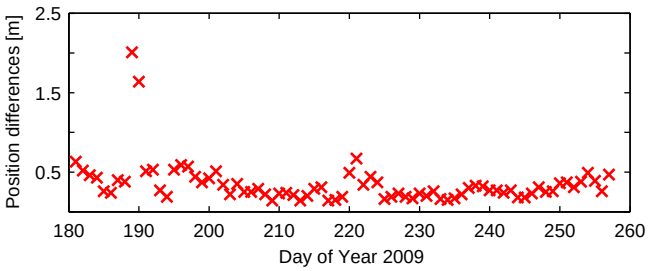

Fig. 8.9: Daily 3D RMS position differences between GIOVE–B satellite orbits derived from SLR and microwave observations.

obtained during the eclipse period of GIOVE–B. The mean RMS position differences exhibit a median value of 27 cm, which is roughly twice the value of the RMS SLR residuals of the microwave orbits discussed above. Due to the distance of the GIOVE–B satellite, the SLR residuals mainly evaluate the radial component of the microwave orbits and are, therefore much smaller than the RMS position difference of the SLR and microwave orbits. Despite the limited SLR tracking coverage, the SLR-only orbit determination can provide a few decimeter accuracy, which is well compatible with the needs of a Standard Positioning Service (SPS). This result is of particular interest for other GNSS satellites such as COMPASS-M1, which are not presently supported by any of the global GNSS tracking networks.

8.4 Summary

The CONGO network offers the possibility of a continuous tracking of the GIOVE satellites. The orbit determination shows an accuracy that is on the few decimeter level. For orbit arcs longer than three days, the full set of nine RPR parameters shows a better performance than the reduced set of five RPR parameters. Orbit predictions agree with the final orbits on a level of one meter after one day with the largest differences in the along–track direction. The current work provides the first independent validation of results achieved earlier by the ESA project teams with dedicated infrastructure. Overall, a similar accuracy is achieved despite a smaller amount of tracking stations and the use of commercial off-the-shelf receivers and antennas. This is of high relevance for the future scientific exploitation of Galileo which will rely on a global IGS-type infrastructure rather than the mission-specific ground network. The orbit predictions of the operational CONGO processing are used by DLR for the computation of real–time clocks with the Real–Time Clock Estimation (RETICLE) system (Hauschild and Montenbruck, 2008) that was enhanced for the capability to process GIOVE data (Cao et al, 2010). Recently, three more stations have been added to the CONGO network: O'Higgins in Antarctica, Stanford in the United States, and La Laguna (Tenerife). A further extension of the CONGO network is planned for the near future.

Acknowledgements

We'd like to thank BKG (Georg Weber) for providing Ntrip infrastructure and support and the station operators Uwe Hessels (Geodetic Observatory Wettzell, Germany), Richard Langley (UNB, Canada), Peter Mumford (UNSW, Australia), Ludwig Combrinck (HartRAO, South Africa), Narayanaswamy Nagarajan (NTU, Singapore), Thoralf Noack (DLR, Germany), and Dan O'Gara (University of Hawaii, USA) for their support.

Bibliography

Becker M, Zeimetz P, Schönemann E (2010) Antenna chamber calibrations and antenna phase center variations for new and existing GNSS signals. In: IGS Workshop 2010, 28 June – 2 July 2010, Newcastle

Benedicto J, Gatti G, Garutti A, Paffet J, Bradford A, Jackson C, Rooney E (2006) The triumph of GIOVE-A – the first Galileo satellite. ESA Bulletin 127:62–69

Beutler G, Brockmann E, Gurtner W, Hugentobler U, Mervart L, Rothacher M, Verdun A (1994) Extended orbit modeling techniques at the CODE Processing Center of the International GPS Service (IGS): Theory and initial results. Manuscripta Geodaetica 19:367–386

Beutler G, Brockmann E, Mervart L, Rothacher M, Weber R (1996) Combining consecutive short arcs into long arcs for precise and efficient GPS orbit determination. Journal of Geodesy 70(5):287–299, DOI 10.1007/BF00867349

Bock H, Dach R, Jäggi A, Beutler G (2009) High-rate GPS clock corrections from CODE: support of 1 Hz applications. Journal of Geodesy 83(11):1083–1094, DOI 10.1007/s00190-009-0326-1

Cao W, Hauschild A, Steigenberger P, Langley R, Urquhart L, Santos M, Montenbruck O (2010) GPS/GIOVE integrated precise point positioning performance evaluation. In: Proceedings of ION ITM 2010, pp 540–552

Dach R, Hugentobler U, Fridez P, Meindl M (eds) (2007) Bernese GPS Software Version 5.0. Astronomical Institute, University of Bern, Bern, Switzerland

Dow J, Neilan R, Rizos C (2009) The International GNSS Service in a changing landscape of Global Navigation Satellite Systems. Journal of Geodesy 83(3-4):191–198, DOI 10.1007/s00190-008-0300-3

Falcone M, Navarro-Reyes D, Hahn J, Otten M, Piriz R, Pearlman M (2006) GIOVE's Track. GPS World 17(11):34–37

García ÁM, Píriz R, Fernández V, Navarro-Reyes D, González F, Hahn J (2009) GIOVE orbit and clock determination and prediction: Experimentation results. In: Proceedings of the European Navigation Conference – Global Navigation Satellite Systems

Giraud J, Borrel V, Crisci M (2009) Latest Achievements in GIOVE Signal and Sensor Station Experimentations. In: Proceedings of ION GNSS 2009, pp 3025–3036

GPS World (2008) JAVAD GNSS unveils new survey products. GPS World 19(3):28

Gurtner W, Estey L (2007) RINEX, The Receiver Independent Exchange Format, Version 3.00. Tech. rep., URL `ftp://ftp.igs.org/pub/data/format/rinex300.pdf`

Hauschild A, Montenbruck O (2008) Real-time clock estimation for precise orbit determination of LEO-satellites. In: Proceedings of ION GNSS 2008, pp 581–589

Kirchner M, Schmidt R, Vilzmann J (2009) Results of GIOVE Data Processing to Allow Evaluation of Principal System Performance Drivers. In: Proceedings of the European Navigation Conference – Global Navigation Satellite Systems

Kraft B (2009) Orbit and clock determination of the GIOVE satellites from SLR and GNSS measurements. Diplomarbeit, Lehrstuhl für Raumfahrttechnik, Technische Universität München

Luceri V, Bianco G (2007) The temporary ILRS reference frame: SLRF2005. In: ILRS Fall Meeting, 24 – 28 September 2007, Grasse, URL `http://ilrs.gsfc.nasa.gov/docs/AWG_GRASSE_24.09.2007.pdf`

Lyard F, Lefevre F, Letellier T, Francis O (2006) Modelling the global ocean tides: modern insights from FES2004. Ocean Dynamics 56(5-6):394–415, DOI 10.1007/s10236-006-0086-x

Malik M, Gatti G, Alpe V, Johansson M, Kieffer R, Robertson G (2009) GIOVE-B Satellite & Payload Overview. In: Proceedings of the European Navigation Conference – Global Navigation Satellite Systems

Marini J (1972) Correction of satellite tracking data for an arbitrary tropospheric profile. Radio Science 7(2):223–231, DOI 10.1029/RS007i002p00223

McCarthy D, Petit G (2004) IERS Conventions (2003). IERS Technical Note 32, Verlag des Bundesamtes für Kartographie und Geodäsie, Frankfurt am Main

Montenbruck O, Hauschild A, Hessels U, Steigenberger P, Hugentobler U (2009) CONGO – first GPS/GIOVE tracking network for science, research. GPS World 20(9):56–62

Montenbruck O, Hauschild A, Hessels U (2011) Characterization of GPS/GIOVE sensor stations in the CONGO network. GPS Solutions 15(3):193–205, DOI 10.1007/s10291-010-0182-8

Pearlman MR, Degnan JJ, Bosworth JM (2002) The International Laser Ranging Service. Advances in Space Research 30(2):125–143, DOI 10.1016/S0273-1177(02)00277-6

Scherneck HG (1991) A parametrized solid Earth tide model and ocean loading effects for global geodetic base-line measurements. Geophysical Journal International 106(3):677–694, DOI 10.1111/j.1365-246X.1991.tb06339.x

Schmid R, Steigenberger P, Gendt G, Ge M, Rothacher M (2007) Generation of a consistent absolute phase center correction model for GPS receiver and satellite antennas. Journal of Geodesy 81(12):781–798, DOI 10.1007/s00190-007-0148-y

Schönemann E, Springer T, Otten M, Becker M, Dow J (2007) GIOVE-A precise orbit determination from microwave and satellite laser ranging data – first perspectives for the Galileo constellation and its scientific use. In: Proceedings of the First Colloquium on Scientific and Fundamental Aspects of the Galileo Programme 2007

Simsky A, Sleewaegen JM, Wilde WD, Wilms F (2007) Overview of Septentrio's Galileo receiver development strategy. In: Proceedings of ION GNSS 2007, pp 1888–1895

Svehla M D Heinze, Rothacher M, Steigenberger P, Dähnn M, Kirchner M (2008) Combined processing of GIOVE-A and GPS measurements using zero- and double-differences. Geophysical Research Abstracts 10, sRef-ID: 1607-7962/gra/EGU2008-A-11383

Urschl C, Beutler G, Gurtner W, Hugentober U, Ploner M (2008) Orbit determination for GIOVE-A using SLR tracking data. In: Luck J, Moore C, Wilson P (eds) Extending the Range, Proceedings of the 15th International Workshop on Laser Ranging, pp 40–46, http://cddis.gsfc.nasa.gov/lw15/docs/papers/Orbit%20Determination%20for%20GIOVE-A%20using%20SLR%20Tracking%20Data.pdf

Weber G, Dettmering D, Gebhard H, Kalafus R (2005) Networked transport of RTCM via Internet Protocol (Ntrip) – IP-streaming for real-time GNSS applications. In: Proceedings of ION GNSS 2005, pp 2243–2247

Zandbergen R, Navarro D (2009) Specification of Galileo and GIOVE space segment properties relevant for satellite laser ranging. Tech. Rep. ESA-EUING-TN/10206, rev. 3.2, European Space Agency

9 Galileo Orbit Determination using Combined GNSS and SLR Observations

Originally published as:

Hackel S., Steigenberger P., Hugentolber U., Uhlemann M., Montenbruck O. (2014): Galileo orbit determination using combined GNSS and SLR observations, GPS Solutions, doi: 10.1007/s10291-013-0361-5

The final publication is available at Springer via `http://dx.doi.org/10.1007/s10291-013-0361-5`.

Abstract

The first two Galileo In-Orbit Validation (IOV) satellites were launched in October 2011 and started continuous signal transmission on all frequencies in early 2012. Both satellites are equipped with two different types of clocks, namely Rubidium clocks and Hydrogen masers. Based on two test periods the quality of the Galileo orbit determination based on GNSS and SLR observations is assessed. The estimated satellite clock parameters are used as quality indicator for the orbits: A bump at orbital periods in the Allan deviation indicates systematic errors in the GNSS-only orbit determination. These errors almost vanish if SLR observations are considered in addition. As the internal consistency is degraded by the combination, the offset of the SLR reflector is shifted by $+5$ cm resulting in an improved orbit consistency as well as accuracy. Another approach to reduce the systematic errors of the GNSS-only orbit determination employs constraints for the clock estimates with respect to a linear model. In general, one decimeter orbit accuracy could be achieved.

9.1 Introduction

The European Space Agency (ESA) is currently building up the space segment of the European Global Navigation Satellite System (GNSS) Galileo. The first navigation satellites of ESA, the so-called Galileo in Orbit Validation Element (GIOVE), were GIOVE-A (Rooney et al, 2007) and GIOVE-B (Robertson and Kieffer, 2009) launched in December 2005 and April 2008, respectively. The primary task of GIOVE-A was transmitting Galileo signals from space to ensure the frequency allocation. GIOVE-B was the first satellite with a highly stable Passive Hydrogen Maser (PHM) onboard. GIOVE-A and GIOVE-B were decommissioned by ESA in June and July 2012, respectively. Results of the GIOVE orbit determination are given in, e.g., García et al (2008), Kirchner et al (2009), ESA (2011), Gendt et al (2011), and Steigenberger et al (2011). In general, orbit accuracy at the few decimeter level could be achieved by the different groups.

The four satellites of the Galileo In-Orbit Validation (IOV) phase are placed in two different orbital planes and will be part of the operational Galileo constellation. The first two IOV satellites were launched in October 2011. They are denoted as PFM (Proto-Flight Model) and FM2 (Flight Model 2) and reported as E11 and E12 in RINEX (Gurtner and Estey, 2009) observation files. The second pair of IOV satellites (FM3 and FM4) was launched on 12 October 2012 and started signal transmission in December of the same year. All IOV satellites (Chiarini et al, 2008) are equipped with two Passive Hydrogen Masers (PHMs) and two Rubidium Atomic Frequency Standards (RAFSs).

To assess the accuracy of GNSS-derived satellite orbits, Satellite Laser Ranging (SLR) measurements can be used as a validation tool (Pavlis and Beard, 1996; Appleby and Otsubo, 2000; Urschl et al, 2005). As the optical SLR observations are independent from the microwave GNSS measurements, they can help to identify systematic errors of the GNSS analysis: Flohrer (2008) found a systematic dependency of the SLR residuals on the elevation β of the Sun above the orbital plane and in addition showed a dependency on the a priori orbit model for GPS satellites.

However, SLR observations cannot only be used for validation purposes but also for the orbit parameter estimation itself. The SLR-only orbit determination of GIOVE-A of Urschl et al (2008) resulted in meter-level orbit accuracy.

A joint adjustment of GPS and SLR observations was reported in Urschl et al (2007) although no significant improvement of the orbit quality could be achieved due to the small number of available SLR observations. A combined orbit determination based on GNSS and SLR observations of the GIOVE satellites is discussed in Schönemann et al (2007), Schönemann et al (2009), and Hidalgo et al (2008a). The orbit quality of the combined orbits improves by up to 20% compared to the GNSS-only orbits even if only few SLR observations are available. First results of Galileo IOV orbit and clock determination based on five days are published in Steigenberger et al (2013a). They achieved a decimeter level orbit quality and the SLR validation of these orbits showed standard deviations of one decimeter with a systematic offset of about 6 cm. Montenbruck et al (2012) analyzed the PHM of GIOVE-B and identified periodic variations of the apparent clock that show up as a bump in the Allan deviation at the orbital period. Inclusion of SLR data in the orbit determination helped to mitigate these systematic effects indicating a corresponding improvement in orbit determination accuracy. Further results of GIOVE clock analysis are given in Hahn et al (2007), Hidalgo et al (2008b), and Waller et al (2010).

We address orbit determination and analysis of the first two Galileo IOV satellites based on GNSS-only processing and a combination of GNSS and SLR observations. First, the GNSS and SLR data as well as the processing strategies for both techniques are discussed. The quality of the GNSS-only and combined GNSS+SLR orbits with different arc lengths and different orbit parameterization is assessed by day boundary discontinuities, orbit fit RMS values, and SLR residuals. The impact of the different orbit modeling strategies on the apparent satellite clocks is studied. The inclusion of SLR observations in the orbit determination helps to mitigate systematic effects seen in the GNSS-only analysis. As the IOV satellites are equipped with highly stable PHMs, clock constraints with respect to a linear model can be applied to stabilize the parameter estimation. The impact of these constraints on the orbit and clock estimates is analyzed. In general an improvement in orbit accuracy evaluated by SLR could be achieved by applying clock constraints.

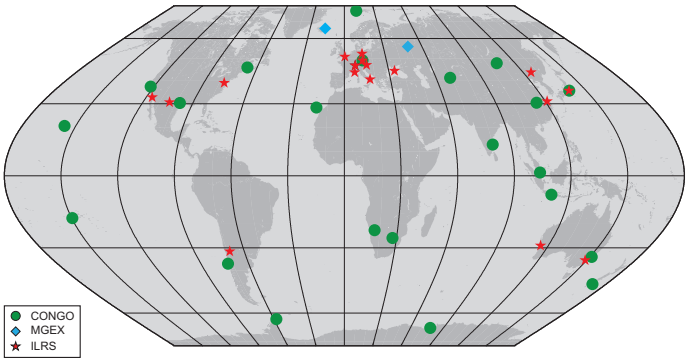

Fig. 9.1: Distribution of GNSS and SLR tracking stations.

9.2 GNSS and SLR Processing

Data from 24 multi-GNSS stations shown in Fig. 9.1 are used. The majority (22) of them are part of the Cooperative Network for GIOVE Observation (CONGO; Montenbruck et al, 2010). In addition, two stations of the Multi-GNSS Experiment (MGEX; Weber, 2012) of the International GNSS Service (IGS; Dow et al, 2009) are used to densify the network. A detailed analysis of the data quality of the CONGO stations is given in Montenbruck et al (2010). They report a similar tracking performance for the GPS and GIOVE signals, a conclusion which is also valid for the Galileo data used in our studies

- *Period A*: 9 April until 14 May 2012: Day-of-Year (DoY) 100 – 140, high β-angle (58 – 70°), RAFS
- *Period B*: 26 July until 1 August 2012: DoY 208 – 214, low β-angle (2 – 8°), PHM.

GNSS and SLR data are both processed with a modified version of the Bernese GPS Software (Dach et al, 2007). The processing scheme was inherited from the GIOVE processing of Steigenberger et al (2011) with a modified preprocessing for a more reliable detection of outliers and cycle slips. GNSS data are processed in a two-step approach:

1. *GPS-only analysis*: station coordinates, receiver clock parameters, troposphere zenith delays and gradients are estimated from GPS observations only with a Precise Point Positioning (PPP) utilizing rapid orbit and clock products of the Center for Orbit Determination in Europe (CODE; Dach et al, 2009).

Processing option	Applied model
Basic observables	GPS L1/L2 and Galileo E1/E5a carrier phase and smoothed code observations
Modeled observables	Ionosphere-free linear combination of GPS L1/L2 and Galileo E1/E5a
Observation weighting	Elevation-dependent weighting: $\cos^2 z$ with zenith distance z
Sampling	30 s
Elevation cutoff angle	10°
Tropospheric a priori model	Hydrostatic Niell mapping function (NMF; Niell, 1996); a priori delays according to Dach et al (2007)
Wet tropospheric delay	Estimated as piece-wise linear function with 2h parameter spacing, no constraints applied
	Wet NMF (Niell, 1996)
Troposphere gradients	Tilting model of Meindl et al (2003), estimated as piece-wise linear function with 24h parameter spacing and the wet NMF
GPS satellite antenna model	igs08.atx (Rebischung et al, 2012)
Galileo satellite antenna model	Antenna offsets in accord with IGS MGEX (Rizos et al, 2013); no antenna phase center variations considered
Receiver antenna model	Anechoic chamber calibrations for L1/E1, L2, E5a (Becker et al, 2010); igs08.atx calibrations for antennas without chamber calibrations, L2 calibrations used for E5a
Phase polarization effect	Wu et al (1993)
Attitude model	Nominal yaw attitude (navigation antenna pointing to the center of the Earth, solar panel axes perpendicular to the Sun-satellite direction; Bar-Sever, 1996; Kouba, 2009)
Galileo spacecraft mass	GIOVE-B mass (530 kg; ESA, 2011)

Tab. 9.1: Options used for the GNSS processing.

2. *Galileo orbit and clock determination*: the parameters of the GPS-only PPP are kept fixed to solve for the Galileo orbit and clock parameters.

A detailed list of processing options is given in Table 9.1. Both steps are based on ionosphere-free linear combinations of dual-frequency code and phase observations (L1/L2 for GPS, E1/E5a for Galileo) and include an outlier detection based on the post-fit residuals. The mean phase residuals for one particular day after the residual screening are shown in Fig. 9.2. They are in general at the $1-2$ cm level, similar to that of GIOVE-B (Steigenberger et al, 2011) and slightly better than for QZS-1, the first satellite of the Japanese Quasi-Zenith Satellite System (QZSS; Steigenberger et al, 2013b). The GPS residuals of the first step are about 1 cm, i.e., the Galileo residuals are worse by $20-30$%. The larger magnitude of the Galileo residuals compared to GPS might be caused by deficiencies in the modeling of the Galileo observations like the assumptions about the phase center offsets, neglecting the antenna phase center variations, and the attitude behavior. The latter is in particular important during the eclipse seasons. For GPS, special models are available accounting for technical limitations of the yaw rates during the noon and midnight turns (Bar-Sever, 1996; Kouba, 2009). The lack of such a model for Galileo is a further potential error source compared to GPS.

The code residuals are in general at the few decimeter level since smoothed code observations are used. They are not shown in Fig. 9.2 as their weight in the parameter estimation is smaller by a factor of 100 compared to the phase observations. The GIOVE-B code residuals given in Steigenberger et al (2011) are larger by a factor of $5-10$ since they used raw code instead of smoothed code data. The consistency of code and phase observations has been examined via the multipath combinations of code and dual-frequency carrier phase measurements for selected stations and data arcs but did not provide indications of clear systematic errors. To account for systematic differences of the Galileo and GPS code observations, corresponding inter-frequency/inter-system-bias parameters are estimated for all stations but one.

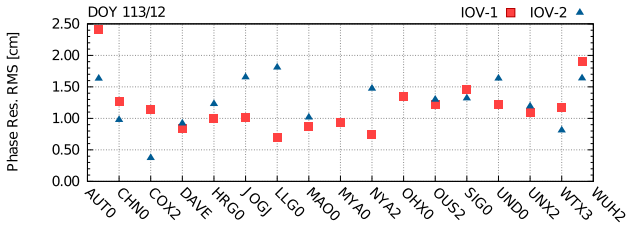

Fig. 9.2: 2-day orbit fit RMS computed from the middle days of two consecutive 3-day solutions.

The orbit parameters of the second step consist of six Kepler elements and five or nine Radiation Pressure (RPR) parameters of the model by Beutler et al (1994) without applying any a priori model. The five parameter model consists of three constant terms in direction of the Sun (D), in the direction of the solar panel axis (Y), and in direction perpendicular to D and Y (B), as well as sine/cosine terms in B-direction. The nine parameter model consists of the three constant terms and sine/cosine terms in each direction. 1-day Normal Equations (NEQs) are saved for the combination with SLR as well as GNSS-only multi-day solutions. In these multi-day solutions, only one set of Kepler elements and RPR parameters is estimated per three or five day interval to strengthen the stability of the orbital arc.

For comparison purposes, Deutsches Deutsches GeoForschungsZentrum (GFZ) provided IOV orbit solutions for data arc B based on the same set of Galileo tracking stations (Uhlemann et al, 2012). The delivered orbits are derived from 3-day arcs with 5 RPR parameters. However, the Galileo data are processed in one step together with GPS data from a global network of 110 stations with the GFZ EPOS.P8 software. In addition, GPS ambiguities are fixed to integers according to Ge et al (2007). Therefore, the network geometry should be strengthened compared to the two-step approach.

In the two time periods considered, the IOV satellites were tracked by 17 stations of the International Laser Ranging Service (ILRS; Pearlman et al, 2002) indicated by red stars in Fig. 9.1. In total 1039 normal points are available for IOV-1, 917 for IOV-2. SLR normal points are also processed with the Bernese GPS Software to guarantee full consistency due to identical modeling and parameterization. For validation purposes, the GNSS-derived satellite orbits are fixed and residuals of the SLR observations with respect to these orbits are computed. For orbit determination purposes of a combined GNSS+SLR processing, the same set of orbital parameters as in the GNSS-only analysis is estimated. In both cases, station coordinates are fixed to SLRF2008 (Pavlis, 2009). Outliers exceeding a limit of 25 cm are excluded from both the validation as well as the orbit determination.

9.3 Orbit Results

To assess the orbit quality, the following performance metrics are used:

- *Day Boundary Discontinuities (DBDs)*: 3D differences of the orbit positions at midnight of two consecutive orbital arcs.
- *2-day orbit fit RMS values*: a 2-day orbit arc is fitted through two consecutive 1-day arcs and the RMS of the new orbit w.r.t. the original orbits is computed. For multi-day arcs only the middle day is considered, see Fig. 9.3. For a more detailed description see Steigenberger et al (2011).
- *SLR residuals*: offset and Standard Deviation (STD) of SLR normal points w.r.t. the microwave-derived orbit. An example of SLR residual time series is given in Fig. 9.4.

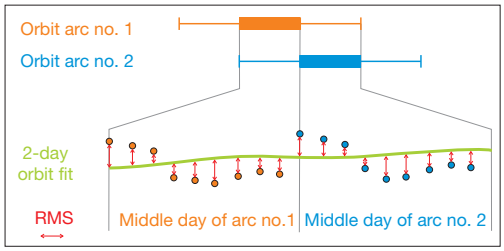

Fig. 9.3: 2-day orbit fit RMS computed from the middle days of two consecutive 3-day solutions.

Whereas the first two methods only allow for an assessment of the internal consistency as all orbits might be affected by systematic biases, the latter method is an independent validation, as it is based on a different observation technique (optical vs. microwave).

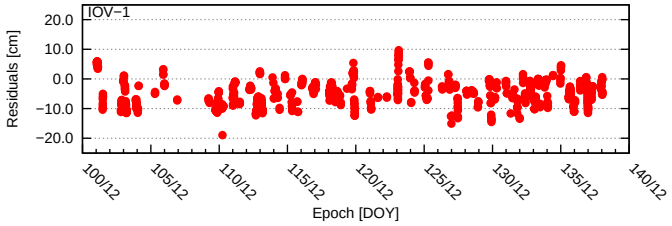

Fig. 9.4: SLR residual time series (observed computed) in time interval A of IOV-1 for GNSS-only orbit products based on 3-day arcs with 5 RPR parameters. A systematic bias of −5 cm is obvious from the residuals.

9.3.1 GNSS-only Analysis

Table 9.2 lists the orbit quality criteria discussed above for GNSS-only orbits of different arc lengths and different number of RPR parameters for time period A. The internal consistency in general improves with increasing arc length and reduced set of RPR parameters. The 1-day orbits show orbit fit RMS values on the level of two to three decimeters, the DBDs are even worse by a factor of two to three. The 1-day orbits with 9 RPR parameters have the worst internal consistency and also the largest SLR standard deviation indicating that this solution is over-parameterized, in particular in view of the orbit modeling deficiencies already mentioned in Sect. 9.2. The overparameterization is also visible in the formal errors of the orbital elements: as an example, the formal errors of the semi-major axis are larger by a factor of 12 for the 9 RPR parameter solution compared to the 5 RPR parameter solution.

Arc length [d]	No. of RPR param.	Sat.	2-d orbit fit RMS [mm]	3D orbit discont. [mm]	SLR residuals Mean [mm]	SLR residuals STD [mm]
1	5	IOV-1	181	385	−12	60
		IOV-2	270	436	−18	78
	9	IOV-1	277	563	18	113
		IOV-2	218	656	−49	126
3	5	IOV-1	26	89	−47	45
		IOV-2	26	98	−54	42
	9	IOV-1	41	126	18	65
		IOV-2	41	135	−14	88
5	5	IOV-1	15	50	−55	45
		IOV-2	17	58	−63	46
	9	IOV-1	28	133	2	54
		IOV-2	29	159	−12	61

Tab. 9.2: Orbit quality of GNSS-only analysis with different arc length and number of RPR parameters for time interval A.

Starting with 3-day arcs, the limited set of 5 RPR parameters introduces a bias in the SLR residuals of about −5 cm (see also Fig. 9.4). This bias is significantly smaller for 9 RPR parameters in interval A, although the STD increases by 1−4 cm. On the other hand, the radial bias of the 9 RPR parameter solution is notably larger than that of the 5 RPR parameter solution in case of data arc B, see Table 9.3. All solutions with 5 RPR parameters show a negative bias, i.e., the distance measured with SLR is shorter than the distance derived from the microwave orbits. However, the 9 RPR parameter solutions have a worse internal consistency compared to 5 RPR parameters. This effect is in particular visible for the DBDs of the 5-day solution which are larger by a

factor of up to three for the 9 RPR parameter solution. IOV-1 and IOV-2 in general show a similar behavior for the different solution types. Compared to the GIOVE-B results of Steigenberger et al (2011), the IOV orbit quality is better by a factor of about two. The main reason for this improvement is likely due to the larger tracking network of 24 stations compared to nine stations used in the previous study. Due to the limited accuracy, 1-day orbits are not considered in the further analysis.

Sol.	Time period	No. of RPR param.	Sat.	2-d orbit fit RMS [mm]	3D orbit discont. [mm]	SLR residuals Mean [mm]	SLR residuals STD [mm]
TUM	A	5	IOV-1	26	89	−47	45
			IOV-2	26	98	−54	42
	B	5	IOV-1	18	80	−65	72
			IOV-2	20	127	−82	70
GFZ	B	5	IOV-1	21	48	−79	92
			IOV-2	26	79	−62	88
TUM	A	9	IOV-1	41	126	18	65
			IOV-2	41	135	−14	88
	B	9	IOV-1	15	19	−118	77
			IOV-2	15	54	−134	81

Tab. 9.3: Orbit quality of GNSS-only analysis with 3 days arc length and different number of RPR parameters for time intervals A and B.

Table 9.3 compares 3-day orbits with 5 and 9 RPR parameters of the two different time intervals. In addition, the GFZ solution for analysis interval B with 5 RPR parameters is included. The systematic bias in the SLR residuals can also be seen in the GFZ solution indicating that this offset is a true signal and not a software- or processing-specific artifact. The GFZ orbits in general show a slightly better internal consistency but a slightly worse performance in the SLR validation. However, no clear superiority of GFZs network-based single-step approach compared to the two-step PPP method can be seen.

Concerning the values of SLR biases indicated in the above analysis it may be noted that biases of similar order have long been encountered in the analysis of GPS orbit products (Urschl et al, 2005). Also, biases of similar magnitude have been observed in earlier GIOVE analyses (Steigenberger et al, 2011). It would be speculative at present, however, to attribute these biases to inadequate spacecraft parameters until the orbit and radiation pressure modeling of the Galileo satellites is fully understood and the systematic errors discussed below are completely removed.

	Sat.	Radial [mm]	Along-track [mm]	Cross-track [mm]
Mean	IOV-1	−3	61	17
	IOV-2	−1	7	12
STD	IOV-1	26	78	77
	IOV-2	29	68	66

Tab. 9.4: Orbit comparison between 3-day orbits with 5 RPR parameters determined by TUM and GFZ.

A direct comparison of the 3-day orbits with 5 RPR parameters of TUM and GFZ is given in Table 9.4. With millimeter-level biases and STDs below 3 cm the agreement is best for the radial component. For the along-track and cross-track direction the biases are in general below 2 cm, except for the along-track component of IOV-1. The STDs vary between 6 and 8 cm. As the two solutions were generated with different software packages and different approaches, the differences also give an impression of the orbit precision of the GNSS-only analysis which is at the one decimeter level.

As already mentioned, the elevation of the Sun above the orbital plane (β-angle) is high for interval A ($\beta \approx 64°$) whereas it is low for interval B ($\beta \approx 5°$). Offset as well as STD of the SLR residuals are larger for the time period with smaller β-angle. The behavior of the orbit fit RMS values is vice versa: the lower β-angle results

Laser Retroreflector Array (LRA) offset	No. of RPR param.	Sat.	2-d orbit fit RMS [mm]	3D orbit discont. [mm]	SLR residuals Mean [mm]	SLR residuals STD [mm]
Navarro-Reyes et al (2011)	5	IOV-1	45	222	−10	19
		IOV-2	48	238	−12	20
	9	IOV-1	23	70	1	13
		IOV-2	30	123	0	15
Navarro-Reyes et al (2011) shifted by +5 cm	5	IOV-1	29	79	3	19
		IOV-2	32	115	2	21
	9	IOV-1	21	61	2	16
		IOV-2	25	92	2	19

Tab. 9.5: Orbit quality of combined GNSS+SLR analysis based on 3-day arcs with different number of RPR parameters for time interval A.

in a better internal consistency. The differences between SLR validation and internal consistency are even more pronounced for the solutions with 9 RPR parameters: the SLR bias is increased by about 10 cm for period B compared to A whereas the orbit fit RMS values and DBDs are smaller by a factor of 3−4. These results provide evidence of a notable correlation between radiation pressure parameters and other estimation parameters (orbit parameters, phase ambiguities, satellite clocks). These inhibit a reliable estimation of the mean orbital radius, when solving for the harmonic once-per-rev components (sine/cosine terms in D- and Y-direction) of the RPR model of Beutler et al (1994).

9.3.2 Combined GNSS+SLR Analysis

GNSS and SLR observations are combined at the normal equation level. The orbit quality indicators of the combined GNSS+SLR orbits of time interval A are listed in the upper part of Table 9.5. For the solution with 5 RPR parameters, the systematic offset of the SLR residuals is reduced by almost a factor of five. However, it is still on the one centimeter level whereas it is almost zero for the solutions with 9 RPR parameters. In addition, the internal consistency of the combined 5 RPR parameter solution degrades compared to the GNSS-only solution. For the orbits with 9 RPR parameters the internal consistency improves significantly.

The systematic −5 cm bias of the solutions with 5 RPR parameters on the one hand and the degraded internal consistency of the GNSS-only orbits with 9 RPR parameters on the other hand were motivation for additional solutions where the radial offset value of the laser retroreflector array (LRA) as given in Navarro-Reyes et al (2011) is shifted by +5 cm. The results are listed in the lower part of Table 9.5. The internal consistency of all solutions with the shifted LRA offset improves compared to the original LRA offsets. In particular the consistency of the solution with 5RPR parameters is improved: one third for the orbit fit RMS values and more than a factor of two for the DBDs. The offset of the SLR residuals almost vanishes for the solution with 5 RPR parameters whereas the STD is almost the same. For the 9 parameter solution the offsets as well as the SLR STDs slightly increase. This could be an indicator that this type of solution is overparameterized.

Although the orbit quality improves when correcting for the IOV GNSS/SLR bias, its origin is not fully clear. However, parts of the bias could be explained by unmodeled effects in the orbit determination, namely Earth radiation pressure and antenna thrust. Rodriguez-Solano et al (2012) report a reduction of the orbit height of about 2 cm in the case of GPS if both effects are considered. For Galileo IOV an increased contribution of radiation thrust can be suspected compared to GPS in view of a larger transmit antenna power and a smaller spacecraft mass. Albedo effects, on the other hand, are considered to be of similar magnitude in view of similar effective area-to-mass ratios. However, a more detailed model of spacecraft properties and non-gravitational forces acting on the IOV satellites would be required to fully explain the observed GNSS/SLR offset.

9.4 Impact of Orbits on Satellite Clock Estimates

Radial orbit errors are highly correlated with the satellite clock estimates. Therefore, orbit errors are mapped to the clock estimates and are visible in the Allan Deviation (ADEV) used here for assessing the clock stability.

Therefore, the stability of the apparent clock will be used as a quality indicator for the orbits in this section. Two analysis periods were chosen in order to cover both clock types onboard the IOV satellites. In data arc A the RAFSs were active on both satellites, in data arc B the PHMs. The clock switches from the RAFSs to the PHMs took place on 16 and 23 July 2012 for IOV-1 and IOV-2, respectively. The discussion is focused on IOV-1 but IOV-2 in general shows a similar behavior.

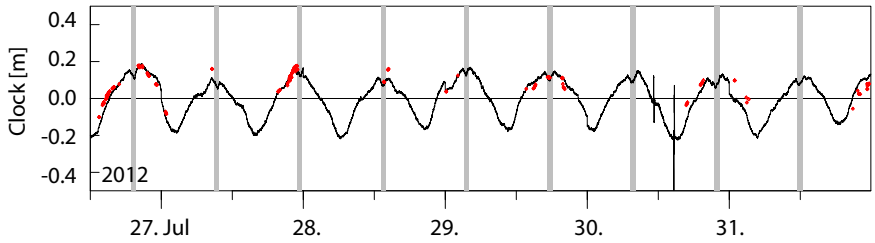

Fig. 9.5: Satellite clock residuals of IOV-1 GNSS-only solutions of time interval B. SLR residuals are indicated by red dots, eclipses by gray-shaded areas.

9.4.1 GNSS-only Analysis

The clock residuals of 3-day solutions with 5 RPR parameters as obtained from a concatenation of the middle days are shown in Fig. 9.5 for IOV-1. The clock datum is defined by a common reference clock (H-maser at Yellowknife, Canada) for all days and is taken from the CODE rapid solution. In a second step, offset and drift of the daily clock solutions are removed. A clear periodic signal with one Cycle-per-Revolution (CPR), referred to the orbit period of 14 h, and a peak-to-peak amplitude of almost 40 cm can be seen in the clock residuals.

In addition, the SLR orbit residuals are plotted as red dots in Fig. 9.5. They show a high correlation with the clock residuals indicating that the periodic signal in the clock residuals is an artifact from errors in the orbit determination. Montenbruck et al (2012) already showed the same effect for GIOVE-B but with slightly smaller amplitude. No periodic signal can be seen in the clock residuals of analysis period A with a high β-angle (not shown here). This suggests that the periodic signal only occurs for low β-angles like in analysis period B. While it is tempting to conclude the absence of 1-CPR signals during the A period is consistent with lower orbit errors linked to high β-angles, it is not possible to confirm this due to the instability of the RAFS clocks. Complementary investigations during periods with PHM use at high β-angle are therefore required for a full characterization of 1-CPR errors in the Galileo IOV orbit determination.

Figure 9.6 shows ADEVs computed from concatenated clocks for both, IOV-1 and IOV-2, as well as the RAFSs and the PHMs of analysis period A and B based on 3-day arcs with 9 RPR parameters. For data arc B the 1-CPR

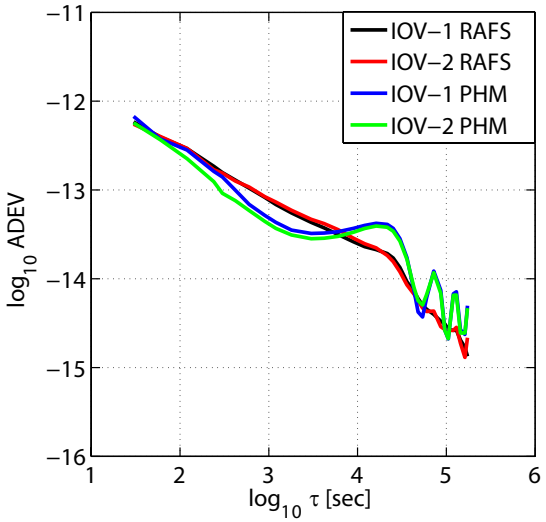

Fig. 9.6: Allan deviations of for data arc A (RAFS) and B (PHM) from GNSS-only analysis.

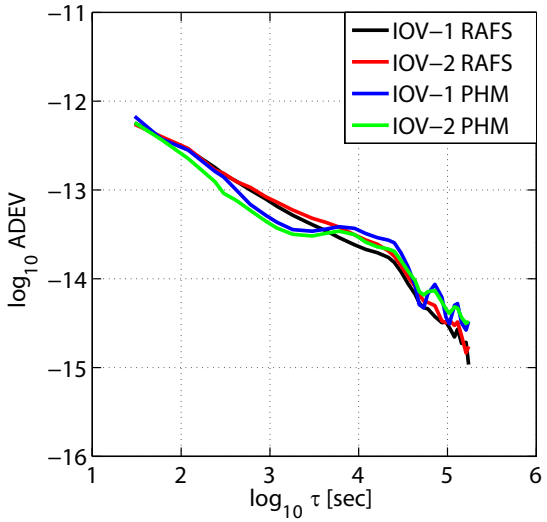

Fig. 9.7: Allan deviations for data arc A (RAFS) and B (PHM) from combined GNSS+SLR analysis.

harmonics cause a pronounced bump with a local maximum of $4 \cdot 10^{-14}$ near 7 h, i.e. half of the orbital period. Thereafter, steep minima are attained at the orbital period of approximately 52,000 s and multiple integers thereof, which clearly reflects the presence of 1-CPR clock variations. The absence of the bump and the minima in the ADEVs of the RAFSs is probably related to the large β-angle during the RAFS analysis period resulting in less pronounced orbit errors and associated 1-CPR variations in the apparent clock solution.

9.4.2 Combined GNSS+SLR Analysis

The ADEVs of clock solutions derived from a combined processing of GNSS and SLR measurements with 9 RPR parameters are shown in Fig. 9.7. Interestingly, the bump at approximately 7hours has decreased from $4 \cdot 10^{-14}$ in case of the GNSS-only solutions to $2.7 \cdot 10^{-14}$ in case of the combined solution. As the SLR data have a strong contribution to the combined orbit and due to the fact that the bump gets much smaller in case of the combined solution it can be stated that the bump at half of the orbital period is mainly caused by deficits in orbit modeling. For the RAFSs the impact of the combination is much smaller as no pronounced bump in the ADEVs is present due to the high β-angle.

Figures 9.8 (a) and (b) show clock and SLR residuals as in Fig. 9.5 but derived from GNSS *and* SLR observations with 5 and 9 RPR parameters, respectively. In case of 5 RPR parameters in Fig. 9.8 (a) the pronounced 1-CPR signal of the GNSS-only solution has vanished but the residuals are now dominated by a 3-CPR signal evidencing small remaining orbit modeling errors. In case of the 9 RPR parameter solutions in Fig. 9.8 (b), the 1-CPR signal is still present although its amplitude is slightly reduced by including the SLR observations. However, the correlations of the SLR residuals with the clock residuals are reduced compared to Fig. 9.5.

Figures 9.8 (c) and (d) demonstrate the impact of the shifted LRA offset on the clock and SLR residuals. The periodic variations have almost vanished for the solution with 5 RPR parameters in Fig. 9.8 (c) indicating that this type of solution provides the best quality of the solutions discussed up to now. Contrary to the 5 RPR parameter solution, the clock and SLR residual behavior of the solution with 9 RPR parameters is almost unaffected when changing the LRA offset. This means that the impact of the biased LRA offset is almost completely absorbed by the estimated RPR parameters, in particular the sine/cosine terms that are not estimated within the 5 RPR parameter solution.

The impact of shifting the LRA offset by 5 cm on the ADEVs of the clocks determined from combined GNSS+SLR observations is shown in Fig. 9.9. Whereas changing the LRA offset has almost no impact on the solution with 9 RPR parameters, the ADEVs of the 5 RPR parameter solutions get significantly flatter. Therefore, the bumps in the other solution types are an effect of degraded orbit determination accuracy and the GNSS+SLR solution with 5 RPR parameters and biased LRA offset provides the best upper bound for the true stability of the PHM. Thermal instabilities as observed for GIOVE-A (ESA, 2011) are definitely smaller than this bound.

9.4.3 Impact of Clock Constraints

Usually satellite clock parameters are either eliminated by forming double differences or they are estimated as independent epoch-wise parameters in an undifferenced analysis. Highly stable clocks like the PHMs of the IOV satellites allow revisiting this strategy. Weinbach and Schön (2013) already showed that modeling the GRACE ultra-stable oscillator with a 60 s piece-wise linear function improves the quality of the satellite orbits by up to 40%, in particular in radial direction. The clock behavior can also be modeled by a polynomial or constraints with respect to a simple a priori model could by applied. We use a linear clock model (offset and drift) as a priori model, estimate epoch-wise clock corrections, and apply absolute constraints with different weights. Absolute constraints are introduced to the normal equation system as pseudo-observations P_i for parameter i with the weight $P_i = \sigma_0^2/\sigma_i^2$. The symbol σ_0 denotes the a priori weight of GNSS phase observations (set to 1 mm) and σ_i is the weight for the constraints.

Table 9.6 lists the orbit quality criteria of IOV-1 for 3-day arcs with 9 RPR parameters for an unconstrained solution and solutions with clock constraints between 30 and 0.1 ps. The internal consistency of the orbits gets worse when applying clock constraints. However, the SLR offset as well as residuals improve and show the best performance for clock constraints of 3 ps.

Based on the orbits obtained with clock constraints, unconstrained clock solutions were estimated to assess the orbit quality. The Allan deviations of these clocks in Fig. 9.10 clearly show the impact of the clock constraints on the orbit-related 1-CPR term and its harmonics. Whereas it is pronounced for the unconstrained solution,

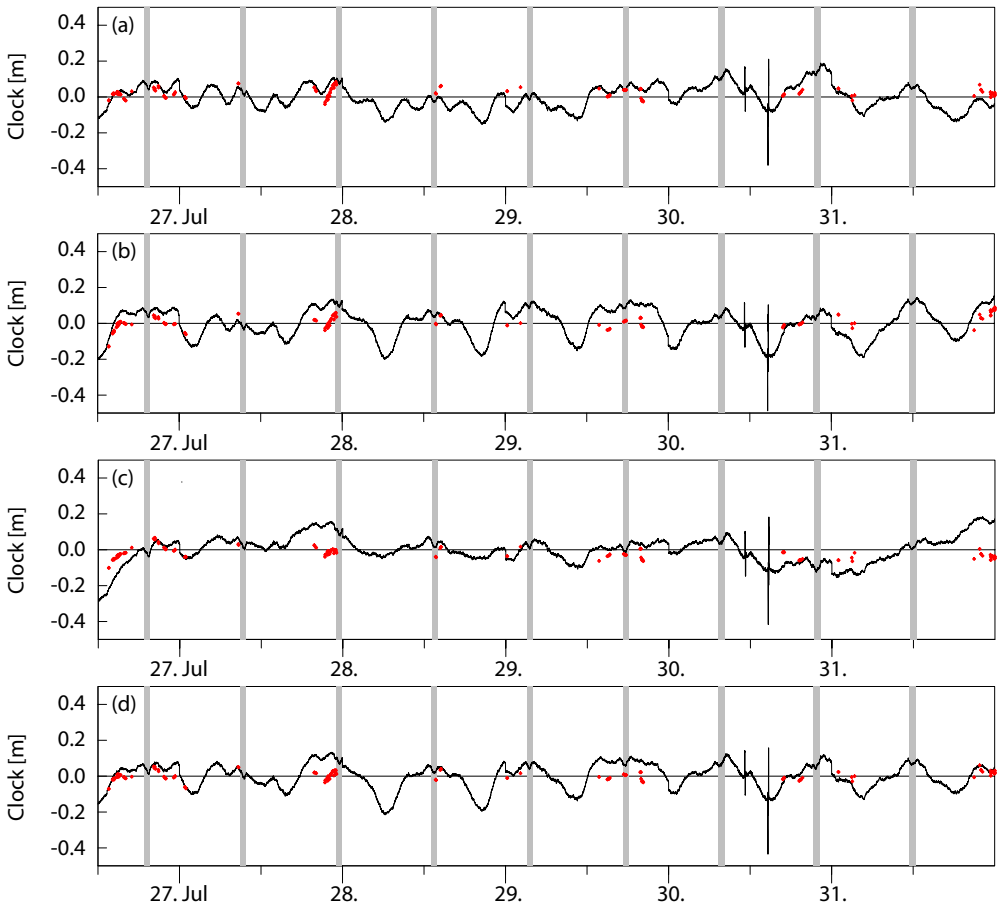

Fig. 9.8: Satellite clock residuals of IOV-1 combined GNSS+SLR solutions of data arc B: (a) original LRA offset with 5 RPR parameters; (b) original LRA offset with 9 RPR parameters; (c) shifted LRA offset with 5 RPR parameters; (d) shifted LRA offset with 9 RPR parameters. SLR residuals (computed − observed) are indicated by red dots, eclipses by gray-shaded areas.

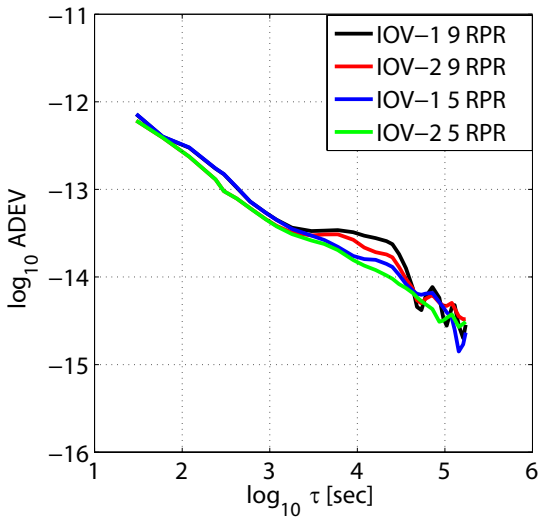

Fig. 9.9: Allan deviations for data arc B (PHM) from combined GNSS+SLR analysis with the LRA offset shifted by +5 cm.

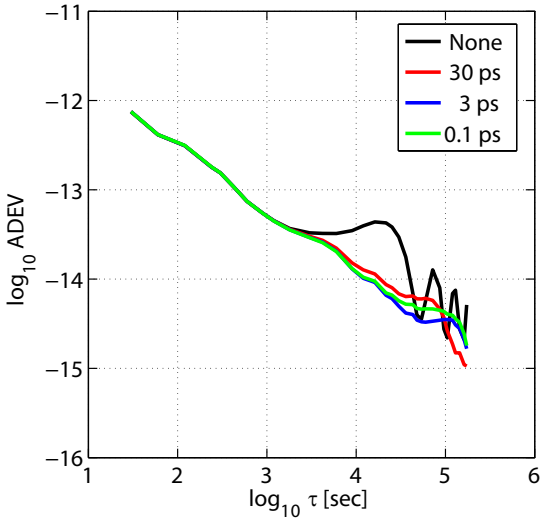

Fig. 9.10: Allan deviations of GNSS-only solutions with different clock constraints applied in the orbit determination as given in Table 9.6.

the 1-CPR bump vanishes when applying clock constraints in the orbit determination and the solution with 3 ps constraints shows the best performance.

Clock constr. [ps]	2-d orbit fit RMS [mm]	3D Orbit Discont. [mm]	SLR residuals Offset [mm]	SLR residuals STD [mm]
none	15	19	−118	77
30.0	24	110	−67	36
3.0	19	159	−43	34
0.1	35	223	−32	37

Tab. 9.6: Impact of clock constraints on GNSS-only orbits. Results of 3-day arcs with 9 RPR parameters for analysis period B are given.

9.5 Conclusions

The 3D accuracy and precision of the Galileo IOV orbits determined with a network of 24 multi-GNSS stations is at the one decimeter level. For comparison, representative consistencies at the few decimeter level have been achieved within the early days of GPS among the various IGS analysis centers (Kouba and Mireault, 1996). As such slightly better performance is achieved for Galileo today using networks of comparable size and float ambiguity estimation. However, the Galileo orbits determined with GNSS-only observations suffer from systematic 1-CPR effects visible in the ADEVs of the clock estimates as well as systematic biases in the SLR residuals. In addition, the biases depend on the elevation of the Sun above the orbital plane. These errors can be mitigated by a combination with SLR observations or by applying satellite clock constraints with respect to a linear model. As the internal consistency is significantly degraded by the combination with SLR due to the systematic GNSS/SLR bias of −5 cm in case of the 5 RPR parameter solution, the LRA offset was shifted by +5 cm to compensate for this bias. As a consequence, the most stable clock results could be achieved by estimating 5 RPR parameters from GNSS and SLR observations with this modified LRA offset. The orbit improvements by including SLR observations emphasize deficiencies in the GNSS-only orbit determination. In the near future, the orbit determination might benefit from a denser Galileo tracking network and an increased number of Galileo satellites allowing for an ambiguity fixing and thus providing a stabilization of the equation system. In addition concise information on attitude control as well as the antenna phase center variations and offsets from the satellite provider would be useful to overcome current deficiencies in the orbit modeling due to lack of information.

Galileo IOV orbit and clock products are provided within the IGS MGEX project. They are available at the IGS data centers, e.g., at `ftp://cddis.gsfc.nasa.gov/pub/gps/products/mgex/`.

Acknowledgements

We would like to thank all local CONGO station hosts for their support. The International GNSS Service (IGS) is acknowledged for providing Galileo observation data in the framework of its Multi-GNSS Experiment (MGEX).

Bibliography

Appleby G, Otsubo T (2000) Comparison of SLR measurements and orbits with GLONASS and GPS microwave orbits. In: 12th International Workshop on Laser Ranging, Matera, November 13 – 17

Bar-Sever YE (1996) A new model for GPS yaw attitude. Journal of Geodesy 70(1):714–723, DOI 10.1007/BF00867149

Becker M, Zeimetz P, Schönemann E (2010) Antenna chamber calibrations and antenna phase center variations for new and existing GNSS signals. In: IGS Workshop 2010, 28 June – 2 July 2010, Newcastle

Beutler G, Brockmann E, Gurtner W, Hugentobler U, Mervart L, Rothacher M, Verdun A (1994) Extended orbit modeling techniques at the CODE processing center of the international GPS service for Geodynamics (IGS): theory and initial results. Manuscripta Geodaetica 19:367–386

Chiarini JC, Mathew C, Honold HP, Smith D (2008) A Satellite for the Galileo Mission. In: Del Re E, Ruggieri M (eds) Satellite Communications and Navigation Systems, Signals and Communication Technology, Springer, pp 109–132, DOI 10.1007/978-0-387-47524-0_9

Dach R, Hugentobler U, Fridez P, Meindl M (eds) (2007) Bernese GPS Software Version 5.0. Astronomical Institute, University of Bern, Bern, Switzerland

Dach R, Brockmann E, Schaer S, Beutler G, Meindl M, Prange L, Bock H, Jäggi A, Ostini L (2009) GNSS processing at CODE: status report. Journal of Geodesy 83(3-4):353–365, DOI 10.1007/s00190-008-0281-2

Dow JM, Neilan RE, Rizos C (2009) The International GNSS Service in a changing landscape of Global Navigation Satellite Systems. Journal of Geodesy 83(3-4):191–198, DOI 10.1007/s00190-008-0300-3

ESA (2011) GIOVE Experimentation Results: A Success Story. Tech. Rep. SP-1320, European Space Agency, Noordwijk

Flohrer C (2008) Mutual validation of satellite-geodetic techniques and its impact on GNSS orbit modeling. vol 75, Swiss Geodetic Commission, Zürich, Switzerland

García Á, Píriz R, Fernández V, Navarro-Reyes D, González F, Hahn J (2008) GIOVE orbit and clock determination and prediction: Experimentation Results. In: Proceedings of ENC GNSS 2008

Ge M, Gendt G, Rothacher M, Shi C, Liu J (2007) Resolution of GPS carrier-phase ambiguities in Precise Point Positioning (PPP) with daily observations. Journal of Geodesy 82(7):389–399, DOI 10.1007/s00190-007-0187-4

Gendt G, Altamimi Z, Dach R, Söhne W, Springer T, The GGSP Prototype Team (2011) GGSP: Realisation and maintenance of the Galileo Terrestrial Reference Frame. Advances in Space Research 47(2):174–185, DOI 10.1016/j.asr.2010.02.001

Gurtner W, Estey L (2009) RINEX, The Receiver Independent Exchange Format, Version 3.01. Tech. rep., available at ftp://ftp.igs.org/pub/data/format/rinex301.pdf

Hahn J, González F, Waller P, Navarro-Reyes D, Piriz R, Mozo A, Fernandez V, Cueto M, Tavella P, Sesia I (2007) GIOVE-A apparent clock assessment and results. In: 39th Annual Precise Time and Time Interval (PTTI) Meeting, pp 95–114

Hidalgo I, Mozo A, Navarro P, Piriz R, Navarro-Reyes D (2008a) Use of SLR observations to improve GIOVE-B orbit and clock determination. In: Schilliak S (ed) Proceedings of the 16th International Workshop on Laser Ranging, Space Research Centre, Polish Academy of Sciences, vol 2, pp 71–84, available at http://cddis.gsfc.nasa.gov/lw16/docs/papers/sci_1_Hidalgo_p.pdf

Hidalgo I, Piriz R, Mozo A, Tobias G, Tavella P, Sesia I, Crerretto G, Waller P, González F, Hahn J (2008b) Estimation and prediction of the GIOVE clocks. In: 40th Annual Precise Time and Time Interval (PTTI) Meeting, pp 361–374

Kirchner M, Schmidt R, Vilzmann J (2009) Results of GIOVE data processing to allow evaluation of principal system performance drivers. In: Proceedings of the European Navigation Conference – Global Navigation Satellite Systems, Naples, Italy, May 3 – 6

Kouba J (2009) A simplified yaw-attitude model for eclipsing GPS satellites. GPS Solutions 13(1):1–12, DOI 10.1007/s10291-008-0092-1

Kouba J, Mireault Y (1996) IGS analysis coordinator report. In: International GPS Service for Geodynamics 1995 Annual Report, Jet Propulsion Laboratory, Pasadena, pp 45–76

Meindl M, Schaer S, Hugentobler U, Beutler G (2003) Tropospheric Gradient Estimation at CODE: Results from Global Solutions. In: International Workshop on GPS Meteorology

Montenbruck O, Hauschild A, Hessels U (2010) Characterization of GPS/GIOVE sensor stations in the CONGO network. GPS Solutions 15(3):193–205, DOI 10.1007/s10291-010-0182-8

Montenbruck O, Steigenberger P, Schönemann E, Hauschild A, Hugentober U, Dach R, Becker M (2012) Flight Characterization of New Generation GNSS Satellite Clocks. Navigation, Journal of the Institute of Navigation 59(4):291–302

Navarro-Reyes D, Gonzalez F, Svehla D, Zandbergen R (2011) ILRS SLR Mission Support Request for Galileo-101 and Galileo-102. Available at http://ilrs.gsfc.nasa.gov/docs/ILRS_MSR_Galileo_201106.pdf

Niell A (1996) Global mapping functions for the atmosphere delay at radio wavelengths. Journal of Geophysical Research 101(B2):3227–3246, DOI 10.1029/95JB03048

Pavlis E (2009) SLRF2008: The ILRS reference frame for SLR POD contributed to ITRF2008. In: 2009 Ocean Surface Topography Science Team Meeting, Seattle

Pavlis E, Beard R (1996) The Laser Retroreflector Experiment on GPS-35 and 36. In: Beutler G, Hein G, Melbourne W, Seeber G (eds) GPS trends in precise terrestrial, airborne and spaceborne applications, Springer, Berlin, Heidelberg, New York, International Association of Geodesy Symposia, vol 115, pp 154–158, ISBN: 3-540-60872-9

Pearlman M, Degnan J, Bosworth J (2002) The International Laser Ranging Service. Advances in Space Research 30(2):125–143, DOI 10.1016/S0273-1177(02)00277-6

Rebischung P, Griffiths J, Ray J, Schmid R, Collilieux X, Garayt B (2012) IGS08: the IGS realization of ITRF2008. GPS Solutions 16(4):483–494, DOI 10.1007/s10291-011-0248-2

Rizos C, Montenbruck O, Weber R, Weber G, Neilan R, Hugentobler U (2013) The IGS MGEX experiment as a milestone for a comprehensive multi-GNSS service. In: ION PNT 2013, pp 289–295

Robertson G, Kieffer R (2009) GIOVE-B Satellite Design and Performance Validation. In: ION GNSS 2009, pp 3008–3016

Rodriguez-Solano C, Hugentobler U, Steigenberger P (2012) Impact of albedo radiation on GPS satellites. In: Geodesy for Planet Earth, Springer, International Association of Geodesy Symposia, vol 136, pp 113–119, DOI 10.1007/978-3-642-20338-1_14

Rooney E, Unwin M, Gatti G, Falcone M, Binda S, Malik M, Hannes D (2007) Giove-A in orbit testing results. In: ION GNSS 2007, pp 467–477

Schönemann E, Springer T, Otten M, Becker M, Dow J (2007) GIOVE-A precise orbit determination from microwave and satellite laser ranging data – first perspectives for the Galileo constellation and its scientific use. In: Proceedings of the First Colloquium on Scientific and Fundamental Aspects of the Galileo Programme 2007, Toulouse, France, October 1 – 4, available at http://ilrs.gsfc.nasa.gov/docs/2007_Schoenemann_Toulouse_paper.pdf

Schönemann E, Springer TA, Otten M, Becker M (2009) Where is GIOVE-A exactly? GPS World 20(7):42–50

Steigenberger P, Hugentobler U, Montenbruck O, Hauschild A (2011) Precise orbit determination of GIOVE-B based on the CONGO network. Journal of Geodesy 85(6):357–365, DOI 10.1007/s00190-011-0443-5

Steigenberger P, Hauschild A, Montenbruck O, Hugentobler U (2013a) Galileo, Compass und QZSS: Aktueller Stand der neuen Satellitennavigationssysteme. zfv 138(1):53–59

Steigenberger P, Rodriguez-Solano C, Hugentobler U, Hauschild A, Montenbruck O (2013b) Orbit and clock determination of QZS-1 based on the CONGO network. Navigation, Journal of the Institute of Navigation 60(1):31–40, DOI 10.1002/navi.27

Uhlemann M, Ramatschi M, Gendt G (2012) GFZ's global multi-GNSS network and first data processing results. In: IGS Workshop 2012

Urschl C, Gurtner W, Hugentobler U, Schaer S, Beutler G (2005) Validation of GNSS orbits using SLR observations. Advances in Space Research 36(3):412–417, DOI 10.1016/j.asr.2005.03.021

Urschl C, Beutler G, Gurtner W, Hugentobler U, Schaer S (2007) Contribution of SLR tracking data to GNSS orbit determination. Advances in Space Research 39(10):1515–1523, DOI 10.1016/j.asr.2007.01.038

Urschl C, Beutler G, Gurtner W, Hugentober U, Ploner M (2008) Orbit determination for GIOVE-A using SLR tracking data. In: Luck J, Moore C, Wilson P (eds) Extending the Range, Proceedings of the 15th International Workshop on Laser Ranging, pp 40–46

Waller P, Gonzalez F, Binda S, Rodriguez D, Tobias G, Cernigliaro A, Sesia I, Tavella P (2010) Long-term performance analysis of GIOVE clocks. In: Proceedings of the 42nd Annual Precise Time and Time Interval Meeting, pp 171–179

Weber R (2012) IGS GNSS Working Group. In: Meindl M, Dach R, Jean Y (eds) International GNSS Service Technical Report 2011, Jet Propulsion Laboratory, Pasadena, pp 159–163

Weinbach U, Schön S (2013) Improved GRACE kinematic orbit determination using GPS receiver clock modeling. GPS Solutions 17(4):511–520, DOI 10.1007/s10291-012-0297-1

Wu J, Wu S, Hajj G, Bertiger W, Lichten S (1993) Effects of antenna orientation on GPS carrier phase. Manuscripta Geodaetica 18:91–98

10 Signal, Orbit and Attitude Analysis of Japan's First QZSS Satellite Michibiki

Originally published as:

Hauschild A., Steigenberger P., Rodriguez-Solano C. (2012): Signal, orbit and attitude analysis of Japan's first QZSS satellite Michibiki, GPS Solutions, Vol. 16, Nr. 1, pp 127-133, doi: 10.1007/s10291-011-0245-5

The final publication is available at Springer via `http://dx.doi.org/10.1007/s10291-011-0245-5`.

Abstract

Results are presented for Michibiki, the first satellite of Japan's Quasi-Zenith Satellite System. Measurements for the analysis have been collected with five GNSS tracking stations in the service area of QZSS, which track five out of the six signals transmitted by the satellite. The analysis discusses the carrier-to-noise density ratio as measured by the receiver for the different signals. Pseudorange noise and multipath are evaluated with dual-frequency and triple-frequency combinations. QZSS uses two separate antennas for signal transmission, which allows the determination of the yaw-orientation of the spacecraft. Yaw-angle estimation results for an attitude mode switch from yaw-steering to orbit normal orientation are presented. Estimates of differential code biases between QZSS and GPS observations are shown in the analysis of the orbit determination results for Michibiki. The estimated orbits are compared to the broadcast ephemerides and their accuracy is assessed with overlap comparisons.

10.1 Quasi-Zenith Satellite System Overview and Tracking Network

Japan's Quasi-Zenith Satellite System (QZSS) is a regional augmentation system, which provides GPS compatible signals as well as integrity information and differential corrections. The first satellite Michibiki, or QZS-1, has been launched on September 11, 2010 and is depicted in Fig. 10.1. The complete constellation will consist of three satellites with a common ground path. The geosynchronous, inclined, elliptical orbits are designed to provide extended visibility periods of the satellite with high elevation angles over Japan. The first main objective of the new constellation is the availability enhancement of positioning solutions in challenging environments like urban canyons. For this purpose, the QZSS satellites offer four signals (C/A, L1C, L2C, and L5), which are interoperable with GPS and allow for the combined processing of both systems. The second objective is the enhancement of the real-time navigation accuracy and reliability. Two dedicated signals of QZSS provide integrity and correction information. The Submeter-class Augmentation with Integrity Function (SAIF) signal is broadcast on L1 from a dedicated transmit antenna onboard the satellite. It contains wide area differential correction data (Kishimoto et al, 2011). The L-Band Experimental (LEX) signal is broadcast at the center frequency of the Galileo E6 frequency (1278.75 MHz) and contains high-precision corrections for GPS satellite clock and orbit errors, tropospheric and ionospheric delays (Kishimoto et al, 2011; Saito et al, 2011).

A subset of receivers of the Cooperative Network for GIOVE Observation (CONGO; Montenbruck et al, 2011) has been upgraded shortly after the first signals have been emitted by QZS-1. The stations are located in Chofu, Japan (CHOF), Singapore (SING), Sydney, Australia (UNSX), Maui, Hawaii (MAHO), and Papeete, Tahiti (THTX). All sites are equipped with Javad TRE-G3TH receivers and are connected to geodetic antennas. The receivers are able to track GPS, GLONASS, GIOVE, SBAS, and QZSS signals. For the latter, all signals except for LEX are supported. The analysis provided is based on measurements from the five CONGO stations.

Fig. 10.1: Michibiki (or QZS-1), the first QZSS satellite (imagery courtesy: JAXA)

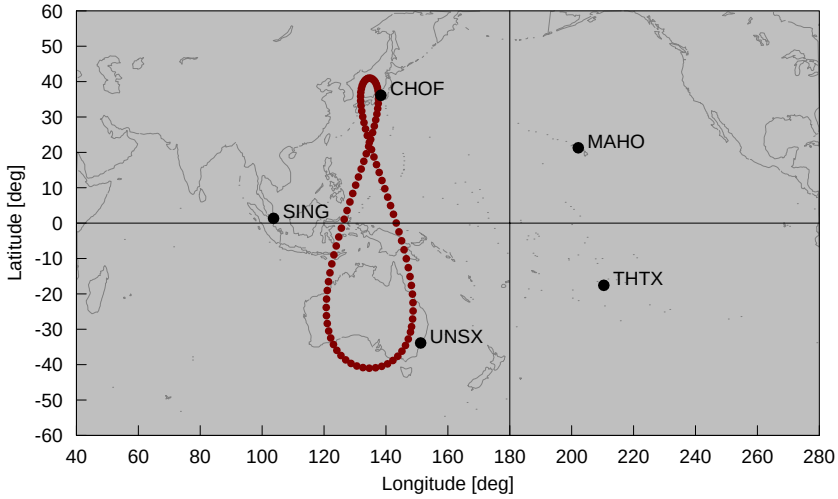

Fig. 10.2: Tracking stations of the CONGO network with QZSS tracking capabilities. The ground track of QZSS is indicated as a dotted line with a step size of 15 minutes.

10.2 Carrier-to-Noise Density Ratio

Figure 10.3 depicts the carrier-to-noise density ratio (C/N0) for QZS-1 and GPS as a function of satellite elevation as measured by the TRE-G3TH receiver in Chofu, Japan. Measurements for a period of three days from July 8-10, 2011, have been used. Only the first Block IIF satellite SVN62 and all Block IIR-M satellites except for SVN49 have been included in this analysis. It becomes obvious that the C/A code signals of GPS are approximately $4-5$ dB more powerful than the signal of QZS-1 over the entire elevation range. A similar result is found for L5, where the curve for GPS is about 2 dB higher compared to QZSS. It should be noted at this point that SVN62 is the only satellite contributing to L5 for GPS. The carrier-to-noise density ratio for L2C, on the other hand, has a comparable level for both systems at low to medium elevation angles. However, close to zenith the received signal for QZSS is approximately $1.5-2$ dB less powerful compared to GPS. Since the QZSS signals are GPS-compatible signals, the attenuations and amplifications in the antenna and the receiver are identical to GPS. Therefore, the differences in the C/N0 levels for QZSS and GPS result from actual differences in the power level or transmit antenna gain pattern at the satellite. It is furthermore interesting to note, that due to the high eccentricity of the QZSS orbit, the orbit height differs by approximately 6300 km between apogee over the northern hemisphere and perigee over the southern hemisphere. Correspondingly, the path loss for the satellite at zenith changes from 161.27 dB/m^2 at perigee to 162.81 dB/m^2 at apogee. As a result, receivers tracking QZS-1 at zenith in the southern hemisphere receive higher signal power than receivers in the northern hemisphere under the same tracking conditions. However, this orbit design is advantageous for users in Japan, since the satellite remains longer in the northern hemisphere than in the southern hemisphere.

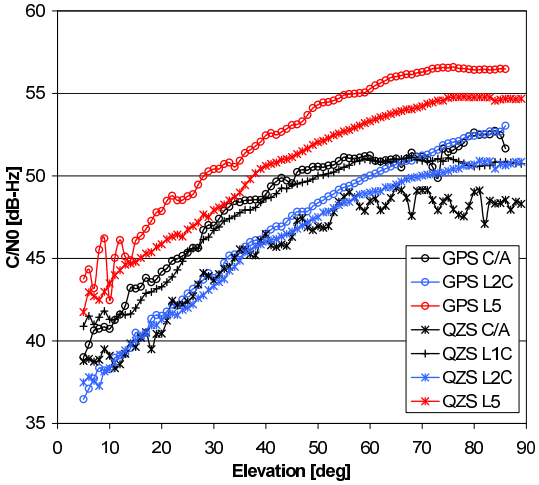

Fig. 10.3: Carrier-to-noise density ratios as a function of satellite elevation for a TRE-G3TH receiver connected to a Trimble Zephyr Geodetic 2 antenna (station CHOF) for GPS and QZSS L1 (black), L2 (blue), and L5 (red) signals for a 3-day period from July 8 – 10, 2011. Satellites contributing to GPS data are limited to the first Block-IIF satellite SVN62 and the Block IIR-M satellites except for SVN49.

10.3 Noise and Multipath Analysis

For the analysis of pseudorange noise and multipath errors, the multipath (MP) combination (Kee and Parkinson, 1994) is computed from

$$\mathrm{MP}_A = \rho_A - (\alpha + 1) \cdot \phi_A + \alpha \cdot \phi_B + b \quad \text{with } \alpha = \frac{2 \cdot f_B^2}{f_A^2 - f_B^2} \tag{10.1}$$

where MP_A is the code multipath of the signal A, ρ_A and ϕ_A are pseudorange and carrier phase on signal A, ϕ_B is a carrier phase on signal B, and b is a bias. The corresponding frequencies are f_A and f_B. This combination eliminates all errors except for receiver noise, multipath errors, and bias variations from the pseudorange observation. Results of the MP combination of C/A, L1C, L2C, and L5 for the station in Sydney (UNSX) and Chofu (CHOF) are depicted in Fig. 10.4. The station UNSX is equipped with a TRE-G3TH receiver and a Leica AR25.R3 antenna. CHOF uses the same receiver but a Trimble Zephyr Geodetic 2 antenna. The plots show the standard deviation of the multipath combination over satellite elevation. The MP combination of signals on L1 has been formed with the carrier phase from L2, the L2C and L5 MP combinations have been formed with carrier phase from L1. QZS-1 and all GPS satellites except for SVN49 (PRN01) have been used in this analysis.

It becomes obvious that the L5 signals for QZSS exhibit the lowest noise and multipath errors for both stations. This superior performance could be suspected since the L5 signal has the highest chip rate with 10.23 Mbps and is therefore least susceptible to multipath. The standard deviation is on the order of 5 cm or less for high elevation angles. In comparison, the GPS L5 multipath and receiver noise are significantly larger for both receivers. This is an unexpected result, since both signals are interoperable and should yield the same multipath performance. However, it must be kept in mind that the statistics for the GPS L5 multipath combination are based on the observations from a single Block IIF satellite only, which is obviously affected by higher multipath compared to Michibiki. For the L2C signal, the multipath performance for GPS and QZSS is comparable for both stations. The standard deviation reaches a level of 10 cm for high elevations in both cases. However, at elevation angles of less than 10° the station in Chofu seems to be affected by higher multipath and noise. The C/A code signals for GPS and QZSS also exhibit comparable performance. At Chofu, the multipath and receiver noise for QZSS C/A is approximately 60 cm at 5° elevation and about 15 cm at zenith. GPS C/A code has a similar performance at 5° elevation but exceeds QZSS for higher elevation angles and reaches a level of 10 cm at zenith. At UNSX, the errors are smaller compared to CHOF at low elevation angles. For higher elevation angles both GPS and QZSS reach a level of 15 cm. It is interesting to note that L1C, which is only available for QZSS, has a superior performance at both stations compared to the C/A code signals.

Figure 10.5 depicts a triple-frequency combination of the C/A, L2C, and L5 pseudorange and carrier phase measurements of QZS-1 over a period of one week. The combination used for this plot is equivalent to the difference of the Ionosphere-free (IF) combination of C/A code and L2C and the IF combination of C/A code

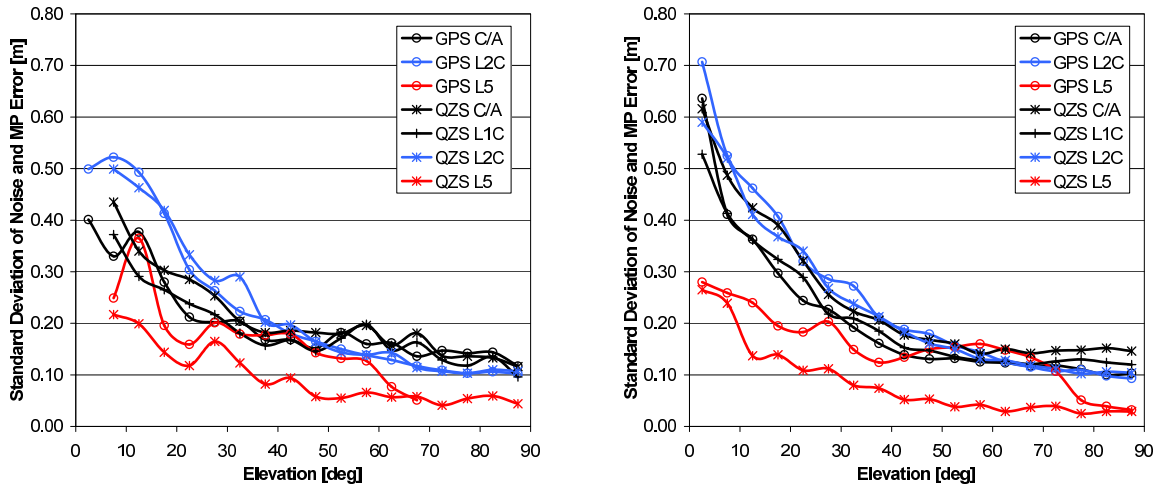

Fig. 10.4: Standard deviation of the noise and multipath error of the multipath combination for GPS and QZSS signals for station UNSX (left plot) and CHOF (right plot). Observations from a period of 5 days from July 13 – 17, 2011, have been used. For GPS, all satellites except for SVN49 (PRN01) are used. Note that only SVN62 (PRN25) contributes to the GPS L5 signal.

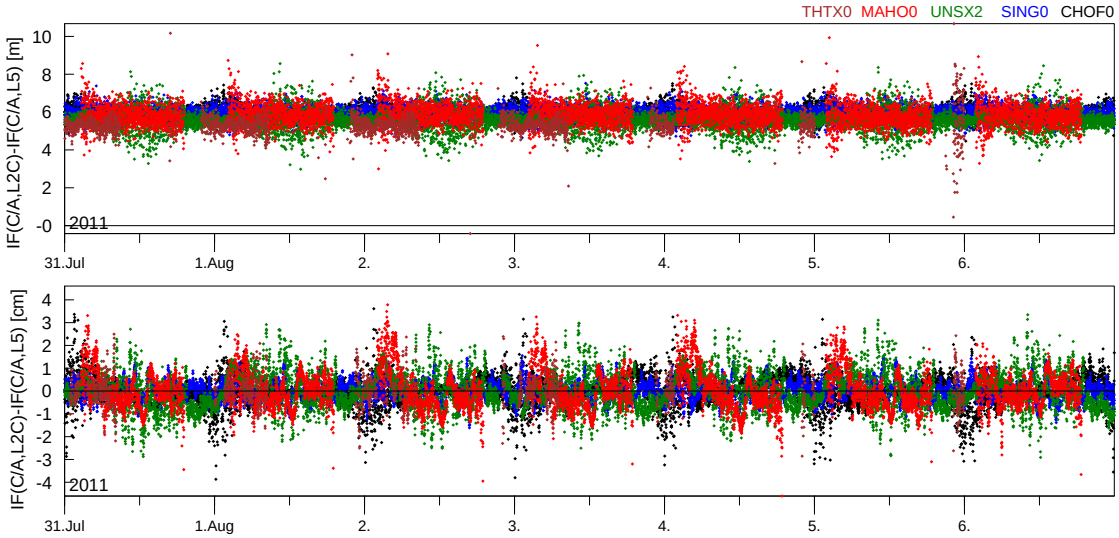

Fig. 10.5: Triple-frequency combination of QZSS pseudoranges (top) and carrier phases (bottom) for a period of one week from July 31 to August 6, 2011.

and L5. It eliminates all effects due to geometry, clock offsets, troposphere, and ionosphere (Montenbruck et al, 2012). The top plot in Fig. 10.5 shows the combination of the pseudorange observables of all five CONGO stations supporting QZSS. The triple-frequency code combinations for all stations are offset by roughly 6 m with small difference between the individual stations. This offset is due to code biases of the individual signals, which do not cancel out. Even though all stations use identical receivers and firmware, the differences in the linear combination of code biases can be explained from different cabling and amplifiers. The bottom plot depicts the combination of carrier phase observations, where the linear combination of ambiguities has been removed for each pass. The higher resolution of the carrier phase makes systematic variations visible, which exhibit a daily repeatability and are uncorrelated between the stations. These effects are most prominent for the station MAHO at noon of each day. A possible explanation for the variations is a change in receiver line biases over time. However, the daily repeatability also suggests carrier phase multipath effects, since the QZSS satellite has basically identical observation geometry for each pass. The triple-frequency pseudorange and carrier phase combinations do not exhibit obvious systematic variations, which are correlated among the receivers. It can therefore be concluded, that satellite dependent line-biases have a sufficient stability to not exceed errors like multipath and receiver noise.

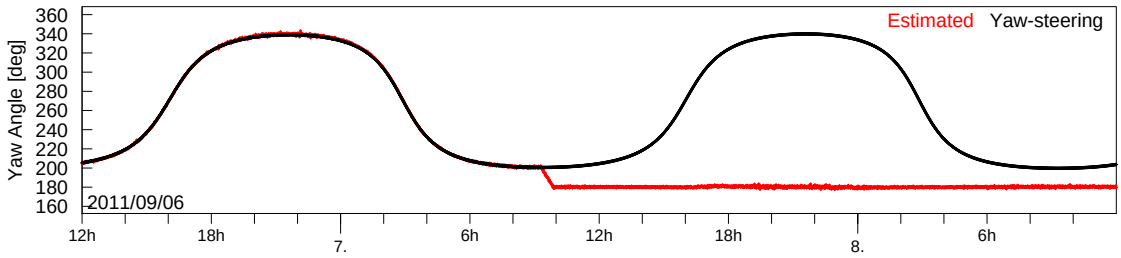

Fig. 10.6: Estimated (red) and modeled (black) yaw attitude of QZS-1 for a 48 hour period centered at September 7, 2011. The attitude mode switch from yaw-steering to orbit-normal orientation starts at 09:20 h UTC on September 7.

10.4 Yaw-Attitude Profile

The SAIF signal has not been considered in the previous analysis, since it is intended as a signal with correction data rather than a ranging signal. Its dedicated antenna is mounted with an offset of about 1.34 m with respect to the main antenna. This feature can be exploited to estimate the yaw-attitude of Michibiki. The method is essentially an inversion of the GNSS-based attitude determination problem, where the orientation of a baseline between two antennas on the ground is estimated using differential measurements from different satellites. In this case, the baseline between the L-band main antenna and the SAIF antenna is estimated based on differences between SAIF and C/A (or L1C) carrier phase observation from different stations (Hauschild et al, 2011).

Contrary to GPS and GLONASS, QZSS uses two different attitude modes depending on the sun's elevation angle β with respect to the orbital plane. For $|\beta| > 20°$, the standard yaw-steering attitude profile is used. In this mode, the satellite's body-fixed z-axis points toward the center of the Earth and the satellite is rotated such that the solar panels are oriented normally to the sun vector (Bar-Sever, 1996). However, for $|\beta| < 20°$ the satellite switches to orbit normal orientation, in which the solar panel axis is oriented normally to the orbital plane and the body-fixed z-axis points towards the Earth (Inaba et al, 2009). Using a different attitude mode for small β eliminates the need to rotate the spacecraft with high yaw-rates, which can exceed the maximal possible hardware yaw-rate if β is close to zero. However, the different attitude modes must be taken into account when processing carrier phase observations of QZSS for high-precision applications. Otherwise the phase wind-up effect can lead to inconsistencies between the observed and modeled carrier phases if an improper attitude model is used. Moreover, the SLR reflector array is not aligned with the center of mass of the satellite, such that attitude errors would appear in the residuals of SLR measurements. Figure 10.6 depicts the yaw angle corresponding to yaw-steering mode in black together with estimated values in red over a time period of 48 hours. During this period, a switch from yaw-steering to orbit-normal attitude takes place at about 09:20 h GPST on September 7, 2011. It is interesting to note that the switch already starts when β is at approximately 20.59°. The threshold of 20° is not reached until 01:20 h GPST on the following day.

The reason for performing the maneuver prior to exceeding the threshold is immediately obvious, since the satellite is closest to its final orientation at this point in time. Similar results have also been found for yaw attitude estimations during the entry and exit of the previous shadow period in spring 2011. However, the exit maneuver in April 2011 has already been executed 34 hour prior to exceeding the threshold. With the help of yaw-angle estimates, profiles of the actual satellite attitude can be derived to remove the uncertainty at which point in time the switch has exactly been performed.

10.5 Orbit Determination

The GPS and QZSS observations of the five CONGO stations are used for an orbit determination on a daily basis. The processing scheme is similar to that of GIOVE-B discussed in Steigenberger et al (2011). A modified version of the Bernese GPS Software (Dach et al, 2007) is used to process dual frequency GPS and QZSS tracking data. In a first step, station positions, troposphere parameters, and epoch wise receiver clock offsets are estimated with GPS data only using the Center for Orbit Determination in Europe (CODE) rapid orbit and satellite clock products. The IF linear combination of L1 and L2 is used for GPS, while that of L1 and L5 is used for QZSS. Code and phase observations are processed simultaneously. The parameters estimated in the first step are kept fixed in the second step, the QZS-1 orbit and clock determination. Epoch wise QZS-1 satellite clock offsets, six Kepler elements and five radiation pressure parameters of the Beutler et al (1994) model are estimated per

	Station Residuals (median)		DCB
	Phase [cm]	Code [cm]	[ns]
CHOF	3.7	35.3	Fixed to zero
MAHO	1.7	56.5	-0.96 ± 0.49
SING	1.1	40.4	0.61 ± 0.24
THTX	5.5	154.3	2.47 ± 0.54
UNSX	1.7	63.1	0.28 ± 0.21

Tab. 10.1: Station-specific residuals and code biases from the orbit and clock determination.

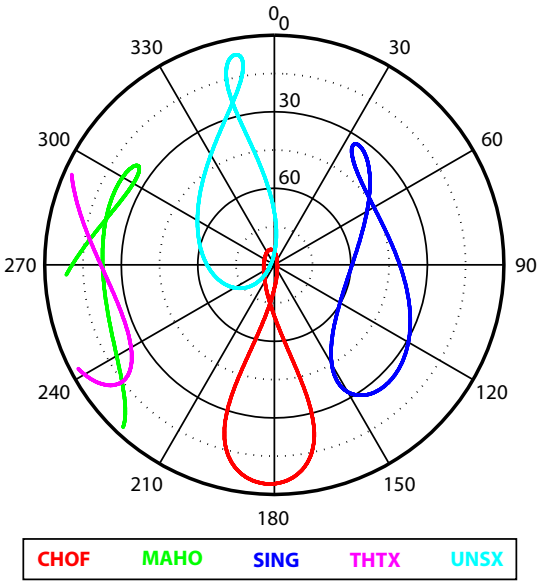

Fig. 10.7: QZS-1 visibility of the five CONGO stations in corresponding local horizontal systems.

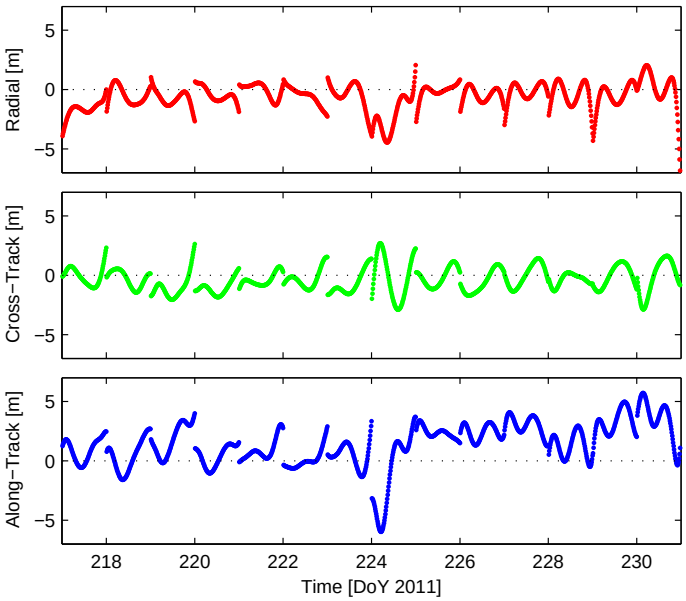

Fig. 10.8: Differences between QZS-1 1-day orbits estimated from the CONGO network and broadcast orbits.

day. In addition to the 1-day solution computed with a latency of about 16 hours, a 5-day solution is computed to achieve a higher stability of the satellite orbits by stacking the orbital elements and radiation parameters of the five consecutive days. In the 5-day solution, the full set of nine radiation pressure parameters according to Beutler et al (1994) is estimated.

A time period of two weeks (DoY 217 - 230 of 2011) has been considered for the following analysis. The median of daily RMS values for phase and code residuals of the orbit and clock determination are given in Tab. 10.2. Since the noise of observations increases with decreasing elevation, the magnitude of the residuals largely depends on the visibility conditions of QZS-1 at the corresponding stations shown in Fig. 10.7. For MAHO and THTX there are no observations above 30° whereas almost all observations of SING have a larger elevation than 30° resulting in the smallest phase residuals. Contrary to the other stations, which provide continuous tracking, MAHO and THTX have QZS-1 visibility periods limited to about 17 and 10 hours, respectively. As these periods are dominated by observations with low elevations, the residuals are larger by a factor of up to five compared to the other stations. The reason for the increased phase residuals at CHOF is unknown.

Since observations of different navigation systems (GPS and QZSS) and different frequencies (L1/L2 and L1/L5) are processed together, the biases between the code observations have to be considered. This is done by estimating DCBs for all stations except for CHOF, which is constrained to zero. The mean biases (composed of inter-system and inter-frequency biases) are listed in Tab. 10.1. The biases are in the order of a few nanoseconds corresponding to less than one meter expressed in range with a standard deviation usually better than half a nanosecond. Compared to the GIOVE (Galileo in Orbit Validation Element) biases also estimated from the CONGO network, the QZSS biases are up to one order of magnitude smaller.

	Broadcast	CONGO 1-day	CONGO 5-day
2-day orbit fit RMS	126	55	3.5
Day boundary discontinuities	75	449	16

Tab. 10.2: Orbit fit residuals and day boundary discontinuities for different orbit types. Units are in centimeters.

The differences between the orbits estimated from the CONGO network and the broadcast orbits provided by JAXA are shown in Fig. 10.8. The mean differences are -0.58, -0.36, and 1.41 m in radial, cross-track, and along-track direction with standard deviations of 1.10, 1.04, and 1.82 m, respectively. As the CONGO orbits are computed from one day of data, the largest differences occur at the day boundaries. Two different measures for the internal consistency of the orbits are given in Tab. 10.2. The 2-day orbit fit RMS is the RMS of two consecutive orbital arcs with respect to a 2-day orbit fitted through the original orbits with the orbital model mentioned above. Since the CONGO orbits were computed with the same orbital model, it is not surprising that the RMS is smaller compared to the broadcast orbits. The very small RMS of 3.5 cm for the 5-day orbits can be explained by the usage of overlapping data intervals for the computation of the 5-day orbits. The day boundary discontinuities given in Tab. 10.2 are the 3D position differences between two orbits at the midnight epoch. The CONGO 1-day orbits are completely independent from each other resulting in the largest day boundary discontinuities of almost 4.5 m. The discontinuities of the broadcast orbits are smaller by a factor of six compared to the 1-day orbits. This is due to the fact that Broadcast Ephemeris (BCE) are fitted to orbit predictions with sufficient overlap to ensure smooth transitions. The longer data interval used for the CONGO 5-day orbits resulting in a smoothing is responsible for the smallest day boundary discontinuities of 16 cm for this orbit type. Based on the orbit comparisons and numerical values given in Tab. 10.2, the orbit accuracy is assumed to be at the few meter level. A meaningful analysis of satellite laser ranging measurements could not be performed since only 17 normal points from a single tracking station are available for the test interval.

10.6 Conclusions

Results were presented for Japan's first navigation satellite Michibiki, which is the first satellite of a new regional navigation system. Five stations of the CONGO network have been upgraded with QZSS-capable firmware and provide measurements for five out of the six signals transmitted by the spacecraft. The carrier-to-noise density ratios of QZSS and GPS have been compared for a receiver in Chofu, Japan. It is interesting to note that contrary to GPS, the path loss of QZSS varies by about 1.5 dB due to the eccentricity of the orbit. The code multipath has been assessed from the multipath combination for two stations. A similar multipath performance is expected for GPS and QZSS, since both systems use the same signal structure. This result can be confirmed for L1 and L2 signals. For L5, however, the single GPS satellite contributing to the statistics is affected by larger multipath errors compared to QZSS at both stations. The triple-frequency combination of the pseudorange and carrier phase observations is stable over a period of one week, which suggests that no notable line-bias variations are present onboard the spacecraft.

One of the unique features of QZSS compared to other navigation satellite systems is the transmission of an L1 signal (SAIF) from a dedicated antenna mounted with an offset to the main L-band antenna, which allows the estimation of the satellites yaw-attitude. Estimation results for an attitude mode switch from yaw-steering to orbit-normal orientation are presented.

The orbit determination accuracy for QZS-1 based on the small network of only five stations has been assessed to be on the order of a few meters. Differential code biases have been estimated in order to process GPS L1/L2 signals and QZSS L1/L5 signals together consistently. The biases are on the order of a few nanoseconds.

Bibliography

Bar-Sever YE (1996) A new model for GPS yaw attitude. Journal of Geodesy 70(1):714–723, DOI 10.1007/BF00867149

Beutler G, Brockmann E, Gurtner W, Hugentobler U, Mervart L, Rothacher M, Verdun A (1994) Extended orbit modeling techniques at the CODE Processing Center of the International GPS Service (IGS): Theory and initial results. Manuscripta Geodaetica 19:367–386

Dach R, Hugentobler U, Fridez P, Meindl M (eds) (2007) Bernese GPS Software Version 5.0. Astronomical Institute, University of Bern, Bern, Switzerland

Hauschild A, Steigenberger P, Rodriguez-Solano C (2011) QZS-1 yaw attitude estimation based on measurements from the CONGO network. In: Proceedings of ION GNSS 2011, pp 1288–1298

Inaba N, Matsumoto A, Hase H, Kogure S, Sawabe M, Terada K (2009) Design concept of quasi zenith satellite system. Acta Astronautica 65(7-8):1068–1075, DOI 10.1016/j.actaastro.2009.03.068

Kee C, Parkinson B (1994) Calibration of multipath errors on GPS pseudorange measurements. In: Proceedings of ION GPS 1994, pp 353–362

Kishimoto M, Myojin E, Kogure S, Noda H, Terada K (2011) QZSS on orbit technical verification results. In: Proceedings of ION GNSS 2011, pp 1206–1211

Montenbruck O, Hauschild A, Hessels U (2011) Characterization of GPS/GIOVE sensor stations in the CONGO network. GPS Solutions 15(3):193–205, DOI 10.1007/s10291-010-0182-8

Montenbruck O, Hugentobler U, Dach R, Steigenberger P, Hauschild A (2012) Apparent clock variations of the Block IIF-1 (SVN62) GPS satellite. GPS Solutions 16(3):303–313, DOI 10.1007/s10291-011-0232-x

Saito M, Sato Y, M M, Omura Y, Shima M, Yoshino T, Asari K (2011) Centimeter-class augmentation system utilizing quasi-zenith satellite. In: Proceedings of ION GNSS 2011, pp 1243–1253

Steigenberger P, Hugentobler U, Montenbruck O, Hauschild A (2011) Precise orbit determination of GIOVE-B based on the CONGO network. Journal of Geodesy 85(6):357–365, DOI 10.1007/s00190-011-0443-5

11 Orbit and Clock Determination of QZS-1 Based on the CONGO Network

This is the peer reviewed version of the following article:

Steigenberger P., Hauschild A., Montenbruck, O., Rodriguez-Solano, C., Hugentobler, U. (2013): Orbit and Clock Determination of QZS-1 Based on the CONGO Network, Navigation, Journal of the Institute of Navigation, Vol. 60, No. 1, pp. 31-40, doi: 10.1002/navi.27

which has been published in final form at http://dx.doi.org/10.1002/navi.27. This article may be used for non-commercial purposes in accordance with Wiley Terms and Conditions for self-archiving.

Abstract

Results are presented for Michibiki, the first satellite of Japan's Quasi-Zenith Satellite System. Measurements for the analysis have been collected with five GNSS tracking stations in the service area of QZSS, which track five out of the six signals transmitted by the satellite. The analysis discusses the carrier-to-noise density ratio as measured by the receiver for the different signals. Pseudorange noise and multipath are evaluated with dual-frequency and triple-frequency combinations. QZSS uses two separate antennas for signal transmission, which allows the determination of the yaw-orientation of the spacecraft. Yaw angle estimation results for an attitude mode switch from yaw-steering to orbit normal orientation are presented. Estimates of differential code biases between QZSS and GPS observations are shown in the analysis of the orbit determination results for Michibiki. The estimated orbits are compared to the broadcast ephemerides and their accuracy is assessed with overlap comparisons.

11.1 Introduction

The Japanese Quasi-Zenith Satellite System (QZSS; Inaba et al, 2009) is a regional augmentation system for Global Positioning System (GPS) users in Asia and the Pacific. In particular, users with difficult visibility conditions (like urban canyons) shall benefit from this system. Therefore, the orbit was designed in such a way, that the visibility close to the zenith over Japan is maximized. As a consequence, an inclined geosynchronous orbit was chosen resulting in the ground track shown in Fig. 11.1. The orbit has an eccentricity of 0.076, an inclination of 40.8° and a semi-major axis of 42,160 km resulting in orbit heights above the Earth's surface between 32,600 and 38,980 km. First, a constellation of three satellites was envisaged but recently the number of planned satellites was increased to seven (Langley, 2011). However, the orbit design for the additional satellites is not yet finalized.

QZSS satellites transmit navigation signals in the L1, L2, and L5 band interoperable with GPS, see Table 11.1. Furthermore, a SAIF (Submeter-class Augmentation with Integrity Function) signal on the L1 frequency and a LEX (L-Band Experimental) signal at 1278.25 MHz (E6) are transmitted. The first QZSS satellite QZS-1 was launched by the Japan Aerospace Exploration Agency (JAXA) in September 2010 and started to transmit its standard codes in December 2010. It was declared healthy in June 2011 (Kishimoto et al, 2011).

The Cooperative Network for GIOVE Observation (CONGO; Montenbruck et al, 2009, 2010) was primarily established for signal analysis, orbit, and clock determination of the Galileo in Orbit Validation Element (GIOVE) satellites. It is a global real-time GNSS tracking network of currently 22 stations jointly operated by Deutsches Zentrum für Luft- und Raumfahrt (DLR, Oberpfaffenhofen, Germany), Bundesamt für Kartographie und Geodäsie (BKG, Frankfurt, Germany), Deutsches GeoForschungsZentrum (GFZ, Potsdam, Germany), and Centre National d'Etudes Spaciales (CNES, Toulouse, France) in cooperation with a number of local station hosts (see Acknowledgements). Five Javad Triumph receivers (JAVAD TRE_G3TH DELTA) of the CONGO network (see Fig. 11.1 and Table 11.2) were upgraded with a prototype firmware providing QZSS tracking capability. These receivers are able to track all QZSS signals except for the LEX signal. The QZSS as well as GPS signals used for the

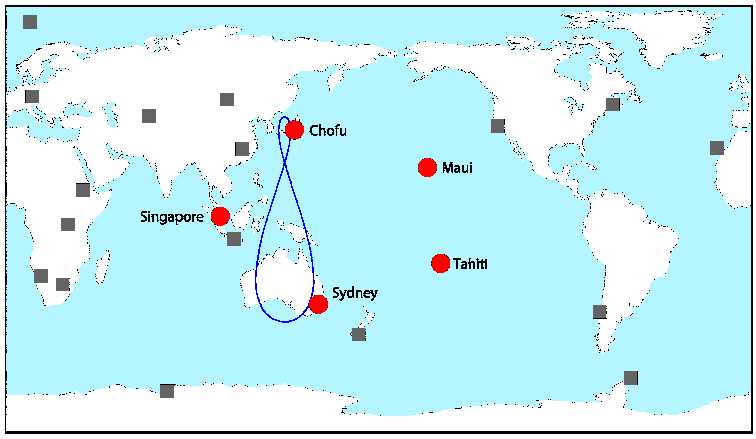

Fig. 11.1: Tracking stations of the Cooperative Network for GIOVE Observation (CONGO). QZSS-capable stations are shown as red circles. The QZS-1 ground track is plotted in blue.

Band	Frequency	QZSS	CONGO Usage	
		Signal	QZSS	GPS
L1	1575.42 MHz	L1C	C1C	C1W
		L1 C/A		
		SAIF		
E6	1278.75 MHz	LEX		
L2	1227.60 MHz	L2C	C2X	C2W
L5	1176.45 MHz	L5	C5X	

Tab. 11.1: Signals transmitted by QZS-1 (Japan Aerospace Exploration Agency, 2010) and usage of QZSS and GPS code signals in the CONGO processing. The abbreviations for the code signals refer to the RINEX 3 format description (Gurtner and Estey, 2007).

processing described in the next section are listed in Table 11.1. GPS L2C and L5 observations are not used as currently too few satellites are able to transmit these signals. A signal analysis as well as first results of the QZS-1 orbit determination are given in Hauschild et al (2012).

Precise orbit and clock parameters are a prerequisite for most GNSS applications. Therefore, the goal of the studies discussed in this paper is to set up a processing scheme to derive QZSS orbit and clock parameters and to evaluate their quality. As the QZSS orbit design differs significantly from other GNSS like GPS, different orbit parameterizations have to be tested to find the optimal set of parameters for QZS-1. Due to the fact that only five tracking stations are available, the orbit quality achievable with such a small network is another topic of interest. The atomic frequency standard is the heart of each GNSS satellite. Therefore, a characterization of the clock behavior is mandatory to assess the general performance of QZS-1.

First, the general options used for the estimation of QZS-1 orbit and clock parameters are described. Different orbit parameterizations (arc length and number of estimated radiation pressure parameters) are compared and

Abb.	Location	Antenna
CHF0	Chofu, Japan	TRM57971.00
MAO0	Maui, Hawaii	LEIAR25.R3
SIG0	Singapore	LEIAR25.R3
THX0	Tahiti, French Polynesia	LEIAR25.R3
UNX2	Sydney, Australia	LEIAR25.R3

Tab. 11.2: QZSS-capable stations of the CONGO network. All stations are equipped with JAVAD TRE_G3TH DELTA receivers.

the precision and accuracy of these different solutions as well as the broadcast orbits is evaluated by day boundary discontinuities, orbit fit RMS values, and satellite laser ranging residuals. In addition, solutions computed from different frequencies are compared. Finally, the QZS-1 clock quality is evaluated with different methods and the clock performance is compared to the GPS Block IIF clocks.

11.2 GNSS Processing

The general orbit and clock determination strategy is similar to that of GIOVE-B described in Steigenberger et al (2011). The time period from 22 July until 7 September 2011 (day of year 173 – 250/2011) was used to process dual-frequency GPS and QZSS data of the five QZSS-capable CONGO stations with a modified version of the Bernese GPS Software (Dach et al, 2007) in daily batches. QZS-1 was set unhealthy from 16 till 23 July 2011 (day of year 197 – 204/2011) during the RESSOX (Remote Synchronization for an Onboard Crystal Oscillator) campaign (Iwata et al, 2010; JAXA, 2011b,c). However, as no degradation of the orbit determination could be detected, this time period was considered for analysis of the orbit results but excluded for the analysis of the clock results.

First, a GPS-only PPP solution for the contributing stations is computed with the ionosphere-free linear combination of L1 and L2. Outliers and cycle-slips are detected from smoothed code observations. Station coordinates, troposphere zenith delays (2-h resolution) and gradients (24-h resolution), receiver clock parameters (epoch-specific) and float ambiguities are estimated in this step. GPS satellite orbits and clocks are fixed to those of the Center for Orbit Determination in Europe (CODE; Dach et al, 2009). In a second step, the orbit and clock parameters of QZS-1 as well as float ambiguities and station-specific differential code biases are estimated based on different sets of observations:

(1) ionosphere-free linear combination of L1 and L2,
(2) ionosphere-free linear combination of L1 and L5.

In this step, the station coordinates, troposphere parameters, and receiver clocks of the first step are fixed. The QZS-1 a priori orbits are generated from the broadcast navigation message of received at UNX2.

The orbit parameters consist of six Keplerian elements and three, five, or nine Radiation Pressure (RPR) parameters of the model of Beutler et al (1994). A Sun-oriented coordinate system is used for the RPR parameters:

D-axis: pointing from the satellite to the Sun,

Y-axis: parallel to the satellite's solar panel axis,

X-axis: completing a right-handed system and pointing in the hemisphere containing the Sun.

In each direction, the RPR parameters are split into a constant term (index 0), a sine term (index S), and a cosine term (index C) depending on the argument of latitude u:

$$D(u) = D_0 + D_S \cdot \sin u + D_C \cdot \cos u \tag{11.1a}$$
$$Y(u) = Y_0 + Y_S \cdot \sin u + Y_C \cdot \cos u \tag{11.1b}$$
$$X(u) = X_0 + X_S \cdot \sin u + X_C \cdot \cos u \tag{11.1c}$$

The following subsets of RPR parameters are used:

3 par.: D_0, X_0, Y_0

5 par.: D_0, X_0, Y_0, X_S, X_C

9 par.: D_0, X_0, Y_0, D_S, D_C, Y_S, Y_C, X_S, X_C

To account for the seasonal changes of the radiation pressure due to variations of the distance Earth/Sun, the RPR parameters are multiplied with a scaling factor computed from current and mean distance between Earth and Sun.

An elevation cutoff angle of 3° and a 30 s sampling are applied in the data processing. Gross outliers due to erroneous measurements exceeding a limit of 1 m for phase and 100 m for code observations are excluded. The remaining observations are weighted according to their elevation ϵ with $w = \sin^2 \epsilon$. As no frequency-dependent QZS-1 satellite antenna offsets are available, the offsets provided by Kogure (2011) are used for L1, L2, and L5. Recently, updated antenna offsets were provided by JAXA and are available at `http://igs.org/mgex/Status_`

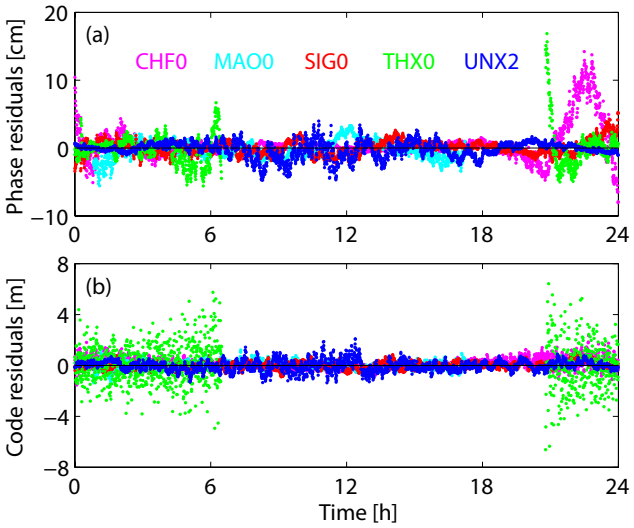

Fig. 11.2: QZS-1 L1/L5 ionosphere-free carrier phase (a) and code (b) residuals for 28 August 2011.

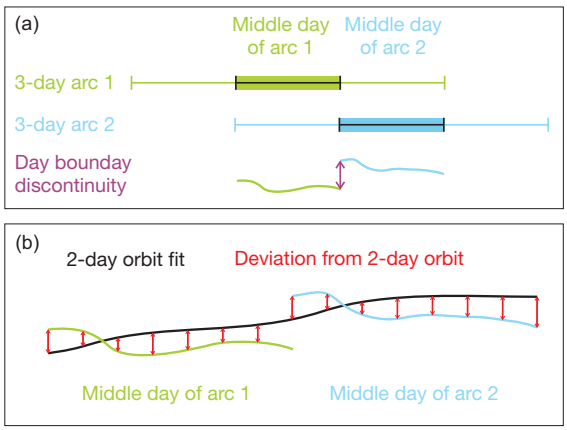

Fig. 11.3: Orbit quality measures. 3-day arcs are shown as example: (a) day boundary discontinuity; (b) 2-day orbit fit RMS computed from the deviations of two individual days (green and blue lines) w.r.t. the 2-day orbit (black line).

`QZSS.htm`. No QZSS satellite antenna phase center variations are considered. Frequency-dependent receiver antenna calibrations (offsets and phase center variations) for the two different antennas at the QZSS-capable CONGO stations determined in an anechoic chamber were provided by Becker et al (2010) and Zeimetz (2010). For the GPS satellite antennas, the `igs08.atx` model (Rebischung et al, 2012) is used.

The number of CONGO stations tracking QZS-1 varies between three and five as Maui and Tahiti do not provide continuous tracking due to their location. Altogether, the average QZS-1 observation number is 22,650 observations (code and phase) per day. Medians of daily station-specific RMS values of the residuals range from 1.0 to 4.1 cm for the ionosphere-free carrier phase observations and from 29 to 154 cm for the code observations. These numbers are similar to the earlier analysis of a shorter time period by Hauschild et al (2012). As an example, Fig. 11.2 shows the time series of phase and code residuals for 28 August 2011. The largest phase residuals of up to 17 cm occur for low elevation data: shortly before signal loss or after signal acquisition of THX0, or for the period of lowest elevation for CHF0 before midnight. The code residuals can reach up to 6.6 m for THX0 but are in general below 1 m for the other stations. The reason for the in general larger code residuals of THX0 is the fact, that the receiver-internal smoothing corrections for this station are not transmitted due to bandwidth problems of the internet connection. As an intermediate product of the daily processing, normal equations containing orbit parameters and differential code biases are saved for multi-day orbit combinations discussed in the next section.

11.3 Orbit Results

Different orbital arc lengths and numbers of RPR parameters were tested to find an optimum parameterization for the orbit determination. Normal equations with orbital elements and radiation pressure parameters of 3, 5, and 7 consecutive days were combined to multi-day solutions. Only the middle day of these multi-day solutions is considered in the following analysis. In addition, the number of estimated RPR parameters can be changed on the normal equation level to the subsets listed in the previous section. The following quantities were used as orbit quality indicators:

Day Boundary Discontinuities: Absolute value of the 3-dimensional difference of the orbit positions of two consecutive days at midnight, see Fig. 11.3 (a). It is clear that the day boundary discontinuities get smaller with increasing arc length. Therefore, this type of quality measure can only be used for comparisons of orbits with the same arc length but different number of radiation pressure parameters.

2-day Orbit Fit RMS: A 2-day orbital arc is fitted through the orbit positions of two consecutive days, see Fig. 11.3 (b). The RMS of the new arc with respect to the two original arcs is computed (represented by the red arrows in Fig. 11.3 (b)). As for the day boundary discontinuities, decreasing RMS values are expected with increasing arc length.

Arc Length [days]	No. RPR Param.	Solution ID	Day Boundary Discont. [cm]	Orbit Fits RMS [cm]	SLR Validation STD [cm]	SLR Validation Offset [cm]
3	3	C33	24.3	3.2	36.4	−1.8
	5	C35	16.4	3.1	32.5	−1.7
	9	C39	35.3	7.6	61.9	−1.1
5	3	C53	18.3	2.4	34.3	−0.4
	5	C55	16.7	3.0	33.1	0.4
	9	C59	17.3	4.0	50.1	34.2
7	3	C73	12.7	1.5	34.2	−0.6
	5	C75	16.3	2.6	34.7	3.4
	9	C79	10.9	2.3	39.7	18.2
Broadcast		BRD	87.0	15.0	48.4	23.8

Tab. 11.3: Quality measures of QZS-1 orbits with different arc length and different number of RPR parameters.

SLR Residuals: Optic Satellite Laser Ranging (SLR) measurements allow for an independent validation of the QZS-1 orbits determined from microwave observations. On request of JAXA (Nakamura and Kishimoto, 2010), QZS-1 is regularly tracked by selected SLR stations of the International Laser Ranging Service (ILRS; Pearlman et al, 2002). The QZS-1 SLR retroreflector offsets are given in Nakamura and Kishimoto (2010). 330 normal points from six different stations are available for the time period considered. Outliers exceeding a limit of 3 m were excluded from the computation of standard deviation (STD) and mean values of the SLR residuals. As all outliers originate from a certain time interval of one station, technical problems of this particular station are probably the reason for these outliers.

11.3.1 QZS-1 Orbit Quality

The quality measures mentioned above are listed in Table 11.3 for multi-day solutions with 3, 5, and 7 days arc length and 3, 5, or 9 estimated radiation pressure parameters computed from L1 and L5 observations. The solution ID listed in the third column is composed of three characters. The first character indicates the CONGO network as origin for the solution, the second character stands for the arc length and the third character for the number of RPR parameters. The broadcast orbits provided by JAXA are also included for comparison purposes. For the day boundary discontinuities median values are given and for the orbit fits median values of the RMS computed from 2 days are listed.

Most solutions derived from the CONGO network show a better performance than the broadcast orbits. This is not astonishing as the broadcast orbits are predicted orbits whereas all CONGO orbits are computed in a post-processing mode. The number of nine RPR parameters is obviously too high for QZSS orbit determination with a small station network: the solutions C39, C59, and C79 have the largest SLR STDs, solution C39 has the largest day boundary discontinuities, and solutions C59 and C79 show a significant SLR offset. As an example, Fig. 11.4 shows time series of the quality measures discussed above for solution C55. The day boundary discontinuities and orbit fit RMS values seem to increase with decreasing elevation of the Sun above the orbital plane shown in Fig. 11.5 (a). However, longer time series are necessary to confirm this hypothesis.

Solutions C35 and C55 with 5 RPR parameters as well as solution C73 with 3 RPR parameters have a similar quality level with the best performance in the SLR validation, the lowest day boundary discontinuities per arc length, and (except for C55) also the smallest orbit fit RMS values per arc length. The 3D RMS differences of these three solutions range from 31 cm (C35 vs. C55) to 64 cm (C55 vs. C73). The comparison of all orbit solutions amongst each other results in 3D RMS differences between 17 cm (C73 vs. C75) and 89 cm (C35 vs. C79). For a final assessment, which orbit solution performs best, the clock characteristics of the different orbit solutions discussed in the next section will serve as another quality indicator.

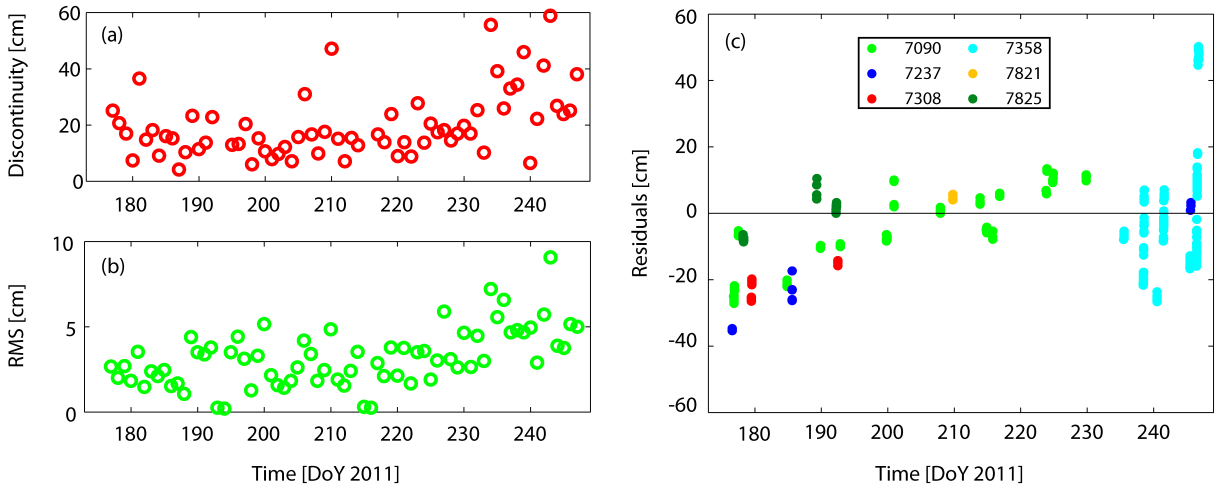

Fig. 11.4: Time series of (a) day boundary discontinuities; (b) orbit fit RMS; (c) SLR residuals of 5-day orbits with 5 RPR parameters (solution C55).

11.3.2 Radiation Pressure

Time series of the estimated RPR parameters of solution C55 are shown in Fig. 11.5. In addition, the elevation of the Sun above the orbital plane β_0 is given in Fig. 11.5 (a). The constant term into direction of the Sun (D_0) has a mean value of $-1.55 \cdot 10^{-7}$ ms^{-2} and is about two orders of magnitude larger than the other RPR parameters. D_0 and X_0 show a clear dependence on the β_0 angle whereas the variations of Y_0 are much smaller. The scatter of D_0 decreases for decreasing β_0 angle. For X_C the situation is vice versa: the scatter increases with decreasing β_0 angle.

The β_0-dependence of D_0 can be explained with the effective area of the satellite in the direction of the Sun. If one assumes a satellite bus height/width ratio of 2:1, one gets a variation of the effective area of about 2 %. This values nicely agrees with the variation of D_0 w.r.t. the mean value of D_0 which is 1.9 %. At least parts of the variations of the other RPR parameters are related to the determinability of these parameters as well as correlations of the RPR parameters amongst each other.

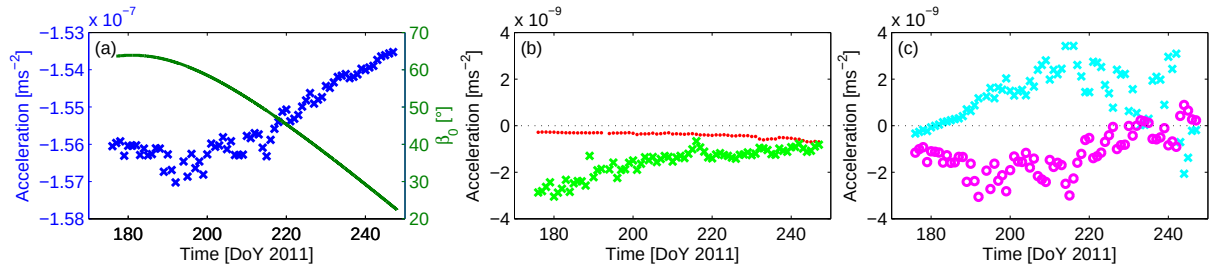

Fig. 11.5: Time series of radiation pressure parameters of solution C55: (a) D_0 (blue crosses) and elevation of the Sun above the orbital plane β_0 (green line), (b) Y_0 (red dots) and X_0 (green crosses), (c) X_S (magenta circles) and X_C (cyan crosses).

11.3.3 Different Frequencies

As QZS-1 transmits ranging signals on different frequencies, ionosphere-free linear combinations of either L1/L2 or L1/L5 can be used for the orbit determination. When different observables of GPS and QZSS or even different frequencies are processed together (see Table 11.1), biases between the corresponding code observations have to be considered. Therefore, differential code biases (DCBs) are estimated for all stations but Chofu, which is constrained to zero. As an example, Fig. 11.6 shows the L1/L5 DCB time series of station Sydney. The three-fold formal errors are indicated by error bars. A discontinuity of 0.7 ns can clearly be seen at day 193/2011. The reason for this discontinuity is unknown. Since the Singapore station also shows such a discontinuity, the

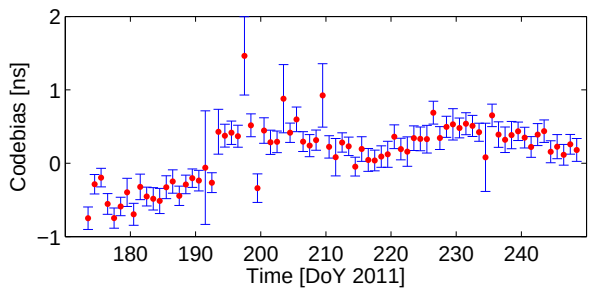

Fig. 11.6: Differential L1/L5 code biases of station Sydney. The error bars indicate the three-fold formal errors. The reason for the discontinuity at day 193/2011 is unknown.

Frequency	L1/L2		L1/L5	
Station	Median [ns]	STD [ns]	Median [ns]	STD [ns]
Maui	−1.24	0.36	−0.93	0.43
Singapore	0.13	0.28	0.44	0.27
Sydney	−1.15	0.23	0.34	0.25
Tahiti	0.32	0.62	2.83	0.60

Tab. 11.4: Differential code biases of QZS-1 w.r.t. the receiver at Chofu for the ionosphere-free linear combinations of QZSS C1C/C2X vs. GPS C1C/C2W (denoted as L1/L2) and QZSS C1C/C5X vs. GPS C1C/C2W (denoted as L1/L5), respectively.

time period for computing median biases and their standard deviations listed in Table 11.4 was limited to day 193 – 250/2011. For station Maui, the end time was set to 235/2011 as a receiver change at that date resulted in a DCB discontinuity of 1.5 ns.

The mean L1/L2 as well as L1/L5 biases are in the order of a few nanoseconds with a standard deviation usually better than half a nanosecond. The L1/L2 standard deviations are very similar to the corresponding L1/L5 values. However, keeping in mind that 1 ns refers to about 30 cm expressed in range, the code biases have to be considered for precise applications.

Orbits obtained with completely identical solution setup except for the frequencies used for forming the ionosphere-free linear combination are compared in Fig. 11.7 for a selected time interval of two weeks. 1-day orbits were used, as these are more sensitive compared to multi-day orbits. The differences in the estimated orbit positions can reach up to 30 cm in the along-track direction with mean values of 3 cm in radial, −3 cm in cross-track, and 15 cm in along-track direction. The corresponding standard deviations are 3 cm, 12 cm, and 7 cm, respectively. However, these differences are well below the accuracy level of the orbits discussed in the previous section.

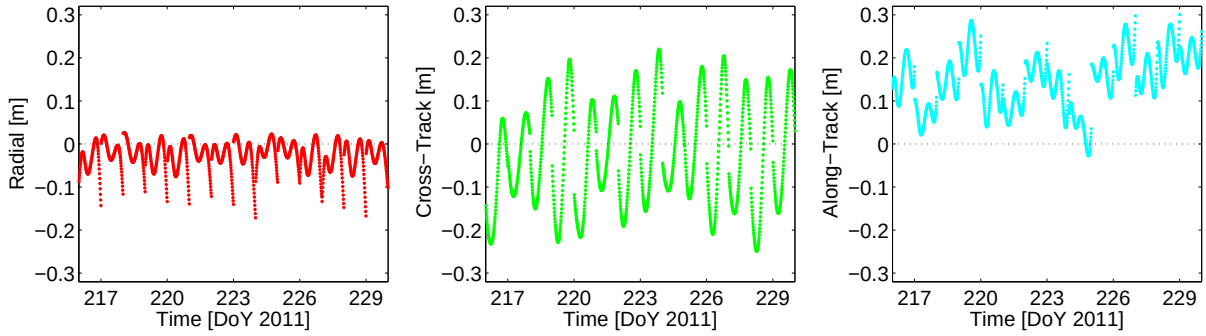

Fig. 11.7: Differences between orbits estimated from the ionosphere-free linear combination of L1/L2 and L1/L5, respectively.

11.4 Clock Results

QZS-1 is equipped with a similar type of Rubidium Frequency Standard (RFS) as the GPS Block IIF satellites (Mallette et al, 2010). More details on this particular clock as well as on its in space performance can be found in Dupuis et al (2010), Montenbruck et al (2012), and Montenbruck et al (2011). To generate clocks consistent with the orbits listed in Table 11.3, these orbits as well as the GPS-derived station coordinates, receiver clock and troposphere parameters are fixed and epoch wise clock parameters as well as DCBs are estimated. The days 197 – 204/2011 are not considered for the clock analysis due to the RESSOX campaign mentioned above. Four additional days were excluded due to clock jumps or the fact that the satellite was set unhealthy.

When looking at the detrended time series of clock estimates, a short-term variation in all different orbit/clock solutions is obvious. Figure 11.8 shows 2 hours of the 30 s L1/L5 clock estimates of QZS-1 after removing

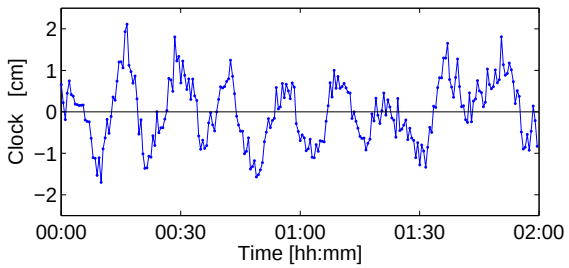

Fig. 11.8: Time series of QZS-1 clock estimates from L1/L5 observations with a sampling of 30 s for 2 hours of 28 August 2011. Long-periodic effects were removed with a higher-order polynomial.

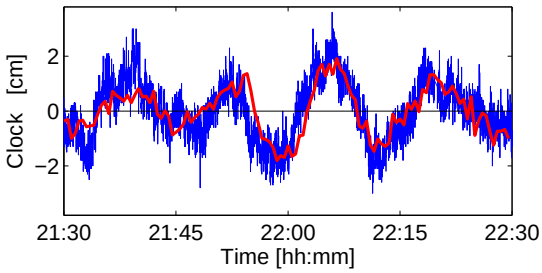

Fig. 11.9: Detrended 1 s QZS-1 clock parameters derived from three-way carrier phase measurements of UNX2 and TIDB for 28 August 2011 (blue). Clock estimates according to Fig. 11.8 (30 s sampling) are given in red.

long-periodic effects with a higher-order polynomial. A periodic variation with a peak-to-peak amplitude of up to 4 cm can clearly be identified. This variation is also present in the clock estimates based on the ionosphere-free linear combination of L1 and L2. Spectral analysis of the clock parameter time series reveals different periods for this signal. Three different time intervals with periods between 13.6 and 15.5 minutes could be identified, see Table 11.5. The changes of the period coincide with the RESSOX experiment already mentioned above (197–204/2011; JAXA, 2011b,c) and a short time period when the satellite was set unhealthy due to unknown reasons (215–216/2011; JAXA, 2011d). To ensure that these variations are not related to analysis-specific artifacts, the QZS-1 clock was in addition determined with a different method.

Time interval	Period
173–196/2011	15.1 min
205–215/2011	15.5 min
217–250/2011	13.6 min

Tab. 11.5: Period of short-term variations in the QZS-1 clock estimates.

The short-term stability of satellite clocks can also be analyzed with a single receiver if this receiver is connected to a highly stable clock (e.g., a hydrogen maser). As none of the QZSS-capable stations of the CONGO network is equipped with such a clock, this one-way carrier phase (1WCP) method (Delporte et al, 2010) cannot be used. However, the clock information can be transferred from a second station that is connected to a maser via a GPS satellite visible by both stations with a three-way carrier phase (3WCP) approach (Hauschild et al, 2013).

Figure 11.9 shows 3WCP-derived clock parameters of QZS-1 based on 1 Hz carrier phase observations of the CONGO station UNX2 in Sydney and the IGS station TIDB in Tidbinbilla (Australia). L1 and L5 observations of QZS-1 and L1 and L2 measurements of the GPS satellite SVN54 (which had a high elevation for both stations) were used. The short-period variations identified in the clock estimates can also clearly be seen in the 3WCP results and confirm the existence of these signals with an independent method.

As the 3WCP analysis was done with 1 s data (whereas the resolution of the estimated clock parameters was 30 s) the short-term behavior of the apparent QZS-1 clock can also be analyzed. It must be noted, though, that the 3WCP analysis is affected by a notably higher contribution of measurement noise than the traditional 1WCP concept. As such, the results given in Fig. 11.10 provide primarily an upper limit to the Allan deviation of the QZS-1 RFS itself. The first GPS Block IIF satellite (PRN25/SVN62) is included for comparison purposes. For periods below 100 s, the observed RFS performance of the GPS SVN62 and QZS-1 satellite are almost identical. At 1 s intervals, an Allan deviation of $2 \cdot 10^{-11}$ is obtained. This is about a factor of 5 worse than results obtained previously with a 1WCP analysis in Montenbruck et al (2011) and suggests that the actual QZSS clock exhibits an even better performance. The build-up of a QZSS-capable monitoring station connected to a hydrogen maser is therefore encouraged to enable a more rigorous characterization of the QZS-1 RFS short term stability. The QZS-1 clock specifications according to Kishimoto et al (2011) are also shown in Fig. 11.10. Despite the short-periodic variations discussed above (visible as a bump at about 400 s) the QZS-1 clock fully meets its specifications.

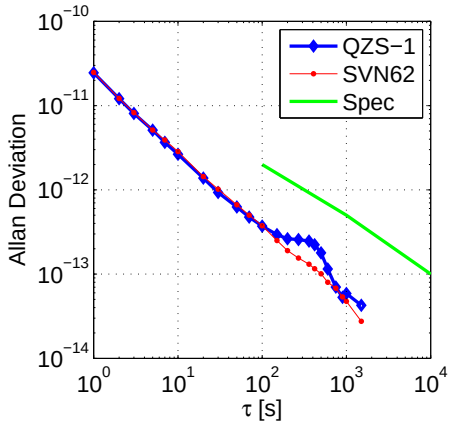

Fig. 11.10: Allan deviations of QZS-1 (blue diamonds) and GPS SVN62 (red dots) based on one hour of 3WCP analysis. The QZS-1 clock specifications according to Kishimoto et al (2011) are given as green line.

As QZS-1 transmits simultaneously on multiple frequencies, a geometry- and ionosphere-free linear combination can be formed from the L1, L2, and L5 carrier phase observations Montenbruck et al (2012). This three carrier linear combination only contains the difference between the L1/L5 and the L1/L2 clock and a constant ambiguity term. Figure 11.11 shows this linear combination for four days in August 2011: based on the observations of the five QZSS-capable CONGO stations, pass-specific offsets were estimated and the observations were combined to a single time series of L1/L5-minus-L1/L2 clock differences. The short-period clock variations discussed above can not be seen Fig. 11.11, only some small systematic effects at the day boundaries are visible. This is an indicator, that the periodic short-term variations are a frequency-independent clock effect. Frequency-dependent line biases that have a peak-to-peak amplitude of 10 – 40 cm for GPS SVN62 (Montenbruck et al, 2012) can not be identified in the three carrier linear combination of QZS-1.

As the periodic variations of the observed QZS-1 clock offset can be attributed to the time and frequency system rather than frequency dependent line bias variations, we consider them to be an artifact of the time keeping system. Due to its small order of magnitude (several centimeters), this effect is not relevant for navigation applications using code signals only. High-precision applications estimating epoch-wise satellite clock parameters without any constraints are also not affected. On the other hand, any high-precision applications utilizing a clock model or constrained satellite clock estimates or even predicted satellite clocks are affected by the short-period clock variations and have to consider them.

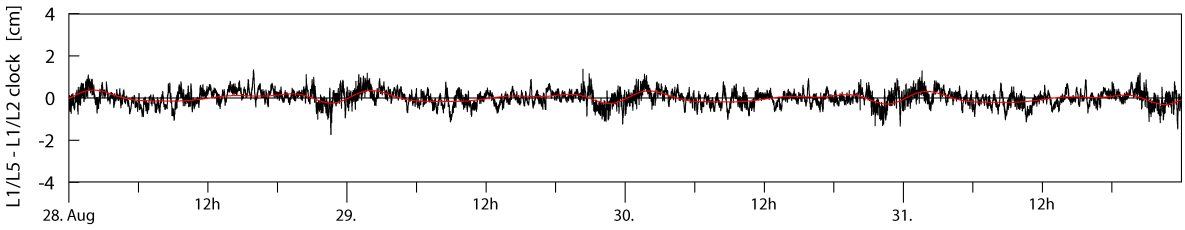

Fig. 11.11: QZS-1 L1/L2-minus-L1/L5 clock offset derived from a triple-frequency linear combination of carrier phase observations for four days in August 2011.

Whereas the previous analysis focused on the short-term stability of the QZS-1 RFS, clock estimates computed in daily batches are used for the following analysis. Mean modified Allan deviations of the clocks computed from the orbits listed in Table 11.3 are shown in Fig. 11.12. The Allan deviation of GPS SVN62 computed from the CODE final clock products (Bock et al, 2009) is also included for comparison purposes. At the shortest time interval of 100 s considered in the Allan deviation computation, the CONGO-based QZS-1 clock solutions exhibit a marginally higher noise than the CODE clock solutions for SVN62. This can be understood by a substantially larger number of monitoring stations in the two networks that contribute simultaneous observations of the respective satellites at each epoch. In any case the network based clock solutions indicate a substantially lower noise level than the 3WCP analysis discussed above. The bump in the SVN62 Allan deviation around 10,000 s is related to line bias variations as discussed by Montenbruck et al (2012). The bump of all QZS-1 clock estimates at about 400 s is related to the short-period variations discussed before.

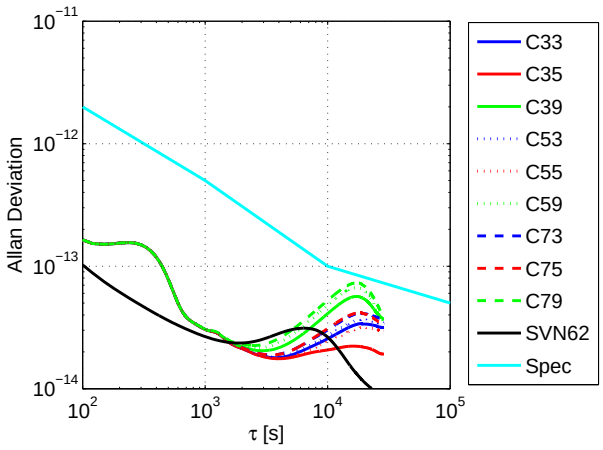

Fig. 11.12: Mean modified Allan deviations computed from the time interval 176 – 247/2011.

As radial orbit errors and clock parameters are one-to-one correlated, the Allan deviation can also be used as quality indicator for the different orbit solutions discussed in the previous section if the clock errors are dominated by orbit errors. This seems to be the case for our QZSS orbits, as the mean modified Allan deviations in Fig. 11.12 differ for different orbit parameterizations at time scales above 1,000 s. Clocks computed from orbits with 9 RPR parameters clearly show the worst stability in the long term domain. All solutions with 3 RPR parameters as well as the 5-day and 7-day solutions with 5 RPR parameters have a very similar behavior. However, the 3-day solution C35 with 5 RPR parameters shows the flattest behavior at longer time scales indicating a higher stability of this particular orbit/clock solution. As solution C35 is also one of the three solutions with the best orbit performance discussed in the previous section, this parameterization seems to be the best one for the current tracking network of five stations only. However, the situation might change if observation data of more stations is available.

11.5 Conclusions

QZS-1 orbit and clock parameters were estimated from a network of five stations only. Despite the small network size, a sub-meter orbit accuracy could be achieved. Based on the orbit and clock analysis, an arc length of 3 days and the estimation of 5 RPR parameters gives the best results. The QZS-1 clock performs very similar to the GPS Block IIF clocks for periods below 100 s. The QZS-1 clock is affected by short-term variations with a peak-to-peak amplitude of about 4 cm and changing periods. Periods between 13.6 and 15.5 minutes could be identified for three different time intervals. However, this effect is well below the specifications of the QZS-1 clock and has to be considered only for a limited set of high precision applications involving clock constraining or prediction. At longer time periods, the QZS-1 clock estimates are dominated by orbit errors. Mitigating these errors (e.g., by refining the RPR modeling) remains a challenging task for the future. However, the orbit and clock products will also benefit from a densified tracking network like JAXA's Multi-GNSS Tracking Network (JAXA, 2011a).

Acknowledgements

We'd like to thank the local CONGO station hosts Dan O'Gara (University of Hawaii, USA), Peter Mumford (University of New South Wales, Australia), Narayanaswamy Nagarajan (Nanyang Technological University, Singapore), Tsujii Toshiaki (JAXA), and Youri Verschelle (Université de la Polynésie Française, French Polynesia) for their support. The International GNSS Service (IGS; Dow et al, 2009) is acknowledged for providing high-rate observation data.

Bibliography

Becker M, Zeimetz P, Schönemann E (2010) Antenna chamber calibrations and antenna phase center variations for new and existing GNSS signals. In: IGS Workshop 2010, 28 June – 2 July 2010, Newcastle

Beutler G, Brockmann E, Gurtner W, Hugentobler U, Mervart L, Rothacher M, Verdun A (1994) Extended orbit modeling techniques at the CODE processing center of the international GPS service for Geodynamics (IGS): theory and initial results. Manuscripta Geodaetica 19:367–386

Bock H, Dach R, Jäggi A, Beutler G (2009) High-rate GPS clock corrections from CODE: support of 1 Hz applications. Journal of Geodesy 83(11):1083–1094, DOI 10.1007/s00190-009-0326-1

Dach R, Hugentobler U, Fridez P, Meindl M (eds) (2007) Bernese GPS Software Version 5.0. Astronomical Institute, University of Bern, Bern, Switzerland

Dach R, Brockmann E, Schaer S, Beutler G, Meindl M, Prange L, Bock H, Jäggi A, Ostini L (2009) GNSS processing at CODE: status report. Journal of Geodesy 83(3-4):353–365, DOI 10.1007/s00190-008-0281-2

Delporte J, Boulanger C, Mercier F (2010) Simple methods for the estimation of the short-term stability of GNSS on-board clocks. In: Proceedings of the 42nd Annual Precise Time and Time Interval Meeting, pp 215–223

Dow JM, Neilan RE, Rizos C (2009) The International GNSS Service in a changing landscape of Global Navigation Satellite Systems. Journal of Geodesy 83(3-4):191–198, DOI 10.1007/s00190-008-0300-3

Dupuis R, Lynch T, Vaccaro J, Watts E (2010) Rubidium frequency standard for the GPS IIF program and modifications for the RAFSMOD program. In: ION GNSS 2010, Portland, pp 781–788

Gurtner W, Estey L (2007) RINEX, The Receiver Independent Exchange Format, Version 3.00. Tech. rep., URL `ftp://ftp.igs.org/pub/data/format/rinex300.pdf`

Hauschild A, Steigenberger P, Rodriguez-Solano C (2012) Signal, orbit and attitude analysis of Japan's first QZSS satellite Michibiki. GPS Solutions 16(1):127–133, DOI 10.1007/s10291-011-0245-5

Hauschild A, Montenbruck O, Steigenberger P (2013) Short-term analysis of GNSS clocks. GPS Solutions 17(3):295–307, DOI 10.1007/s10291-012-0278-4

Inaba N, Matsumoto A, Hase H, Kogure S, Sawabe M, Terada K (2009) Design concept of quasi zenith satellite system. Acta Astronautica 65(7-8):1068–1075, DOI 10.1016/j.actaastro.2009.03.068

Iwata T, Machita K, Matsuzawa T (2010) Actual operation simulation of RESSOX ground experiments. In: Proceedings of the 42nd Annual Precise Time and Time Interval Meeting, pp 141–160

Japan Aerospace Exploration Agency (2010) Quazi-Zenith Satellite System Navigation Service, Interface Specification for QZSS (IS-QZSS) Draft V1.2. Tech. rep.

JAXA (2011a) Call for applications: Hosting sites for multi-GNSS monitoring network. URL `http://www.satnavi.jaxa.jp/e/news/qz-110601_e.html`

JAXA (2011b) Notice Advisory to QZSS Users, NAQU Message 2011002. URL `http://qz-vision.jaxa.jp/USE/en/naqu_detail?name=2011002`

JAXA (2011c) Notice Advisory to QZSS Users, NAQU Message 2011003. URL `http://qz-vision.jaxa.jp/USE/en/naqu_detail?name=2011003`

JAXA (2011d) Notice Advisory to QZSS Users, NAQU Message 2011008. URL `http://qz-vision.jaxa.jp/USE/en/naqu_detail?name=2011008`

Kishimoto M, Myojin E, Kogure S, Noda H, Terada K (2011) QZSS on orbit technical verification results. In: ION GNSS 2011, Portland, pp 1206–1211

Kogure S (2011) personal communication

Langley R (2011) Constellation updates from ION GNSS 2011. GPS World 22(11):16–17

Mallette LA, White J, Rochat P (2010) Space qualified frequency sources (clocks) for current and future GNSS applications. In: Proceedings of IEEE/ION PLANS 2010, Indian Wells, pp 903–908, DOI 10.1109/PLANS.2010.5507225

Montenbruck O, Hauschild A, Hessels U, Steigenberger P, Hugentobler U (2009) CONGO – First GPS/GIOVE tracking network for science, research. GPS World 20(9):56–62

Montenbruck O, Hauschild A, Hessels U (2010) Characterization of GPS/GIOVE sensor stations in the CONGO network. GPS Solutions 15(3):193–205, DOI 10.1007/s10291-010-0182-8

Montenbruck O, Steigenberger P, Schönemann E, Hauschild A, Hugentober U, Dach R, Becker M (2011) Flight characterization of new generation GNSS satellite clocks. In: ION GNSS 2011, Portland, pp 2959–2969

Montenbruck O, Hugentobler U, Dach R, Steigenberger P, Hauschild A (2012) Apparent clock variations of the Block IIF-1 (SVN62) GPS satellite. GPS Solutions 16(3):303–313, DOI 10.1007/s10291-011-0232-x

Nakamura S, Kishimoto M (2010) ILRS SLR mission support request for QZS-1. Available online: `http://ilrs.gsfc.nasa.gov/docs/ILRS_retroreflector_QZS_20100729.pdf`

Pearlman MR, Degnan JJ, Bosworth JM (2002) The International Laser Ranging Service. Advances in Space Research 30(2):125–143, doi: 10.1016/S0273-1177(02)00277-6

Rebischung P, Griffiths J, Ray J, Schmid R, Collilieux X, Garayt B (2012) IGS08: the IGS realization of ITRF2008. GPS Solutions 16(4):483–494, DOI 10.1007/s10291-011-0248-2

Steigenberger P, Hugentobler U, Montenbruck O, Hauschild A (2011) Precise orbit determination of GIOVE-B based on the CONGO network. Journal of Geodesy 85(6):357–365, DOI 10.1007/s00190-011-0443-5

Zeimetz P (2010) Zur Entwicklung und Bewertung der absoluten GNSS-Antennenkalibrierung im HF-Labor. PhD thesis, Rheinische Friedrich-Wilhelms-Universität Bonn

12 Orbit and Clock Analysis of Compass GEO and IGSO Satellites

Originally published as:

Steigenberger P., Hugentobler U., Hauschild A., Montenbruck O. (2013): Orbit and clock analysis of Compass GEO and IGSO satellites, Journal of Geodesy, Vol. 87, No. 6, pp. 515-525, doi: 10.1007/s00190-013-0625-4

The final publication is available at Springer via `http://dx.doi.org/10.1007/s00190-013-0625-4`.

Abstract

China is currently focussing on the establishment of its own global navigation satellite system called Compass or BeiDou. At present, the Compass constellation provides four usable satellites in geostationary Earth orbit (GEO) and five satellites in inclined geosynchronous orbit (IGSO). Based on a network of six Compass-capable receivers orbit and clock parameters of these satellites were determined. The orbit consistency is on the one- to two-decimeter level for the IGSO satellites and on the several decimeter level for the GEO satellites. These values could be confirmed by an independent validation with satellite laser ranging. All Compass clocks show a similar performance but have a slightly lower stability compared to Galileo and the latest generation of GPS satellites. A Compass-only precise point positioning based on the products derived from the six receiver network provides an accuracy of several centimeters compared to the GPS-only results.

12.1 Introduction

Since the 1990s China is working on the development of its own satellite navigation system called Compass or BeiDou. BeiDou-1 was a regional system consisting of two geostationary satellites (BeiDou 1A and 1B launched in October and December 2000, respectively) and a backup satellite (BeiDou 1C launched in May 2003). The BeiDou-1 services were declared operational in mid of 2003 (Qian et al, 2012) and were available for civilian users since April 2004 (Chen et al, 2009). Positioning with BeiDou-1 was based on two-way transmissions and could provide an accuracy of about 100 m (Dragon in Space, 2012).

In contrast to BeiDou-1 with regional coverage and a two-way measurement principle, Compass/BeiDou-2 is ultimately conceived as a Global Navigation Satellite System (GNSS) based on one-way measurements like the U.S. Global Positioning System (GPS), the Russian GLONASS, or the European Galileo system. The first satellite Compass M-1 was launched in April 2007 (Jun et al, 2012). Starting with 2010 the number of launches per year was significantly increased (see Tab. 12.1) resulting in currently 14 active Compass satellites. In contrast to other GNSSs, Compass consists of three different types of orbits:

- Medium Earth Orbit (MEO): comparable to the GPS, GLONASS, and Galileo orbits with an altitude of about 27,900 km, an inclination of 55° and a period of revolution of $12^h\ 53^m$.
- Inclined Geosynchronous Orbit (IGSO) with an altitude of about 35,787 km, an inclination of 55°, an eccentricity of $e < 0.003$, and a period of revolution of $23^h\ 56^m$ resulting in a daily repeat groundtrack with a symmetric figure of eight, see Fig. 12.1.
- GEO also with an altitude of about 35,787 km. According to their name, these satellites have an almost constant position in an Earth-fixed system. However, due to a non-zero inclination of $0.7-1.7°$, a certain north-south movement can be seen in Fig. 12.1. To compensate the east-west drift, regular maneuvers have to be performed which are discussed in detail in Sect. 12.3.2.

Whereas MEO satellites provide global coverage, the IGSO and GEO satellites are visible within a limited area, therefore providing only regional services. By the end of 2012, phase 1 of Compass should be concluded with an

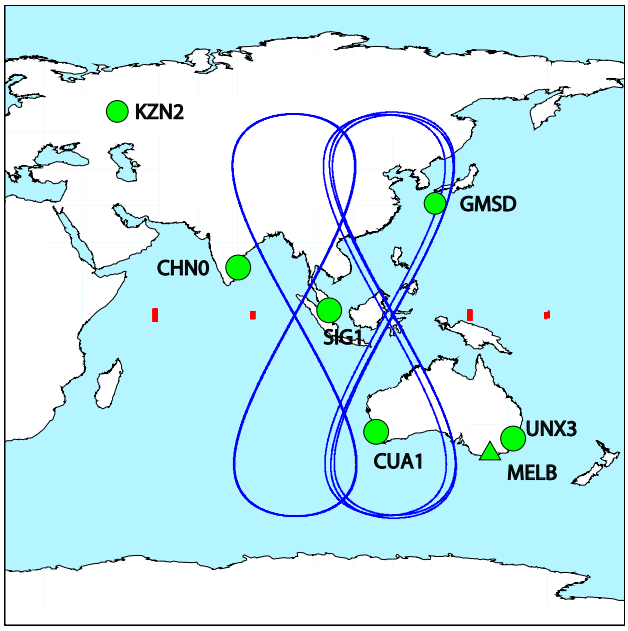

Fig. 12.1: Compass-capable tracking stations and ground tracks of the IGSO (blue) and GEO (red) satellites. Stations used in the orbit and clock determination are indicated by circles. The Melbourne station used for the positioning experiment is indicated by a triangle.

Satellite	PRN	NORAD-ID	COSPAR-ID	Launch Date	Mean Longitude
G1	C01	36287	2010-001A	16 January 2010	140.0°E
G2	C02	34779	2009-018A	14 April 2009	n/a
G3	C03	36590	2010-024A	02 June 2010	84.0°E
G4	C04	37210	2010-057A	31 October 2010	159.9°E
G5	C05	38091	2012-008A	14 February 2012	58.7°E
I1	C06	36828	2010-036A	31 July 2010	120.1°E
I2	C07	37256	2010-068A	17 December 2010	117.9°E
I3	C08	37384	2011-013A	09 April 2011	119.9°E
I4	C09	37763	2011-038A	26 July 2011	94.8°E
I5	C10	37948	2011-073A	01 December 2011	94.7°E
M1	C30	31115	2007-011A	13 April 2007	–
M3	C11	38250	2012-018A	29 April 2012	–
M4	C12	38251	2012-018B	29 April 2012	–
M5	C13	38774	2012-050A	18 September 2012	–
M6	C14	38775	2012-050B	18 September 2012	–

Tab. 12.1: Compass constellation status. The first character of the satellite name refers to the orbit type: G – geostationary orbit, I – inclined geosynchronous orbit, M – medium Earth orbit. C02 does not transmit navigation signals and is drifting unstabilized in the equatorial plane (Flohrer et al, 2011).

Band	Freq. [MHz]	Comment
B1	1561.098	close to GPS L1
B2	1207.14	same as Galileo E5b
B3	1268.52	close to Galileo E6

Tab. 12.2: Frequencies of the three Compass bands.

emphasis on these regional navigation capabilities and a constellation of 5 GEO, 5 IGSO, and 4 MEO satellites (Shi et al, 2013). In phase 2 global coverage is aimed to be achieved by increasing the number of MEO satellites to 27 by 2020 (accompanied by 5 GEO and 3 IGSO satellites). The investigations discussed in this paper are limited to the currently active four GEO and five IGSO satellites. The MEO satellites are not considered due to the problems of Compass M-1 described in Hauschild et al (2012) and the lack of global tracking data.

All Compass satellites transmit triple-frequency navigation signals as listed in Tab. 12.2. The B1 band is close to the GPS L1 frequency of 1575.42 MHz and the B3 band close to the Galileo E6 with 1278.52 MHz. The B2 frequency is identical with Galileo E5b. End of 2011, a draft version of the Compass Interface Control Document (ICD) was released (China Satellite Navigation Office, 2011) and initial operational capability of the regional service was declared. However, the draft ICD only contains information on the B1 frequency. A tracking of the B2 and B3 signals is only possible due to knowledge about the signal structure and ranging codes obtained from analyses with a high-gain antenna (Gao et al, 2009).

A general overview of the Compass system design is given in Qian et al (2012). First results on Compass signal analysis and clock performance are discussed in Gong et al (2012), Hauschild et al (2013), Jun et al (2012), and Montenbruck et al (2013). The Compass satellite orbits determined by Shi et al (2012) have a radial orbit precision of 10 cm. Ge et al (2012) also report radial orbit overlap RMS values of about one decimeter. However, as the RMS values in along-track direction are much larger, Ge et al (2012) give 3D overlaps of 3.3 m for the GEO and 0.5 m for the IGSO satellites. Based on broadcast orbits and clocks, Gao et al (2012) achieved a positioning accuracy of 20 m for the horizontal and 30 m for the vertical component. Using precise orbit products for a relative positioning on a baseline of a few hundred meters, Shi et al (2013) and Shi et al (2012) reached accuracies of $1-4$ cm for a kinematic solution. Static Precise Point Positioning (PPP) resulted in RMS differences of $2-5$ cm w.r.t. GPS-only solutions, similar accuracies are also reported by Ge et al (2012). Montenbruck et al (2013) even achieved a sub-centimeter accuracy on a very short baseline of 8 m by resolving extra-wide-lane ambiguities based on triple-frequency observations.

This publication aims at the determination of precise Compass orbit and clock products as well as their application for positioning. It is based on the experiences obtained from the orbit and clock determination of the Galileo test satellite GIOVE-B (Steigenberger et al, 2011) and QZS-1, the first satellite of the Japanese Quasi-Zenith Satellite System (QZSS; Steigenberger et al, 2012). However, several modifications in the processing were necessary due to different frequencies and in particular due to different characteristics of the GEO orbits (attitude mode, orbit parameterization, maneuver detection and handling). All Compass-related studies of Chinese authors listed before are based on tracking data of national GNSS equipment and possibly non-public information about the Compass system (e.g., antenna offsets and attitude behavior). In contrast to that, our studies are based on independently developed GNSS hardware with well-characterized tracking performance for legacy navigation systems. Furthermore, the processing is strictly based on publicly available information and can thus provide an independent evaluation of the Chinese results.

Section 12.2 introduces the GNSS tracking network and the processing strategy for orbit and clock determination. The code biases originating from using different GNSS, different frequencies, different receivers, and even different firmware versions are discussed. In contrast to Montenbruck et al (2013) who only used 1-day orbits, multi-day arcs are computed to achieve a better orbit accuracy. The impact of different sets of orbit parameters as well as orbital arc lengths on the orbit precision is evaluated in Sect. 12.3 and the maneuvers of the GEO satellites are analyzed. Section 12.4 demonstrates the Compass clock performance. Finally, the Compass orbit and clock products are utilized for a Compass-only precise point positioning whose results are compared with GPS-only solutions in Sect. 12.5.

Abb.	Location	Country	Receiver	Antenna	Radome
CHNO	Chennai	India	TRIMBLE NETR9	TRM55971.00	NONE
CUA1	Curtin	Australia	TRIMBLE NETR9	TRM59800.00	SCIS
GMSD	Nakatane	Japan	TRIMBLE NETR9	TRM59800.00	SCIS
KZN2	Kazan	Russia	TRIMBLE NETR9	TRM59800.00	SCIS
MELB	Melbourne	Australia	TRIMBLE NETR9	TRM55971.00	SCIS
SIG1	Singapore	Rep. of Singapore	TRIMBLE NETR9	LEIAR25.R3	LEIT
UNX3	Sydney	Australia	SEPT ASTERX3	LEIAR25.R3	LEIT

Tab. 12.3: Compass-capable tracking stations.

Basic observable GPS	L1 and L2 code and carrier phase observations
Basic observable Compass	B1 and B2 code and carrier phase observations
Modeled observable	ionosphere-free linear combination
Observation weighting	elevation-dependent weighting with $\frac{1}{\cos^2 z}$ relative weighting of code and phase observations: 1:100
Sampling rate	30 s
Elevation cutoff angle	5°
Tidal displacements	IERS Conventions 2003 (McCarthy and Petit, 2004), FES2004 (Lyard et al, 2006)
Troposphere modeling	NMF (Niell, 1996), hydrostatic a priori delays according to Dach et al (2007)
Phase polarization	Wu et al (1993)
Relativistic effects	IERS Conventions 2003 (McCarthy and Petit, 2004)

Tab. 12.4: Important options of the GNSS processing.

12.2 GNSS Processing

The orbit and clock analysis presented in this paper is based on up to six stations listed in Tab. 12.3 and shown in Fig. 12.1. The stations in Singapore and Sydney are part of the Cooperative Network for GIOVE observation (CONGO; Montenbruck et al, 2010). Data from the Kazan and Nakatane stations are provided via the Multi-GNSS Experiment (MGEX) of the International GNSS Service (IGS; Dow et al, 2009; Weber, 2012). Chennai data is provided by Trimble, the Curtin station is operated by Curtin University. The orbit and clock results discussed in this paper are based on these six stations for the time period 19 March until 7 May 2012 (day of year 79 - 128/2012). Data from the Melbourne station were provided for five complete days by Trimble through Curtin University and was used for Compass-only precise point positioning discussed in Sect. 12.5.

Two different types of receivers are employed at the seven stations. Whereas the Trimble NetR9 is capable of tracking all three Compass frequencies, the Septentrio AsteRx3 only provides B1 and B2 observations. Therefore, the analysis in this paper is limited to these two frequencies. The various antenna types employed at the stations are all designed for multi-GNSS use and cover the full set of Compass and GPS frequency bands.

12.2.1 Processing Strategy

In general, there are two different approaches to determine Compass orbit and clock parameters: (1) all parameters are estimated from Compass observations only; (2) GPS observations are used in addition to derive parameters common to both GNSS (in particular station coordinates, but also receiver clock and troposphere parameters). The latter approach benefits from the fully employed GPS constellation and results in a better quality of the estimated parameters. Therefore, we use this approach and process dual-frequency GPS and Compass data with a modified version of the Bernese GPS Software (Dach et al, 2007; Svehla et al, 2008). A first step is based on a GPS-only PPP utilizing the rapid products of the Center for Orbit Determination in Europe (CODE; Dach et al, 2009) followed by a Compass-only step as discussed for the Galileo test satellite GIOVE-B in Steigenberger et al

Station	Receiver/Firmw.	DCB [ns]	STD [ns]
CHNO	NetR9 FW 4.60	31.9	0.35
CUA1	NetR9 FW 4.4x	1931.1	0.73
GMSD	NetR9 FW 4.4x	1943.9	0.48
KZN2[1]	NetR9 FW 4.4x	1571.8	0.77
KZN2[2]	NetR9 FW 4.4x	1939.7	0.43
SIG1	NetR9 FW 4.4x	1938.1	0.34

[1] 79 – 95/2012
[1] 96 – 125/2012

Tab. 12.5: Differential code biases with respect to the reference receiver in Sydney (Septentrio AsteRx3). Mean values for the time period 79 – 125/2012 and corresponding standard deviations (STD) are given. Due to a significant discontinuity the KZN2 time series is splitted into two time intervals. DCB estimates of NetR9 receivers with FW 4.4x include an offset of about 2 μs related to a firmware problem (see text).

(2011). GPS and Compass data in RINEX 3 (Gurtner and Estey, 2009) format are processed with a sampling rate of 30 s. Station coordinates, troposphere zenith delays and gradients as well as receiver clock parameters are estimated from GPS code and phase observations. These parameters are kept fixed when solving for the Compass-related parameters: Six Keplerian elements, one to nine Radiation Pressure (RPR) parameters (see Sect. 12.3.1) of the model of Beutler et al (1994), epoch-wise satellite clock corrections, and (Differential Code Biases (DCBs).

For Compass, ionosphere-free linear combinations of B1 and B2 code and phase observations are used. To account for systematic differences of the Compass code observables w.r.t. the GPS L1 and L2 code data, DCBs are estimated. The bias of the Sydney station is fixed to zero as a reference since the biases cannot be determined in an absolute sense. As a description of the broadcast message is not available, Compass a priori orbits are taken from Two-Line Elements (TLE) provided by `https://www.space-track.org`. However, the orbit quality of these a priori orbits is fairly limited (differences of several 10s of km to the estimated orbit). Therefore, three orbit iterations have to be done to ensure a converged solution.

Due to the limited public information about the Compass spacecraft design, several assumptions have to be made:

- For the IGSO satellites yaw attitude as for the GPS satellites (Bar-Sever, 1996) is assumed.
- For the GEO satellites it is assumed that the solar panels are oriented to the Sun and normal to the orbital plane (in accord with common practice of geostationary telecommunication satellites; Soop, 1994).
- Satellite vertical antenna offsets are assumed to be 1.093 m, i.e., the z-offset of the SLR retroreflector for GEO (Weiguang, 2011a) as well as IGSO (Weiguang, 2011b) satellites.
- Horizontal satellite antenna phase center offsets as well as the phase center variations are assumed to be zero even though some images of the Compass satellites suggest offsets at the level of several decimeters.

Receiver antenna calibrations from an anechoic chamber for GPS L1 and L2 and all Galileo bands were provided by Becker et al (2010) for the `LEIAR25.R3` and `TRM55971.00` antennas. The GPS L1 and Galileo E5b calibrations were used for the Compass B1 and B2 bands. For the `TRM59800.00` antennas, the GPS L1 and L2 calibrations were used. The `igs08.atx` antenna calibrations (Rebischung et al, 2012) were used for the GPS satellites. For further processing options, see Tab. 12.4.

12.2.2 Code Biases

Receiver-specific DCBs are estimated to account for systematic differences between various receiver types as well as inter-system and inter-frequency biases between GPS and Compass. These biases are composed of GNSS- and frequency-dependent delays in the satellite and receiver electronics. Different Firmware (FW) versions can significantly influence these delays. For the NetR9 receivers, several different firmware versions were used in the time interval considered. Versions 4.43, 4.46, and 4.48 do not result in different bias estimates. Therefore, they are summarized as version 4.4x in the following.

The code bias of the Sydney station (Septentrio AsteRx3) is fixed to zero. Mean DCBs and corresponding standard deviations for the time interval 19 March until 4 May 2012 are listed in Tab. 12.5. The NetR9 receivers with FW 4.4x show an offset of almost 2 μs w.r.t. the reference receiver whereas the bias of the Chennai receiver with FW 4.6 is only 32 ns. According to Riley (2012) the 2 μs bias is caused by the 4.4x firmware of the NetR9 receivers and has been fixed in later firmware releases. The firmware update to version 4.6x results in a bias consistency of the different NetR9 receivers on the level of about 10 ns. For the NetR9 at Kazan, two time intervals with significantly different DCB could be identified. The reason for this behavior is unknown, the day of the DCB discontinuity does not coincide with any equipment changes or firmware updates. The standard deviation of the daily DCB estimates is well below 1 ns for all stations.

For comparison, the DCBs of the Japanese Quasi-Zenith Satellite System (QZSS) discussed in Steigenberger et al (2012) amount to just a few nanoseconds and are thus smaller than the Compass DCBs. With an average STD below 0.5 ns, they are also more stable than the Compass DCBs. However, one has to keep in mind that QZSS and GPS both use the same L1 and L2 signal frequencies. GPS/Galileo DCBs are on the level of $\pm$5 ns for the same receiver type and on the 30 – 50 ns level for different receiver types with a mean STD of 0.7 ns (Hauschild and Steigenberger, 2012).

12.2.3 Post-fit Residuals

The mean post-fit residuals of ionosphere-free code and phase observations obtained from the Compass parameter estimation are listed in Tab. 12.6. The code residuals are on the 0.9 to 1.5 m level and range from 0.64 to 2.23 m for individual satellites (not shown here). The largest code residuals occur at the GMSD station for C05 due to an elevation of only 6.8°. However, one has to remember that observations with low elevations are down-weighted in the parameter estimation (see Sect. 12.2.1). Montenbruck et al (2013) report single-frequency pseudorange errors (including multipath) between 20 and 40 cm for mid and high elevations and up to 1 m for low elevations. Keeping in mind that these errors are amplified by a factor of about three when forming the ionosphere-free linear combination, the code residuals listed in Tab. 12.6 are only slightly worse.

Station	Code [m]		Phase [cm]	
	IGSO	GEO	IGSO	GEO
CHNO	1.30	1.16	2.7	2.8
CUA1	1.29	1.32	1.7	2.9
GMD1	1.06	1.19	1.6	14.1
KZN2	0.81	1.51	2.0	3.1
SIG1	1.08	0.89	1.5	1.6
UNX3	1.45	1.24	1.8	1.9

Tab. 12.6: Station-specific mean values of the post-fit code and phase residuals (ionosphere-free linear combination) of Compass GEO and IGSO satellites.

The phase residuals in Tab. 12.6 are in general on the several centimeter level with a range of 1 to 53 cm for individual satellites (C05 at GMSD again has the largest residuals). All phase residuals are larger for the GEO satellites compared to the IGSO satellites. However, the differences are only 1 mm for half of the stations. For the other stations, the increased GEO residuals can be explained by one particular satellite at low elevation. Montenbruck et al (2013) give single-frequency phase noise and multipath errors of 1 – 3 mm. When excluding the GEO phase residuals of GMSD, the phase residuals listed in Tab. 12.6 are larger by a factor of 3 – 5 reflecting the unmodeled or not properly modeled effects mentioned in Sect. 12.2.1.

The code residuals are in general on the same level as the residuals of GIOVE-B reported by Steigenberger et al (2011) whereas the phase residuals are in general larger by a factor of about 1.5. However, one has to be aware that different receiver types were used and that it is in general difficult to directly draw conclusions from the residuals about the orbit accuracy.

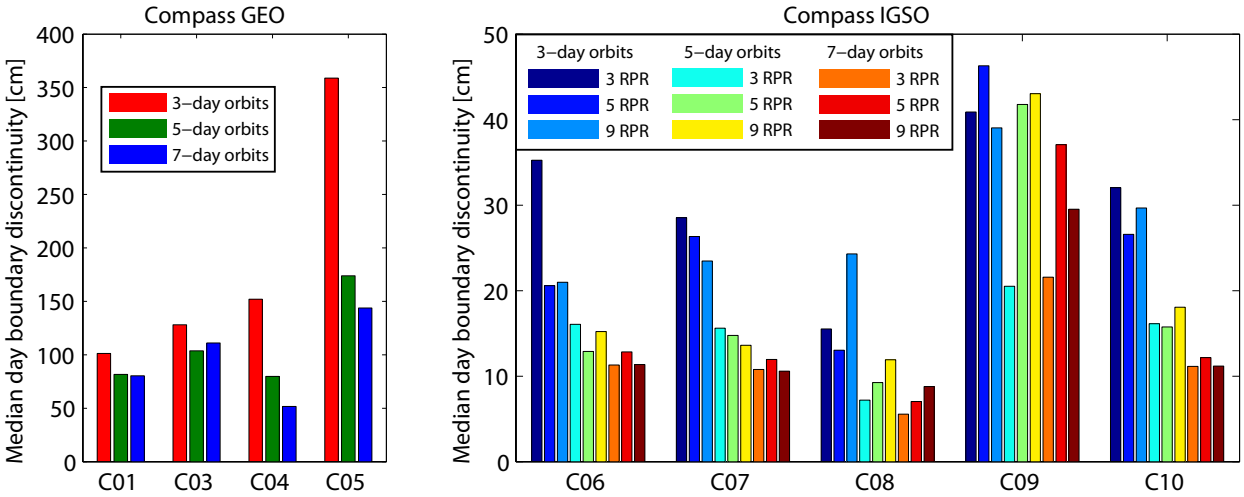

Fig. 12.2: Median day boundary discontinuities of Compass GEO (left) and IGSO (right) satellites. Please note the different scale of the y-axis. For the GEO satellites only one direct radiation pressure parameter was estimated.

12.3 Orbit Results

12.3.1 Orbit Parameterization

In addition to the six Keplerian elements, dynamic parameters accounting for the RPR of the Sun have to be estimated in the orbit determination process. The model of Beutler et al (1994) comprises a total of nine constant and periodic terms in the three axes of a Sun-oriented coordinate system. Within this paper the following subsets of RPR parameters are considered for estimation in the orbit determination process:

- 1 parameter: direct RPR term
- 3 parameters: three constant terms only
- 5 parameters: three constant terms and one pair of sine/cosine terms in the direction perpendicular to the direction of the Sun and the solar panel axis
- 9 parameters: full set

In general a small parameter set results in a more robust orbit determination whereas a larger parameter set may provide an improved modeling of the actual orbit dynamics. In order to stabilize the orbit parameter estimates determined from a very small network of six stations only, the orbit parameters of consecutive days are combined to multi-day solutions. In the following, orbital arc lengths of three, five, and seven days are used. That means, only one set of Keplerian elements and RPR parameters is estimated per arc (except for maneuvers, see Sect. 12.3.2).

As a quality indicator for the internal consistency of the orbits, *day boundary discontinuities* of two consecutive days are used, i.e., the 3D difference of the orbit positions at midnight between two consecutive days. Another quantity for the orbit quality is the *2-day orbit fit RMS*: a new orbit is fitted through the orbit positions of two consecutive days. The RMS of the new orbit w.r.t. the original orbit is a measure for the consistency of the original orbits (see Steigenberger et al (2011) for a more detailed description). Finally, Satellite Laser Ranging (SLR) residuals provide an independent validation of the microwave-derived orbits (e.g., Urschl et al, 2005). From the multi-day solutions, only the middle day of the arc is used for the computation of the day boundary discontinuities, the orbit fit RMS values, and the SLR residuals.

First tests with these parameterizations resulted in a very bad orbit quality of the GEO satellites, in particular in the along-track direction. Depending on their location and outages of individual stations, the GEO satellites are observed by 2 – 6 stations simultaneously. More important, the changes of the observation geometry of the GEO satellites are much smaller compared to the IGSO satellites: as a consequence, strong correlations occur between the orbital elements, radiation pressure parameters, ambiguities, and DCBs. In particular, it is no longer possible to estimate a constant Y-bias in the solar radiation pressure model due to a pronounced correlation with the location of the orbital plane relative to the geocenter.

As a consequence of these correlations, large differences of more than 10 m occur at the day boundaries even if only three RPR parameters are estimated and multi-day arcs are used. In order to cope with these correlations, only one RPR parameter in the direction of the Sun is estimated for the GEO satellites. This reduction of estimated parameters significantly improves the orbit quality of the GEO satellites although it is still worse compared to the IGSO satellites.

Day boundary discontinuities for solutions with different arc length (GEO and IGSO satellites) and different number of estimated RPR parameters (IGSO satellites only) are shown in Fig. 12.2. The orbit quality of the IGSO satellites is on the one to four decimeter level whereas it is worse by a factor of up to 5−7 for the GEO satellites resulting in day boundary discontinuities on the one meter level. The quality of the GEO satellite C05 is even worse as it is only tracked by three stations resulting in a fairly limited orbit quality. The benefit of increasing the arc length is in particular pronounced for C05: the day boundary discontinuities decrease by a factor of two when extending the arc length from three to five days. A further extension to seven days results in a much smaller improvement of only 17%.

In general, the orbit quality improves with increasing arc length. For most IGSO satellites, a 7-day arc with three RPR parameters provides the best performance (except for C07). Independent from the solution, C09 shows the worst day boundary discontinuities of the IGSO satellites. The IGSO orbit quality of the best solutions is on the one to two decimeter level which is similar to results for QZSS reported in Steigenberger et al (2012) based on a regional tracking network with five stations.

The 2-day orbit fit RMS values are listed in Tab. 12.7 for the GEO and in Tab. 12.8 for the IGSO satellites. They are in general on the two decimeter level for the GEO satellites with only small changes due to different arc length. However, C05 (which already showed a bad performance in the day boundary discontinuities) is worse by a factor three for the 3-day solutions but only a factor two for the 5- and 7-day solutions. Compared to Fig. 12.2, the orbit fit RMS values are smaller by a factor of about five than the day boundary discontinuities. This result is expected as the day boundary discontinuities represent the differences between two individual orbit positions at one epoch whereas the orbit fits are some kind of average over two days. Although the orbit fit RMS values are by far too optimistic due to the smoothing effect of multi-day solutions (the longer the arc length, the larger the smoothing effect), they allow for a relative assessment of solutions with the same arc length but different number of RPR parameters (IGSO satellites only).

Arc length	RPR	C01	C03	C04	C05
3-day	1	23.2	23.2	23.3	65.6
5-day	1	22.1	22.9	18.7	37.0
7-day	1	21.6	23.2	18.1	34.7

Tab. 12.7: 2-day orbit fit RMS values of Compass GEO satellites in centimeters.

The orbit fits of the IGSO satellites in Tab. 12.8 are all below one decimeter and even below one centimeter for the best performing satellites/solutions. Independent from the solution, C09 shows the worst performance of the IGSO satellites (factor 1.9 to 5.7 worse than the best performing IGSO satellite per solution) as for the day boundary discontinuities. The reason for this behavior is unknown. In contrast to the orbit quality, the clock quality of C09 is the best of the IGSO satellites, see Sect. 12.4. For the 3-day solutions three or five RPR parameters give the best RMS values. For the 5- and 7-day solutions, three RPR parameters give the smallest RMS values. Nine RPR parameters in general result in the worst RMS values for a fixed arc length.

Independent from the arc length, the 2-day orbit fits of the GEO satellites show a clear time dependency: the RMS values get larger with increasing elevation of the Sun above the orbital plane (close to zero at the beginning of the time interval, about 16° at the end). This effect is probably related to problems with the orbit modeling: estimating only one direct RPR parameter might be a too simple model and/or the attitude assumption of Sect. 12.2.1 could be erroneous. However, no information about the true attitude behavior is available. A similar behavior is visible in the time series of day boundary discontinuities but less pronounced. The IGSO satellites do not show such a time dependency.

Whereas day boundary discontinuities and orbit fit RMS values only allow to evaluate the precision of the satellite orbits, Satellite Laser Ranging (SLR) residuals provide the opportunity to assess the orbit accuracy as they are based on an independent observation technique. SLR retroreflector offsets for the GEO and IGSO satellites are given in Weiguang (2011a) and Weiguang (2011b), respectively. Although all Compass satellites are equipped with laser retroreflectors, only three of the GEO and IGSO satellites are presently tracked by the stations of the

Arc length	RPR	C06	C07	C08	C09	C10
3-day	3	3.7	3.1	1.8	4.9	3.4
	5	3.0	3.0	1.8	8.1	3.2
	9	3.8	4.8	5.2	7.4	5.4
5-day	3	1.7	1.6	0.8	3.8	1.7
	5	1.8	1.9	1.3	6.5	2.0
	9	3.0	2.5	2.2	8.6	3.1
7-day	3	1.3	1.0	0.7	2.7	1.0
	5	1.7	1.6	0.9	5.1	1.5
	9	2.2	1.8	1.3	5.9	1.9

Tab. 12.8: 2-day orbit fit RMS values of Compass IGSO satellites in centimeters.

International Laser Ranging Service (Pearlman et al, 2002). For the time period considered in this paper, only a very limited number of Normal Points (NPs) of the GEO satellite C01 and the IGSO satellite C08 are available (SLR tracking of C10 started only in July 2012): two SLR stations tracked C01 (Changchun, Yarragadee: 10 NPs) and three SLR stations tracked C08 (Changchun, Shanghai, Yarragadee: 42 NPs). One C08 pass of Changchun (7 NPs) had to be excluded from the SLR analysis due to unreasonable NP-to-NP variations of up to 1.7 m.

Offset, standard deviation, and RMS of the SLR residuals are listed in Tab. 12.9. With STDs below one decimeter and offsets on the one-to-two decimeter level, these validation results are even better compared to the day boundary discontinuities, in particular for the GEO satellite C01. However, one has to keep in mind that the SLR validation primarily assesses the radial component whereas the largest errors occur in the along-track direction.

Satellite	# NP	Offset	STD	RMS
C01	10	−13.1 cm	7.1 cm	14.7 cm
C08	35	21.8 cm	9.7 cm	23.9 cm

Tab. 12.9: SLR validation of the GEO satellite C01 and the IGSO satellite C08 (5-day solution with 5 RPR parameters).

12.3.2 GEO Orbit Maneuvers

Compass is the only GNSS with geostationary satellites being a part of the nominal satellite constellation. Due to gravitational perturbations of Earth, Sun, and Moon, station-keeping maneuvers are necessary in regular intervals to maintain the designated positions in the equatorial plane (Soop, 1994). According to Jun et al (2012) east-west (or longitude) station keeping maneuvers are performed every 25 to 35 days and north-south (or inclination) maneuvers every two years. The maneuvers of the Compass GEO satellites detected from the orbit analysis of the 50-day test period are listed in Tab. 12.10. All maneuvers are east-west maneuvers. The main velocity change occurs in the along-track direction with velocity changes of up to 100 mm/s. The negative sign stands for decelerating the satellite and thus lowering the orbital height.

In the case of a maneuver, separate sub-arcs are set up for the maneuvering satellite in a multi-day solution, i.e., separate orbital elements and radiation pressure parameters before and after the maneuver are estimated. For an ideal maneuver modeling, the two independent orbital arcs would intersect in one point. However, due to errors in the orbit determination, the two orbits in general do not intersect. Therefore, the maneuver time as well as the velocity changes listed in Tab. 12.10 are determined from the closest approach of these two separate arcs.

C01 is the only satellite with two maneuvers separated by 26 days, for each of the other GEO satellites only a single maneuver takes place. However, as only a 50-day time interval is considered in the analysis, the maneuver frequency is well within the general operations concept given by Jun et al (2012). The sub-satellite longitude of individual GEOs varies by $\pm 0.1^\circ$ to $\pm 0.15^\circ$ and the latitude by $\pm 0.8^\circ$ to $\pm 1.8^\circ$. Compared to other GEO satellites, this control box is large: typical values are $\pm 0.1^\circ$ in east-west and north-south direction (Withers, 1999).

Date		Time	Sat.	Velocity change [mm/s]				Drift accel.	Maneuver rate
				Total	Radial	Along-Track	Cross-Track	[mdeg/d^2]	[mm/s/month]
6 Apr	2012	4:43	C01	84.3	3.5	−84.1	−5.3	−1.37	116
2 May	2012	11:00	C01	103.6	−2.1	−103.3	−7.7		
16 Apr	2012	9:11	C03	77.1	−7.1	−76.6	−4.8	−0.62	53
23 Apr	2012	7:32	C04	31.6	−2.3	−31.1	−5.3	−0.14	12
10 Apr	2012	∼1:00	C05			n/a		1.07	−91

Tab. 12.10: Maneuvers of Compass GEO satellites. The exact time and the velocity change of the maneuver of C05 could not be determined properly due to only 2 − 3 stations tracking this satellite. Following the estimated Δv the drift acceleration due to asphericity of the Earth is provided for the respective sub-satellite longitude of each GEO. The last column lists the maneuver magnitude needed to compensate for the drift acceleration.

The drift accelerations given in Tab. 12.10 were derived from Montenbruck (2009) based on the mean longitude given in Tab. 12.1. The drift acceleration of C04 is small compared to the other GEO satellites as it is located close to an unstable point at 162°E where the acceleration is almost zero. The last column of Tab. 12.10 lists the velocity changes necessary to compensate for the drift acceleration accumulated during one month. Assuming a common control window size for all Compass GEOs would require a maneuver spacing of 22 − 79 days, i.e., a wider range than the 25 − 35 days given in Jun et al (2012).

12.4 Clock Results

All Compass satellites are equipped with Rubidium clocks from manufacturers in Switzerland and China (Han et al, 2011). To assess the performance of the Compass on board clocks, modified Allan deviations computed from the 30 s clock estimates are shown in Fig. 12.3. Median values per satellite were derived from all days with complete clock estimates (i.e., no data gaps). In general, the clock performance of the IGSO and GEO satellites is on the same level. The bad orbit performance of C05 mentioned in Sect. 12.3 reflects itself in an increased modified Allan deviation of the apparent clock at longer integration times which is most likely unrelated to the physical clock behavior. Compared to the Rubidium clock of the first Galileo in-orbit validation satellite (IOV-1), the apparent performance of the Compass clocks is in general worse by a factor of about two, in particular at longer integration times. However, at shorter periods the C03 clock seems to be competitive with the IOV-1 clock although both do not reach the stability level of the latest generation of GPS Rubidium clocks (G25 shown as an example for the GPS IIF satellites).

At an integration time of 1000 s the GEO satellites show an Allan deviation between 8 and $12 \cdot 10^{-14}$, the performance of the IGSO clocks is similar with values between 8 and $17 \cdot 10^{-14}$. These results are in general slightly better than those of Montenbruck et al (2013) based on a three-way carrier phase approach (Hauschild et al, 2013). The degraded clock performance of C10 compared to the other IGSO satellites already mentioned by Montenbruck et al (2013) is also evident in Fig. 12.3.

The Allan deviation of the best performing IGSO satellite C09 given in Gong et al (2012) is also slightly worse compared to the present study. Gong et al (2012) show Allan deviations of $40 \cdot 10^{-14}$ at an integration time of 100 s and $10 \cdot 10^{-14}$ at 1000 s with smoothed broadcast ephemeris compared to $30 \cdot 10^{-14}$ and $8 \cdot 10^{-14}$ in the present study (see Fig. 12.3). This effect might have two different explanations: (1) degraded orbit quality of the smoothed broadcast orbits compared to our post-processed multi-day orbits; (2) quality of the reference clock. The reference clock for the clock solutions shown in Fig. 12.3 is a highly stable hydrogen maser used in the CODE solution as reference whereas the reference clock is not explicitly specified in Gong et al (2012).

Median values of the clock drift are given in Tab. 12.11. For C05, two different time intervals are given due to a changed clock behavior, probably due to a clock adjustment. Except for the first time period of C05, all clock drifts are in the range of 0.7 − 7 μs/d. These values are in good agreement with Montenbruck et al (2013) and in the same order of magnitude as the GPS satellite clocks.

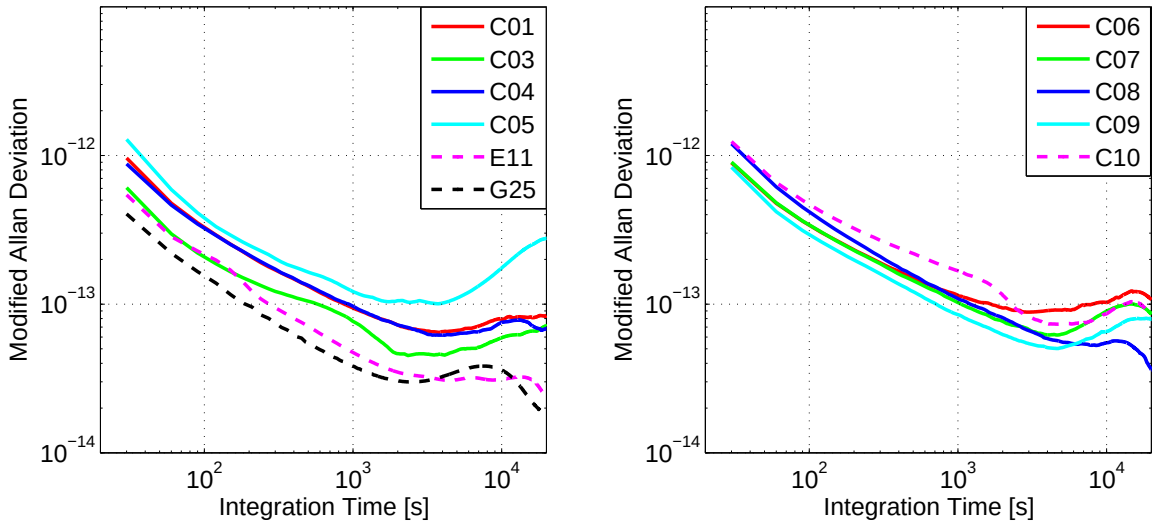

Fig. 12.3: Modified Allan deviation of Compass GEO (left) and IGSO (right) satellites. Median values for the time period 79 – 128/2012 are shown. For comparison purposes, the performance of the first Galileo IOV satellite (E11) and the first GPS Block IIF satellite (G25) Rubidium clocks are also shown in the left plot.

Satellite	PRN	No. days	Drift [μs/d]
G1	C01	38	3.56
G3	C03	29	0.67
G4	C04	37	−0.66
G5	C05	15 [1]	−27.39
		17 [2]	1.23
I1	C06	41	1.37
I2	C07	42	0.67
I3	C08	46	1.34
I4	C09	44	−6.47
I5	C10	48	−2.08

[1] 79 – 106/2012
[1] 107 – 128/2012

Tab. 12.11: Median values of Compass clock drift. Only full days without gaps are considered.

12.5 Compass-only PPP

For five days (28 March – 1 April 2012), data of an additional tracking station in Melbourne (MELB, Australia) were provided by Trimble and Curtin University (Perth, Australia) to test the PPP performance of the orbit and clock products discussed above. The Compass visibility is quite limited at Melbourne with 5 to 8 satellites simultaneously visible mainly in the north-west quadrant. As a consequence, the GDOP varies between 3.6 and 8.2. In addition to the station coordinates, troposphere zenith delays with 2 hours parameter spacing, epoch-wise receiver clocks, and float ambiguities were estimated.

The RMS differences between GPS-only and Compass-only coordinate estimates shown in Tab. 12.12 are on the several centimeter level. Although the GEOs have a worse orbit accuracy compared to the IGSOs, they significantly improve the Compass-only positioning accuracy, in particular for the height component. The accuracy of the Compass-only PPP is in the same order of magnitude as the results of Shi et al (2012). They used a larger ground network of 15 stations but only four IGSO and three GEO satellites for the generation of satellite orbits and clocks used for their PPP experiment also covering a period of five days. The RMS differences in Tab. 12.12 are slightly better than results given in Montenbruck et al (2013) based on four days of the same receiver at

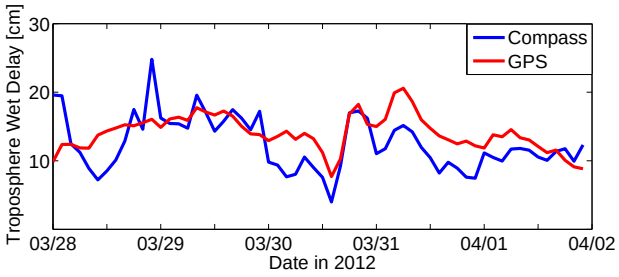

Fig. 12.4: GPS-only and Compass-only troposphere wet delays of station Melbourne (2 h parameter spacing).

Melbourne. The reason for this improvement is the better accuracy of orbits and clocks based on multi-day solutions compared to the 1-day products used by Montenbruck et al (2013).

Satellites	North [cm]	East [cm]	Up [cm]
IGSO + GEO	1.7	4.1	6.4
IGSO	2.0	5.1	11.7

Tab. 12.12: Results of Compass-only PPP: RMS differences of five daily solutions w.r.t. GPS-only station coordinates.

The PPP performance of the orbits and clocks computed with different arc length and number of RPR parameters is on a similar level: the RMS differences w.r.t. the GPS-only solution range from 1.4 to 2.7 cm for the north component, 2.8 to 4.9 cm for the east component and 5.2 to 7.1 cm for the height component. No clearly superior solution could be identified.

The troposphere Zenith Wet Delays (ZWDs) derived from GPS and Compass (Fig. 12.4) in general show a similar behavior. However, due to the smaller and more variable satellite number, the Compass ZWDs are much more noisy. This is not astonishing due to the smaller observation number and reduced coverage of the sky for Compass compared to GPS. The GPS/Compass ZWD differences show a bias of 1.5 cm and have a standard deviation of 3.4 cm.

Systematic biases of the GPS and Compass become manifest in the receiver clock estimates. The mean bias (DoY 89 excluded due to an outage-induced clock jump) between the GPS-only and Compass-only receiver clock parameters is with 1953.7 ns in the same order of magnitude as the DCBs of the NetR9 receivers with firmware 4.4x used in the orbit and clock determination (see Tab. 12.5).

12.6 Conclusions

Compass orbit and clock parameters were estimated with a small tracking network of four to six stations. An orbit accuracy on the several decimeter level for the GEO and few decimeter level for the IGSO satellites could be achieved. Due to the limited knowledge of the Compass system, several assumptions had to be made that might be erroneous. More detailed knowledge of the satellite behavior will contribute to an improved modeling of the satellites and as a consequence to a better orbit quality. In particular, information on Compass attitude modes and antenna offsets will be required to fully exploit the accuracy of the available observations.

However, the largest problem of the GEO orbit determination are the small changes in the observation geometry responsible for large correlations between the estimated parameters. Limiting the number of RPR parameters to only one direct parameter helped to cope with these correlations but the dependence of the orbit quality on the position of the Sun above the orbital plane also shows the deficits of this approach. On the other hand, the large orbit errors encountered in the GEO orbit determination do not render them useless for positioning, since the large along-track errors have only a 5 – 10% contribution to the modeled pseudorange on average.

Code biases due to different satellite systems and frequencies are on the level of up to 10 ns for the same receiver type but can reach up to 30 ns if different receivers are used. The stability of the Compass GEO and IGSO clocks is on a similar level although it is slightly worse compared to other GNSS. Precise orbit and clock products for the regional Compass system allow for a precise point positioning with Compass observations only. Although the

Compass visibility conditions for the Compass-only PPP were not optimal, a few centimeter accuracy compared to GPS could be achieved.

A larger tracking network, in particular a network providing global coverage for the MEO satellites is an important step for the further improvement of the Compass orbit and clock products. However, this is probably only a matter of time, as more and more Compass capable receivers are employed, in particular in the framework of the IGS MGEX project. A major deficiency of Compass (in particular for real-time users) is the lack of public availability of broadcast orbits as the corresponding information is not published in the preliminary version of the ICD. The situation will hopefully change in the near future with the publication of the full ICD.

Acknowledgements

We'd like to thank the station operators Shinichi Nakamura (Japan Aerospace Exploration Agency), Noor Raziq (Curtin University, Australia), and Renat Zagretdinov (Kazan Federal University, Russia) for their support. The efforts of the IGS MGEX campaign (Weber, 2012) in providing multi-GNSS data are acknowledged. CHN0 tracking data were kindly provided by Trimble.

Bibliography

Bar-Sever Y (1996) A new model for GPS yaw attitude. Journal of Geodesy 70(1):714–723, DOI 10.1007/BF00867149

Becker M, Zeimetz P, Schönemann E (2010) Antenna chamber calibrations and antenna phase center variations for new and existing GNSS signals. In: IGS Workshop 2010, 28 June – 2 July 2010, Newcastle

Beutler G, Brockmann E, Gurtner W, Hugentobler U, Mervart L, Rothacher M, Verdun A (1994) Extended orbit modeling techniques at the CODE processing center of the international GPS service for geodynamics (IGS): theory and initial results. Manuscripta Geodaetica 19:367–386

Chen H, Huang Y, Chiang K, Yang M, Rau R (2009) The performance comparison between GPS and BeiDou-2/COMPASS: a perspective from Asia. Journal of the Chinese Institute of Engineers 32(5):679–689

China Satellite Navigation Office (2011) BeiDou Navigation Satellite System Signal In Space Interface Control Document (Test Version). Tech. rep., URL http://www.beidou.gov.cn/attach/2011/12/27/201112273f3be6124f7d4c7bac428a36cc1d1363.pdf

Dach R, Hugentobler U, Fridez P, Meindl M (eds) (2007) Bernese GPS Software Version 5.0. Astronomical Institute, University of Bern, Bern, Switzerland

Dach R, Brockmann E, Schaer S, Beutler G, Meindl M, Prange L, Bock H, Jäggi A, Ostini L (2009) GNSS processing at CODE: status report. Journal of Geodesy 83(3-4):353–365, DOI 10.1007/s00190-008-0281-2

Dow J, Neilan R, Rizos C (2009) The International GNSS Service in a changing landscape of Global Navigation Satellite Systems. Journal of Geodesy 83(3-4):191–198, DOI 10.1007/s00190-008-0300-3

Dragon in Space (2012) URL http://web.archive.org/web/20121028161922/http://www.dragoninspace.com/navigation/beidou.aspx, accessed 04-09-2012

Flohrer T, Choc R, Bastida B (2011) Classification of Geosynchronous Objects. Issue 13, European Space Agency, Space Debris Office, Darmstadt, GEN-DB-LOG-00074-OPS-GR

Gao GX, Chen A, Lo S, Lorenzo DD, Walter T, Enge P (2009) Compass-M1 broadcast codes in E2, E5b, and E6 frequency bands. IEEE Journal of Selected Topics in Signal Processing 3(4):599–612, DOI 10.1109/JSTSP.2009.2025635

Gao Z, Zhang H, Hu Z, Peng J (2012) Performance analysis of BeiDou Satellite Navigation System (4IGSO + 3GEO) in standard positioning and navigation. In: China Satellite Navigation Conference (CSNC) 2012 Proceedings, Springer, Lecture Notes in Electrical Engineering, vol 159, pp 177–186, DOI 10.1007/978-3-642-29187-6_17

Ge M, Zhang H, Jia X, Song S, Wickert J (2012) What is achievable with current COMPASS constellation? In: ION GNSS 2012, pp 331–339

Gong H, Yang W, Wang Y, Zhu X, Wang F (2012) Comparison of short-term stability estimation methods of GNSS on-board clock. In: Sun J, Liu J, Yang Y, Fan S (eds) China Satellite Navigation Conference (CSNC) 2012 Proceedings, Springer, Lecture Notes in Electrical Engineering, vol 160, pp 503–513, DOI 10.1007/978-3-642-29175-3_46

Gurtner W, Estey L (2009) RINEX, The Receiver Independent Exchange Format, Version 3.01. Tech. rep., URL ftp://ftp.igs.org/pub/data/format/rinex301.pdf

Han C, Yang Y, Cai Z (2011) BeiDou Navigation Satellite System and its time scales. Metrologia 48(4):S213–S218, DOI 10.1088/0026-1394/48/4/S13

Hauschild A, Steigenberger P (2012) Combined GPS and GALILEO real-time clock estimation with DLR's RETICLE system. In: ION GNSS 2012, pp 302–309

Hauschild A, Montenbruck O, Sleewaegen J, Huisman L, Teunissen P (2012) Characterization of Compass M-1 signals. GPS Solutions 16(1):117–126, DOI 10.1007/s10291-011-0210-3

Hauschild A, Montenbruck O, Steigenberger P (2013) Short-term analysis of GNSS clocks. GPS Solutions 17(3):295–307, DOI 10.1007/s10291-012-0278-4

Jun X, Jingang W, Hong M (2012) Analysis of Beidou Navigation Satellites In-orbit State. In: China Satellite Navigation Conference (CSNC) 2012 Proceedings, Springer, Lecture Notes in Electrical Engineering, vol 161, pp 111–122, DOI 10.1007/978-3-642-29193-7_10

Lyard F, Lefevre F, Letellier T, Francis O (2006) Modelling the global ocean tides: modern insights from FES2004. Ocean Dynamics 56(5-6):394–415, DOI 10.1007/s10236-006-0086-x

McCarthy DD, Petit G (2004) IERS Conventions (2003). IERS Technical Note 32, Verlag des Bundesamtes für Kartographie und Geodäsie, Frankfurt am Main

Montenbruck O (2009) Orbital mechanics. In: Ley W, Wittmann K, Hallmann W (eds) Handbook of Space Technology, Wiley, pp 52–82

Montenbruck O, Hauschild A, Hessels U (2010) Characterization of GPS/GIOVE sensor stations in the CONGO network. GPS Solutions 15(3):193–205, DOI 10.1007/s10291-010-0182-8

Montenbruck O, Hauschild A, Steigenberger P, Hugentobler U, Teunissen P, Nakamura S (2013) Initial assessment of the COMPASS/BeiDou-2 regional navigation satellite system. GPS Solutions 17(2):211–222, DOI 10.1007/s10291-012-0272-x

Niell A (1996) Global mapping functions for the atmosphere delay at radio wavelengths. Journal of Geophysical Research 101(B2):3227–3246, DOI 10.1029/95JB03048

Pearlman M, Degnan J, Bosworth J (2002) The International Laser Ranging Service. Advances in Space Research 30(2):125–143, DOI 10.1016/S0273-1177(02)00277-6

Qian S, Jun Z, Yanbo Z (2012) China Compass PNT service architecture and outlook. In: Proceedings of ION ITM 2012, pp 848–854

Rebischung P, Griffiths J, Ray J, Schmid R, Collilieux X, Garayt B (2012) IGS08: the IGS realization of ITRF2008. GPS Solutions 16(4):483–494, DOI 10.1007/s10291-011-0248-2

Riley S (2012) personal communication

Shi C, Zhao Q, Li M, Tang W, Hu Z, Lou Y, Zhang H, Niu X, Liu J (2012) Precise orbit determination of Beidou satellites with precise positioning. Science China Earth Sciences 55(7):1079–1086, DOI 10.1007/s11430-012-4446-8

Shi C, Zhao Q, Hu Z, Liu J (2013) Precise relative positioning using real tracking data from COMPASS GEO and IGSO satellites. GPS Solutions 17(1):103–119, DOI 10.1007/s10291-012-0264-x

Soop E (1994) Handbook of Geostationary Orbits. Kluwer, ISBN 0-7923-3054-4

Steigenberger P, Hugentobler U, Montenbruck O, Hauschild A (2011) Precise orbit determination of GIOVE-B based on the CONGO network. Journal of Geodesy 85(6):357–365, DOI 10.1007/s00190-011-0443-5

Steigenberger P, Hauschild A, Montenbruck O, Rodriguez-Solano C, Hugentobler U (2012) Orbit and clock determination of QZS-1 based on the CONGO network. In: Proceedings of ION ITM 2012, pp 1265–1274

Svehla D, Heinze M, Rothacher M, Steigenberger P, Dähnn M, Kirchner M (2008) Combined processing of GIOVE-A and GPS measurements using zero- and double-differences. Geophysical Research Abstracts 10, sRef-ID: 1607-7962/gra/EGU2008-A-11383

Urschl C, Gurtner W, Hugentobler U, Schaer S, Beutler G (2005) Validation of GNSS orbits using SLR observations. Advances in Space Research 36(3):412–417, DOI 10.1016/j.asr.2005.03.021

Weber R (2012) IGS GNSS Working Group. In: Meindl M, Dach R, Jean Y (eds) International GNSS Service Technical Report 2011, Jet Propulsion Laboratory, Pasadena, pp 159–163

Weiguang G (2011a) ILRS SLR mission support request for Compass-G1. URL `http://ilrs.gsfc.nasa.gov/docs/ilrsmsr_G11.pdf`

Weiguang G (2011b) ILRS SLR mission support request for Compass-I3. URL `http://ilrs.gsfc.nasa.gov/docs/ilrsmsr_I31.pdf`

Withers D (1999) Radio Spectrum Management. Institution of Engineering and Technology

Wu J, Wu S, Hajj G, Bertiger W, Lichten S (1993) Effects of antenna orientation on GPS carrier phase. Manuscripta Geodaetica 18:91–98

Part III

Appendices

A Abbreviations

1WCP	One-way Carrier Phase
3WCP	Three-way Carrier Phase
AC	Analysis Center
ACC	Analysis Center Coordinator
ADEV	Allan Deviation
AltBOC	Alternative Binary Offset Carrier
BCE	Broadcast Ephemeris
BDS	BeiDou Navigation Satellite System
BINEX	BINary EXchange (Format)
BKG	Bundesamt für Kartographie und Geodäsie, Frankfurt am Main, Germany
BMBF	Bundesministerium für Bildung und Forschung, Germany
CDDIS	Crustal Dynamics Data Information System
CDMA	Code Division Multiple Access
CHAMP	Challenging Minisatellite Payload
CLS	Collecte Localisation Satellites
CNES	Centre National d'Etudes Spaciales
CONGO	Cooperative Network for GIOVE Observation
CODE	Center for Orbit Determination in Europe
COSPAR	Committee on Space Research
COST	European Cooperation in Science and Technology
CPF	Consolidated Prediction Format
CPR	Cycle-per-Revolution
CS	Commercial Service
CSR	Center for Space Research, University of Texas, Austin, USA
CUT	Curtin University, Australia
DBD	Day Boundary Discontinuity
DCB	Differential Code Bias
DFG	Deutsche Forschungsgemeinschaft
DGFI	Deutsches Geodätisches Forschungsinstitut, München, Germany
DLR	Deutsches Zentrum für Luft- und Raumfahrt, Germany
DoD	Department of Defense
DoY	Day of Year
DORIS	Doppler Orbitography and Radiopositioning Integrated by Satellite
DREF	Deutsches GPS-Referenz Netz

DTM	Digital Terrain Model
EC	European Commission
ECMWF	European Centre for Medium-Range Weather Forecasts
EGNOS	European Geostationary Navigation Overlay System
EOP	Earth Orientation Parameter
ERP	Earth Rotation Parameter
ESA	European Space Agency
FDMA	Frequency Division Multiple Access
FM	Flight Model
FOC	Full Operational Capability
FW	Firmware
GA	Geoscience Australia
GAGAN	GPS-Aided Geo-Augmented Navigation
GDOP	Geometric Dilution of Precision
GEO	Geostationary Earth Orbit
GESS	Galileo Experimental Sensor Station
GFZ	Deutsches GeoForschungsZentrum, Potsdam, Germany
GGOS	Global Geodetic Observing System
GGTO	GPS Galileo Time Offset
GIA	Global Isostatic Adjustment
GIOVE	Galileo in Orbit Validation Element
GLDAS	Global Land Data Assimilation Systems
GLONASS	Globalnaya Navigatsionnaya Sputnikovaya Sistema (Global Navigation Satellite System)
GMF	Global Mapping Function
GNSS	Global Navigation Satellite System
GOCE	Gravity field and steady-state Ocean Circulation Explorer
GPS	Global Positioning System
GPST	GPS Time
GPT	Global Pressure and Temperature (model)
GRACE	Gravity Recovery And Climate Experiment
GRGS	Groupe de Recherche de Géodésie Spatial
GSTB	Galileo System Test Bed
HartRAO	Hartebeesthoek Radio Astronomy Observatory
IAG	International Association of Geodesy
ICD	Interface Control Document
IERS	International Earth Rotation and Reference Systems Service
IF	Ionosphere-free
IGEX	International GLONASS Experiment
IGG	Institut für Geodäsie und Geoinformation, Universität Bonn, Germany

IGN	Institut Géographique National
IGS	International GNSS Service
IGLOS-PP	International GLONASS Service Pilot Project
IGSO	Inclined Geosynchronous Orbit
ILRS	International Laser Ranging Service
IMF	Isobaric Mapping Function
IOC	Initial Operational Capability
IOV	In-Orbit Validation
IRNSS	Indian Regional Navigation Satellite System
ISRO	Indian Space Research Organisation
ITRF	International Terrestrial Reference Frame
ITRS	International Terrestrial Reference System
ITU	International Telecommunication Union
IVS	International VLBI Service for Geodesy & Astrometry
JAXA	Japan Aerospace Exploration Agency
JPL	Jet Propulsion Laboratory, Pasadena, USA
JPS	Javad Positioning Systems
KEG	Kommission für Erdmessung und Glaziologie der Bayerischen Akademie der Wissenschaften, München, Germany
KFU	Kazan Federal University, (Russia)
LB2	Leica Binary 2 (Format)
LC	Ionosphere-free linear combination
LEO	Low Earth Orbit
LEX	L-Band Experimental (Signal)
LMV	Lantmaeteriverket (National Land Survey of Sweden)
LOD	Length of Day
LRA	Laser Retroreflector Array
MADEV	Modified Allan Deviation
MEO	Medium Earth Orbit
MGEX	Multi-GNSS Experiment
ML	Maximum Likelihood
MP	Multipath
MW	Microwave
NAVSTAR	Navigation System with Time and Ranging
NCEP	National Centers for Environmental Prediction
NEQ	Normal Equation (System)
NMF	Niell Mapping Function
NNR	No-Net-Rotation
NORAD	North American Aerospace Defense Command

NP	Normal Point
Ntrip	Networked Transport of RTCM via Internet Protocol
NTU	Nanyang Technological University
OHB	Orbitale Hochtechnologie Bremen
OOC	On-Orbit-Checkout
OS	Open Service
PCO	Phase Center Offset
PCV	Phase Center Variation
PFM	Proto-Flight Model
PHM	Passive Hydrogen Maser
PPP	Precise Point Positioning
PRN	Pseudo-Random Noise
PRS	Public Regulated Service
QZS	Quasi-Zenith Satellite
QZSS	Quasi-Zenith Satellite System
RAFS	Rubidium Atomic Frequency Standard
RESSOX	Remote Synchronization for an Onboard Crystal Oscillator
RETICLE	Real–Time Clock Estimation
RFS	Rubidium Frequency Standard
RINEX	Receiver Independent Exchange (Format)
RMS	Root Mean Square
RPR	Radiation Pressure
RTCM	Radio Technical Commission for Maritime Services
SA	Selective Availability
SAIF	Submeter-class Augmentation with Integrity Function
SAR	Search and Rescue
SBAS	Satellite Based Augmentation System
SBF	Septentrio Binary Format
SLR	Satellite Laser Ranging
SST	Satellite-to-Satellite Tracking
STD	Standard Deviation
SPS	Standard Positioning Service
SVN	Space Vehicle Number
TLE	Two-Line Elements
TRF	Terrestrial Reference Frame
TUD	Technische Universiteit Delft, Netherlands
TUM	Technische Universität München, Germany
UNB	University of New Brunswick, Canada
UNSW	University of New South Wales, Australia

USNO	United States Naval Observatory, USA
UTC	Universal Time Coordinated
UTCSR	University of Texas Center for Space Research, USA
VLBI	Very Long Baseline Interferometry
VMF1	Vienna Mapping Function 1
WAAS	Wide Area Augmentation System
WRMS	Weighted RMS
ZD	Zenith Delay
ZWD	Zenith Wet Delay

B Multi-GNSS Receiver Tracking Capabilities

Receiver	GPS			GLONASS			Galileo					BeiDou			QZSS				SBAS		Channels
	L1	L2	L5	L1	L2	L3	E1	E5a	E5b	E5	E6	B1	B2	B3	L1	L2	L5	LEX	L1	L5	
JAVAD TRE_G2T DELTA	x	x	x				x	x				[a]							x	x	216
JAVAD TRE_G3TH DELTA	x	x	x	x	x	[c]	x	x	[c]	[c]		[b]	[c]		x	x	x		x	x	216
LEICA GRX1200+GNSS	x	x	x	x	x		[d]	[d]	[d]	[d]									x		120
SEPT ASTERX3	x	x	x	x	x	x	x	x	x	x		x	x		x	x	x		x		136
SEPT GENERX	x	x					x	x	x	x	x										16
SEPT POLARX4TR	x	x	x	x	x	x	x	x	x	x		x	x						x		264
TRIMBLE NETR9	x	x	x	x	x	x	x	x	x	x		x	x	x	x	x	x	x	x	x	440

[a] Board TRE_G2TH_4 or newer
[b] Board TRE_G3TH_4 or newer
[c] Board TRE_G3TH_8 or newer
[d] tracking only possible for satellites with synchronized clocks

Tab. B.1: Tracking capabilities of multi-GNSS receivers used in the CONGO and MGEX networks. E5 stands for the E5 AltBOC signal.

C Lists of Multi-GNSS stations

C.1 Cooperative Network for GNSS Observation

Abb.	Location	Country	Inst.	Receiver	Format	Caster
AUTO	Austin	USA	DLR	JAVAD TRE_G3TH DELTA	JPS	MGEX
CHOF[a]	Chofu	Japan	DLR	JAVAD TRE_G2T DELTA	JPS	MGEX
COX1	Concepcion	Chile	BKG	SEPT GENERX	decommissioned	
CONX	Concepcion	Chile	BKG	JAVAD TRE_G3TH DELTA	JPS	MGEX
DAVE	Davis	Antarctica	GA	LEICA GRX1200+GNSS	LB2	BKG
HRAG	Hartebeesthoek	South Africa	DLR	JAVAD TRE_G2T DELTA	JPS	MGEX
JOGJ[b]	YogYakarta	Indonesia	GFZ	JAVAD TRE_G3TH DELTA	decommissioned	
JOG2	YogYakarta	Indonesia	GFZ	JAVAD TRE_G3TH DELTA	JPS	GFZ
LLAG	LaLaguna	Teneriffe	DLR	JAVAD TRE_3TH DELTA	JPS	MGEX
LPGS	La Plata	Argentina	GFZ	JAVAD TRE_G3TH DELTA	JPS	GFZ
MAOO[a]	Maui	Hawaii, USA	DLR	JAVAD TRE_G3T DELTA	JPS	MGEX
NURK	Kigali	Ruanda	GFZ	JAVAD TRE_G3TH DELTA	JPS	GFZ
NYA2	Ny Alesund	Norway	GFZ	JAVAD TRE_G3TH DELTA	JPS	GFZ
OHIX	O'Higgins	Antarctica	BKG	LEICA GRX1200+GNSS	LB2	MGEX
OUS2	Dunedin	New Zealand	GFZ	JAVAD TRE_G3TH DELTA	JPS	GFZ
RIO2	Rio Grande	Argentina	GFZ	JAVAD TRE_G3TH DELTA	JPS	GFZ
SGOC	Colombo	Sri Lanka	GFZ	JAVAD TRE_G3TH DELTA	RINEX	offline
SIN0[a]	Singapore	Rep. of Singapore	DLR	JAVAD TRE_G2T DELTA	JPS	MGEX
SIN1[a]	Singapore	Rep. of Singapore	DLR	TRIMBLE NETR9	BINEX	MGEX
STFU	Stanford	USA	DLR	JAVAD TRE_3TH DELTA	JPS	MGEX
TASH	Tashkent	Uzbekistan	GFZ	JAVAD TRE_G3TH DELTA	JPS	GFZ
THTX[a]	Papeete	Tahiti	DLR	JAVAD TRE_3TH DELTA	RINEX	offline
ULAB	Ulaanbataar	Mongolia	GFZ	JAVAD TRE_G3TH DELTA	JPS	GFZ
UNBD	New Brunswick	Canada	UNB	JAVAD TRE_G2T DELTA	JPS	MGEX
UNX1	Sydney	Australia	DLR	SEPT GENERX	decommissioned	
UNX2[a]	Sydney	Australia	DLR	JAVAD TRE_3TH DELTA	JPS	MGEX
UNX3	Sydney	Australia	DLR	SEPT ASTERX3	SBF	MGEX
WIND	Windhook	Namibia	GFZ	JAVAD TRE_G3TH DELTA	JPS	GFZ
WTZ1	Wettzell	Germany	DLR	SEPT GENERX	decommissioned	
WTZ2	Wettzell	Germany	BKG	LEICA GRX1200+GNSS	LB2	MGEX
WTZ3	Wettzell	Germany	DLR	JAVAD TRE_G2T DELTA	JPS	MGEX

[a] QZSS-capable
[b] CONGO receiver moved from JOGJ to JOG2 on 06 February 2013

Tab. C.1: GNSS tracking stations of the CONGO network.

C.2 IGS Multi-GNSS Experiment

Abb.	Location	Country	Inst.	Receiver	Format	Caster
ABMF	Les Abymes	Guadeloupe	IGN	TRIMBLE NETR9	RTCM3	MGEX
DLF1	Delft	Netherlands	TUD	TRIMBLE NETR9	RINEX	offline
FTNA	Maopo'opo	Wallis and Futuna	CNES	TRIMBLE NETR9	RINEX	offline
GMSD	Nakatane	Japan	JAXA	TRIMBLE NETR9	BINEX	DLR
KIR8	Kiruna	Sweden	LMV	TRIMBLE NETR9	RTCM3	MGEX
KOUG	Kourou	French Guiana	CNES	LEICA GR10	RINEX	offline
KRGG	Port aux Francais	Kerguelen Island	CNES	LEICA GR10	RINEX	offline
KZN2	Kazan	Russia	KFU	TRIMBLE NETR9	BINEX	KFU
NKLG	N'Koltang	Gabon	CNES	TRIMBLE NETR9	RTCM3	MGEX
NRMG	Noumea	New Caledonia	CNES	TRIMBLE NETR9	RTCM3	MGEX
MYVA	Reykjahlid	Iceland	KEG	LEICA GR10	LB2	offline
ONS1	Onsala	Sweden	LMV	TRIMBLE NETR9	RTCM3	MGEX
REUN	Le Tampon	La Reunion	IGN	TRIMBLE NETR9	RTCM3	MGEX
SCRZ	Santa Cruz	Bolivia	DGFI	LEICA GR10	LB2	MGEX
SEYG	Pointe Larue	Seychelles	CNES	TRIMBLE NETR9	RINEX	offline
USN4	Washington	USA	USNO	SEPT POLARX4TR	RINEX	offline

Tab. C.2: Selected GNSS tracking stations of the IGS MGEX network used for Galileo, BeiDou, and QZSS orbit and clock determination.

C.3 Additional Stations

Abb.	Location	Country	Institution	Receiver	Format	Caster
CHEN	Chennai	India	Trimble	TRIMBLE NETR9	RINEX	offline
CUTA	Curtin	Australia	CUT	TRIMBLE NETR9	BINEX	DLR
MELB	Melbourne	Australia	Trimble	TRIMBLE NETR9	RINEX	offline

Tab. C.3: Additional GNSS tracking stations used in this thesis.

Acknowledgements

First of all I'd like to thank Urs Hugentobler for initiating and supervising this habilitation. He gave me valuable input for the studies presented in this theses. Thanks to Thomas Wunderlich (TUM) and Harald Schuh (GFZ) who were my official mentors. The studies on new GNSSs would not have been possible without a global network of multi-GNSS stations. Oliver Montenbruck (DLR) initiated the CONGO network as well as many studies on the new GNSSs. As chair of the IGS Multi-GNSS Working Group he pushed me to provide operational products for MGEX and he always had an answer to my scientific as well as technical questions. I am grateful to André Hauschild (DLR) and Carlos Rodriguez-Solano (TUM, now at Trimble) for supporting my analysis of the new GNSS and to Maik Uhlemann (GFZ, now at Alberding GmbH) for providing Galileo orbit and clock solutions for comparison purposes. Stefan Hackel (TUM, now at DLR) did many studies on the combination of Galileo microwave and SLR observations during his master thesis which is the basis for the results discussed in Sect. 9. Thanks to Ralf Schmid for an extremely careful proofreading of all papers he co-authored and his support regarding all antenna-related issues. I'd like to thank Thomas Artz (IGG Bonn), Sarah Tesmer (IGG Bonn, now at GeoInformation Bremen), and Volker Tesmer (DGFI, now at OHB) for computing VLBI solutions and many interesting discussions on this technique as well as Manuela Seitz (DGFI) for providing multi-technique combination results. Finally I'd like to thank all persons involved in the operation and maintenance of the CONGO and MGEX sites as well as infrastructure, in particular Uwe Hessels (BKG, Geodetic Observatory Wettzell), Georg Weber (BKG, Frankfurt), Markus Ramatschi (GFZ), and Richard Langley (UNB).